Magneto-optical determination of the in-depth magnetization profile in magnetic multilayers

Jaroslav Hamrle

▶ To cite this version:

HAL Id: tel-00002948

https://theses.hal.science/tel-00002948

Submitted on 4 Jun 2003

University Paris XI
UFR Scientifique d'Orsay
and
Faculty of Mathematics and Physics
Charles Univeristy in Prague

THESIS

Presented to obtain

THE DEGREE OF DOCTOR OF PHILOSOPHY
in the
UNIVERSITY PARIS XI IN ORSAY
and of the
CHARLES UNIVERSITY IN PRAGUE

by

Jaroslav HAMRLE

Subject:

Magneto-optical determination of the in-depth magnetization profile in magnetic multilayers

Defended on March, 24 2003 in front of the commission:

Jean-François Bobo .... Referee
Alain Brun .... President
Jacques Ferré .... Director
Ivan Ohlídal .... Member
Jaromír Pištora .... Referee
Štefan Višňovský ...... Director

"A Paul et Virginie
au tenon et à la mortaise
à la chèvre et au chou
à la paille et à la poutre
au dessus et au dessous du panier
à Saint Pierre et à Miquelon
à la une et à la deux
à la mygale et à la fourmi
au zist et au zest
à votre santé et à la mienne
au bien et au mal
à Dieu et au Diable
à Laurel et à Hardy"
et à ma petite Janďulka.

Acknowledgement

I have done my PhD thesis in the frame of a "co-tutelle" collaboration between two laboratories belonging to two Universities (the Charles University in Praha and the University Paris-Sud at Orsay). In this context, I have benefited of the complementary scientific knowledge and competence of two communities since I was working half time in Orsay and half time in Praha. I was pleased to have benefited of a grant from the French Minister of Foreign Affairs under the initial proposal of the French Embassy in Praha. I wish to acknowledge them for this exceptional opportunity. I am particularly grateful to the European Community for the granting of the final stage of my PhD through a Marie Curie Fellowship.

First I would like to express my great thanks to Prof. Ing. Štefan Višňovský, DrSc. I was really pleased to start magnetooptics with him. I am grateful to him for introducing me into this interesting research area and international research community. He strongly proposed me to develop a very fruitful scientific collaboration with the group of Dr. Jacques Ferré at the Laboratoire Physique des Solides in Orsay. We can now appreciate the efficiency of this collaboration.

Dr. Jacques Ferré is the person to whom I wish to present my deepest thanks. A large part of my work presented here has been done under his leadership. He has introduced me into many interesting and up-to-date problems. I have appreciated his permanent encouragements for solving many non trivial scientific problems. I wish also to thank him for his large amount of patience and his deep human understanding. Simply I would like to thank him to be a very nice and openminded boss.

I'm very grateful to Dr. Jean-François Bobo for his interest to my work and especially for reporting on my manuscript in a so short time. My large thanks belong to RNDr. Vladimír Kamberský who agreed to review on my thesis, but unfortunately could not come. I'm very grateful to Prof. Jaromír Pištora who agreed immediately to be reviewer and to provide his report in due time, even under such complex circumstances. I wish also to express my thanks to Prof. Alain Brun and Prof. Ivan Ohlídal who agreed to be members of my PhD jury.

Many projects could not be realized without my collaboration with the group of Dr. Pierre Beauvillain. I would like to express my best thanks to him for the very nice and fruitful cooperation, particularly about research on FM/non-FM interfaces and SHG generation.

I would like to thank a lot the official consultant of my these Dr. Miroslav Nývlt since he has spent much time to introduce me into many fields of physics and for his permanent pertinent advices. I'm grateful to him for the time and energy he reserved to me which far exceeded his consultant's duties. As an example, without his large help and patience, the project about FM/non-FM interface would not be realized.

i

Preamble

How to introduce my present work? What physics means today? Ask child at elementary school. The answer you usually obtain is: A boring subject. His/her parents answer that they also didn't understand it well and notice something uncertain about Einstein. Then, when you precise that your subject is not the general relativity but optics, they ask you what camera is the best to buy.

But today physics is something on the half way between these two points of view. Now, it is not a philosophy and the period when great men like sir Isaac Newton, Michael Faraday, Albert Einstein, Paul Heisenberg, Wolfgang Pauli, etc... founded their theories to try to better understand basics principles of the world, is an old history. On the other hand, physics is neither the techniques or technology. physics laboratories are not a companies creating or improving some useful stuff like the camera.

The general definition for the old dame Physics, coming from Aristoteles's times, is "a science describing nature and discovering it's principles". But even the honorable old dame Physics needs to adapt to the society where she lives. The fact is that she now belongs to society where the fundamental interaction is business and particles responsible for this interaction is money. Simply, our honorable old Dame needs money. And, fortunately, she has founded how to reach them and hold her face. To get the money means to produce something useful, so finally she produces some knowledge useful for improving and creating technical stuff which makes life easier. You know, people are disposed to pay a lot for an easier life.

So, if you see Physics like an honorable old Dame coming from Aristoteles's time, this work contributed a little bit to her richness. I walked along one way laying between two old domains – optics and magnetism. This narrow path is called magnetooptics and in last twenty years a lot of physicists followed it. We can consider that almost everything along this path was discovered. But if you walk slowly and attentively you find out a great richness even along paths followed by hundreds of people.

On the other hand, if you see Physics like a flexible Dame accepting and following ideas of the society where she lives she must be able to bring the small florets to the overfeed market. I'm happy that it's possible to introduce my florets like useful "goods" without white lying advertisement.

However, many people prefer numbers to flowers. How to express my contribution to the old dame Physic for them? Maybe a good feeling can be that my work has added about 3 new millimeters of physical papers to kilometers of physical journals stored on shelves.

Contents

Chapter 1

Introduction

Magnetism is an old subject in physics and the basic magnetic properties of bulk materials are now quite well understood. Nevertheless, since the 80's, there was a growing interest for metallic thin film magnetism. This was directly related to the new offered possibilities to prepare high quality ultrathin films, multilayers and even superlattices and to characterize them at a nanometer scale (e.g. by scanning microscopes like STM, AFM). Thin film engineering is a new area developing fast since decades. By that way, it became possible to design multilayer structures with targeted magnetic properties. This improvement allowed to discover new phenomena, such as the giant magnetoresistance, a property that was exploited rapidly to manufacture recording heads. New hybrid structures including non-magnetic or magnetic oxide layers are now extensively studied to improve the tunnel magnetoresistance or to strengthen the exchange biased anisotropy. The tendency is now to reduce and control the lateral dimensions of thin magnetic elements down to the nanometer range. This has generated the new nano-magnetism area. The nano-structuration of magnetic thin film structures is obviously of great interest to realize, for example, high density recording media and a new generation of Magnetic Random Access Memories (MRAMs).

All these new applications require well controlled ultrathin metallic thin film structures. The static magnetic properties (e.g. hysteresis loop) of the full film structure are generally determined by sensitive magnetometry measurements. However, it is often difficult to separate the magnetic contributions of all the involved ultrathin magnetic layers, while a clear interpretation of the magnetization reversal process requires such an information. The techniques able to partly answer to this challenge, which is crucial for applications, are generally time consuming (Mössbauer) or need large scale instruments (polarized neutrons, XMCD). On the other hand, it is well known that optical interferometry (for example, the Michelson) is a perfect tool to check small distance variations down to 0.1 nm. As a consequence, polarized light interferometry must give information on the in-depth profile of the magnetization in a multilayer structure, which is one of the goals of this work.

In Chapter 2, I will recall the change of the light polarization state by magnetism, introduce and define the Magneto-Optical Kerr Effect (MOKE) and describe MOKE set-ups. The next Chapter 3 is dedicated to the calculation of MOKE; here I present a rigorous mathematical background required in the rest of this work.

Most of the magnetic properties in ultrathin film structures are driven by interface characteristics. It is an extremely hard task to check the magnetic properties of each

interface. This is due to the small amount of material forming the interfaces and to the difficulty of testing buried interfaces. In Chapter 4, I will propose a new technique allowing MOKE to give some insight about the magneto-optical properties of buried interfaces. This technique is then successfully used to determine magneto-optical properties of the Co/Au interfaces.

In Chapter 5, I will show how MOKE can be used to separate the magnetic contributions of the different magnetic ultrathin layers, even for non-magnetic spacer layers as thin as 1 nm. This depth sensitivity is obviously related to the variation of the optical path, but it is still true if layers are built with the same material. In other words, chemical selectivity is not needed here as for XMCD. In Chapter 5, I have also developed a simple theory for determining the most pertinent parameters responsible of the in-depth sensitivity of MOKE. This theory was tested satisfactorily in Co/Au, $TbFe/Si_3N_4$ model structures and in GaMnAs double tunnel junctions.

Another interesting application of MOKE is the investigation of the magnetism of ultrathin ferromagnetic films (thickness<1 nm) deposited on vicinal surfaces, as treated in Chapter 6. We discovered a new magneto-optical effect, called VISMOKE, which I describe theoretically by the lowering of the symmetry at the vicinal surface.

It has been shown recently [for overview see e.g. [1, 2]] that non-magnetic and magnetic properties of surfaces may be elegantly probed by a new emergent technique, the Magneto-Optics on the Second Harmonic Generation (MOSHG) of light. More interesting is that this technique can be also used to check the magnetism of buried interfaces in multilayer structures. Up to now, only one paper was reporting qualitatively on that task [3], because there is only an available theoretical treatment for free surfaces [4].

In Chapters 7 and 8, I will propose a new theoretical treatment of SHG and MOSHG in multilayer structures based on electric point dipoles located on the interfaces. In spite of the ignorance of most of the non-linear susceptibility tensor elements, it is possible to state some general rules about the SHG and MOSHG interface selectivity. I applied this theory to interpret important features in MOSHG hysteresis loops exhibited by interesting film structures like NiFe/NiO/Co spin-valve (showing a 90° coupling between FeNi and Co in-plane spins), and DyFeCo a magneto-optical perpendicular recording media, capped with FeSi showing in-plane anisotropy. I demonstrated the complementarity of the results obtained by MOKE and MOSHG in different optical geometries.

These new techniques will be important in future for performing layer-selective magneto-optical domain microscopy and high frequency dynamics in multilayer structures, designed for applications to spin-electronics. It is exciting to say that there is still place for new outstanding developments in magneto-optics for investigating thin film structures and even nano-magnetic structures in far and near-field configurations.

Chapter 2

Magneto-optical effects

This work is devoted to the study of Ferromagnetic (FM) metallic multilayer structures by means of Magneto-Optics (MO). The aim of this Chapter is to introduce and define Magneto-Optical Kerr Effect (MOKE) and to describe the used MOKE set-ups.

Historically, the first manifestation of a magneto-optical effect was demonstrated by Michael Faraday in 1846 [5]. He found that the linear polarization of the light was rotated after passing through a glass rod submitted to a magnetic field. This rotation, known as Faraday rotation, is proportional to the applied magnetic field H. The first observation of the modification of the light polarization state by a magnetized metallic iron mirror was done by John Kerr in 1877 [6]. He found that this MO effect in reflection was proportional to the sample magnetization M. Today, MOKE is widely used as a tool to investigate the field or temperature magnetization state in FM and ferrimagnetic samples, as it combines several advantages with respect to other techniques [7]:

- MOKE is a very sensitive technique that can compete with the best SQUID magnetometry, especially to study the magnetism of ultrathin films [8]. It can detect the magnetization of a fraction of Atomic Layer (AL) of the FM material.

- MOKE can be a very fast method and the short duration of the light/matter interaction allows time resolved measurements of the magnetization. Using a femtosecond pulsed laser, time resolution down to 100 fs has been achieved [9].

- MOKE provides a rather good lateral resolution, down to $0.2\,\mu$m. Thus, it allows to observe magnetic domains [10, 11] or to study the spatial distribution of the magnetization in wedge samples or nanostructures like FM wires [12, 13], patterned magnetic arrays [14], self-organized magnetic structures [15], etc.

- MOKE is depth sensitive and thus, in principle, it can provide independent informations on the magnetic state of several FM layers in a multilayer structure. I will focus here on this property since it is one of the main goals of my work (see Chapter 5). This selectivity comes from the variation of the MOKE phase originating from FM layers located at different depths inside the multilayer structure. Thus, it will be demonstrated that MOKE can distinguish:

    (i) FM layers made of the *same* FM material, separated by a spacer of thickness down to a few nanometers ("phase contrast").

(ii) FM layers made of *different* materials. Then obviously each FM layer provides a MO signal with a different phase, and thus their contributions can be separated as well, even for zero spacer thickness ("chemical contrast").

MOKE probes samples over a depth which is the penetration depth of light. In the case of metallic multilayer structures (most of the samples treated in this work), the penetration depth is about 20 nm. Thus, compared to integral techniques (e.g. SQUID or sample vibrating magnetometer), MOKE could be considered as a surface sensitive technique, which has been claimed by several authors who even called it Surface MOKE (SMOKE) [16]. On the other hand, compared to magnetometry or magnetic microscopy techniques using electrons, which are only sensitive to a few atomic layers localized at the film surface (e.g. spin polarized LEED, STM or photoemission), MOKE has to be considered as a magnetic in-depth sensitive technique allowing to study buried FM layers.

- Finally, MOKE measurements are relatively easy and cheap to do. Furthermore, it is possible to investigate samples located at a "long distance" from the light source and the detector. This explains why MOKE is so popular to study thin film magnetism inside vacuum chambers or under extreme conditions (field, temperature, etc.).

2.1   Light polarization states

In this Section, I present the basic properties of an electromagnetic (EM) wave, its complex representation and the description of the polarization state of the light.

2.1.1   Time and spatial evolution of an EM wave

Electromagnetic waves are characterized by an electric field $\boldsymbol{E}$ and a magnetic field $\boldsymbol{H}$, related by Maxwell equations. It can be shown that the knowledge of the electric part alone provides a full description of the EM wave [refs. [17] or see Eq. (3.11)].

The EM plane wave at a frequency ω propagates in a direction imposed by the light wavevector $\boldsymbol{k}^{(\omega)}$. The time ($t$) and space ($\boldsymbol{r}$) propagation of the general EM wave, $\boldsymbol{E}^{(\omega)} = [E_x^{(\omega)}, E_y^{(\omega)}, E_z^{(\omega)}]$, is described by the following equations

$$
\begin{aligned}
E_x^{(\omega)}(\boldsymbol{r}, t) &= E_{x,\mathrm{max}}^{(\omega)} \cos(\omega t - \boldsymbol{k}^{(\omega)} \cdot \boldsymbol{r} - \delta_x^{(\omega)}) \\
E_y^{(\omega)}(\boldsymbol{r}, t) &= E_{y,\mathrm{max}}^{(\omega)} \cos(\omega t - \boldsymbol{k}^{(\omega)} \cdot \boldsymbol{r} - \delta_y^{(\omega)}) \\
E_z^{(\omega)}(\boldsymbol{r}, t) &= E_{z,\mathrm{max}}^{(\omega)} \cos(\omega t - \boldsymbol{k}^{(\omega)} \cdot \boldsymbol{r} - \delta_z^{(\omega)}),
\end{aligned}
\tag{2.1}
$$

where $E_{x,\mathrm{max}}^{(\omega)}$, $E_{y,\mathrm{max}}^{(\omega)}$, $E_{z,\mathrm{max}}^{(\omega)}$ are the maximum values of the electric field components in the x, y, z directions, having phase retardations $\delta_x^{(\omega)}$, $\delta_y^{(\omega)}$, $\delta_z^{(\omega)}$. Thus, such a description of the EM wave requires the knowledge of these 6 parameters.

To provide a simple description, the complex representation and the polarization state of the EM wave, are introduced in the following.

2.1.2   Complex representation of the electromagnetic wave

As the EM wave in each x, y, z direction is described by both its maximal value $E_{j,\mathrm{max}}$ and its absolute phase δ_j, $j = \{x, y, z\}$, one prefers to use the complex representation of
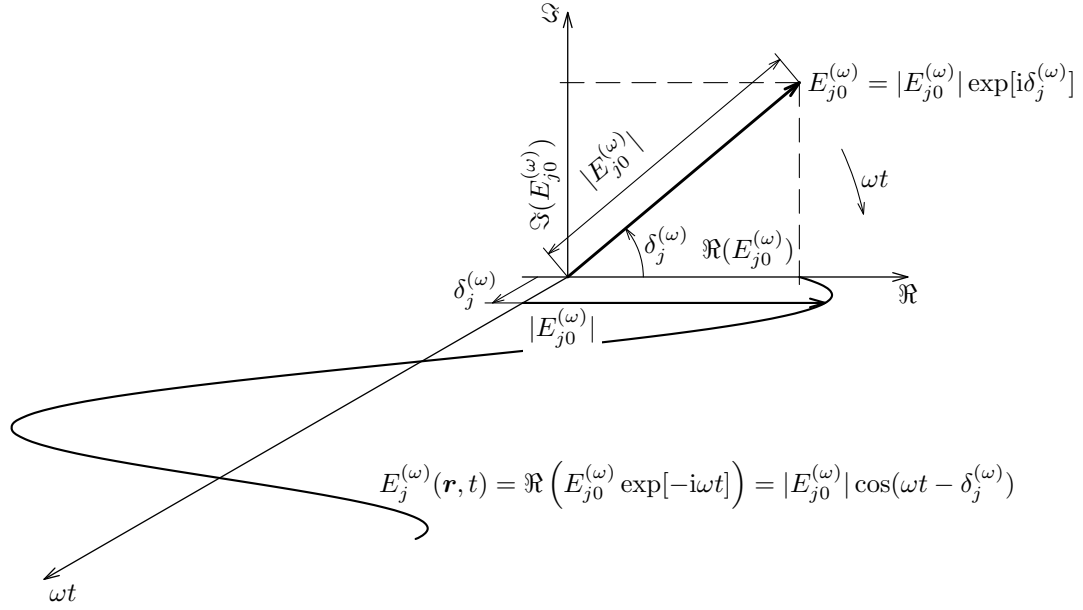
Figure 2.1: Relation between the complex representation of the j-th component of the electric field $E_{j0}^{(\omega)} = |E_{j0}^{(\omega)}| \exp[i\delta_j^{(\omega)}]$ and the time dependence of the measurable value of the electric field. As the time t increase, the electric field vector in the complex plane rotates clockwise, its phase being $(\delta_j^{(\omega)} - \omega t)$. The projection of the vector onto the real axis corresponds to the actual, real (i.e. measurable) value of the electric field $\Re(E_{j0}^{(\omega)} \exp[-i\omega t])$. Note that a clockwise rotation of the electric field is only a matter of convention, corresponding here to the used "time convention $\exp[-i\omega t]$".

the electric field. In this representation, both $E_{j,\max}^{(\omega)}$ and $\delta_j^{(\omega)}$, are expressed by only one complex variable $E_{j0}^{(\omega)}$:

$$E_{j0}^{(\omega)} = E_{j,\max}^{(\omega)} \exp[i\delta_j^{(\omega)}], \quad j = \{x, y, z\}, \tag{2.2}$$

where obviously $E_{j,\max}^{(\omega)} = |E_{j0}^{(\omega)}|$ and $\delta_j^{(\omega)} = \arg(E_{j0}^{(\omega)})$. Thus, the time and the spatial dependence of the EM wave, equivalent to Eq. (2.1), can be expressed as (Figure 2.1)

$$E_j^{(\omega)}(\boldsymbol{r}, t) = \Re\left(E_{j0}^{(\omega)} \exp[-i\omega t + i\boldsymbol{k}^{(\omega)} \cdot \boldsymbol{r}]\right), \quad j = \{x, y, z\}, \tag{2.3}$$

where $\Re$ denotes the real part of the following expression and $E_j^{(\omega)}(\boldsymbol{r}, t)$ is the real, i.e. measurable component of the electric field, $E_{j0}^{(\omega)}$ being expressed in the *complex representation*. In the real word, the electric field is *never* complex. Since this complex representation of the electric field is very powerful, all alternating variables at light frequency ω, e.g. the electric field $\boldsymbol{E}^{(\omega)}$, electric induction $\boldsymbol{D}^{(\omega)}$, magnetic induction $\boldsymbol{H}^{(\omega)}$ and magnetic field $\boldsymbol{B}^{(\omega)}$ will be *always expressed in the complex representation*.

Note that the sign of the exponent in Eqs. (2.2) and (2.3) derives only from the convention used in this work. In articles and books, such convention is usually called "time convention $\exp[-i\omega t]$".

2.1.3 Introduction of the light polarization

The solution of Maxwell equations imposes that the EM wave is transverse in case of an isotropic medium. This means that $\boldsymbol{E}^{(\omega)}$ and $\boldsymbol{H}^{(\omega)}$ are perpendicular to each other and

to the direction of light propagation $\boldsymbol{k}^{(\omega)}$, i.e. $\boldsymbol{E}^{(\omega)} \cdot \boldsymbol{k}^{(\omega)} = 0$, $\boldsymbol{H}^{(\omega)} \cdot \boldsymbol{k}^{(\omega)} = 0$ [17]. Hence, the electric field $\boldsymbol{E}^{(\omega)}$ at a given position and time can be expressed in a 2D basis,

$$\boldsymbol{E}^{(\omega)} = \mathcal{E}_{\mathtt{s}}^{(\omega)} \hat{e}_{\mathtt{s}}^{(\omega)} + \mathcal{E}_{\mathtt{p}}^{(\omega)} \hat{e}_{\mathtt{p}}^{(\omega)} \qquad (2.4)$$

where $\hat{e}_{\mathtt{s}}^{(\omega)}$, $\hat{e}_{\mathtt{p}}^{(\omega)}$ are the *modal vector polarizations*, both perpendicular to $\boldsymbol{k}^{(\omega)}$ and having unitary lengths. Furthermore, both vector modal polarizations are perpendicular to each other, i.e. $\hat{e}_{\mathtt{s}}^{(\omega)} \cdot \hat{e}_{\mathtt{p}}^{(\omega)} = 0$. From a mathematical point of view, the vector modal polarizations form a basis of a 2D space, in which any electric field vector $\boldsymbol{E}^{(\omega)}$, propagating in the $\boldsymbol{k}^{(\omega)}$ direction, can be expressed. $\mathcal{E}_{\mathtt{s}}^{(\omega)}$, $\mathcal{E}_{\mathtt{p}}^{(\omega)}$ are the *modal amplitudes*, weighting the contributions of the vector modal polarizations $\hat{e}_{\mathtt{s}}^{(\omega)}$, $\hat{e}_{\mathtt{p}}^{(\omega)}$. As follows from Eq. (2.4), their values can be determined from the relations $\mathcal{E}_{\mathtt{s}}^{(\omega)} = \boldsymbol{E}^{(\omega)} \cdot \hat{e}_{\mathtt{s}}^{(\omega)}$ and $\mathcal{E}_{\mathtt{p}}^{(\omega)} = \boldsymbol{E}^{(\omega)} \cdot \hat{e}_{\mathtt{p}}^{(\omega)}$, with $\mathcal{E}_{\mathtt{s/p}}^{(\omega)} = |\mathcal{E}_{\mathtt{s/p}}^{(\omega)}| \exp[i\delta_{\mathtt{s/p}}]$.

For a given pair $\hat{e}_{\mathtt{s}}^{(\omega)}$, $\hat{e}_{\mathtt{p}}^{(\omega)}$, and for given ω and $\boldsymbol{k}^{(\omega)}$, it is possible to describe completely the EM wave by only a pair of modal amplitudes $\mathcal{E}_{\mathtt{s}}^{(\omega)}$, $\mathcal{E}_{\mathtt{p}}^{(\omega)}$, which are generally complex [in spite of 6 parameters needed to describe the EM wave by Eq. (2.1)].

Typical vector modal polarizations can be either linearly or circularly polarized [18]. In this work, for isotropic media, we will use only the linearly polarized basis $\hat{e}_{\mathtt{s}}^{(\omega)}$, $\hat{e}_{\mathtt{p}}^{(\omega)}$ where the $\mathtt{s}$ and $\mathtt{p}$ directions are respectively perpendicular and parallel to the plane of incidence of the light (Appendix A). Figure 2.2 shows how an EM wave can be decomposed into $\mathtt{s}$ and $\mathtt{p}$ linearly polarized waves.

2.1.4   Elliptic polarization state

One of the characteristics of the light is its polarization state. The space and time dependence of the $\mathtt{s}$ and $\mathtt{p}$ modal amplitudes write [Eqs. (2.3)(2.4)]

$$\begin{aligned}
\mathcal{E}_{\mathtt{s}}^{(\omega)}(\boldsymbol{r}, t) &= \Re\left(\mathcal{E}_{\mathtt{s0}}^{(\omega)} \exp[-i\omega t + i\boldsymbol{k}^{(\omega)} \cdot \boldsymbol{r}]\right) \\
\mathcal{E}_{\mathtt{p}}^{(\omega)}(\boldsymbol{r}, t) &= \Re\left(\mathcal{E}_{\mathtt{p0}}^{(\omega)} \exp[-i\omega t + i\boldsymbol{k}^{(\omega)} \cdot \boldsymbol{r}]\right).
\end{aligned} \qquad (2.5)$$

Let us look to the time dependence of the extremity of $\boldsymbol{E}^{(\omega)}$ [Eq. (2.4)] at a given position $\boldsymbol{r}$. In general, its extremity describes an elliptic trajectory, called the polarization ellipse, which fully describes the polarization state of the light (Figure 2.2).

To describe[1] a general elliptic polarization, we need to know the values of two of following four quantities (see Fig. 2.2):

- **the azimuth θ_a:** is the rotation angle between the principal axis of the polarization ellipse and the $\mathtt{s}$ direction. By convention, a positive azimuth is characterized by an anti-clockwise rotation of the polarization ellipse when looking onto the incoming light beam.

- **the ellipticity ϵ_a:** is related to the ratio between the minor, b, and principal, a, axes of the polarization ellipse, by $\tan \epsilon_a = b/a$. A positive ellipticity corresponds to a clock-wise rotation of the extremity of $\boldsymbol{E}^{(\omega)}$ when looking onto the incoming light beam. In this case, we have a so-called right-handed polarized wave.

---

[1]We do not take into account the absolute light phase and light intensity.
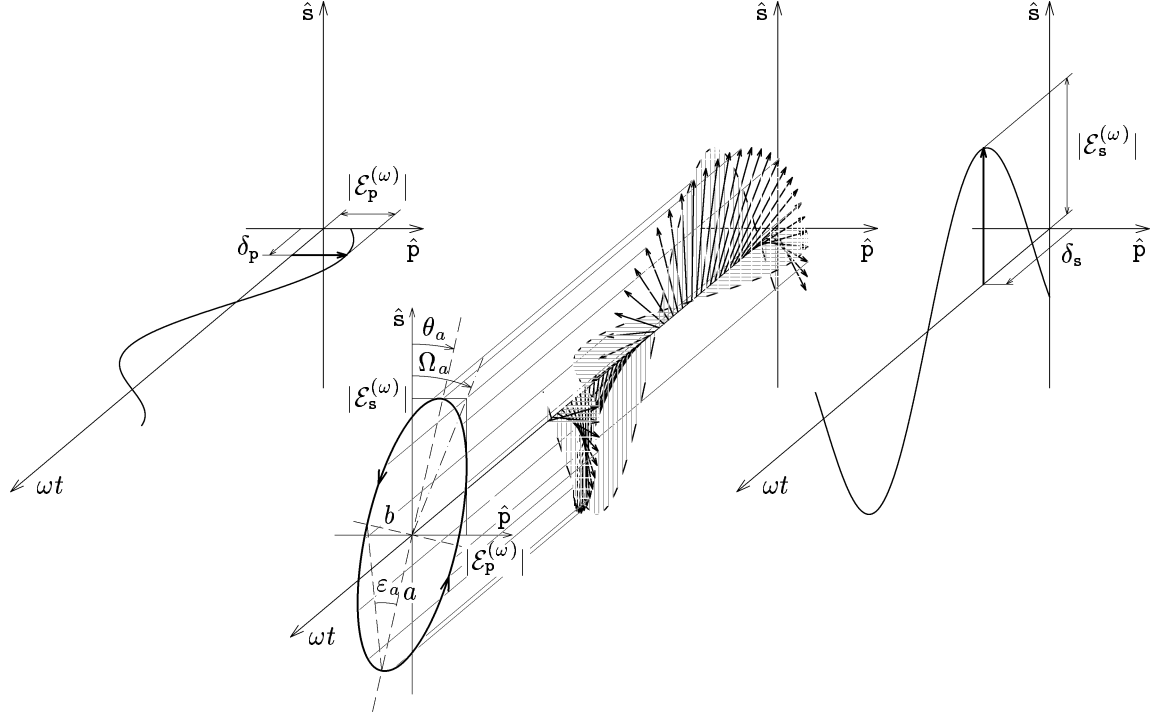
Figure 2.2: Time evolution of the electric field vector $\boldsymbol{E}^{(\omega)}$ at a given spatial position, decomposed along the **s** (right) and **p** (left) directions. When looking along the incoming light beam, the extremity of $\boldsymbol{E}^{(\omega)}$ describes a polarization ellipse (center). The presented polarization ellipse has a positive azimuth θ_a and a negative ellipticity ϵ_a.

- **the ratio between p and s modal amplitudes:** $\tan \Omega_a = |\mathcal{E}_{\mathrm{p}}^{(\omega)}|/|\mathcal{E}_{\mathrm{s}}^{(\omega)}| = |\mathcal{E}_{\mathrm{p}0}^{(\omega)}|/|\mathcal{E}_{\mathrm{s}0}^{(\omega)}|$. It expresses the ratio of the maximal values of the electric field in the p and s directions.

- **the phase shift between p and s modal amplitudes**: $\xi_a = \arg(\mathcal{E}_{\mathrm{p}}^{(\omega)})-\arg(\mathcal{E}_{\mathrm{s}}^{(\omega)}) = \arg(\mathcal{E}_{\mathrm{p}0}^{(\omega)}) - \arg(\mathcal{E}_{\mathrm{s}0}^{(\omega)}) = \delta_p - \delta_s$.

As already told, the variables ϵ_a, θ_a, Ω_a, ξ_a are not independent to each other. For example, they are related by the following three independent relations [18]

$$\tan 2\theta_a = \tan 2\Omega_a \cos \xi_a \tag{2.6}$$

$$\sin 2\epsilon_a = \sin 2\Omega_a \sin \xi_a \tag{2.7}$$

$$\tan \Omega_a \exp[i\xi_a] = \frac{\mathcal{E}_{\mathrm{p}}^{(\omega)}}{\mathcal{E}_{\mathrm{s}}^{(\omega)}} = \frac{\mathcal{E}_{\mathrm{p}0}^{(\omega)}}{\mathcal{E}_{\mathrm{s}0}^{(\omega)}} = \frac{\tan \theta_a - i \tan \epsilon_a}{1 + i \tan \theta_a \tan \epsilon_a}. \tag{2.8}$$

2.1.5   Jones formalism

When a polarized light passes through optical elements, its polarization state is, in general, modified. This can be described in the framework of the Jones formalism [18, 19]. In the following, we restrict ourselves to the Jones formalism within a proper base of linearly polarized s and p waves. The Jones vector J is defined by the pair of modal amplitudes $\mathcal{E}_s^{(\omega)}$, $\mathcal{E}_p^{(\omega)}$ for s or p polarized light as

$$J = \begin{bmatrix} \mathcal{E}_s^{(\omega)} \\ \mathcal{E}_p^{(\omega)} \end{bmatrix}. \tag{2.9}$$

Assuming, that the polarization response of optical elements such as the sample, mirror, polarizer, etc, is linear in $\mathcal{E}_s^{(\omega)}$, $\mathcal{E}_p^{(\omega)}$, it can be expressed by a matrix product. For example, the change of the polarization state, caused by reflection on a sample, is described by the reflection matrix R

$$\begin{aligned} J_- &= R \cdot J_+ \\ \begin{bmatrix} \mathcal{E}_{s,-}^{(\omega)} \\ \mathcal{E}_{p,-}^{(\omega)} \end{bmatrix} &= \begin{bmatrix} r_{ss} & r_{sp} \\ r_{ps} & r_{pp} \end{bmatrix} \begin{bmatrix} \mathcal{E}_{s,+}^{(\omega)} \\ \mathcal{E}_{p,+}^{(\omega)} \end{bmatrix} \end{aligned} \tag{2.10}$$

where J_+ and J_- are Jones vectors of the incident (+) and reflected (-) beams, respectively. The sign $+$ or $-$ is related to the light beam propagation in or against the z-direction. The Jones matrices reported in Appendix B for some other optical elements.

2.2   Definition of Magneto-Optical Kerr Effect (MOKE)

Let us consider a magnetized sample submitted to a linearly polarized s-wave. After reflection, the outcoming wave becomes partly p-polarized, so that the reflected beam becomes elliptically polarized (Figure 2.3). MOKE is related to the change of the polarization state after reflection on the sample. Depending whether the incident light beam is s or p-polarized, we will distinguish s or p-MOKE.

There are *two equivalent* definitions of MOKE. The first is based on the polarization state of the reflected light beam. The second relates MOKE to the ratio between reflection coefficients.

(i) In the first definition, the Kerr rotation θ stands for the clock-wise rotation of the main axis of the polarization ellipse (when looking at the incoming light beam) with respect to the incident s or p polarization. This definition corresponds to the ancient definition of Voigt postulating that a positive rotation corresponds to the direction of an electric current in a coil producing magnetic field in the z-direction, i.e. when the magnetic field is oriented along the sample normal, with direction of the normal incident beam. Comparing this definition to that of the azimuth angle θ_a (Section 2.1.4), we found following relationships

$$\theta_s = -\theta_a \qquad \theta_p = -\theta_a + 90°. \tag{2.11}$$

The s (p)-Kerr ellipticity ϵ_s, (ϵ_p) is defined as the ellipticity of the reflected light state, i.e.

$$\epsilon_s = \epsilon_a \qquad \epsilon_p = \epsilon_a. \tag{2.12}$$
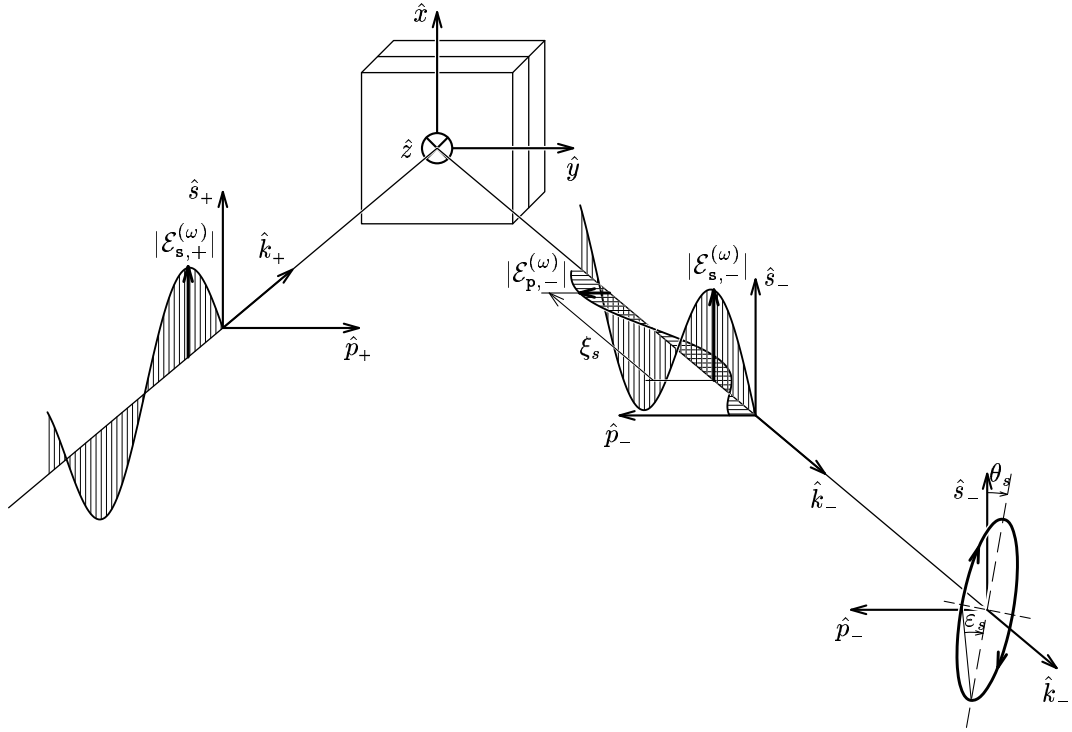
Figure 2.3: s-MOKE $\Phi_{\mathsf{s}} = \theta_{\mathsf{s}} + i\epsilon_{\mathsf{s}} = \Omega_s \exp[i\xi_{\mathsf{s}}]$ provided after reflection on the sample. The s-Kerr rotation θ_{s} and s-Kerr ellipticity ϵ_{s} describe the azimuth and ellipticity of the polarization ellipse. The s-Kerr phase ξ_{s} denotes the phase shift between p and s-components of the reflected wave. On this Figure, $\theta_{\mathsf{s}} > 0$, $\epsilon_{\mathsf{s}} > 0$.

This MOKE definition is independent on any sign convention, which is the main advantage. However, for practical use this definition is often unadapted.

(ii) Thus, MOKE is preferably defined as the ratio between reflection coefficients. From the comparison of Eqs. (2.11)(2.12) with Eq. (2.8), and taking into account that $\theta \ll 1$ and $\epsilon \ll 1$, the complex Kerr effect writes (for sign conventions, see Appendix A):

$$\Phi_{\mathsf{s}} = -\frac{\mathcal{E}_{\mathsf{p},-}^{(\omega)}}{\mathcal{E}_{\mathsf{s},-}^{(\omega)}} = -\frac{r_{\mathsf{ps}}}{r_{\mathsf{ss}}} = \theta_{\mathsf{s}} + i\epsilon_{\mathsf{s}} = \Omega_{\mathsf{s}}e^{i\xi_{\mathsf{s}}}$$

$$\Phi_{\mathsf{p}} = \frac{\mathcal{E}_{\mathsf{s},-}^{(\omega)}}{\mathcal{E}_{\mathsf{p},-}^{(\omega)}} = \frac{r_{\mathsf{sp}}}{r_{\mathsf{pp}}} = \theta_{\mathsf{p}} + i\epsilon_{\mathsf{p}} = \Omega_{\mathsf{p}}e^{i\xi_{\mathsf{p}}},$$

$$(2.13)$$

where Φ_{s}, (Φ_{p}) are s, (p) complex MOKE, later called s, (p)-MOKE, respectively. The coefficients r_{ss}, r_{pp} are the diagonal, whereas r_{sp}, r_{ps} are the off-diagonal elements of the reflection matrix **R** [defined by Eq. (2.10)]. $\mathcal{E}_{\mathsf{s},-}^{(\omega)}$, $\mathcal{E}_{\mathsf{p},-}^{(\omega)}$ are the modal amplitudes of light reflected by the sample. Because modal amplitudes and reflection coefficients are, in general, complex numbers, MOKE is obviously expressed by a complex number as well. The real part of MOKE is the Kerr rotation θ, while the imaginary part is the Kerr ellipticity ϵ [Eq. (2.8)]. We introduce MOKE in its
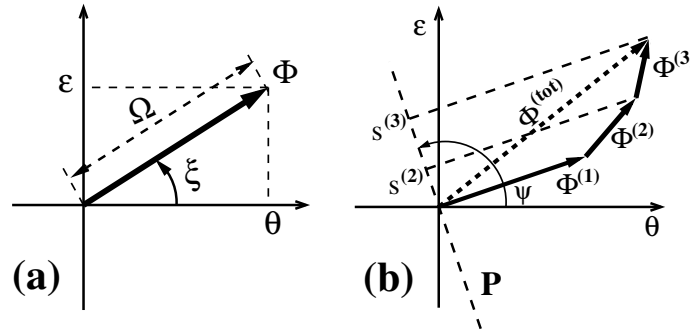
Figure 2.4: Representation of MOKE in the $\theta\epsilon$-plane. (a) The Kerr vector Φ is described either by Kerr rotation θ and Kerr ellipticity ϵ, or by the Kerr amplitude Ω and Kerr phase ξ. (b) The total Kerr effect $\Phi^{(\text{tot})}$ is given by the sum over different Kerr contributions $\Phi^{(i)}$. The measured Kerr signal $s^{(i)}$ for each FM layer is deduced from the *projection* of the Kerr vector $\Phi^{(i)}$ on the projection axis P, the orientation of which is determined by the projection angle ψ.

polar form $\Phi = \Omega \exp[i\xi]$, where Ω is the Kerr amplitude and ξ the Kerr phase [Figure 2.4(a)]. I chose this representation to simplify the formalism in our further study of the MOKE in-depth resolution (Chapter 5). The physical meaning of Ω and ξ are the following: For p-MOKE, the Kerr amplitude $\Omega_{\mathsf{p}} = |\mathcal{E}_{\mathsf{s},-}^{(\omega)}|/|\mathcal{E}_{\mathsf{p},-}^{(\omega)}|$ is the ratio between the modal amplitudes of the s and p parts of the reflected light. The Kerr phase is equal to the phase shift between these two waves, i.e.

$$
\begin{aligned}
\xi_{\mathsf{p}} &= \arg(\mathcal{E}_{\mathsf{s},-}^{(\omega)}) - \arg(\mathcal{E}_{\mathsf{p},-}^{(\omega)}) = \delta_{\mathsf{s}} - \delta_{\mathsf{p}} = \xi_a && \text{(for p−MOKE)} \\
\xi_{\mathsf{s}} &= \arg(\mathcal{E}_{\mathsf{p},-}^{(\omega)}) - \arg(\mathcal{E}_{\mathsf{s},-}^{(\omega)}) = \delta_{\mathsf{p}} - \delta_{\mathsf{s}} = -\xi_a && \text{(for s−MOKE)}.
\end{aligned}
\tag{2.14}
$$

2.2.1   Basic geometries of MOKE:

The sample normal direction and the plane of incidence (yz) naturally define the pertinent directions in the light-sample referential system. These directions coincide with the axes $\hat{x}$, $\hat{y}$, $\hat{z}$ of the Cartesian referential (Appendix A) and serve also as reference directions for the magnetization (see also Fig. 2.3). The coefficients of the reflection matrix $\mathbf{R}$ (and thus of MOKE) depend differently on each reduced sample magnetization components $m_j = M_j/M$, where $j = \{x, y, z\}$ and M_j, M are the j-th component and the total sample magnetization, respectively. The dependence of MOKE on the sample magnetization is treated in detail in Section 3.3; here we will just give a qualitative picture considering symmetry arguments.

Historically, the generic MOKE arrangements were called polar ($\boldsymbol{M} \parallel \hat{z}$), longitudinal ($\boldsymbol{M} \parallel \hat{y}$), and transverse ($\boldsymbol{M} \parallel \hat{x}$) configurations. These situations correspond to the magnetization purely oriented along the normal of the sample (polar), in the plane of incidence (longitudinal) and perpendicular to it (transverse). The reflection matrix corresponding to these MOKE configurations and its parity with the incidence angle φ are reported in Table 2.1.

On Table 2.1, the positive direction of polar and transverse magnetizations is opposite to that of the z and x axis, respectively. This is a consequence of the historical convention [20, 21] supposing that the correct sign for the polar and transverse MOKEs is given for normalized sample magnetizations $\boldsymbol{m} = [0, 0, -1]$ and $\boldsymbol{m} = [-1, 0, 0]$, respectively.
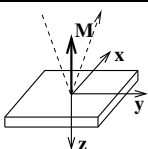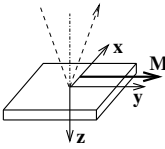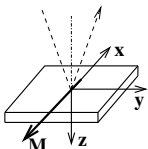
		normal incidence $\varphi = 0$	oblique incidence $\varphi \neq 0$	symmetries of the reflection coefficients
polar $\boldsymbol{m} = [0, 0, -1]$		$\begin{bmatrix} r_{\mathrm{ss}} & r_{\mathrm{ps}} \\ r_{\mathrm{ps}} & -r_{\mathrm{ss}} \end{bmatrix}$	$\begin{bmatrix} r_{\mathrm{ss}} & r_{\mathrm{ps}} \\ r_{\mathrm{ps}} & r_{\mathrm{pp}} \end{bmatrix}$	$r_{\mathrm{ss}}, r_{\mathrm{pp}}$: indep. on m_z even in φ $r_{\mathrm{sp}} = r_{\mathrm{ps}}$: odd in m_z even in φ
longitudinal $\boldsymbol{m} = [0, 1, 0]$		$\begin{bmatrix} r_{\mathrm{ss}} & 0 \\ 0 & -r_{\mathrm{ss}} \end{bmatrix}$	$\begin{bmatrix} r_{\mathrm{ss}} & -r_{\mathrm{ps}} \\ r_{\mathrm{ps}} & r_{\mathrm{pp}} \end{bmatrix}$	$r_{\mathrm{ss}}, r_{\mathrm{pp}}$: indep. on m_y even in φ $r_{\mathrm{sp}} = -r_{\mathrm{ps}}$: odd in m_y odd in φ
transverse $\boldsymbol{m} = [-1, 0, 0]$		$\begin{bmatrix} r_{\mathrm{ss}} & 0 \\ 0 & -r_{\mathrm{ss}} \end{bmatrix}$	$\begin{bmatrix} r_{\mathrm{ss}} & 0 \\ 0 & r_{\mathrm{pp}}^{(0)} + r_{\mathrm{pp}}^{(\mathrm{mag})} \end{bmatrix}$	$r_{\mathrm{ss}}, r_{\mathrm{pp}}^{(0)}$: indep. on m_x even in φ $r_{\mathrm{pp}}^{(\mathrm{mag})}$: odd in m_x odd in φ

Table 2.1: Reflection matrices **R** for different configurations of the sample magnetization $\boldsymbol{M}$ with respect to the light referential $(\hat{x}, \hat{y}, \hat{z})$. The last column shows the symmetry of MO observables with sample magnetization and incidence angle φ. The coefficient $r_{\mathrm{pp}}^{(0)}$ and $r_{\mathrm{pp}}^{(\mathrm{mag})}$ express the part of the r_{pp} reflection coefficient, which is constant and linear with m_x magnetization component, respectively.

From Table 2.1, it follows that polar m_z and longitudinal m_y magnetization components induce the off-diagonal reflection coefficients r_{sp} and r_{ps}. Thus, MOKE Φ, defined by Eq. (2.13), depends only on polar and longitudinal magnetization components. MOKE signals induced by these magnetization components are called Polar (PMOKE) and Longitudinal (LMOKE) MOKE, respectively. Both PMOKE and LMOKE configurations have in common that the magnetization lies in the plane of incidence. This is not the case anymore in the transverse configuration. In this case, the transverse magnetization m_x induces only a variation of the diagonal reflection coefficient r_{pp} at non-zero incidence angle $\varphi \neq 0$ (Table 2.1). Thus, no Kerr rotation and ellipticity are expected in this configuration. However, analogously to the MOKE definition [Eq. (2.13)], the Transverse MOKE (TMOKE) $\tilde{\Phi}_{\mathrm{tra}}$ is defined as

$$\tilde{\Phi}_{\mathrm{tra}} = \frac{r_{\mathrm{pp}}^{(\mathrm{mag})}}{r_{\mathrm{pp}}^{(0)}}. \qquad (2.15)$$

Since TMOKE is a different physical quantity than PMOKE and LMOKE, one only has to measure a variation of intensity. TMOKE can be measured by a simple arrangement: laser – polarizer (p) – sample – analyzer(p) – detector. Then the measured light intensity I_{p} varies with m_x as:

$$I_{\mathrm{p}} \sim |r_{\mathrm{pp}}^{(0)}|^2 + 2\Re \left(r_{\mathrm{pp}}^{(\mathrm{mag})} (r_{\mathrm{pp}}^{(0)})^{\dagger} \right) m_x = |r_{\mathrm{pp}}^{(0)}|^2 \left[1 + 2\Re(\tilde{\Phi}_{\mathrm{tra}})m_x \right], \qquad (2.16)$$

where † denotes the complex conjugate. We have neglected the quadratic contribution in m_x, since $|r_{\mathrm{pp}}^{(0)}| \gg |r_{\mathrm{pp}}^{(\mathrm{mag})}|$. The experimental set-ups measuring PMOKE and LMOKE

will be presented later in Section 2.4.

2.2.2 Different types of MO effects

In the previous Section, I introduced the generic MOKE effects: Polar (PMOKE), Longitudinal (LMOKE) and Transverse (TMOKE). In this Section, I give an overview of all first order MO effects, linear in magnetization. MO effects quadratic in magnetization [10, 22, 23] will not be considered in this work. Hence, MO effects linear in magnetization can be classified in different ways:

- One important classification of MO effects refers to the detected light frequency, compared to that probing the sample (at frequency ω). Thus, the light intensity can be measured either at the same frequency ω or at harmonic frequencies 2ω, 3ω, etc. The second harmonic (2ω) MO effects are treated only in Chapters 7 and 8. Before only MOKE measured at the fundamental frequency ω is considered.

- MO effects can be measured in light reflection (usually called Kerr effects) or in transmission (called Faraday effects).

- It is sometimes important to distinguish whether the MO effect depends on the sample magnetization $\boldsymbol{M}$ or on the external magnetic field $\boldsymbol{H}$. This can give some insight about the microscopic origin of a given MO effect (see Section 2.3). I shall consider only the effect proportional to $\boldsymbol{M}$

- The MO signal can be measured in "far field" (i.e. that the distance between the sample and the detector is much larger than the light wavelength) or in 'near-field', (i.e. in the opposite case). Here only far-field investigations are reported.

- Depending on the direction of the magnetic field, with respect to the sample normal and the plane of light incidence, one distinguishes three generic MO effects, called polar ($\boldsymbol{M} \parallel \hat{z}$), longitudinal ($\boldsymbol{M} \parallel \hat{y}$) and transverse ($\boldsymbol{M} \parallel \hat{x}$) one, as already discussed for MOKE (Table 2.1). Faraday effect in transmission is obviously able to measure polar magnetization, but also longitudinal and transverse components for a sample tilted in the light beam (i.e. $\varphi \neq 0$).

- New types of Kerr effects can arise under particular conditions. Cite for example:
  - the gradient MOKE [24], which is proportional to the *gradient* of the magnetization. This effect was evidenced in domain walls.
  - the Vicinal Induced Surface MOKE (VISMOKE) originally reported in the present work (Chapter 6), which is linear in magnetization, but induced by a coupling at second order between magnetic and structural perturbations.

2.2.3 Graphical representation of MOKE in the $\theta\epsilon$-plane

Because the MOKE Φ is described by a complex number, it can be visualized as a Kerr vector in the complex plane, here called $\theta\epsilon$-plane. Then, the variation with incidence angle, photon energy, thickness of the overlayer, etc. can be described by a variation of the Kerr vector in the $\theta\epsilon$-plane. The representation of MOKE in the $\theta\epsilon$-plane fulfills the following general properties [Fig. 2.4(a)(b)]:

- The projection of the Kerr vector on the real axis gives the Kerr rotation θ, and on the imaginary axis, the Kerr ellipticity ϵ. The length of the Kerr vector corresponds to the Kerr amplitude Ω and its orientation to the Kerr phase ξ [Eq. (2.13)].

- In a multilayer structure containing several FM layers, the individual MOKE, $\Phi^{(i)}$, originating from the i-th FM layer is proportional to components of the related normalized magnetization $\boldsymbol{m}^{(i)} = [m_x^{(i)}, m_y^{(i)}, m_z^{(i)}]$. Since MOKE is insensitive to the transverse component m_x at the first perturbation order in magnetization (Section 2.2.1), the total measured MOKE $\Phi^{(\text{tot})}$ is given by the sum of all individual polar and longitudinal contributions:

$$\Phi^{(\text{tot})} = \sum_i \Phi_{\text{pol}}^{(i)} \, m_z^{(i)} + \sum_i \Phi_{\text{lon}}^{(i)} \, m_y^{(i)}. \tag{2.17}$$

  where $\Phi_{\text{pol}}^{(i)}$, $\Phi_{\text{lon}}^{(i)}$ are the saturated values of the PMOKE, LMOKE, respectively, originating from the i-th layer. The additivity property of MOKE is represented on Fig. 2.4(b) by the summation of Kerr vectors for all individual FM layers.

- In the most general case, the experimental set-up measures a Kerr signal s, which is the projection of the complex Kerr effect Φ onto a projection axis making an angle ψ with the real axis θ [Fig. 2.4(b)]:

$$s = \Re\left(\Phi e^{-i\psi}\right). \tag{2.18}$$

  If the experimental set-up is designed so that the projection axis is parallel to the real axis ($\psi = 0$), then the Kerr rotation $s = \theta = \Re(\Phi)$ is measured. If the projection angle is $\psi = \pi/2$, one measures Kerr ellipticity $s = \epsilon = \Im(\Phi) = \Re(\Phi e^{-i\pi/2})$. The continuous variation of the projection angle ψ can be realized with a Babinet-Soleil compensator, as it will be shown in the Section 2.4.2.

2.3 Microscopic origin of the MO effects

Figure 2.5 shows the rather complicated way for evaluating the MO signal from microscopic informations. The measured MO signal is, within the microscopic world, proportional to the thermal and spatial average spin value $\langle \boldsymbol{S} \rangle$, proportional to the sample magnetization $\boldsymbol{M}$ in transition metals. In the following, we will go through the diagram presented on Figure 2.5 and comment on the influence of magnetism at each step.

2.3.1 Modification of the electronic structure by the "magnetic" Hamiltonian

Firstly, let us discuss how the magnetization modifies the electronic states of a bulk FM material. Neglecting the Zeeman term, the most important perturbations lifting the degeneracy of electronic states are the spin-orbit (SO) coupling and the exchange interaction.

The SO coupling, $\mathcal{H}_{SO} = \xi_{SO}\hat{\boldsymbol{L}} \cdot \hat{\boldsymbol{S}}$, is an interaction between the atomic orbital momentum $\hat{\boldsymbol{L}}$ and the atomic spin momentum $\hat{\boldsymbol{S}}$, ξ_{SO} being the interaction strength. In the frame of classical mechanics, the electron movement on its orbit is equivalent to a current loop creating a magnetic field [25]. In this atomic magnetic field, the spins of each
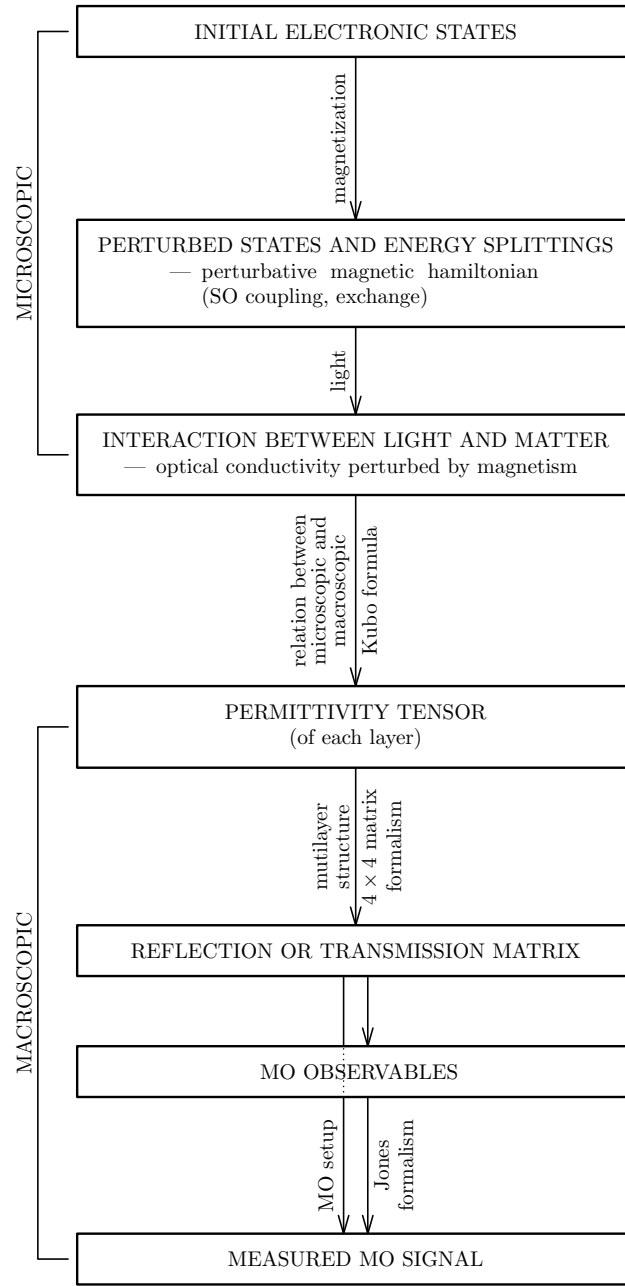
Figure 2.5: Schematic way relating the measured MO signal to microscopic parameters.

electron tending to align along the magnetization direction are energetically favored, as long as the Hund's rules are not violated. Intrinsically, the SO Hamiltonian, $\mathcal{H}_{SO}$, comes from relativistic effects [25, 26]. When the velocity of electrons is small as compared to the light speed in vacuum, $\mathcal{H}_{SO}$ can be considered as a small perturbation, and thus is treated within a perturbative approach.

The exchange interaction between the resulting spins of two neighboring atoms writes $\mathcal{H}_{\mathrm{ex}} = -J\hat{\boldsymbol{S}}_a\hat{\boldsymbol{S}}_b$, J being the exchange integral. Their parallel alignment is energetically
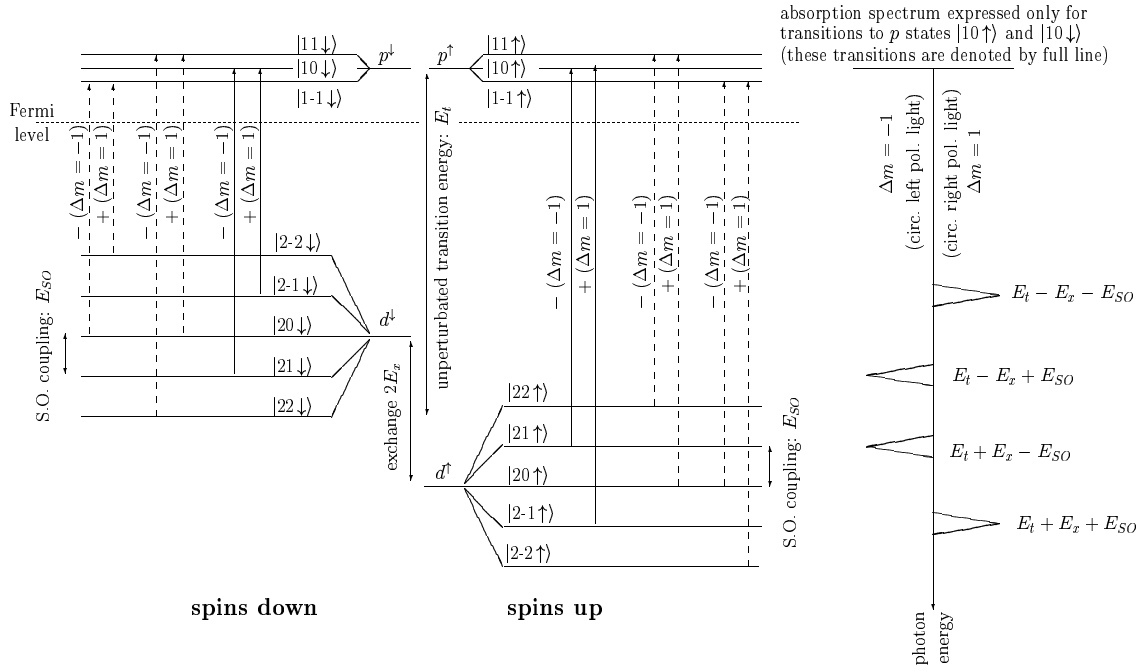
Figure 2.6: Schematic modification of the electronic structure of p and d states by "magnetic" perturbations. The arrows indicate the allowed electric dipole transitions. The right side of the picture shows the absorption spectra for left and right polarized light (inspired by [28]).

more favorable. This interaction comes from the Pauli principle and has a pure electrostatic origin [25, 27].

These perturbative "magnetic" Hamiltonians $\mathcal{H}_{SO}$ and $\mathcal{H}_{ex}$ induce energy level splittings. The exchange interaction splits the energy levels of the electronic states having up or down spins. Assuming a FM material magnetized along the "up" direction z, the up-spins electrons have smaller energy than the down-spins electrons. In the example presented on Figure 2.6, the exchange splitting in p levels is neglected. The left part of the figure shows the energy levels of electrons having "up" ($\uparrow$) and "down" ($\downarrow$) spin orientation. In the notation $|lm\uparrow\rangle$, $|lm\downarrow\rangle$, l is orbital number ($l = 1$ for p states and $l = 2$ for d states) and m stands for the magnetic number which takes integer values in the interval $\langle -l, l \rangle$. The SO coupling lifts the energy level degeneracy of m for both p or d states. Note that for up spins, the energy increases with m, although the situation is reversed for down spins (Figure 2.6).

2.3.2 Interaction between light and matter

The direct interaction between the magnetic field of the EM wave and the FM material spins is neglected, because spins are too "slow" to follow the alternating magnetic field at optical frequencies. Thus, the relative permeability of matter at optical frequencies is very close to $\mu_r = 1$ [17].

The most common mechanism for the interaction of light with matter is the absorption of *one* photon by *one* electron through an electric *dipole transition*. In this absorption process, the total energy and total linear, angular and spin momenta in the electron-photon

system are conserved. The conservation laws results to the selection rules [25], presented in Table 2.2.

$E_f - E_i = \hbar\omega$	: the energy between the final and initial state corresponds to the absorbed photon energy.
$\hbar\omega/c \approx 0$	: since the photon linear momentum is negligible compared to that of the electron, the linear angular momentum of the electron is approximately conserved (so-called vertical transitions).
$\Delta s = 0$	: the spin direction of the electron is not modified for an electric dipole transition.
$\Delta l = \pm 1$	: the total orbital momentum is conserved because the photon has an angular momentum equal to 1 (in units of $\hbar$). This rule specifies that the electric dipole transitions are allowed only between $s \leftrightarrow p$, $p \leftrightarrow d$, etc. states.
$\Delta m = \pm 1$	: the total orbital momentum along one (usually z) direction is conserved. The value of Δm specifies, if the absorbed photon is circularly left (-1) or right (+1) polarized, respectively.

Table 2.2: Selection rules for electric dipole transitions.

The electronic structure of matter is modified in the presence of the magnetization, as both the distance between energy levels and their population depend on magnetization. This obviously modifies the optical properties as well.

More quantitatively, the optical properties of an ion can be expressed by the Kubo formula [29, 30, 28]. Then, the dissipative parts of the conductivity tensor $\boldsymbol{\sigma}$ in a solid[2] can be expressed as ($\omega > 0$)

$$
\begin{aligned}
\Re[\sigma_{xx}(\omega)] &= \frac{\pi e^2}{2m_e^2\omega\Omega_c} \sum_{i,f} f(E_i)[1 - f(E_f)] \times \left[|\langle i|\hat{p}_+|f\rangle|^2 + |\langle i|\hat{p}_-|f\rangle|^2\right] \times \delta(E_f - E_i - h\omega) \\
\Im[\sigma_{xy}(\omega)] &= \frac{\pi e^2}{4m_e^2\omega\Omega_c} \sum_{i,f} f(E_i)[1 - f(E_f)] \times \left[|\langle i|\hat{p}_-|f\rangle|^2 - |\langle i|\hat{p}_+|f\rangle|^2\right] \times \delta(E_f - E_i - \hbar\omega),
\end{aligned}
$$
$$(2.19)$$

where ω is the light frequency, Ω_c the unit cell volume, $\hat{p}_\pm = \hat{p}_x \pm \hat{p}_y$ are the linear momentum operators (e.g. $\hat{p}_x = -i\hbar\,\partial/\partial x$). The summation runs over all "initial" $|i\rangle$ and "final" states $|f\rangle$. The constants e and m_e are the charge and the mass of the electron, respectively. The functions $f(E_i)$ and $[1 - f(E_f)]$ are Fermi functions, expressing the occupancy of the initial states and non-occupancy of the final states having energies E_i and E_f, respectively. The Dirac δ-function insures the energy conservation. The matrix elements $\langle i|\hat{p}_+|f\rangle$ and $\langle i|\hat{p}_-|f\rangle$ are the transitions probabilities for left (σ_+) and right (σ_-) polarized light, respectively. It can be shown [25], that these elements are non-zero, only if they respect the selection rules, given in Table 2.2.

An example of electric dipole transitions between d and p states is presented on Figure 2.6. As discussed in the previous Section 2.3.1, the energy levels are split by both the

---

[2]The relation between the conductivity tensor σ_{ij} and the permittivity tensor ε_{ij} writes $\varepsilon_{ij} = \delta_{ij} + (i/\omega)\sigma_{ij}$, as can be found from the Maxwell equations.

exchange and spin-orbit interactions. As follows from the selection rules (Table 2.2), all transitions are not allowed. In general, all $d \to p$ transitions have not the same energy. Furthermore, the variation of the magnetic number m of initial and final electronic states tells if the absorbed photon is σ_+ or σ_- polarized. Hence, the absorption spectra for σ_+ and σ_- polarized light are different, as it is sketched on the right side of Figure 2.6. Note that these σ_+, σ_- absorption spectra are identical only if exchange *or* spin-orbit interaction is zero. Thus, *to obtain MO active material, both spin-orbit coupling and exchange interaction have to be present*, in the ground or the excited states, as already pointed out by Hulme [31] in 1932.

So, in this Section, I have shown how the conductivity tensor $\boldsymbol{\sigma}$, thus the permittivity tensor $\boldsymbol{\varepsilon}$, and more specially the MOKE properties, can be evaluated for a bulk material.

2.3.3   Reflection matrix of the multilayer structure

In the case of a multilayer structure, it is assumed that the bulk optical parameters are valid even for a thin film [32]. Thus, we consider a multilayer structure as a stack of homogeneous (but generally optically anisotropic) layers separated by sharp interfaces, so that the in-depth profile of the optical properties is step-like. Within this framework of an idealized multilayer structure, the reflection matrix of the entire multilayer structure can be calculated (for details, see Chapter 3).

2.3.4   Reflection matrix and MOKE

The sample reflection matrix **R** is the only information accessible by means of optical measurements. Usually, the optical set-ups are designed to measure established MO observables, for example the s-Kerr rotation $\theta_s = -\Re(r_{ps}/r_{ss})$. However, depending on the type of optical set-up, one can measure different combinations of the reflection coefficients. In the following Section 2.4, we describe two types of MO set-up used in this work.

2.4   MOKE set-ups

There are numerous types of MO set-ups which can measure MOKE [33]. To significantly increase the sensitivity of MOKE measurements and improve the signal to noise ratio, it is preferable to use modulation techniques, associated to a lock-in phase detection. In the following Sections, I present two MO arrangements, where the modulation device is either a photoelastic modulator (Section 2.4.1) or a Faraday rotator (Section 2.4.3). Moreover, by adding a Babinet Soleil, the Kerr signal measured at a general projection angle ψ can be obtained (Section 2.4.2).

2.4.1   MOKE set-up using a photoelastic modulator

In this Section, I describe one of the MOKE set-up used at the Laboratoire de Physique des Solides at Orsay, working with a photoelastic modulator. I have extended its capabilities to work at variable wavelengths.

The photoelastic modulator [34] provides a time-dependent phase shift $\zeta = \zeta_0 \sin 2\pi f t$ at frequency $f \approx 50\,\text{kHz}$ between the incoming light polarization components. When the modulator principal axis coincides with s or p directions, the modulator response, in the
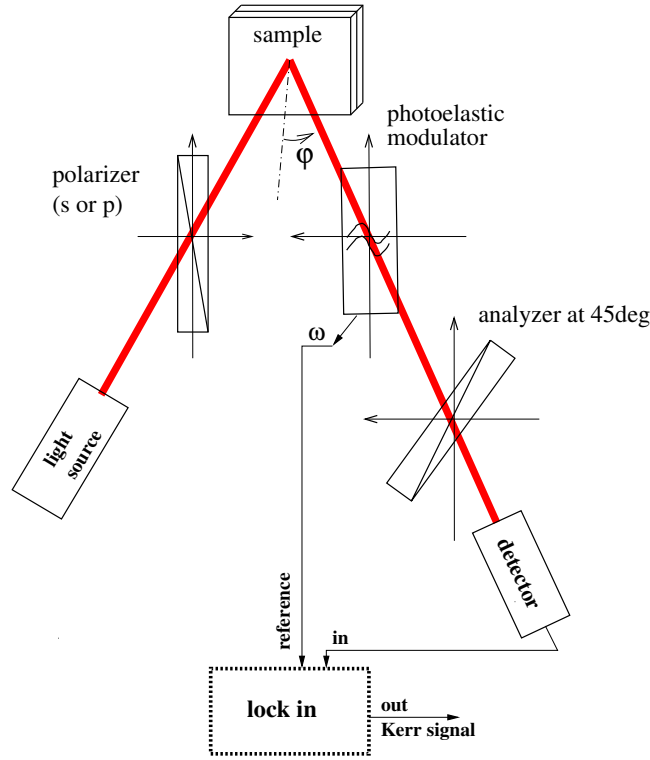
Figure 2.7: Sketch of the MO set-up using a photoelastic modulator.

framework of the Jones formalism, writes (Appendix B)

$$\mathsf{M} = \begin{bmatrix} \exp[-i\zeta/2] & 0 \\ 0 & \exp[i\zeta/2] \end{bmatrix}, \tag{2.20}$$

where the phase between **s** and **p** components of the incoming wave is changing with time. In another words, if it is positioned after the sample, the photoelastic modulator gives a modulation of the Kerr phase ξ, introduced in Eq.(2.13). For example, if the incident light beam is linearly polarized at $45°$, then the polarization of the outgoing light is varied between linear (for $\zeta = 0$, $\pm\pi$, etc.) and circular (for $\zeta = \pm\pi/2$, $\pm3\pi/2$, etc.) light polarization states.

The sketch of the corresponding MO set-up is shown on Figure 2.7. The light beam is generated by either an He-Ne laser emitting at wavelength 632 nm or a Xe lamp followed by a variable wavelength color filter working in the $420 - 900$ nm range. After the polarizer, the light is either **s**- or **p**-polarized. Then, the light beam is reflected on the sample and goes through a photoelastic modulator (with its principal axes parallel to the **s** and **p** directions), an analyzer (at $45°$), and the light intensity is collected on a detector (photomultiplier). The electric signal generated by the detector is processed by a lock-in phase detector, in order to select signals proportional to the modulator frequency f or at twice its frequency $2f$.

The optical response, treated in the Jones formalism for each optical element, is presented in Appendix B. If the polarizer transmits only **s**-polarized light, the polarization
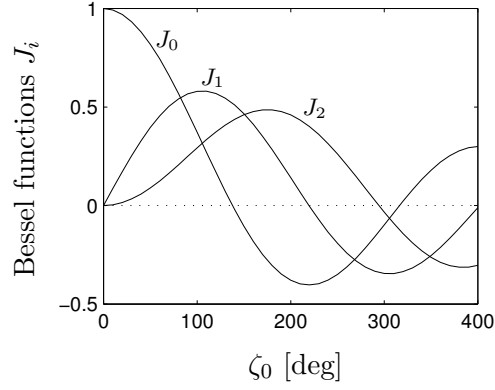
Figure 2.8: The angular dependence of Bessel functions $J_i(\zeta_0)$ for orders $i = \{0, 1, 2\}$.

state $\boldsymbol{J}_{\mathsf{s},\text{out}}$ on the detector is

$$\boldsymbol{J}_{\mathsf{s},\text{out}} = \mathbf{A}(45°)\mathbf{M}\mathbf{R}\boldsymbol{J}_{\mathsf{s},\text{in}} = \begin{bmatrix} 1 & 1 \\ 1 & 1 \end{bmatrix} \begin{bmatrix} e^{i\zeta/2} & 0 \\ 0 & e^{-i\zeta/2} \end{bmatrix} \begin{bmatrix} r_{\mathsf{ss}} & r_{\mathsf{sp}} \\ r_{\mathsf{ps}} & r_{\mathsf{pp}} \end{bmatrix} \begin{bmatrix} 1 \\ 0 \end{bmatrix} = \begin{bmatrix} r_{\mathsf{ss}}e^{i\zeta/2} + r_{\mathsf{ps}}e^{-i\zeta/2} \\ r_{\mathsf{ss}}e^{i\zeta/2} + r_{\mathsf{ps}}e^{-i\zeta/2} \end{bmatrix},$$
(2.21)

where $\zeta = \zeta_0 \sin 2\pi f t$. Similarly, for an initial p-polarized light beam, the same expression [Eq. (2.21)] is obtained, but the s- and p-components (1 and 0) of the light coming from the polarizer are interchanged. Coming back to the definition of the complex MOKE, $\Phi_{\mathsf{s}} = \theta_{\mathsf{s}} + i\epsilon_{\mathsf{s}} = -r_{\mathsf{ps}}/r_{\mathsf{ss}}$ and $\Phi_{\mathsf{p}} = \theta_{\mathsf{p}} + i\epsilon_{\mathsf{p}} = r_{\mathsf{sp}}/r_{\mathsf{pp}}$ [Eq. (2.13)], the light intensity measured by the detector is

$$\frac{I_{\mathsf{s},\text{out}}}{2} \approx |r_{\mathsf{ss}}|^2 + 2\Re(r_{\mathsf{ps}}r_{\mathsf{ss}}^\dagger e^{-i\zeta}) = |r_{\mathsf{ss}}|^2 + 2|r_{\mathsf{ss}}|^2(-\theta_{\mathsf{s}}\cos\zeta - \epsilon_{\mathsf{s}}\sin\zeta),$$
(2.22)
$$\frac{I_{\mathsf{p},\text{out}}}{2} \approx |r_{\mathsf{pp}}|^2 + 2\Re(r_{\mathsf{sp}}r_{\mathsf{pp}}^\dagger e^{i\zeta}) = |r_{\mathsf{pp}}|^2 + 2|r_{\mathsf{pp}}|^2(\theta_{\mathsf{p}}\cos\zeta - \epsilon_{\mathsf{p}}\sin\zeta)$$

where $\dagger$ denotes the complex conjugate form. In Eq. (2.22) we have neglected the small quadratic $|r_{\mathsf{sp}}|^2$, $|r_{\mathsf{ps}}|^2$ terms.

Using the Bessel functions J_i (presented on Figure 2.8), $\sin\zeta$ and $\cos\zeta$ can be expressed (up to the second harmonic modulation frequency $2f$) as [35]

$$\sin\zeta \approx 2J_1(\zeta_0)\sin 2\pi f t$$
$$\cos\zeta \approx J_0(\zeta_0) + 2J_2(\zeta_0)\cos 4\pi f t.$$
(2.23)

The light intensities are renormalized by I_0, the constant part of the detected MO signal. Finally, the measured fundamental (f) and second harmonic ($2f$) quantities are [33, 36, 37]

$$\frac{I_{\mathsf{s}}(f)}{I_0} = \frac{-4J_1(\zeta_0)\epsilon_{\mathsf{s}}}{1 - 2J_0(\zeta_0)\theta_{\mathsf{s}}} \qquad \frac{I_{\mathsf{s}}(2f)}{I_0} = \frac{-4J_2(\zeta_0)\theta_{\mathsf{s}}}{1 - 2J_0(\zeta_0)\theta_{\mathsf{s}}}$$
$$\frac{I_{\mathsf{p}}(f)}{I_0} = \frac{-4J_1(\zeta_0)\epsilon_{\mathsf{p}}}{1 + 2J_0(\zeta_0)\theta_{\mathsf{p}}} \qquad \frac{I_{\mathsf{p}}(2f)}{I_0} = \frac{4J_2(\zeta_0)\theta_{\mathsf{p}}}{1 + 2J_0(\zeta_0)\theta_{\mathsf{p}}}.$$
(2.24)

The contribution of θ_{s} and θ_{p} at the denominators of Eq.(2.24) are usually negligible compared to 1. However, it is better to set $\zeta_0 \approx 140°$ to fix $J_0 = 0$ (see Figure 2.8). Then, the f and $2f$ Kerr signals are rigorously proportional to the Kerr ellipticity ϵ and Kerr rotation θ, respectively.

2.4.2   Role of a Babinet-Soleil compensator

This Section reports on the influence of a Babinet-Soleil compensator on the measured Kerr signal, if it is inserted on the path of the reflected light beam, just after the sample. Then, the effective reflection matrix for the compensator – sample system expresses as

$$\mathbf{R}' = \begin{bmatrix} r'_{\mathrm{ss}} & r'_{\mathrm{sp}} \\ r'_{\mathrm{ps}} & r'_{\mathrm{pp}} \end{bmatrix} = \begin{bmatrix} e^{i\delta/2} & 0 \\ 0 & e^{-i\delta/2} \end{bmatrix} \cdot \begin{bmatrix} r_{\mathrm{ss}} & r_{\mathrm{sp}} \\ r_{\mathrm{ps}} & r_{\mathrm{pp}} \end{bmatrix} = \begin{bmatrix} r_{\mathrm{ss}}e^{i\delta/2} & r_{\mathrm{sp}}e^{i\delta/2} \\ r_{\mathrm{ps}}e^{-i\delta/2} & r_{\mathrm{pp}}e^{-i\delta/2} \end{bmatrix}, \qquad (2.25)$$

where δ is the phase retardation introduced by the Babinet-Soleil compensator.

Then, instead of measuring the ratios $\Phi_{\mathrm{s}} = -r_{\mathrm{ps}}/r_{\mathrm{ss}}$ and $\Phi_{\mathrm{p}} = r_{\mathrm{sp}}/r_{\mathrm{pp}}$, the MO set-up measures now the new ratios

$$\begin{aligned} \Phi'_{\mathrm{s}} &= -r'_{\mathrm{ps}}/r'_{\mathrm{ss}} = \Phi_{\mathrm{s}}e^{-i\delta} = (\theta_{\mathrm{s}}\cos\delta + \epsilon_{\mathrm{s}}\sin\delta) + i(\epsilon_{\mathrm{s}}\cos\delta - \theta_{\mathrm{s}}\sin\delta) \\ \Phi'_{\mathrm{p}} &= r'_{\mathrm{sp}}/r'_{\mathrm{pp}} = \Phi_{\mathrm{p}}e^{i\delta} = (\theta_{\mathrm{p}}\cos\delta - \epsilon_{\mathrm{p}}\sin\delta) + i(\epsilon_{\mathrm{p}}\cos\delta + \theta_{\mathrm{p}}\sin\delta). \end{aligned} \qquad (2.26)$$

If $\delta = 0$, the Kerr rotation, $\theta = \Re(\Phi)$, is measured. When the phase retardation is increased, the measured MOKE signal becomes a mixture of both the Kerr rotation and the Kerr ellipticity. For $\delta = 90°$, the MOKE signal is only the Kerr ellipticity.

Comparing Eqs. (2.18) and (2.26), we find that the variation of the projection angle ψ corresponds to that of the phase retardation δ. Depending whether the measured Kerr signal is s or p-MOKE, and whether the MO setup for $\delta = 0$ measures Kerr rotation or Kerr ellipticity, the relation between δ and ψ takes different forms, presented on Table 2.3.

projection angle ψ	exp. set-up measures:	
	Kerr rotation $\psi_0 = 0$	Kerr ellipticity $\psi_0 = \pi/2$
s-MOKE	$\psi = \delta$	$\psi = \pi/2 + \delta$
p-MOKE	$\psi = -\delta$	$\psi = \pi/2 - \delta$

Table 2.3: Relation between the projection angle ψ and the phase shift δ of the Babinet-Soleil compensator for different types of MO setups.

2.4.3   MOKE set-up using a Faraday rotator

In this Section I describe the MO set-up developed at The Charles University in Praha [32], which uses an azimuthal modulation of the polarization state of the light. We measure the spectral dependence of MOKE in the $1.2\,\mathrm{eV}$ – $5\,\mathrm{eV}$ spectral range. In the following, I restrict my presentation to p-MOKE measurements. The relations for s-MOKE measurements can be analogously derived.

The sketch of the MO set-up is presented on Figure 2.9. The light source is a high-pressure Xe-lamp, producing white light in the $1\,\mathrm{eV}$ – $6\,\mathrm{eV}$ spectral range. The photon energy is selected by a monochromator. The light is linearly polarized by the polarizer. Although we measure p-MOKE (i.e. quantity $\Phi_{\mathrm{p}} = r_{\mathrm{sp}}/r_{\mathrm{pp}}$) the polarizer is set up to transmit linearly s-polarized light. Then, the light beam crosses successfully two Faraday rotators FR1 and FR2. The azimuth of the polarization of the light after passing through a Faraday rotator is rotated by an angle proportional to the current established in the encircling solenoid. The first rotator FR1 serves to modulate the azimuth of the linearly
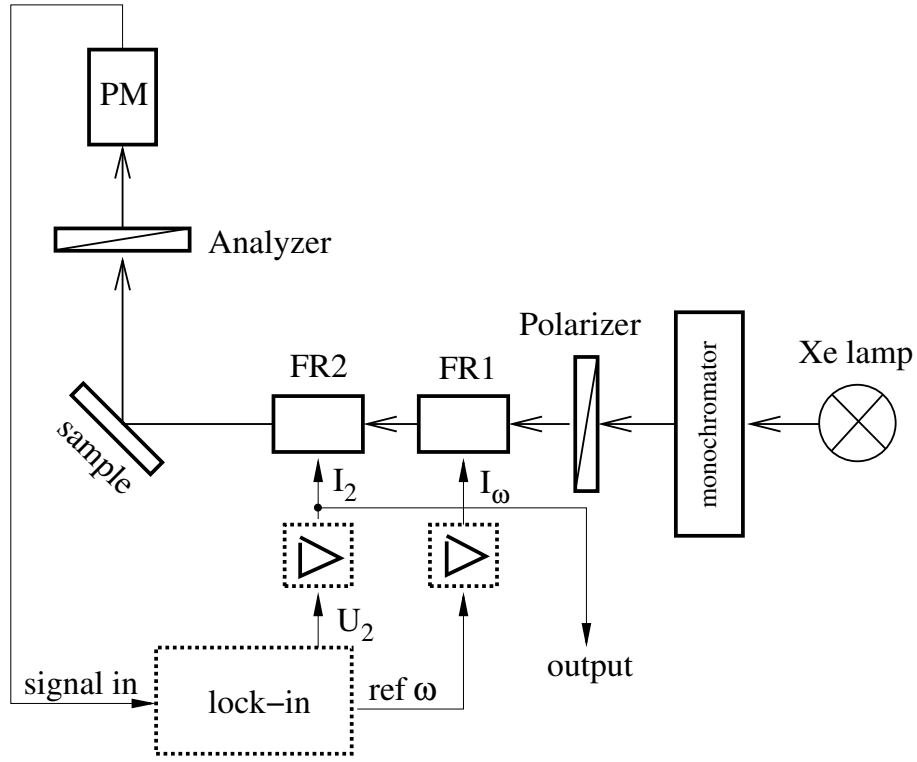
Figure 2.9: Sketch of the MO set-up using the Faraday rotators (FR1 and FR2).

polarized state at frequency $f \approx 12\,\text{kHz}$ by an angle $\zeta_1 \sin 2\pi ft$. The second rotator FR2 serves to compensate the sample Kerr rotation by a fixed angle ζ_2. Hence, after FR2, the resulting light polarization is described by a Jones vector

$$\boldsymbol{J}_+ = \begin{bmatrix} \cos\zeta \\ \sin\zeta \end{bmatrix}, \tag{2.27}$$

where

$$\zeta = \zeta_2 + \zeta_1 \sin 2\pi ft. \tag{2.28}$$

After reflection on the sample, characterized by a reflection matrix $\mathbf{R}$ (see Appendix B); the new polarization state becomes:

$$\boldsymbol{J}_- = \mathbf{R} \cdot \boldsymbol{J}_+. \tag{2.29}$$

Then, the analyzer selects only the p-component of the light polarization. Thus, the light intensity detected by the photomultiplier PM is

$$I_{\text{p}}/I_0' = |r_{\text{pp}}|^2 \sin\zeta \left[\sin\zeta + 2\Re\left(\frac{r_{\text{ps}}}{r_{\text{pp}}}\right) \cos\zeta \right], \tag{2.30}$$

where I_0' is the light intensity issued from FR2. After a lock-in phase detection of the signal, only its component at frequency f is selected. Taking into account that $\zeta \ll 1$, $|\Phi| \ll 1$, the detected light intensity at frequency f is expressed as [Eq. (2.28)]

$$I_f/I_0' = 2|r_{\text{pp}}|^2 \zeta_1 \left[\zeta_2 + \Re\left(\frac{r_{\text{ps}}}{r_{\text{pp}}}\right) \right] \sin 2\pi ft. \tag{2.31}$$

In order to measure the MOKE signal with high accuracy, FR2 is used to compensate I_f automatically with a feedback procedure to keep $I_f = 0$ (Figure 2.9). Then the electric current I_{FR2} in the solenoid placed around FR2 is adjusted automatically so that [Eq. (2.31)]

$$\zeta_2 = -\Re \left(\frac{r_{\mathsf{ps}}}{r_{\mathsf{pp}}} \right). \tag{2.32}$$

The MO signal is directly proportional to I_{FR2}, so that $\zeta_2 = A_{FR2} I_{FR2}$. The value of A_{FR2} depends obviously on the used photon energy, and thus the set-up has to be calibrated first.

Note that the experimental set-up measures a MO signal equal to $\tilde{\theta}_{\mathsf{p}} = -\Re(r_{\mathsf{ps}}/r_{\mathsf{pp}})$, although the p-Kerr rotation, defined as $\theta_{\mathsf{p}} = -\Re(r_{\mathsf{sp}}/r_{\mathsf{pp}})$, involves different off-diagonal reflection coefficients. However, as expressed in Table 2.1, $r_{\mathsf{sp}} = r_{\mathsf{ps}}$ for polar magnetization, and $r_{\mathsf{sp}} = -r_{\mathsf{ps}}$ for longitudinal magnetization. Hence, the value of the Kerr rotation θ can be expressed by

$$\theta_{\mathsf{p}} = g \, \Re \left(\frac{r_{\mathsf{ps}}}{r_{\mathsf{pp}}} \right) \qquad \theta_{\mathsf{s}} = g \, \Re \left(\frac{r_{\mathsf{sp}}}{r_{\mathsf{ss}}} \right), \tag{2.33}$$

where $g = \pm 1$ (see Table 2.4).

value of g	p-Kerr rotation	s-Kerr rotation
PMOKE	1	-1
LMOKE	-1	1

Table 2.4: Value of g determining the sign between the measured Kerr signal and the Kerr rotation [Eq. (2.33)].

The measurement of the Kerr ellipticity ϵ can be provided by an additional phase plate with a phase retardation $\delta = \pi/2$. A very similar situation has been already discussed in Section 2.4.2 (for details see [36]). Since the presented set-up measures the ratios $\Re(r_{\mathsf{ps}}/r_{\mathsf{pp}})$ or $\Re(r_{\mathsf{sp}}/r_{\mathsf{ss}})$, the phase plate has to be inserted between FR2 and the sample. As follows from results presented in the precedent Section 2.4.2, adding a Babinet Soleil compensator which fixes δ in the MO set-up, one measures a mixture of Kerr rotation and Kerr ellipticity. Thus, the Kerr ellipticity ϵ can be isolated if the phase retardation δ and Kerr rotation θ are known [36].

"...placer ensuite la toile contre un arbre
dans un jardin
dans un bois
ou dans une forêt
se cacher derrière l'arbre
sans rien dire
sans bouger ..."

Chapter 3

Calculation of the Magneto-Optical Kerr Effect (MOKE)

This Chapter starts by a definition of the mathematical spaces, in which electric field (and other alternating variables) can be expressed. In order to better describe the electromagnetic (EM) field inside a multilayer sample, I introduce a new mathematical space (q-space), where I choose to particularize the z direction to match to the sample "geometry", as the multilayer can be considered to be infinite in the plane (2D infinite), whereas it is finite along the growth direction (z). This definition is convenient in the case of MOKE, but it becomes essential later (Chapter 7), for the calculation of the light radiated by an oscillating electric point dipole, applied to Magneto-Optical Second Harmonic Generation of light (MOSHG).

Then, the classical calculation of MOKE by the 4×4 matrix formalism is introduced. This formalism gives the exact optical response of an ideal multilayer structure. The basic hypothesis are:

(i) All layers are homogeneous, generally anisotropic and separated by sharp interfaces, i.e. the profile of optical parameters is supposed to be step-like.

(ii) The optical properties of all layers are solely described by a second-rank permittivity tensor $\varepsilon_{ij}^{(\omega)}$ [38], relating the electric induction $\boldsymbol{D}^{(\omega)}$ to the electric field $\boldsymbol{E}^{(\omega)}$ so that $D_i^{(\omega)} = \varepsilon_0 \sum_j \varepsilon_{ij}^{(\omega)} E_j^{(\omega)}$, where $i, j = \{x, y, z\}$, and ε_0 is the permittivity of vacuum.

Although the 4×4 matrix formalism is valid for any type of multilayer structure fulfilling the above conditions, I use it here for the case of FM metallic multilayers. From an optical point of view, as already discussed in Section 2.3, the sample magnetization only modifies the permittivity tensor, giving rise to non-zero antisymmetric off-diagonal permittivity tensor elements for the FM layers ($\varepsilon_{ij}^{(\omega)} = -\varepsilon_{ji}^{(\omega)}$), with $i \neq j$.

The first presentation of the 4×4 matrix formalism to calculate MOKE was reported by D.O. Smith in 1964 [39]. Later, in 1980, this formalism was used by P. Yeh [40] to describe the light propagation in layered birefringent media. With the increase of interest

for magneto-optical recording media in the 1980's, calculations of magneto-optical effects by the 4×4 matrix formalism were widely used [16, 41, 42, 43]. The first numerical implementation of this formalism to magnetic multilayers was done by Š. Višňovský in 1991 [42, 44]. This 4×4 matrix formalism is rigorous with a relatively easy-to-program algorithm. However, a general analytical treatment by this formalism provides long and complex expressions. This is a consequence of the analytical expressions of proper modes of light propagating inside FM layers. Despite of the complexity of the expressions, J. Zak *et al.* in 1990 [45] used this formalism to derive analytical MOKE expressions in FM multilayers. These expressions can be simplified making some additive assumptions, for example, introducing the ultrathin FM film approximation, i.e. when the thickness of the FM layer is much smaller than the light wavelength, or for a special geometry [32, 45, 46, 47].

In order to give a more transparent derivation of MOKE, several approaches were proposed, assuming either small magnetic perturbations of the FM layer permittivity tensor, or using the ultrathin FM layer approximation. For example,

- A. Hubert *et al.* in 1992-1993 heuristically derived analytical forms of the first-order contribution to Kerr and Faraday effects from computer simulations [48], and consequently found additional terms originating from multiple reflections [49].

- Š. Višňovský *et al.* [36, 32, 50] expressed PMOKE from the diagonal reflectivity r of the non-magnetized sample, in the case of polar magnetization:

$$\Phi = -i\frac{\Delta r}{r} = -i\frac{1}{r}\left(\frac{\partial r}{\partial N^{(\mathrm{fm})}}\Delta N^{(\mathrm{fm})}\right), \tag{3.1}$$

  where $N^{(\mathrm{fm})}$ is the non-magnetic part of the refractive index of the FM layer. $\Delta r = (r_+ - r_-)/2$ and $\Delta N = (N_+ - N_-)/2$ are the differences between *circular* reflection coefficients and circular birefringence, respectively, for "up" and "down" magnetizations lying along the z-axis. For an arbitrary layered structure, the non-magnetized sample reflection coefficient r can be determined e.g. from the so-called Airy recursive formulae [19], that calculate the reflection coefficients of the entire multilayer structure by means of recursive fractions, each interface being represented by one "iteration".

- Recently, P. Bertrand *et al.* [51] used a perturbation approach to calculate MOKE. The electric induction of the FM layer, $\boldsymbol{D} = \varepsilon^{(\mathrm{iso})}\varepsilon_0\boldsymbol{E} + \Delta\boldsymbol{P}$, is expressed as the sum of the unperturbed electric induction $\varepsilon^{(\mathrm{iso})}\varepsilon_0\boldsymbol{E}$ and the perturbed polarization $\Delta\boldsymbol{P} = (\varepsilon^{(\mathrm{fm})} - \varepsilon^{(\mathrm{iso})})\varepsilon_0\boldsymbol{E}$, induced by "perturbative" components of the permittivity tensor of the FM layer. Thus, the calculation of the polarization state of the light inside the multilayer is separated into the propagation of the unperturbed (incident) polarization and light radiation generated by a perturbative polarization sheet having a polarization $\Delta\boldsymbol{P}$.

3.1 Mathematical description of the field in an unbounded medium in the q-space

The rigorous definition of a mathematical space, which gives the description of the EM field inside layered structures is often omitted. However, for a description of the EM field radiated by an *electric point dipole*, used later to describe Second Harmonic Generation of light (SHG) (Chapter 7 and Appendix D), its rigorous definition is necessary. That is why I propose here to introduce a new q-space.

3.1.1 Definition of the k and q-space

Before introducing the q-space, let us define the real 3D r-space and Fourier k-space. Any spatial distribution of the electric field can be described either in a real r-space as $\boldsymbol{E}(\boldsymbol{r})$ or in its Fourier transform (so-called k-space) as $\boldsymbol{\mathcal{E}_k}(\boldsymbol{k})$. The relationship between both quantities is a 3D Fourier transformation[1] [see Figure 3.1(a)(c)]

$$\boldsymbol{E}(\boldsymbol{r}) = \frac{1}{(2\pi)^3} \frac{1}{(k_0^u)^3} \iiint \mathrm{d}^3\boldsymbol{k}\, \boldsymbol{\mathcal{E}_k}(\boldsymbol{k})\, \exp[i\,\boldsymbol{k}\cdot\boldsymbol{r}]. \tag{3.2}$$

The factor $(1/k_0^u)^3$ equalizes the field units of $\boldsymbol{E}(\boldsymbol{r})$ and $\boldsymbol{\mathcal{E}_k}(\boldsymbol{k})$. It can be any constant in m^3 units, but without loss of generality, it can be written as $k_0^u = \omega/c$, where ω is the light frequency and c the light velocity in vacuum. The integrand in Eq. (3.2) represents a plane wave of amplitude $\boldsymbol{\mathcal{E}_k}(\boldsymbol{k})$ with wavevector $\boldsymbol{k}$, i.e. propagating in the $\boldsymbol{k}$-direction and having a wavelength $2\pi/|\boldsymbol{k}|$. Because a light *mode* corresponds to light propagating along a given direction $\boldsymbol{k}$, I will call $\boldsymbol{\mathcal{E}_k}(\boldsymbol{k})$ the *modal vector amplitude*.

Usually, thinking again to MOKE experiments, the field is *monochromatic*, i.e., oscillating at *a single frequency* ω. As follow from the solution of the Maxwell equations or the wave equation [Eq. (3.7)], the monochromaticity implies that $\boldsymbol{k}$ can not have arbitrary value. More exactly, the monochromaticity implies that one of its components, for example the z-component, of $\boldsymbol{k}$ can be expressed as a function of the remaining x and y components, the permittivity $\varepsilon_{ij}^{(\omega)}$, light frequency ω and polarization Π, i.e.

$$k_{z,\Pi,d}^{(\omega)} \equiv k_{z,\Pi,d}^{(\omega)}(k_x, k_y, \omega, \varepsilon_{ij}^{(\omega)}). \tag{3.3}$$

The index Π, which takes the values 1 or 2, labels the two orthogonally polarized modes whose $k_{z,\Pi,d}^{(\omega)}$ can be, in general different. Furthermore, the index d refers to the direction of the $\boldsymbol{k}$-vector. In this work, I use $d = +$ and $d = -$ to denote modes propagating in the positive $[\Re(k_{z,\Pi,+}^{(\omega)}) > 0]$ and negative $[\Re(k_{z,\Pi,-}^{(\omega)}) < 0]$ z-directions, respectively. So, for given values of k_x, k_y and ω, there exist four modes of propagation for the EM field in the medium characterized by the permittivity tensor elements $\varepsilon_{ij}^{(\omega)}$. Two modes are propagating in the positive $(d = +)$, and the two other modes in the negative $(d = -)$ direction.

Coming back to the general expression of the electric field at the position $\boldsymbol{r}$ in Eq. (3.2), the light monochromaticity reduces the integration over the entire three-dimensional $\boldsymbol{k}$-space to that over a two-dimensional area, where $\boldsymbol{k} = \boldsymbol{k}^{(\omega)} = [k_x, k_y, k_{z,\Pi,d}^{(\omega)}]$:

---

[1]For conventions of direct and inverse Fourier transformations used in this manuscript, see Appendix A.

(i) In an isotropic medium characterized by the scalar dielectric permittivity $\varepsilon^{(\omega)}$, the integration in Eq. (3.2) is performed over a sphere of radius $k^{(\omega)} = \sqrt{\varepsilon^{(\omega)}}(\omega/c)$.

(ii) For an anisotropic medium characterized by permittivity tensor elements $\varepsilon_{ij}^{(\omega)}$, the situation is more complicated because the length of the vector $\boldsymbol{k}$ depends also on its direction and on the polarization of the propagating light [17].

As discussed above, the consequence of the monochromaticity is that k_z is not a free parameter. Thus one *light mode* (in a given material at given frequency) is fully described by the vector $\boldsymbol{q} = [k_x, k_y]$. Such a light mode contains four plane waves, whose propagation directions are determined by $\boldsymbol{k}_{\Pi,d}^{(\omega)} = [\boldsymbol{q}, k_{z,\Pi,d}^{(\omega)}]$. Thus, the arbitrary spatial distribution of the monochromatic electric field $\boldsymbol{E}(\boldsymbol{r})$ can be expressed as an intagral over all light modes, each parameterized by only one vector $\boldsymbol{q} \equiv [k_x, k_y]$ [see Figure 3.1(b)],

$$\boldsymbol{E}^{(\omega)}(\boldsymbol{r}) = \frac{1}{(2\pi)^2} \frac{1}{(k_0^u)^2} \iint \mathrm{d}^2\boldsymbol{q} \sum_{\Pi=1,2} \sum_{d=\pm} \boldsymbol{\mathcal{E}}_{\boldsymbol{q},\nu,\Pi,d}^{(\omega)}(\boldsymbol{q}, z) \exp[i\,\boldsymbol{q} \cdot \boldsymbol{\rho}], \qquad (3.4)$$

where $\boldsymbol{\rho} \equiv [x, y]$. *This defines the so-called $\boldsymbol{q}$-space.* The term $\boldsymbol{\mathcal{E}}_{\boldsymbol{q},\nu,\Pi,d}^{(\omega)}$ represents the vector modal amplitude in the newly defined $\boldsymbol{q}$-space. It is important to note that the vector modal amplitude $\boldsymbol{\mathcal{E}}_{\boldsymbol{q},\nu,\Pi,d}^{(\omega)}$ depends explicitly on $\boldsymbol{q} = [k_x, k_y]$ and z, i.e. $\boldsymbol{\mathcal{E}}_{\boldsymbol{q},\nu,\Pi,d}^{(\omega)}(\boldsymbol{q}, z)$. This choice is particularly suitable for multilayer structures. If the depth z is not explicit, the superscript ν specifies that $\boldsymbol{\mathcal{E}}_{\boldsymbol{q},\nu,\Pi,d,}^{(\omega)}$ concerns the ν-th layer in the vicinity of the ν-th interface, i.e. inside the ν-th layer just beside the "upper" interface (see Figure 3.2). Only in the case of the superstrate, i.e. for $\nu = 0$, the vector modal amplitude $\boldsymbol{\mathcal{E}}_{\boldsymbol{q},0,\Pi,d}^{(\omega)}$ is determined in the vicinity of the 1-st interface, since there is no 0-th interface.

3.1.2 $\boldsymbol{q}$-space properties

The $\boldsymbol{q}$-space is a Fourier space in the k_x and k_y directions and real space in the z-direction. Thus, any light mode in the multilayer structure is solely determined by the vector $\boldsymbol{q} = [k_x, k_y]$, since $k_{z,\Pi,d}^{(\omega)}$ is determined by $\boldsymbol{q}$, the light frequency ω and the optical properties of the material $\varepsilon_{ij}^{(\omega)}$. Each light mode contains four plane waves, each characterized by four modal amplitudes $\boldsymbol{\mathcal{E}}_{\boldsymbol{q},\Pi,d}^{(\omega)}$ and four wavevectors $\boldsymbol{k}_{\Pi,d}^{(\omega)}$. Two plane waves propagate in the positive z-direction ($d = +$), and the other two in the negative z-direction ($d = -$). Each pair of plane waves contains two mutually orthogonal polarizations, for example $\Pi = \mathtt{s}$ and $\Pi = \mathtt{p}$ waves. Some additional mathematical properties of the $\boldsymbol{q}$-space are reported in Appendix C.

Figure 3.1 shows the graphical representation of a single light mode in an unbound medium in the $\boldsymbol{k}$-space, $\boldsymbol{q}$-space and $\boldsymbol{r}$-space. In general, a single light mode corresponds to four EM plane waves, which are represented differently in each space. In the $\boldsymbol{r}$-space, all four plane waves propagate over the entire space, i.e. in $\boldsymbol{k}_{\nu,\Pi,d}^{(\omega)} = [k_x, k_y, k_{z,\nu,\Pi,d}^{(\omega)}]$ directions, each wave having a modal vector amplitude $\boldsymbol{\mathcal{E}}_{\nu,\Pi,d}^{(\omega)}$. In the $\boldsymbol{k}$-space, these four EM waves are represented by four "point". Mathematically speaking, these four waves are described by four Dirac δ-functions, located at positions $\boldsymbol{k}_{\nu,\Pi,d}^{(\omega)}$. This is a direct consequence of the fact that the Fourier transform of a plane wave is the Dirac δ-function. The $\boldsymbol{q}$-space is a
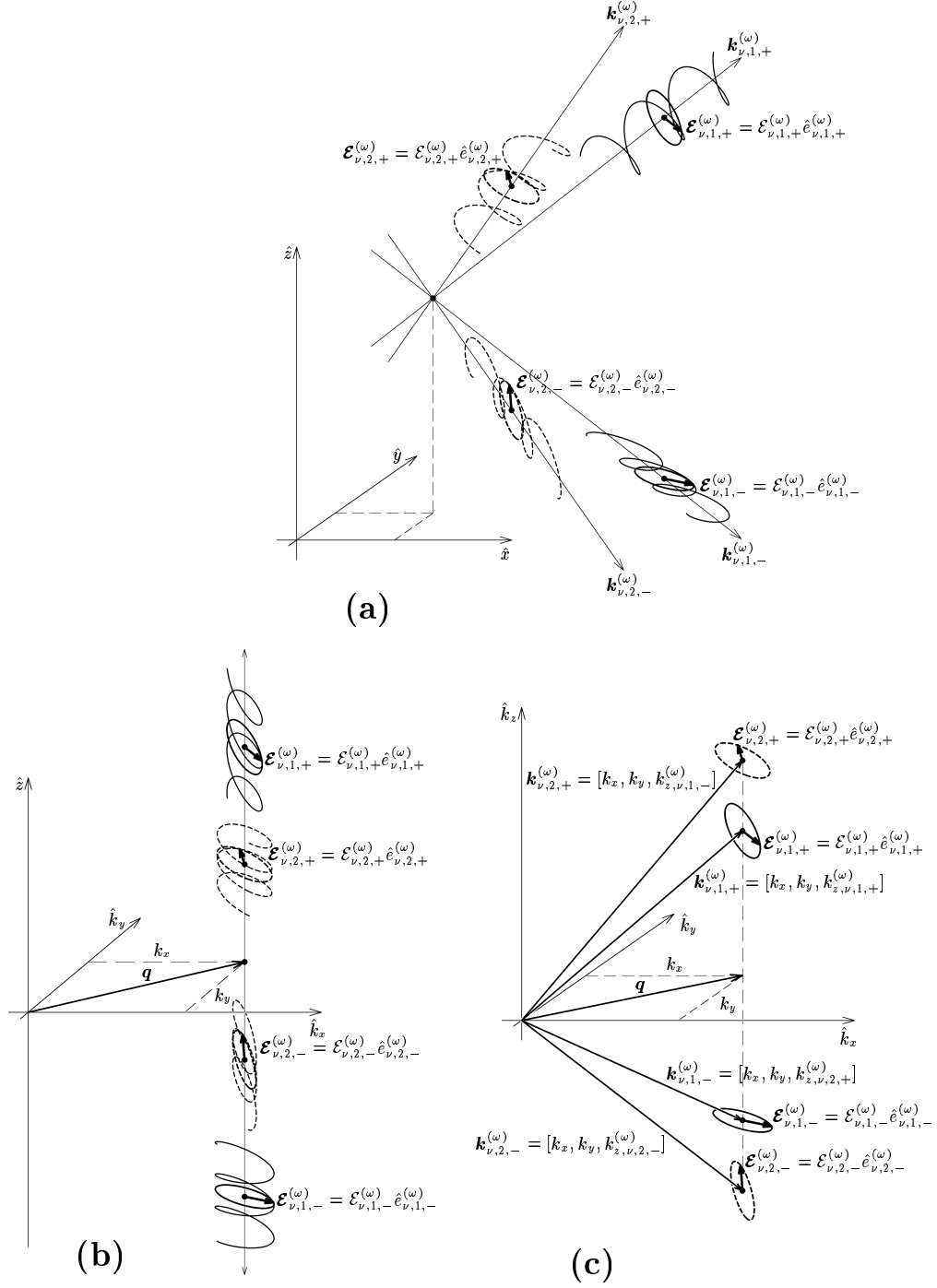
Figure 3.1: Sketches of a single light mode in the (a) r-space (b) q-space and (c) k-space. A single light mode contains four EM plane waves, each having the same $q = [k_x, k_y]$. Two waves propagates "up" (+), and the two others "down"(-), with two light polarizations 1 and 2 for each, are associated. In the r-space, the space is "filled" with these four EM plane waves. In the k-space, each plane wave is represented by point (Dirac δ-function). In the q-space, these four EM waves are represented by *one* point on the $k_x k_y$-plane, but spread over the z direction.

direct space in the z direction, thus all four plane waves spread in a delocalized way. On the other hand, as $\boldsymbol{q}$-space is a Fourier space in the k_x and k_y directions, the plane wave in this $k_x k_y$-plane is represented by a "point", i.e. by Dirac δ-function. Because all four plane waves are associated with a single light mode, all of them have the same $\boldsymbol{q} = [k_x, k_y]$, and thus they are represented by one "point" (or one Dirac δ-function), on $k_x k_y$ plane.

I would like to point out why the $\boldsymbol{q}$-space is so important for introducing a radiating electric point dipole into a multilayer structucture. In the $\boldsymbol{q}$-space, the radiation of such a point dipole can be described by a smooth function (see Appendix D). This is different in the $\boldsymbol{k}$-space, where the electric field radiated by a point dipole is described by a diverging function varying like $\mathcal{E}_{\boldsymbol{k}}^\mu \sim 1/[\boldsymbol{k} \cdot \boldsymbol{k} - (k^{(\omega)})^2]$ [see Eq. (E.7) in Appendix E and related discussion], where $k^{(\omega)}$ is the wavevector length at the point dipole frequency ω and $\boldsymbol{k}$ the wavevector for any light frequencies (recall that the $\boldsymbol{k}$-space is not monochromatic). In another words, the function $1/[\boldsymbol{k} \cdot \boldsymbol{k} - (k^{(\omega)})^2]$, tells that a dipole radiates waves having a $\boldsymbol{k}$-vector of length corresponding to $k^{(\omega)}$, and contributions of waves having other wavevectors are negligible. Thus, the description of a point dipole radiation in the $\boldsymbol{k}$-space is diverging and, consequently it is difficult to consider it for a proper description of a point dipole radiation inside a multilayer structure. However, it is easy to incorporate the dipole radiation into the multilayer structure and express the induced modified boundary conditions. Note that the modification of boundary conditions, in the presence of a radiating point dipole has been already published [4], but without their derivation. Thanks to a rigorous definition of the $\boldsymbol{q}$-space, the derivation is possible. Furthermore, I found that the radiated light intensity is proportional to $I \sim |k_z \mathcal{E}_{\boldsymbol{q}}|^2$ when calculated in $\boldsymbol{q}$-space and not $I \sim |\mathcal{E}_{\boldsymbol{k}}|^2$ when calculated in the usual $\boldsymbol{k}$-space; an important point never pointed out for SHG radiation so far. The radiation of a point dipole embedded inside a multilayer structure will be treated in Chapter 7.

In the following, I will use only the $\boldsymbol{q}$-space to describe the light propagation and radiation in multilayer structures, and thus I will omit the subscript $\boldsymbol{q}$.

The vector modal amplitudes $\boldsymbol{\mathcal{E}}_{\nu,\Pi,d}^{(\omega)}$ will often appear as a sum over either the polarization index Π or the direction d or both. Therefore, I introduce a "summing index" Σ as follows:

$$
\begin{aligned}
\boldsymbol{\mathcal{E}}_{\nu,\Pi,\Sigma}^{(\omega)} &= \sum_{d=\pm} \boldsymbol{\mathcal{E}}_{\nu,\Pi,d}^{(\omega)}, \\
\boldsymbol{\mathcal{E}}_{\nu,\Sigma,d}^{(\omega)} &= \sum_{\Pi=1,2} \boldsymbol{\mathcal{E}}_{\nu,\Pi,d}^{(\omega)}, \\
\boldsymbol{\mathcal{E}}_{\nu,\Sigma,\Sigma}^{(\omega)} &= \sum_{d=\pm} \sum_{\Pi=1,2} \boldsymbol{\mathcal{E}}_{\nu,\Pi,d}^{(\omega)}.
\end{aligned}
\tag{3.5}
$$

For example, $\boldsymbol{\mathcal{E}}_{\nu,\Sigma,\Sigma}^{(\omega)}$, which is the sum of all vector modal amplitude at position z_ν, represents the electric field at the position z_ν, expressed in the $\boldsymbol{q}$-space. Then $\boldsymbol{E}(\boldsymbol{r})$ can be simply written as

$$
\boldsymbol{E}^{(\omega)}(\boldsymbol{r}) = \frac{1}{(2\pi k_0^u)^2} \iint \mathrm{d}\boldsymbol{q} \; \boldsymbol{\mathcal{E}}_{\nu,\Sigma,\Sigma}^{(\omega)} \exp[i\boldsymbol{\rho} \cdot \boldsymbol{q}],
\tag{3.6}
$$

as follow from Eq. (3.4).

To summarize the q-space section:

   (i) The $\boldsymbol{q}$-space is a Fourier space in the k_x, k_y directions, but real in the z direction. Hence, it has a spatial dependence on z for which multilayer properties are modified.

  (ii) The $\boldsymbol{q}$-space is monochromatic. This means that it describes the electric field at only one single light frequency ω.

 (iii) the light mode propagation direction is fully characterized by $\boldsymbol{q} = [k_x, k_y]$.

 (iv) I choose the $\boldsymbol{q}$-space for a better description of the EM field inside a multilayer structure. Furthermore, the definition of the $\boldsymbol{q}$-space becomes necessary to express the boundary conditions in the presence of a radiating point dipole as introduced to calculate SHG radiation (treated in Chapter 7).

3.2 Light propagation in magnetic multilayers

In this Section, I present first the calculations on the light propagation inside a multilayer structure by means of the 4×4 matrix formalism. Finally, I express the reflection and transmission matrix and calculate the profile of the electric field inside the multilayer structure.

3.2.1 Proper modes for light propagation

A *proper mode* of light retains its polarization state during propagation through a material in a given direction. The proper modes of light polarization can be found by substituting the field $\boldsymbol{E}^{(\omega)}(\boldsymbol{r})$ [Eq. (3.4)] into Maxwell equations without free currents and charges. Then, the wave equation expressed in the $\boldsymbol{q}$-space can be derived. In the ν-th layer characterized by permittivity tensor elements $\varepsilon_{ij,\nu}^{(\omega)}$, the wave equation takes the form [41, 43]

$$\left[N_{i,\nu}^{(\omega)} N_{j,\nu}^{(\omega)} + \varepsilon_{ij,\nu}^{(\omega)} \right] \boldsymbol{\mathcal{E}}_{\nu}^{(\omega)} = (N_{\nu}^{(\omega)})^2 \boldsymbol{\mathcal{E}}_{\nu}^{(\omega)}, \tag{3.7}$$

where $N_{i,\nu}^{(\omega)}$ denotes the i-th component of the *normalized wave vector* $\boldsymbol{N}_{\nu}^{(\omega)} = \boldsymbol{k}^{(\omega)}/k_0^{(\omega)} = [0, N_y, N_{z,\nu,\Pi,d}^{(\omega)}]$, where $k_0^{(\omega)} = \omega/c$. Without loss of generality, the x-component of the $\boldsymbol{k}^{(\omega)}$-vector is assumed to be zero. This defines a $\hat{y}\hat{z}$-plane of incidence, in agreement with our conventions reported in Appendix A. Because the term N_y is conserved through all the multilayer structure, the subscript ν is removed. The coefficient $N_{\nu,\Pi,d}^{(\omega)}$ stands for the Pythagorean length of the normalized wavevector, i.e. $\boldsymbol{N}_{\nu,\Pi,d}^{(\omega)} \cdot \boldsymbol{N}_{\nu,\Pi,d}^{(\omega)} = (N_{\nu,\Pi,d}^{(\omega)})^2 = N_y^2 + (N_{z,\nu,\Pi,d}^{(\omega)})^2$.

    The solution of Eq. (3.7) can be found by a treatment similar to the search of eigenvectors and eigen-numbers. The unknown quantities in this equation are the z-component of the normalized wavevector $N_{z,\nu,\Pi,d}^{(\omega)} = k_{z,\nu,\Pi,d}^{(\omega)}/k_0^{(\omega)}$ and the *modal vector polarization* $\hat{e}_{\nu,\Pi,d}^{(\omega)}$, where

$$\boldsymbol{\mathcal{E}}_{\nu,\Pi,d}^{(\omega)} = \mathcal{E}_{\nu,\Pi,d}^{(\omega)} \hat{e}_{\nu,\Pi,d}^{(\omega)}, \qquad \text{with } |\hat{e}_{\nu,\Pi,d}^{(\omega)}| = 1, \tag{3.8}$$

and $\mathcal{E}_{\nu,\Pi,d}$ is the *modal amplitude*, which value is not determined from the wave equation, but by the boundary conditions; this problem is treated in the next Section 3.2.2. Since the solution of the wave equation has been treated in details by Š. Višňovský [41], I will not develop it here. Note that the wave equation has exactly the same form as Eq. (3.7) when solved either in the $\boldsymbol{k}$ or $\boldsymbol{q}$-space.

In case of an isotropic medium, $\varepsilon_{ij,\nu}^{(\omega)} = \varepsilon_\nu^{(\omega)}$, the solution of the wave equation (3.7) leads to arbitrary vector modal polarizations $\hat{e}_{\nu,\Pi,d}^{(\omega)}$, for example s and p-polarizations. The solution of $N_{z,\nu,\Pi,d}^{(\omega)}$ is identical for both polarizations $\Pi = \mathtt{s}, \mathtt{p}$:

$$N_{z,\nu,\pm}^{(\omega)} \equiv N_{z,\nu,\mathtt{s}/\mathtt{p},\pm}^{(\omega)} = \pm\sqrt{\left(N_\nu^{(\omega)}\right)^2 - N_y^2} \tag{3.9}$$

where $N_\nu^{(\omega)} = \sqrt{\varepsilon_\nu^{(\omega)}}$. Finally, note that the relation between the incidence angle φ and $N_y^{(\omega)}$ is $N_y^{(\omega)} = N_0^{(\omega)} \sin\varphi$, where $N_0^{(\omega)}$ is the refractive index of superstrate (often the air).

3.2.2   4×4 matrix formalism

As follows from Eq. (3.4), for one mode, i.e. for a given $\boldsymbol{q}_0 = [0, N_y]$ and $\boldsymbol{\mathcal{E}}_{\nu,\Pi,d}(\boldsymbol{q}) = (2\pi k_0^u)^2 \boldsymbol{\mathcal{E}}_{\nu,\Pi,d}\,\delta(\boldsymbol{q} - \boldsymbol{q}_0)$, the electric field of the EM waves inside the ν-th layer can be written as

$$\boldsymbol{E}_\nu^{(\omega)}(\boldsymbol{\rho}, z) = \sum_{\Pi=1,2} \sum_{d=\pm} \mathcal{E}_{\nu,\Pi,d}^{(\omega)}\, \hat{e}_{\nu,\Pi,d}^{(\omega)} \exp\left[ik_0^{(\omega)}\left(N_{y,\nu}y + N_{z,\nu,\Pi,d}^{(\omega)}(z - z_{\nu-1})\right)\right], \tag{3.10}$$

where $\boldsymbol{\rho} = [x, y]$, and assuming $N_x = 0$. Through Maxwell equations, a similar expression can be derived for the magnetic field of the EM wave inside the ν-th layer

$$\boldsymbol{H}_\nu^{(\omega)}(\boldsymbol{\rho}, z) = \sum_{\Pi=1,2} \sum_{d=\pm} \mathcal{H}_{\nu,\Pi,d}^{(\omega)}\, \hat{h}_{\nu,\Pi,d}^{(\omega)} \exp\left[ik_0^{(\omega)}\left(N_{y,\nu}y + N_{z,\nu,\Pi,d}^{(\omega)}(z - z_{\nu-1})\right)\right], \tag{3.11}$$

where $\mathcal{H}_{\nu,\Pi,d}^{(\omega)} = (N_{\nu,\Pi,d}^{(\omega)}/\eta_0)\,\mathcal{E}_{\nu,\Pi,d}^{(\omega)}$, and $\hat{h}_{\nu,\Pi,d}^{(\omega)} = (\boldsymbol{N}_{\nu,\Pi,d}^{(\omega)} \times \hat{e}_{\nu,\Pi,d}^{(\omega)})/N_{\nu,\Pi,d}^{(\omega)}$, in which $\eta_0 = \sqrt{\mu_0/\varepsilon_0}$ is the vacuum impedance.

As follows from Maxwell equations, in the absence of free charges and currents, the tangential components of the electric field $\boldsymbol{E}^{(\omega)}(\boldsymbol{r})$ and magnetic field $\boldsymbol{H}^{(\omega)}(\boldsymbol{r})$ are continuous at the interface. It should be noted that although in most textbooks this continuity is derived in the real $\boldsymbol{r}$-space, it can be demonstrated that these tangential components are continuous in both $\boldsymbol{k}$- and $\boldsymbol{q}$-space as well. The continuous tangential components of electric and magnetic fields at the $(\nu+1)$-th interface (i.e. between the ν-th and $(\nu+1)$-th layers) can be written in a matrix form [40, 41, 43]

$$\mathbf{D}_\nu^{(\omega)}\mathbf{P}_\nu^{(\omega)}\boldsymbol{A}_\nu^{(\omega)} = \begin{bmatrix} E_{x,\nu}^{(\omega)}(z_{\nu+1} - \epsilon) \\ \eta_0 H_{y,\nu}^{(\omega)}(z_{\nu+1} - \epsilon) \\ E_{y,\nu}^{(\omega)}(z_{\nu+1} - \epsilon) \\ \eta_0 H_{x,\nu}^{(\omega)}(z_{\nu+1} - \epsilon) \end{bmatrix} = \begin{bmatrix} E_{x,\nu+1}^{(\omega)}(z_{\nu+1} + \epsilon) \\ \eta_0 H_{y,\nu+1}^{(\omega)}(z_{\nu+1} + \epsilon) \\ E_{y,\nu+1}^{(\omega)}(z_{\nu+1} + \epsilon) \\ \eta_0 H_{x,\nu+1}^{(\omega)}(z_{\nu+1} + \epsilon) \end{bmatrix} = \mathbf{D}_{\nu+1}^{(\omega)}\boldsymbol{A}_{\nu+1}^{(\omega)}, \tag{3.12}$$

where the distance ϵ to the $\nu + 1$ interface tends to zero. The schematic interpretation of this equation, which is at the basis of the 4×4 matrix formalism, is presented on Figure 3.2. $\boldsymbol{A}_\nu^{(\omega)}$ in Eq. (3.12) is a column vector of all four modal amplitudes $\mathcal{E}_{\nu,\Pi,d}^{(\omega)}$, and is defined by the sequence

$$\boldsymbol{A}_\nu^{(\omega)} = [\mathcal{E}_{\nu,1,+}^{(\omega)}, \mathcal{E}_{\nu,1,-}^{(\omega)}, \mathcal{E}_{\nu,2,+}^{(\omega)}, \mathcal{E}_{\nu,2,-}^{(\omega)}]^{\mathrm{T}}, \tag{3.13}$$
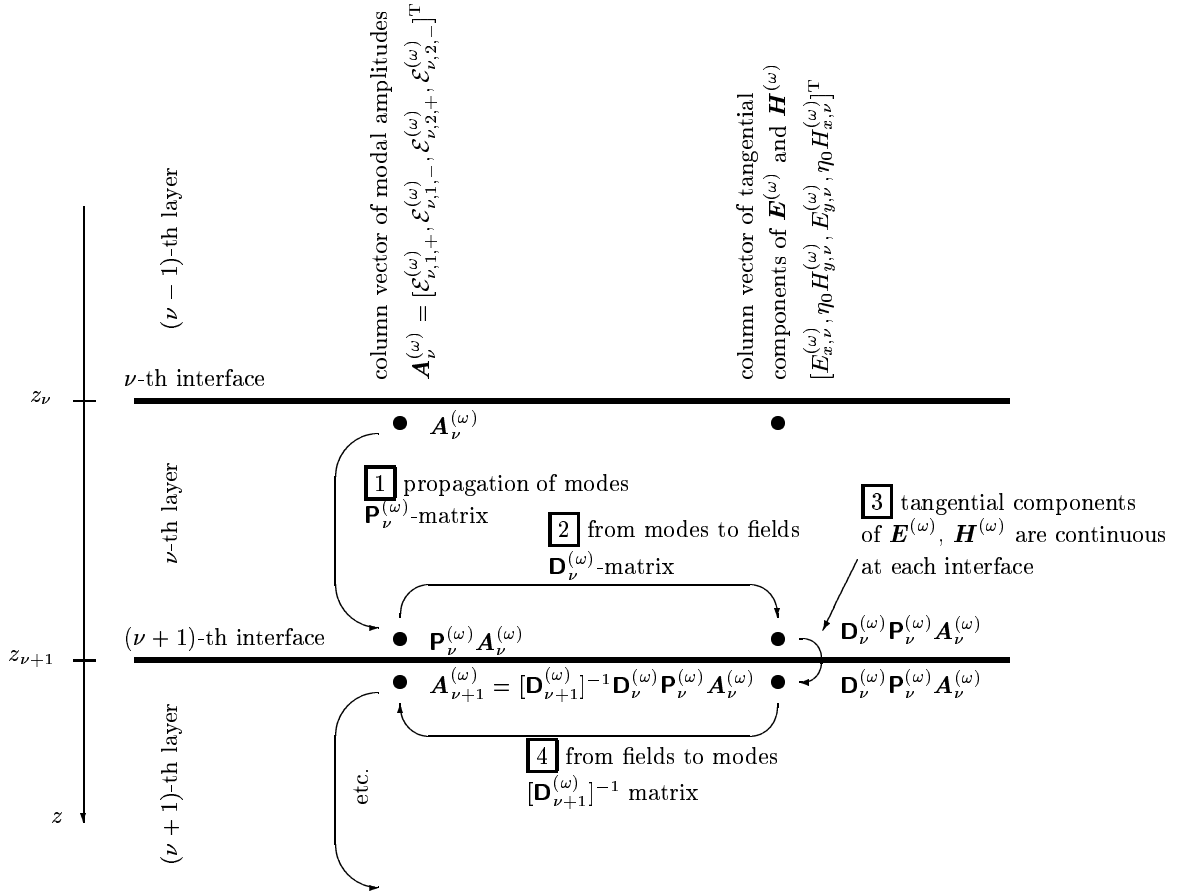
Figure 3.2: Schematic representation of the 4×4 matrix formalism, represented by Eq. (3.12). $\boxed{1}$ The propagation of vector of modal amplitudes $\boldsymbol{A}_\nu^{(\omega)} = [\mathcal{E}_{\nu,1,+}^{(\omega)}, \mathcal{E}_{\nu,1,-}^{(\omega)}, \mathcal{E}_{\nu,2,+}^{(\omega)}, \mathcal{E}_{\nu,2,-}^{(\omega)}]$ through the ν-th layer is described by the propagation matrix $\mathbf{P}_\nu^{(\omega)}$. $\boxed{2}\,\boxed{4}$ The dynamic matrix $\mathbf{D}_\nu^{(\omega)}$ binds the modal amplitudes $\boldsymbol{A}_\nu^{(\omega)}$ to tangential components of $\boldsymbol{E}_\nu^{(\omega)}$ and $\boldsymbol{H}_\nu^{(\omega)}$ fields, $\boxed{3}$ which are continuous at the interface. Note by convention that $\boldsymbol{A}_\nu^{(\omega)}$ is located inside the ν-th layer in the vicinity (i.e. immediately below) of the ν-th interface, as it can be seen on the figure.

where the superscript $^{\mathrm{T}}$ denotes the transposed column vector. Recall that the subscript $\Pi = 1, 2$ (or $\Pi = \mathbf{s}, \mathbf{p}$) stands for the modal polarization and $d = \pm$ for the propagation direction, i.e. $\Re(k_{z,\Pi,+}^{(\omega)}) > 0$, $\Re(k_{z,\Pi,-}^{(\omega)}) < 0$, respectively.

$\mathbf{D}^{(\omega)}$ is called the dynamic matrix and gives a relation between the vector of modal amplitudes $\boldsymbol{A}^{(\omega)}$ in a material and the column vector of the tangential components of the $\boldsymbol{E}_\nu^{(\omega)}$ and $\boldsymbol{H}_\nu^{(\omega)}$ fields. This relationship is defined to be $\mathbf{D}_\nu^{(\omega)}\boldsymbol{A}_\nu^{(\omega)} = [E_{x,\nu}^{(\omega)}, \eta_0 H_{y,\nu}^{(\omega)}, E_{y,\nu}^{(\omega)},$

$\eta_0 H_{x,\nu}^{(\omega)}]^{\mathrm{T}}$. Hence, the matrix $\mathbf{D}_\nu^{(\omega)}$ writes [40, 41]

$$
\mathbf{D}_\nu^{(\omega)} =
\begin{bmatrix}
\hat{e}_{\nu,1,+}^{(\omega)} \cdot \hat{x} & \hat{e}_{\nu,1,-}^{(\omega)} \cdot \hat{x} & \hat{e}_{\nu,2,+}^{(\omega)} \cdot \hat{x} & \hat{e}_{\nu,2,-}^{(\omega)} \cdot \hat{x} \\
N_{\nu,1,+}^{(\omega)}\hat{h}_{\nu,1,+}^{(\omega)} \cdot \hat{y} & N_{\nu,1,-}^{(\omega)}\hat{h}_{\nu,1,-}^{(\omega)} \cdot \hat{y} & N_{\nu,2,+}^{(\omega)}\hat{h}_{\nu,2,+}^{(\omega)} \cdot \hat{y} & N_{\nu,2,-}^{(\omega)}\hat{h}_{\nu,2,-}^{(\omega)} \cdot \hat{y} \\
\hat{e}_{\nu,1,+}^{(\omega)} \cdot \hat{y} & \hat{e}_{\nu,1,-}^{(\omega)} \cdot \hat{y} & \hat{e}_{\nu,2,+}^{(\omega)} \cdot \hat{y} & \hat{e}_{\nu,2,-}^{(\omega)} \cdot \hat{y} \\
N_{\nu,1,+}^{(\omega)}\hat{h}_{\nu,1,+}^{(\omega)} \cdot \hat{x} & N_{\nu,1,-}^{(\omega)}\hat{h}_{\nu,1,-}^{(\omega)} \cdot \hat{x} & N_{\nu,2,+}^{(\omega)}\hat{h}_{\nu,2,+}^{(\omega)} \cdot \hat{x} & N_{\nu,2,-}^{(\omega)}\hat{h}_{\nu,2,-}^{(\omega)} \cdot \hat{x}
\end{bmatrix} . \quad (3.14)
$$

The matrix $\mathbf{P}_\nu^{(\omega)}$ is called the propagation matrix, as it describes the propagation of modal amplitudes $\mathcal{E}_{\nu,\Pi,d}^{(\omega)}$ in the layer thickness through the relation $\boldsymbol{A}_\nu^{(\omega)}(z_\nu+\epsilon) = \mathbf{P}_\nu^{(\omega)}\boldsymbol{A}_\nu^{(\omega)}(z_{\nu+1}-\epsilon)$, $\epsilon \to 0$ (see Figure 3.2). Hence, the matrix $\mathbf{P}_\nu^{(\omega)}$ expresses as

$$
\mathbf{P}_\nu^{(\omega)} =
\begin{bmatrix}
\exp[ik_0^{(\omega)} N_{z,\nu,1,+}^{(\omega)} t_\nu] & 0 & 0 & 0 \\
0 & \exp[ik_0^{(\omega)} N_{z,\nu,1,-}^{(\omega)} t_\nu] & 0 & 0 \\
0 & 0 & \exp[ik_0^{(\omega)} N_{z,\nu,2,+}^{(\omega)} t_\nu] & 0 \\
0 & 0 & 0 & \exp[ik_0^{(\omega)} N_{z,\nu,2,-}^{(\omega)} t_\nu]
\end{bmatrix} ,
$$
$$(3.15)$$

where the values of $\hat{e}_{\nu,\Pi,d}^{(\omega)}$ $\hat{h}_{\nu,\Pi,d}^{(\omega)}$, $N_{\nu,\Pi,d}^{(\omega)}$, $N_{z,\nu,\Pi,d}^{(\omega)}$ are determined as solution of the wave equation (3.7).

The recursive application of boundary conditions in Eq. (3.12) gives relations between vector of modal amplitudes for the 0-th (i.e. superstrate) and ν-th layer

$$
\boldsymbol{A}_0^{(\omega)} = \mathbf{L}_\nu^{(\omega)} \boldsymbol{A}_\nu^{(\omega)}, \tag{3.16}
$$

where the matrix $\mathbf{L}_\nu^{(\omega)}$ is defined as

$$
\mathbf{L}_\nu^{(\omega)} \equiv [\mathbf{D}_0^{(\omega)}]^{-1}\mathbf{D}_1^{(\omega)}[\mathbf{P}_1^{(\omega)}]^{-1} \dots \mathbf{D}_{\nu-1}^{(\omega)}[\mathbf{P}_{\nu-1}^{(\omega)}]^{-1}[\mathbf{D}_{\nu-1}^{(\omega)}]^{-1}\mathbf{D}_\nu^{(\omega)}. \tag{3.17}
$$

In this definition, one assumes $\mathbf{L}_0^{(\omega)} \equiv 1$. The relation between the column vector of modal amplitudes in the superstrate and the substrate can subsequently be written as

$$
\boldsymbol{A}_0^{(\omega)} = \mathbf{L}_{M+1}^{(\omega)} \boldsymbol{A}_{M+1}^{(\omega)}, \tag{3.18}
$$

This is the final relation of this Section, binding the amplitudes of incoming and outcoming light modes in superstrate and substrate. Knowing the matrix $\mathbf{L}_{M+1}^{(\omega)}$, the reflection and transmission coefficients (and thus Faraday and Kerr effects) can be straightforwardly calculated, as presented in Section 3.2.4.

3.2.3   Dynamic and propagation matrices in isotropic media

In an isotropic medium, (i.e. for a diagonal permittivity tensor with $\varepsilon_{ij,\nu}^{(\omega)} = \delta_{ij}\varepsilon_\nu^{(\omega)}$) any polarization state is a proper mode since it is conserved during propagation. Mathematically speaking, in an isotropic medium, any values of modal polarization $\hat{e}_{\nu,\Pi,d}^{(\omega)}$, where $|\hat{e}_{\nu,\Pi,d}^{(\omega)}| = 1$, is a solution of the wave equation (3.7). So, as a proper mode, I will choose

a simple case, i.e. s and p polarizations, although others (e.g. circular or general elliptical) are possible as well [52]. Thus, with sign convention stated on Figure A.1 in Appendix A, modal polarizations take the form

$$
\begin{aligned}
\hat{e}_{\nu,\mathrm{s},\pm}^{(\omega)} &= [1,0,0], \\
\hat{e}_{\nu,\mathrm{p},\pm}^{(\omega)} &= [0, N_{z,\nu,\pm}^{(\omega)}, -N_y]/N_\nu^{(\omega)}.
\end{aligned}
\tag{3.19}
$$

Furthermore, the vector of modal amplitudes $\boldsymbol{A}_\nu^{(\omega)}$ let be defined as the sequence

$$
\boldsymbol{A}_\nu^{(\omega)} = [\mathcal{E}_{\nu,\mathrm{s},+}^{(\omega)}, \mathcal{E}_{\nu,\mathrm{s},-}^{(\omega)}, \mathcal{E}_{\nu,\mathrm{p},+}^{(\omega)}, \mathcal{E}_{\nu,\mathrm{p},-}^{(\omega)}]^{\mathrm{T}}.
\tag{3.20}
$$

Consequently, the matrices $\mathbf{D}_\nu^{(\omega)}$ and $\mathbf{P}_\nu^{(\omega)}$ take the form [Eqs. (3.14)(3.15)]

$$
\mathbf{D}_\nu^{(\omega)} =
\begin{bmatrix}
1 & 1 & 0 & 0 \\
N_{z,\nu,+}^{(\omega)} & N_{z,\nu,-}^{(\omega)} & 0 & 0 \\
0 & 0 & N_{z,\nu,+}^{(\omega)}/N_\nu^{(\omega)} & N_{z,\nu,-}^{(\omega)}/N_\nu^{(\omega)} \\
0 & 0 & -N_\nu^{(\omega)} & -N_\nu^{(\omega)}
\end{bmatrix},
\tag{3.21}
$$

$$
\mathbf{P}_\nu^{(\omega)} =
\begin{bmatrix}
\exp[ik_0^{(\omega)} N_{z,\nu,+}^{(\omega)} t_\nu] & 0 & 0 & 0 \\
0 & \exp[ik_0^{(\omega)} N_{z,\nu,-}^{(\omega)} t_\nu] & 0 & 0 \\
0 & 0 & \exp[ik_0^{(\omega)} N_{z,\nu,+}^{(\omega)} t_\nu] & 0 \\
0 & 0 & 0 & \exp[ik_0^{(\omega)} N_{z,\nu,-}^{(\omega)} t_\nu]
\end{bmatrix},
\tag{3.22}
$$

where $N_{z,\nu,\pm}^{(\omega)} = N_{z,\nu,\mathrm{s},\pm}^{(\omega)} = N_{z,\nu,\mathrm{p},\pm}^{(\omega)} = \sqrt{\varepsilon_\nu^{(\omega)} - N_y^2}$.

3.2.4 Kerr and Faraday effects: relation with transmitted and reflected light

Let us calculate the reflection and transmission coefficients of the entire multilayer structure. Assuming that the light does not enter into the sample from the substrate side, the vector of modal amplitude in substrate has the form

$$
\boldsymbol{A}_{M+1}^{(\omega)} = [\mathcal{E}_{M+1,\mathrm{s},+}^{(\omega)}, 0, \mathcal{E}_{M+1,\mathrm{p},+}^{(\omega)}, 0]^{\mathrm{T}}.
\tag{3.23}
$$

The transmission matrix $\mathbf{T}^{(\omega)}$ is defined by:

$$
\begin{bmatrix}
\mathcal{E}_{M+1,\mathrm{s},+}^{(\omega)} \\
\mathcal{E}_{M+1,\mathrm{p},+}^{(\omega)}
\end{bmatrix}
= \mathbf{T}^{(\omega)} \cdot
\begin{bmatrix}
\mathcal{E}_{0,\mathrm{s},+}^{(\omega)} \\
\mathcal{E}_{0,\mathrm{p},+}^{(\omega)}
\end{bmatrix}.
\tag{3.24}
$$

Hence, considering the $\mathbf{L}_{M+1}^{(\omega)}$ matrix, the transmission matrix $\mathbf{T}^{(\omega)}$ expresses as [see Eq. (3.18)]

$$
\mathbf{T}^{(\omega)} =
\begin{bmatrix}
t_{\mathrm{ss}} & t_{\mathrm{ps}} \\
t_{\mathrm{sp}} & t_{\mathrm{pp}}
\end{bmatrix}
= \left(
\begin{bmatrix}
L_{11,M+1}^{(\omega)} & L_{13,M+1}^{(\omega)} \\
L_{31,M+1}^{(\omega)} & L_{33,M+1}^{(\omega)}
\end{bmatrix}
\right)^{-1}.
\tag{3.25}
$$

In a similar way, the reflection matrix $\mathbf{R}^{(\omega)}$ is defined as

$$\begin{bmatrix} \mathcal{E}_{0,\mathrm{s},-}^{(\omega)} \\ \mathcal{E}_{0,\mathrm{p},-}^{(\omega)} \end{bmatrix} = \mathbf{R}^{(\omega)} \begin{bmatrix} \mathcal{E}_{0,\mathrm{s},+}^{(\omega)} \\ \mathcal{E}_{0,\mathrm{p},+}^{(\omega)} \end{bmatrix} \tag{3.26}$$

and expressed from the $\mathbf{L}_{M+1}^{(\omega)}$ matrix as

$$\mathbf{R}^{(\omega)} = \begin{bmatrix} r_{\mathrm{ss}} & r_{\mathrm{ps}} \\ r_{\mathrm{sp}} & r_{\mathrm{pp}} \end{bmatrix} = \begin{bmatrix} L_{21,M+1}^{(\omega)} & L_{2,3,M+1}^{(\omega)} \\ L_{41,M+1}^{(\omega)} & L_{4,3,M+1}^{(\omega)} \end{bmatrix} \cdot \mathbf{T}^{(\omega)} \tag{3.27}$$

Knowing the reflection matrix $\mathbf{R}^{(\omega)}$, MOKE can be calculated as the ratio of off-diagonal and diagonal coefficients (Eq. 2.13) $\Phi_{\mathrm{s}} = -r_{\mathrm{ps}}/r_{\mathrm{ss}}$, $\Phi_{\mathrm{p}} = r_{\mathrm{sp}}/r_{\mathrm{pp}}$. In a similar manner, the Faraday effect can be determined from the transmission matrix $\mathbf{T}^{(\omega)}$ as [36]: $\Phi_{F,\mathrm{s}} = t_{\mathrm{ps}}/t_{\mathrm{ss}}$ and $\Phi_{F,\mathrm{p}} = -t_{\mathrm{sp}}/t_{\mathrm{pp}}$. This definition of the Faraday effect is consistent with that of the Kerr effect by means of the polarization ellipse (Section 2.2), i.e. the positive real part of Φ_F corresponds to clockwise rotation of the main axis of the polarization ellipse for transmitted light, while the positive imaginary part is linked to the positive ellipticity of the polarization ellipse.

3.2.5   Electric field profile through a multilayer structure

In this Section, I introduce the calculation of the electric field profile through a multilayer structure. This is important for treating Second Harmonic Generation of light (SHG), [1, 4, 2], fluorescence [53] or for some type of MOKE calculations [51].

In the ν-th layer of the multilayer structure, and in the vicinity of the ν-th interface (see Figure 3.2), the vector of modal amplitudes $\boldsymbol{A}_{\nu}^{(\omega)}$ is determined by Eqs. (3.13) (3.16)(3.18)

$$\boldsymbol{A}_{\nu}^{(\omega)} = (\mathbf{L}_{\nu}^{(\omega)})^{-1}\mathbf{L}_{M+1}^{(\omega)}\boldsymbol{A}_{M+1}^{(\omega)}. \tag{3.28}$$

Consequently, the profile of $\boldsymbol{E}^{(\omega)}(\boldsymbol{r})$ through the ν-th layer can be calculated using Eq. (3.10).

$$\boldsymbol{E}_{\nu}^{(\omega)}(\boldsymbol{r}) = \sum_{\Pi=1,2} \sum_{d=\pm} \mathcal{E}_{\nu,\Pi,d}^{(\omega)} \hat{e}_{\nu,\Pi,d}^{(\omega)} \exp\left[ik_0^{(\omega)}\left(N_y y + N_{z,\nu,\Pi,d}^{(\omega)}(z - z_{\nu-1})\right)\right], \tag{3.29}$$

where $\mathcal{E}_{\nu,\Pi,d}^{(\omega)}$ are parts of $\boldsymbol{A}_{\nu}^{(\omega)}$, determined by Eq. (3.28).

However, in the case of SHG calculations, presented in Chapter 7, it is necessary to know the value of the electric field $\boldsymbol{E}^{(\omega)}(\boldsymbol{r})$ at each interface. Its x and y components are continuous through the interface, but not the z-component. There are two ways for determining this electric field profile [4, 54]

(i) An ultrathin vacuum layer is assumed to be located at the ν-th interface. Then, the value of the electric field inside this vacuum layer is

$$\boldsymbol{E}_{\nu}^{(\omega)}(\boldsymbol{\rho}, z_{\nu}) = \sum_{\Pi=\mathrm{s},\mathrm{p}} \sum_{d=\pm} \left(\mathcal{E}_{\mathrm{vac},\nu,\Pi,d}^{(\omega)}\hat{\boldsymbol{e}}_{\mathrm{vac},\Pi,d}^{(\omega)}\right) \exp[ik_0^{(\omega)}N_y y], \tag{3.30}$$

where modal amplitudes $\mathcal{E}_{\mathrm{vac},\nu,\Pi,d}^{(\omega)}$ of $\boldsymbol{A}_{\mathrm{vac},\nu}^{(\omega)} \equiv [\mathcal{E}_{\mathrm{vac},\nu,\mathrm{s},+}^{(\omega)}, \mathcal{E}_{\mathrm{vac},\nu,\mathrm{s},-}^{(\omega)}, \mathcal{E}_{\mathrm{vac},\nu,\mathrm{p},+}^{(\omega)}, \mathcal{E}_{\mathrm{vac},\nu,\mathrm{p},-}^{(\omega)}]^{\mathrm{T}}$ are calculated by the transmission of modal amplitudes from the ν-th layer to the vacuum layer

$$\boldsymbol{A}_{\mathrm{vac},\nu}^{(\omega)} = [\mathbf{D}_{\mathrm{vac}}^{(\omega)}]^{-1}\mathbf{D}_{\nu}^{(\omega)}\boldsymbol{A}_{\nu}^{(\omega)}, \tag{3.31}$$

where all quantities denoted by "vac" are calculated for vacuum, i.e. with $\varepsilon_{\mathrm{vac}} = 1$.

(ii) The z-component of $\boldsymbol{E}_\nu^{(\omega)}$ at the ν-th interface is assumed to be the average of field values in the $(\nu-1)$-th and ν-th layer in the close vicinity of the ν-th interface

$$\boldsymbol{E}_\nu^{(\omega)}(\boldsymbol{\rho}, z_\nu) = \frac{1}{2}\left[\boldsymbol{E}_{\nu-1}^{(\omega)}(\boldsymbol{\rho}, z_\nu - \epsilon) + \boldsymbol{E}_\nu^{(\omega)}(\boldsymbol{\rho}, z_\nu + \epsilon)\right]$$

$$= \frac{1}{2}\sum_{\Pi=1,2}\sum_{d=\pm}\left(\mathcal{E}_{\nu-1,\Pi,d}^{(\omega)}\,\hat{\boldsymbol{e}}_{\nu-1,\Pi,d}^{(\omega)}\exp[ik_0^{(\omega)}N_{z,\nu-1,\Pi,d}^{(\omega)}t_{\nu-1}] + \mathcal{E}_{\nu,\Pi,d}^{(\omega)}\,\hat{\boldsymbol{e}}_{\nu,\Pi,d}^{(\omega)}\right)\exp[ik_0^{(\omega)}N_y y],$$

(3.32)

where $\epsilon \to 0$. For the calculation of the SHG electric fields in Chapter 7, I will use this average approach (ii), because the profile of the permittivity tensor $\boldsymbol{\varepsilon}^{(\omega)}(z)$ in *real structures* is not step-like (as for in an idealized stratified structure), but is continuous across the interface. As a consequence, the electric field across the interface is continuous as well.

In the following, it will be useful to express directly the relation between the incoming Jones vector $\boldsymbol{J}_{0,+}^{(\omega)} = [\mathcal{E}_{0,\mathrm{s},+}^{(\omega)}, \mathcal{E}_{0,\mathrm{p},+}^{(\omega)}]^{\mathrm{T}}$ and the electric field $\boldsymbol{E}_\nu^{(\omega)}$ at the ν-th interface. This relation can be expressed in a compact matrix form

$$\boldsymbol{E}_\nu^{(\omega)}(\boldsymbol{\rho}, z_\nu) = \mathbf{X}_\nu^{(\omega)}\cdot\boldsymbol{J}_{0,+}^{(\omega)}\exp[ik_0^{(\omega)}N_y y],$$

(3.33)

where $\mathbf{X}_\nu^{(\omega)}$ is the 3×2 matrix containing generalized incoming Fresnel elements. That is why, this matrix is called incoming Fresnel matrix. The exponential factor expresses the lateral dependence of $\boldsymbol{E}_\nu^{(\omega)}$ due to the phase variation of the light. The incoming Fresnel matrix $\mathbf{X}_\nu^{(\omega)}$ can be written as [Eqs. (3.10)(3.24)(3.28)(3.32)]

$$\mathbf{X}_\nu^{(\omega)} = \frac{1}{2}\left(\mathbf{U}_{\nu-1}^{(\omega)}\mathbf{P}_{\nu-1}^{(\omega)}[\mathbf{L}_{\nu-1}]^{-1} + \mathbf{U}_\nu^{(\omega)}[\mathbf{L}_\nu^{(\omega)}]^{-1}\right)\mathbf{L}_{M+1}^{(\omega)}\begin{bmatrix}t_{\mathrm{ss}} & t_{\mathrm{sp}} \\ 0 & 0 \\ t_{\mathrm{ps}} & t_{\mathrm{pp}} \\ 0 & 0\end{bmatrix},$$

(3.34)

where t_{ij}, with $i,j = \{\mathrm{s},\mathrm{p}\}$, are the transmission coefficients [see Eq. (3.25)]. The $\mathbf{U}_\nu^{(\omega)}$ matrix in Eq. (3.34) expresses Eq. (3.10) in a matrix form, i.e. the transformation between $\boldsymbol{A}_\nu^{(\omega)}$ and $\boldsymbol{E}_\nu^{(\omega)}$ at the same depth z_ν

$$\boldsymbol{E}_\nu^{(\omega)}(\boldsymbol{\rho}, z_\nu) = \mathbf{U}_\nu^{(\omega)}\boldsymbol{A}_\nu^{(\omega)}\exp[ik_0^{(\omega)}N_y y].$$

(3.35)

Using Eq. (3.10), the matrix $\mathbf{U}_\nu^{(\omega)}$ writes

$$\mathbf{U}_\nu^{(\omega)} = \begin{bmatrix}\hat{e}_{\nu,1,+}^{(\omega)}\cdot\hat{x} & \hat{e}_{\nu,1,-}^{(\omega)}\cdot\hat{x} & \hat{e}_{\nu,2,+}^{(\omega)}\cdot\hat{x} & \hat{e}_{\nu,2,-}^{(\omega)}\cdot\hat{x} \\ \hat{e}_{\nu,1,+}^{(\omega)}\cdot\hat{y} & \hat{e}_{\nu,1,-}^{(\omega)}\cdot\hat{y} & \hat{e}_{\nu,2,+}^{(\omega)}\cdot\hat{y} & \hat{e}_{\nu,2,-}^{(\omega)}\cdot\hat{y} \\ \hat{e}_{\nu,1,+}^{(\omega)}\cdot\hat{z} & \hat{e}_{\nu,1,-}^{(\omega)}\cdot\hat{z} & \hat{e}_{\nu,2,+}^{(\omega)}\cdot\hat{z} & \hat{e}_{\nu,2,-}^{(\omega)}\cdot\hat{z}\end{bmatrix},$$

(3.36)

and, for an isotropic medium

$$\mathbf{U}_{\nu,\mathrm{iso}}^{(\omega)} = \begin{bmatrix}1 & 1 & 0 & 0 \\ 0 & 0 & N_{z,\nu,+}^{(\omega)}/N_\nu^{(\omega)} & -N_y^{(\omega)}/N_\nu^{(\omega)} \\ 0 & 0 & N_{z,\nu,-}^{(\omega)}/N_\nu^{(\omega)} & -N_y^{(\omega)}/N_\nu^{(\omega)}\end{bmatrix}.$$

(3.37)

3.3   Analytical expressions of magneto-optical effects in the ultrathin FM film approximation

When calculating the optical response (i.e. reflection coefficients or MOKE) of a multilayer structure, the exact formula is rather complicated. After some justified simplifications, one can get a clearer physical meaning of MOKE. For that purpose, the ultrathin FM film approximation is used. Let us consider only one FM layer in the structure. Then the approximation assumes that the thickness of the FM layer $t^{(\mathrm{fm})}$ is much thinner than the light wavelength inside the FM material, i.e. $t^{(\mathrm{fm})} \ll 4\pi\lambda^{(\omega)}/|\varepsilon_0^{(\mathrm{fm})}|$ [32, 45, 46, 48, 49, 55, 56]. This assumption simplifies significantly the analytical MOKE formula since, in this approximation, the FM layer is "invisible" from an optical point of view, and influences the optical response only through its "magneto-optical" character, i.e. off-diagonal elements of the permittivity tensor.

3.3.1   Analytical expression of the reflection coefficients for an ultrathin FM layer

In this Section, the reflection coefficients are expressed in the ultrathin FM film approximation. The analytical expressions of MOKE will be presented in the next Section 3.3.2.

The ultrathin FM layer, having a tensor permittivity $\boldsymbol{\varepsilon}^{(\mathrm{fm})}$ and thickness $t^{(\mathrm{fm})}$, is sandwiched between an overlayer of thickness $d^{(\mathrm{nf})}$ and an infinite substrate, both consisting of the same isotropic non-FM material of permittivity $\varepsilon^{(\mathrm{nf})} = (N^{(\mathrm{nf})})^2$. The refractive index of the superstrate (usually air) is denoted by $N^{(0)}$. The sketch of the considered sandwich structure and notations of all used variables are presented in Fig. 3.3(a).
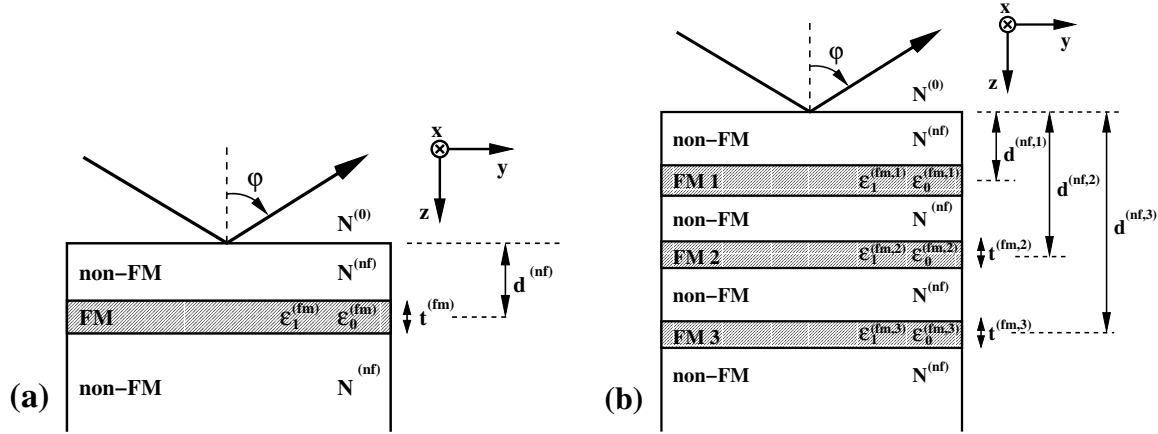
Figure 3.3: Sketch of: (a) a sandwiched FM layer, (b) a multilayer structure composed of a stack of FM and non-FM layers.

The permittivity tensor of the FM layer $\boldsymbol{\varepsilon}^{(\mathrm{fm})}$ has the general form

$$\boldsymbol{\varepsilon}^{(\mathrm{fm})} = \begin{bmatrix} \varepsilon_0^{(\mathrm{fm})} & \varepsilon_{xy}^{(\mathrm{fm})} & \varepsilon_{xz}^{(\mathrm{fm})} \\ \varepsilon_{yx}^{(\mathrm{fm})} & \varepsilon_0^{(\mathrm{fm})} & \varepsilon_{yz}^{(\mathrm{fm})} \\ \varepsilon_{zx}^{(\mathrm{fm})} & \varepsilon_{zy}^{(\mathrm{fm})} & \varepsilon_0^{(\mathrm{fm})} \end{bmatrix}, \tag{3.38}$$

where non-diagonal elements are different. The diagonal elements are assumed here to be equal in order to obtain simple analytic solutions. This approach is usually justified since the reflection coefficients do not depend much on small variations between diagonal elements, as it can be seen from Table 3.1.

The analytic expressions of the reflection coefficients are calculated within the 4×4 matrix formalism introduced in Sections 3.2.1 – 3.2.4. Since these analytic calculations are quite complicated, I present here in Table 3.1 only final results (for more details see for example [46]). The reported expressions are complete up to the first order Taylor series development in FM layer thickness, i.e., $r_{ij} = r_{ij}/_{t^{(\text{fm})}=0} + (\mathrm{d}r_{ij}/\mathrm{d}t^{(\text{fm})})t^{(\text{fm})}$, for $\{i,j\} = \{\text{s}, \text{p}\}$. Thus, there is no missing term of higher order in $\varepsilon_{ij}^{(\text{fm})}$ for $i \neq j$, and these expressions are valid even for large $\varepsilon_{ij}^{(\text{fm})}$, $i \neq j$.

The resulting diagonal reflectivity coefficients r_{ss} and r_{pp} are expressed by the sum of individual contributions reported in Table 3.1

$$
\begin{aligned}
r_{\text{ss}} &= r_{\text{ss}}^{(0)} + r_{\text{ss}}^{(0,t^{(\text{fm})})} + r_{\text{ss}}^{(2)} \\
r_{\text{pp}} &= r_{\text{pp}}^{(0)} + r_{\text{pp}}^{(0,t^{(\text{fm})})} + r_{\text{pp}}^{(1)} + r_{\text{pp}}^{(2)},
\end{aligned}
\tag{3.39}
$$

where superscripts $^{(0)}$, $^{(1)}$ and $^{(2)}$ denote the perturbation order of reflection coefficients with respect to the off-diagonal permittivity elements of the FM layer $\varepsilon_{ij}^{(\text{fm})}$, $i \neq j$. All expressions have been tested numerically. To my knowledge, such calculations of the reflection coefficients in the ultrathin FM film approximation has never been reported so far for a general form of the isotropic permittivity tensor. Usually it is assumed that the permittivity tensor is antisymmetric, as follows from symmetry arguments when magnetization is the alone perturbative term. However, as we shall see later in Chapter 6, for Vicinal Induced Surface MOKE (VISMOKE), a more general permittivity tensor form is needed to treat together magnetic (which are antisymmetric) and structural (which are symmetric) perturbations.

In the expressions of Table 3.1, the coefficient $k_0^{(\omega)}$ stands for the length of the light wavevector in vacuum

$$
k_0^{(\omega)} = 2\pi/\lambda^{(\omega)},
\tag{3.40}
$$

where $\lambda^{(\omega)}$ is the light wavelength in vacuum. The coefficient Q describes the influence of the non-FM overlayer of thickness $d^{(\text{nf})}$ on MO effects

$$
Q = \exp[4i\pi N_z^{(\text{nf})} d^{(\text{nf})}/\lambda^{(\omega)}].
\tag{3.41}
$$

The variation of Q with both photon energy and incidence angle has some consequences on the depth resolution of MOKE, studied in detail in Section 5.4 (see Figures 5.1–5.5). From exact calculations by the 4×4 matrix formalism, I have numerically checked that the accuracy of the ultrathin FM film approximation is better than 1% for $t^{(\text{fm})} = 0.1\,\text{nm}$, and of the order of 5-15% for $t^{(\text{fm})} = 1\,\text{nm}$.

3.3.2   Analytical expressions of MOKE in a FM sandwich structure

In this Section, I give the analytical expressions of MOKE in the ultrathin FM film approximation. Although analytical expressions of MOKE have been proposed by many authors [32, 45, 46, 47, 49, 55], my presentation here introduces two additional new features:

r_{ps}
$\dfrac{2ik_0^{(\omega)}t^{(\mathrm{fm})}QN^{(0)}\cos\varphi}{(N^{(0)}\cos\varphi+N_z^{(\mathrm{nf})})(N^{(0)}N_z^{(\mathrm{nf})}+(N^{(\mathrm{nf})})^2\cos\varphi)}\left[\dfrac{\varepsilon_{zx}\varepsilon_{yz}N_z^{(\mathrm{nf})}}{\varepsilon_0^{(\mathrm{fm})}}-\dfrac{\varepsilon_{zx}N_y(N^{(\mathrm{nf})})^2}{\varepsilon_0^{(\mathrm{fm})}}-\varepsilon_{yx}N_z^{(\mathrm{nf})}\right]$

r_{sp}
$\dfrac{2ik_0^{(\omega)}t^{(\mathrm{fm})}QN^{(0)}\cos\varphi}{(N^{(0)}\cos\varphi+N_z^{(\mathrm{nf})})(N^{(0)}N_z^{(\mathrm{nf})}+(N^{(\mathrm{nf})})^2\cos\varphi)}\left[-\dfrac{\varepsilon_{xz}\varepsilon_{zy}N_z^{(\mathrm{nf})}}{\varepsilon_0^{(\mathrm{fm})}}-\dfrac{\varepsilon_{xz}N_y(N^{(\mathrm{nf})})^2}{\varepsilon_0^{(\mathrm{fm})}}+\varepsilon_{xy}N_z^{(\mathrm{nf})}\right]$

$r_{\mathsf{ss}}=r_{\mathsf{ss}}^{(0)}+r_{\mathsf{ss}}^{(0,t^{(\mathrm{fm})})}+r_{\mathsf{ss}}^{(2)}$	
$r_{\mathsf{ss}}^{(0)}$	$\dfrac{N^{(0)}\cos\varphi-N_z^{(\mathrm{nf})}}{N^{(0)}\cos\varphi+N_z^{(\mathrm{nf})}}$
$r_{\mathsf{ss}}^{(0,t^{(\mathrm{fm})})}=\rho_{\mathsf{ss}}^{(0,t^{(\mathrm{fm})})}\,t^{(\mathrm{fm})}$	$\dfrac{2ik_0^{(\omega)}QN^{(0)}\cos\varphi[\varepsilon_0^{(\mathrm{fm})}-(N_{\mathrm{nf}})^2]}{(N^{(0)}\cos\varphi+N_z^{(\mathrm{nf})})^2}\,t^{(\mathrm{fm})}$
$r_{\mathsf{ss}}^{(2)}=\rho_{\mathsf{ss}}^{(2)}\,t^{(\mathrm{fm})}\varepsilon_{xz}\varepsilon_{zx}$	$-\dfrac{2ik_0^{(\omega)}\,QN^{(0)}\cos\varphi}{\varepsilon_0^{(\mathrm{fm})}\left(N^{(0)}\cos\varphi+N_z\right)^2}\,t^{(\mathrm{fm})}\,\varepsilon_{xz}\varepsilon_{zx}$

$r_{\mathsf{pp}}=r_{\mathsf{pp}}^{(0)}+r_{\mathsf{pp}}^{(0,t^{(\mathrm{fm})})}+r_{\mathsf{pp}}^{(1)}+r_{\mathsf{pp}}^{(2)}$	
$r_{\mathsf{pp}}^{(0)}$	$\dfrac{(N^{(\mathrm{nf})})^2\cos\varphi-N_z^{(\mathrm{nf})}N^{(0)}}{(N^{(\mathrm{nf})})^2\cos\varphi+N_z^{(\mathrm{nf})}N^{(0)}}$
$r_{\mathsf{pp}}^{(0,t^{(\mathrm{fm})})}=\rho_{\mathsf{pp}}^{(0,t^{(\mathrm{fm})})}t^{(\mathrm{fm})}$	$\dfrac{2ik_0^{(\omega)}QN^{(0)}\cos\varphi\left[(N^{(\mathrm{nf})})^4(\varepsilon_0^{(\mathrm{fm})}-N_y^2)-(N_z^{(\mathrm{nf})}\varepsilon_0^{(\mathrm{fm})})^2\right]}{\varepsilon_0^{(\mathrm{fm})}\left[N^{(0)}N_z^{(\mathrm{nf})}+(N^{(\mathrm{nf})})^2\cos\varphi\right]^2}\,t^{(\mathrm{fm})}$
$r_{\mathsf{pp}}^{(1)}=\rho_{\mathsf{pp}}^{(1)}\,t^{(\mathrm{fm})}\left(\varepsilon_{yz}-\varepsilon_{zy}\right)$	$\dfrac{2ik_0^{(\omega)}Q(N^{(\mathrm{nf})})^2N_yN_z^{(\mathrm{nf})}N^{(0)}\cos\varphi}{\varepsilon_0^{(\mathrm{fm})}\left[N^{(0)}N_z^{(\mathrm{nf})}+(N^{(\mathrm{nf})})^2\cos\varphi\right]^2}\,t^{(\mathrm{fm})}\left(\varepsilon_{yz}-\varepsilon_{zy}\right)$
$r_{\mathsf{pp}}^{(2)}=\rho_{\mathsf{pp}}^{(2)}\,t^{(\mathrm{fm})}\varepsilon_{yz}\varepsilon_{zy}$	$\dfrac{2ik_0^{(\omega)}Q(N_z^{(\mathrm{nf})})^2N^{(0)}\cos\varphi}{\varepsilon_0^{(\mathrm{fm})}\left[N^{(0)}N_z^{(\mathrm{nf})}+(N^{(\mathrm{nf})})^2\cos\varphi\right]^2}\,t^{(\mathrm{fm})}\,\varepsilon_{yz}\varepsilon_{zy}$

Table 3.1: Reflection coefficients for an ultrathin FM layer sandwiched between an overlayer and an infinite substrate [presented on Figure 3.3(a)]. The terms $k_0^{(\omega)}$ and Q are defined by Eqs. (3.40) and (3.41), respectively. $N^{(\mathrm{nf})}=\sqrt{\varepsilon_0^{(\mathrm{nf})}}=\sqrt{N_y^2+(N_z^{(\mathrm{nf})})^2}$ is the Pythagorean length of the normalized wavevector inside the non-FM material [Eq. (3.7)]. The final reflection coefficients are given by the sum of all these partial contributions [Eq. (3.39)].

(i) MOKE expressions are determined for a general form of the permittivity tensor, expressed by Eq. (3.38).

(ii) In order to get a better physical understanding of MOKE, I decompose the analytical expression into χ, $V_{\mathbf{s},\mathbf{p}}$, Q terms, each of them having a clear physical meaning.

MOKE is defined by Eq.(2.13) as ratios between the reflection coefficients. Using the expressions of the reflectivity coefficients from Table 3.1, I have expressed $\mathbf{s}$ and $\mathbf{p}$-MOKE as

$$
\Phi_{\mathbf{s}} \equiv -\frac{r_{\mathbf{ps}}}{r_{\mathbf{ss}}} = \chi\, Q\, V_{\mathbf{s}}\, t^{(\mathrm{fm})} \left(i\varepsilon_{yx}^{(\mathrm{fm})} \frac{N_z^{(\mathrm{nf})}}{N^{(\mathrm{nf})}} + \frac{i N_y N^{(\mathrm{nf})} \varepsilon_{zx}^{(\mathrm{fm})}}{\varepsilon_0^{(\mathrm{fm})}} - i\frac{\varepsilon_{zx}^{(\mathrm{fm})}\varepsilon_{yz}^{(\mathrm{fm})} N_z^{(\mathrm{nf})}}{\varepsilon_0^{(\mathrm{fm})} N^{(\mathrm{nf})}} \right)
$$

$$
\Phi_{\mathbf{p}} \equiv \frac{r_{\mathbf{sp}}}{r_{\mathbf{pp}}} = \chi\, Q\, V_{\mathbf{p}}\, t^{(\mathrm{fm})} \left(-i\varepsilon_{xy}^{(\mathrm{fm})} \frac{N_z^{(\mathrm{nf})}}{N^{(\mathrm{nf})}} + \frac{i N_y N^{(\mathrm{nf})} \varepsilon_{xz}^{(\mathrm{fm})}}{\varepsilon_0^{(\mathrm{fm})}} + i\frac{\varepsilon_{xz}^{(\mathrm{fm})}\varepsilon_{zy}^{(\mathrm{fm})} N_z^{(\mathrm{nf})}}{\varepsilon_0^{(\mathrm{fm})} N^{(\mathrm{nf})}} \right),
$$

(3.42)

where $N_y = N^{(0)} \sin\varphi$ and $N_z^{(\mathrm{nf})} = \sqrt{\varepsilon_0^{(\mathrm{nf})} - N_y^2}$ correspond to the y and z-components of the normalized wavevector in the non-FM material.

The three contributions to $\mathbf{s}$-MOKE, $\Phi_{\mathbf{s}}$, and $\mathbf{p}$-MOKE, $\Phi_{\mathbf{p}}$ [Eqs. (3.42)], are the polar MOKE (PMOKE), longitudinal MOKE (LMOKE) and "cross-term" MOKE, respectively. Although PMOKE and LMOKE are well-known contributions, the "cross-term" is often neglected. This last contribution takes place when

(i) the in-plane magnetization has both transverse and longitudinal components. When $m_z^{(\mathrm{fm})} = 0$ and $\varphi = 0$, both PMOKE and LMOKE vanish and if it subsists an effect, this contribution comes from quadratic MO effects [22, 23]

(ii) when a structural off-diagonal permittivity element is present. Then, this "cross-term" contribution gives rise to a magneto-structural MOKE. In Section 6, we measured such an effect (we call it VISMOKE) for FM layers grown on vicinal surfaces.

Now, let us comment on the different terms involved in Eq. (3.42). The coefficient χ has a pure optical origin. It describes the optical influence of the substrate on MOKE at zero angle of incidence ($\varphi = 0$):

$$
\chi = \frac{4\pi N^{(0)}}{\lambda^{(\omega)} \left[(N^{(\mathrm{nf})})^2 - (N^{(0)})^2 \right]}.
$$

(3.43)

Thus, for $\varphi = 0$, the first term of Eq. (3.42), $i\chi\varepsilon_{yx}^{(\mathrm{fm})} t^{(\mathrm{fm})}$, is nothing more that the PMOKE for an ultrathin FM layer with thickness $t^{(\mathrm{fm})}$, deposited on the top of a non-FM bulk material.

The quantities $(N_z^{(\mathrm{nf})}/N^{(\mathrm{nf})})V_j$ and $N_y N^{(\mathrm{nf})}/\varepsilon_0^{(\mathrm{fm})}V_j$, with $j = \{\mathbf{s},\mathbf{p}\}$, describe the variation of PMOKE and LMOKE, respectively, with the incidence angle φ. For $\mathbf{s}$ and $\mathbf{p}$-MOKE, $V_{\mathbf{s}}$ and $V_{\mathbf{p}}$ express as

$$
V_{\mathbf{s}} = \frac{N^{(\mathrm{nf})} \cos\varphi}{N_z^{(\mathrm{nf})} \cos\varphi + N^{(0)} \sin^2\varphi}, \qquad V_{\mathbf{p}} = \frac{N^{(\mathrm{nf})} \cos\varphi}{N_z^{(\mathrm{nf})} \cos\varphi - N^{(0)} \sin^2\varphi}.
$$

(3.44)

At normal incidence, $V_\mathsf{s} = V_\mathsf{p} = 1$.

The coefficient $Q = \exp[4\pi i N_z^{(\mathrm{nf})} d^{(\mathrm{nf})}/\lambda^{(\omega)}]$ [Eq. (3.41)] accounts for the MOKE attenuation with an increase of the thickness $d^{(\mathrm{nf})}$ of the non-FM overlayer. This coefficient is examined in detail in Section 5.4. Note, that the dependence of Q on the incidence angle φ is very small (about 0.5% per nm of overlayer thickness). Thus, the angular dependence of MOKE is mostly described by the quantities $(N_z^{(\mathrm{nf})}/N^{(\mathrm{nf})})V_\mathsf{s,p}$ and $(N_y N^{(\mathrm{nf})}/\varepsilon_0^{(\mathrm{fm})})V_\mathsf{s,p}$.

Similarly to the discussion concerning reflection coefficients, the MOKE expressed by Eqs. (3.42) is described completely up to the first order of the Taylor development $(\mathrm{d}\Phi^{(1)}/\mathrm{d}t^{(\mathrm{fm})})t^{(\mathrm{fm})}$. Thus, in the ultrathin FM film approximation:

(i) Eqs. (3.42) are valid even for large off-diagonal ($i \neq j$) permittivity $\varepsilon_{ij}^{(\mathrm{fm})}$ values.

(ii) there is no missing term of higher order for the off-diagonal permittivity $\varepsilon_{ij}^{(\mathrm{fm})}$.

Taking into account the dependence of the permittivity tensor $\boldsymbol{\varepsilon}^{(\mathrm{fm})}$ on the normalized layer magnetization $\boldsymbol{m}^{(\mathrm{fm})} = [m_x^{(\mathrm{fm})}, m_y^{(\mathrm{fm})}, m_z^{(\mathrm{fm})}]$ (with $|\boldsymbol{m}^{(\mathrm{fm})}| = 1$) [10]

$$\boldsymbol{\varepsilon}^{(\mathrm{fm})} = \begin{bmatrix} \varepsilon_0^{(\mathrm{fm})} & -i\varepsilon_1^{(\mathrm{fm})} m_z^{(\mathrm{fm})} & i\varepsilon_1^{(\mathrm{fm})} m_y^{(\mathrm{fm})} \\ i\varepsilon_1^{(\mathrm{fm})} m_z^{(\mathrm{fm})} & \varepsilon_0^{(\mathrm{fm})} & -i\varepsilon_1^{(\mathrm{fm})} m_x^{(\mathrm{fm})} \\ -i\varepsilon_1^{(\mathrm{fm})} m_y^{(\mathrm{fm})} & i\varepsilon_1^{(\mathrm{fm})} m_x^{(\mathrm{fm})} & \varepsilon_0^{(\mathrm{fm})} \end{bmatrix} \tag{3.45}$$

and neglecting the cross-term contribution in Eq. (3.42), one obtains the usual expressions of MOKE in the ultrathin FM layer approximation [46, 47, 49]

$$\begin{aligned} \Phi_\mathsf{s} &\equiv -\frac{r_\mathsf{ps}}{r_\mathsf{ss}} = -\chi\, Q\, V_\mathsf{s}\, t^{(\mathrm{fm})} \left[\varepsilon_1^{(\mathrm{fm})} \frac{N_z^{(nF)}}{N^{(nF)}} m_z^{(\mathrm{fm})} - \varepsilon_1^{(\mathrm{fm})} \frac{N_y N^{(nF)}}{\varepsilon_0^{(\mathrm{fm})}} m_y^{(\mathrm{fm})} \right] \\ &= \Phi_{\mathrm{pol},\mathsf{s}} m_z^{(\mathrm{fm})} + \Phi_{\mathrm{lon},\mathsf{s}} m_y^{(\mathrm{fm})} \\[6pt] \Phi_\mathsf{p} &\equiv \frac{r_\mathsf{sp}}{r_\mathsf{pp}} = -\chi\, Q\, V_\mathsf{p}\, t^{(\mathrm{fm})} \left[\varepsilon_1^{(\mathrm{fm})} \frac{N_z^{(nF)}}{N^{(nF)}} m_z^{(\mathrm{fm})} + \varepsilon_1^{(\mathrm{fm})} \frac{N_y N^{(nF)}}{\varepsilon_0^{(\mathrm{fm})}} m_y^{(\mathrm{fm})} \right] \\ &= \Phi_{\mathrm{pol},\mathsf{p}} m_z^{(\mathrm{fm})} + \Phi_{\mathrm{lon},\mathsf{p}} m_y^{(\mathrm{fm})}. \end{aligned} \tag{3.46}$$

3.3.3   Analytical expression of MOKE in a multilayer FM structure

The total MOKE $\Phi^{(\mathrm{tot})}$ is given by the sum of contributions from all FM layers [ref. [45] or Eq. (2.17)]. This additivity rule is valid even for thick FM layers. It is a consequence of the fact that MOKE can be considered as a small perturbation of optical properties. Thus,

$$\Phi^{(\mathrm{tot})} = \sum_i \Phi_{\mathrm{pol}}^{(i)} m_z^{(\mathrm{fm},i)} + \sum_i \Phi_{\mathrm{lon}}^{(i)} m_y^{(\mathrm{fm},i)}, \tag{3.47}$$

where $\Phi_{\mathrm{pol}}^{(i)}$, $\Phi_{\mathrm{lon}}^{(i)}$ denote the saturated PMOKE, LMOKE contributions from the i-th FM layer, respectively, and $\boldsymbol{m}^{(i)} = [m_x^{(i)}, m_y^{(i)}, m_z^{(i)}]$ the normalized magnetization of the i-th layer [Fig. 3.3(b)].

If all FM layers together fulfill the ultrathin film approximation (i.e. $\sum_i t^{(\mathrm{fm},i)} |\varepsilon_0^{(\mathrm{fm},i)}| \ll 4\pi\lambda^{(\omega)}$), and if the spacers, overlayer and buffer consists of the same non-FM material, then the PMOKE $\Phi_{\mathrm{pol}}^{(i)}$ and LMOKE $\Phi_{\mathrm{lon}}^{(i)}$ originating from a single i-th FM layer can be expressed by Eqs. (3.46).

3.4 Conclusion of Chapter 3

In the first part of this Chapter, I have demonstrated that the usual Fourier $\boldsymbol{k}$-space is not well adapted to treat the case of radiation of a point dipole (which will be treated in Chapter 7). Thus, I introduced a $\boldsymbol{q}$-space which is a Fourier space in the k_x, k_y-direction and a real space in the z-direction. Along all this manuscript, I treat the light propagation in multilayers in this $\boldsymbol{q}$-space. In the second part, I present the classical 4×4 matrix formalism and calculations of reflection coefficients, magneto-optical Kerr effect (MOKE) and of the profile of the electric field inside a multilayer structure, with arbitrary magnetized layers. In the third part, I extract the expressions of the reflection coefficients and MOKE within the ultrathin FM film approximation.

Chapter 4

Magneto-optical properties of FM/non-FM interfaces

This Chapter reports on the application of MOKE calculations to explain experimental MOKE results obtained from Co/Au interfaces. In a first stage, I present a reliable description of the MO properties of ferromagnetic (FM)/non-ferromagnetic (non-FM) interfaces using an original procedure based on the dependence of MOKE on the thickness of the FM layer. The results presented in this Chapter have been already published (Hamrle *et al.* [57]).

4.1 Introduction

The structure and properties of buried interfaces between FM/non-FM metals attract considerable attention in the field of thin film magnetism. When the thickness of a FM film is substantially reduced (down to few atomic layers), the interface effects, and especially the interface magnetic anisotropy, become more significant and often control a lot of physical effects. The interface anisotropy can overcome the demagnetizing field effect and favors an out-of-plane easy magnetization axis [58, 59, 60] or control spin reorientation transitions [61]. Hence, interfaces have a fundamental importance in practical applications, such as perpendicular magneto-optical recording [43], giant magnetoresistance sensors [62], and random access memories [63].

The interface anisotropy is mainly of electronic origin and primarily related to the spin-orbit coupling interaction from which originate both linear magneto-optical (MO) and non-linear MO effects (Section 2.3). One therefore obviously expects that such interface effects should modify MO properties of FM multilayer systems. From an experimental point of view, the MO properties of interfaces can be more directly studied by means of MOSHG [1, 2], which is sensitive to the breaking in structural symmetry, and consequently selectively dependent on properties of interfaces and surfaces. Up to now, little attention has been paid to linear MOKE induced by FM/noble metal interfaces. This is due to the fact that no MOKE technique was proposed before to separate MO properties coming from the bulk of the FM layer and FM/non-FM interfaces. Until recently, the MOKE interface contribution was deduced from the analysis of the MOKE variation with the FM

film thickness. There are experimental evidences that the *extrapolation* of MOKE to zero FM film thickness is non-zero. Its value is called MOKE interface contribution. This was observed, for example, in Au/Co/Au sandwich structures [42], and in Pd/Co/Pd [64] and Pt/Co/Pt [65] wedges. The non-zero extrapolation of the MOKE signal was assigned to the contribution of FM/non-FM interfaces.

Usually, it is *possible* to deduce MO properties of the interfaces by, e.g., fitting the experimental data to a theoretical model [66]. However, in most cases, this is not accurate enough since it requires the precise knowledge of optical parameters of *all* other layers involved in the multilayer structure. The interface contribution, for a given wavelength, depends upon several parameters, such as the angle of incidence, the initial light polarization, optical properties and thickness of the sandwiching layers, etc. Consequently, it is not straightforward to interpret the MO data to extract interface contributions.

Theoretical models, based on an ideal multilayer structure (i.e. for a step-like profile of optical properties) predict that MOKE cancels when the FM layer thickness goes to zero, in contradiction with experimental observations. Concerning the change of the electronic structure at the FM/non-FM interfaces, it can be explored by *ab-initio* calculations. In principle, there are two possible approaches to this problem.

- In the first approach, the periodic multilayer structure is considered as an artificial superlattice, i.e. as a new bulk material. It has been satisfactorily applied to Cu/Co [67], Pd/Co [68] and Au/Fe(001) [69] superlattices. Although this is a quite straightforward method, it does not provide spatially resolved information about the electronic interactions at the FM/non-FM interfaces.

- The second approach introduces interface interlayers. In this case the multilayer stacking is always considered, but the sharp interfaces between the FM and non-FM materials are substituted by very thin interface layers. This approach allows to include phenomenologically FM/non-FM interface hybridization, strains, effects of stray fields, interface roughness or alloying, etc. Due to a rapid progress of *ab-initio* calculations, the interface interlayer approach is even more fruitful than originally expected. A fully relativistic formalism has recently been developed by Huhne and Ebert [26] to define a layer-resolved frequency-dependent optical conductivity tensor in arbitrary layered system. It can be therefore expected that, in a very near future, it will be possible to make a direct link between the microscopic *ab-initio* calculations and phenomenological interface interlayer models.

In this Chapter, I refine the analysis of the MOKE variation with the FM film thickness in order to account for the experimental results. Moreover, I introduce the deviation of the integral off-diagonal permittivity (described by $\mathcal{E}_A$) from the ideal step-like permittivity profile to describe the MO properties of the buried FM/non-FM interfaces that may be deduced straightforwardly from the experimental data. It is demonstrated that this quantity is independent on the incidence angle of the incoming light, its polarization (s or p) and the thicknesses and the optical parameters of sandwiching layers. Provided that the off-diagonal permittivity elements of the inner part of the ferromagnetic layer are known, this quantity can be used for evaluating the off-diagonal elements of the permittivity tensor of interface interlayers. Furthermore, our technique can be used both for polar and longitudinal geometries of the multilayer magnetization.

This Chapter is organized as follows. In Section 4.2, I summarize analytical formula describing polar MOKE (PMOKE) in structures containing ultrathin magnetic films. In Section 4.3, I introduce integral MO characteristics of the structure which are subsequently used to derive a relation between the optical parameters and the experimental characteristics of the FM/non-FM interface. Section 4.4 summarizes sample preparation and its structural and magnetic properties. Section 4.5 describes experimental procedures used to extract the interface contributions from the total MOKE and presents the MO parameters of the interface. Finally, simple models describing the contributions of the FM/non-FM interface to MOKE are discussed in Section 4.6.

4.2 Experimental PMOKE in a sandwich structure: realistic analytical description

As follows from experiments, at small FM layer thickness, the complex MOKE Φ can, to some extent, be described by a linear function of the FM film thickness $t^{(\mathrm{fm})}$, i.e. $\Phi \sim B\,t^{(\mathrm{fm})}$, where B is a complex number. The exact linearity is predicted by simplified models [49, 32, 46, 70, 71] based on the ultrathin FM film approximation (see Section 3.3.2). The ultrathin FM film approximation is derived under the following assumptions (Section 3.3):

(i) The in-depth optical profile of the multilayer structure is step-like, i.e. all layers are assumed to be optically homogeneous and separated by sharp planar interfaces.

(ii) The FM layer is ultrathin, i.e. its thickness is assumed to be $t^{(\mathrm{fm})} \ll \lambda/(4\pi|N^{(\mathrm{fm})}|)$, where $N^{(\mathrm{fm})}$ is the complex refractive index of the FM film and λ the wavelength of the probing light in vacuum. For example, at $\lambda = 300\,\mathrm{nm}$, the thickness $t^{(\mathrm{fm})}$ of an ultrathin Co film ($|N^{(\mathrm{fm})}| \approx 2.7$) has to be much thinner than $9\,\mathrm{nm}$.

Because the conditions (i) and (ii) are not always perfectly fulfilled in real structures, I propose that the linear expression of Φ has to be corrected by a constant and a quadratic term, i.e.

$$\Phi(t^{(\mathrm{fm})}) = A + B\,t^{(\mathrm{fm})} + C\left(t^{(\mathrm{fm})}\right)^2. \tag{4.1}$$

The coefficients A, B and C are, in general, complex numbers. A accounts for the fact that the actual profile of the off-diagonal element of the permittivity tensor is not described by a step-like function of the depth coordinate across the multilayer stack. The quadratic term is mainly related to the change of the diagonal reflection coefficients r_{ss}, r_{pp}, with the FM layer thickness (ref. [32, 70] or terms $r_{\mathsf{ss}}^{(0,t^{(\mathrm{fm})})}$, $r_{\mathsf{pp}}^{(0,t^{(\mathrm{fm})})}$ in Table 3.1).

In the following, I limit myself to the PMOKE case, i.e. when the magnetization of the FM layer is perpendicular to the film surface ($\boldsymbol{M} \parallel \hat{z}$). For an ideal sandwich structure consisting of an homogeneous *ultrathin* FM layer of thickness $t^{(\mathrm{fm})}$, PMOKE [Eq.(3.42)] is proportional to the off-diagonal element $\varepsilon_1^{(\mathrm{fm})}$ of the permittivity tensor

$$\Phi_{\mathsf{s/p}} = \tilde{\chi}_{\mathsf{s/p}}\,\varepsilon_1^{(\mathrm{fm})}t^{(\mathrm{fm})} = \tilde{\chi}_{\mathsf{s/p}}\,\mathcal{E}, \tag{4.2}$$

where $\tilde{\chi}_{\mathsf{s/p}} = -\chi V_{\mathsf{s/p}} Q N_z^{(\mathrm{nf})}/N^{(\mathrm{nf})}$; all the involved coefficients are defined in Section 3.3.2 (page 37). The newly introduced coefficient $\mathcal{E} = \varepsilon_1^{(\mathrm{fm})}t^{(\mathrm{fm})}$ will be called *integral off-diagonal permittivity*. Please, don't confuse it with $\mathcal{E}_{\nu,\Pi,d}$ which represents the modal amplitude.

The terms $\mathcal{E}$ and $\tilde{\chi}$ are related to the optical and MO properties of the ultrathin FM layer itself and the optical properties of the rest of the sandwiching layers, respectively.

PMOKE described by Eq. (4.2) does not depend on the diagonal optical permittivity $\varepsilon_0^{(\mathrm{fm})}$ of the ultrathin FM layer. Consequently, the MO signal should not depend on its variation near the FM/non-FM interface. On the other hand, for ultrathin FM films, it is the off-diagonal permittivity $\varepsilon_1^{(\mathrm{fm})}$ that contributes to PMOKE. Consequently, PMOKE depends on the variation of $\varepsilon_1(z)$ across the FM layer. The details of this dependence and its variation with the shape of the $\varepsilon_1(z)$ profile are discussed in the following section.

4.3   Interface contributions and integral off-diagonal permittivity excess

The description of the FM/non-FM interface by a step-like profile of the off-diagonal permittivity is unsatisfactory to account for the non-zero MO effect, when the FM layer thickness is extrapolated to zero. For real interfaces, it is possible to approximate the FM layer and its MO active surrounding by a stack of infinitesimally thin sublayers of thickness $t^{(i)}$ with different off-diagonal permittivity $\varepsilon_1^{(i)}$. Due to its additive character [45], the total PMOKE of the stack of FM sublayers is a sum of the individual contributions from all these sublayers, i.e. $\Phi = \sum \Phi^{(i)} = \sum \tilde{\chi}^{(i)} \varepsilon_1^{(i)} t^{(i)}$. This situation is depicted on Fig. 4.1. If the total thickness of all sublayers $\sum t^{(i)}$ satisfies the ultrathin FM film approximation, $\tilde{\chi}^{(i)}$ is constant for all sublayers and will be noted by $\tilde{\chi}$. Consequently, the total PMOKE can be expressed by

$$\Phi = \tilde{\chi} \sum_i \varepsilon_1^{(i)} t^{(i)} \equiv \tilde{\chi}\mathcal{E}. \tag{4.3}$$

From the previous equation, one can see that the stack of discrete sublayers can be substituted by a continuous medium characterized by an adapted profile of the off diagonal permittivity ε_1. Then, the expression of PMOKE can be written in its integral form

$$\Phi = \tilde{\chi} \int_{\mathrm{MO\ active\ region}} \varepsilon_1(\tau)\, \mathrm{d}\tau \equiv \tilde{\chi}\mathcal{E}. \tag{4.4}$$

The quantity $\mathcal{E}$ represents the total MO response of *all* magneto-optically active sublayers. This is why it has been called *integral off-diagonal permittivity*.

Several types of off-diagonal permittivity profiles $\varepsilon_1(\tau)$ across the non-FM/FM/non-FM sandwich can be proposed. Depending on the level of simplification, they can be divided into three categories (Fig. 4.1):

(a) The first one corresponds to an ideal step-like profile. In this case, the partial MO contributions are constant across the thickness of the FM film $t^{(\mathrm{fm})}$ [Fig. 4.1(a)], and the total PMOKE is expressed by $\Phi_{\mathrm{ideal}} = \tilde{\chi}\mathcal{E} = \tilde{\chi}\varepsilon_1^{(\mathrm{fm})} t^{(\mathrm{fm})}$ with $\Phi_{\mathrm{ideal}} \to 0$ if $t^{(\mathrm{fm})} \to 0$.

(b) In the second case, the profile of $\varepsilon_1(\tau)$ is assumed to be composed of three parts [Fig. 4.1(b)]. In the part 1, the value of $\varepsilon_1(\tau)$ is equal to the bulk value of the sandwiching non-FM layers, i.e. $\varepsilon_1(\tau) = \varepsilon_1^{(\mathrm{nF})} = 0$. In the part 2, $\varepsilon_1(\tau)$ is equal to the bulk value $\varepsilon_1^{(\mathrm{fm})}$ of the FM layer, independently of its thickness $t^{(\mathrm{fm})}$. In the
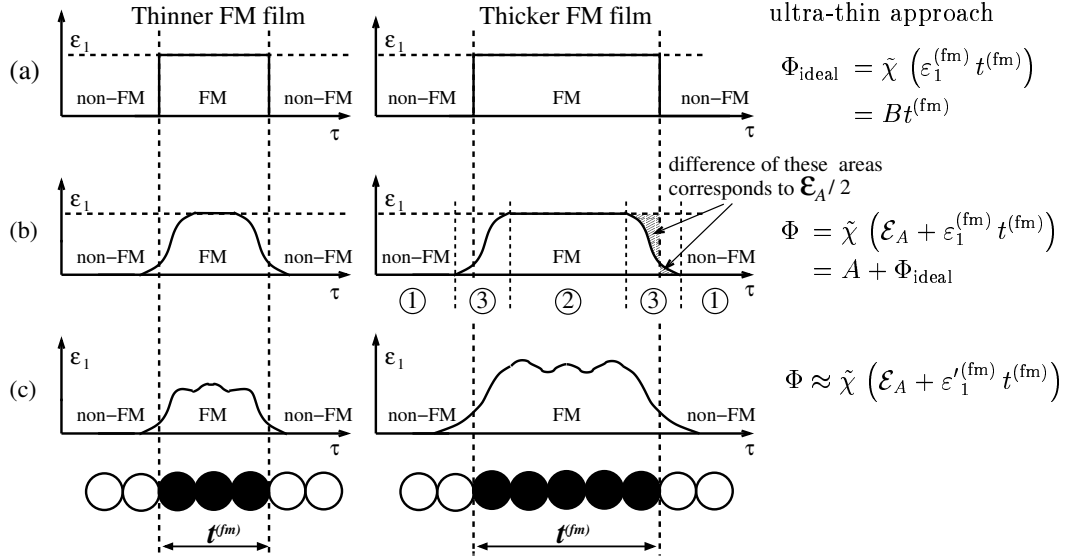
Figure 4.1: Schematic representation of three different profiles $\varepsilon_1(\tau)$ of the off-diagonal optical permittivity tensor elements in a sandwich non-FM/FM/non-FM structure. The case (a) represents the simplest step-like profile for which MOKE Φ is proportional to $t^{(\mathrm{fm})}$. In the case (b) the off-diagonal permittivity changes gradually in the non-FM/FM interface regions 3 and stays constant in the inner part 2 of the FM layer. The case (c) represents a general profile $\varepsilon_1(\tau)$.

part 3, which corresponds to the FM/non-FM interface transition region, the profile is described by a smooth function which is independent on $t^{(\mathrm{fm})}$. Consequently, Equation (4.4) leads to

$$\Phi = \tilde{\chi}\mathcal{E} = \tilde{\chi}(\mathcal{E}_A + \varepsilon_1^{(\mathrm{fm})}t^{(\mathrm{fm})}) = \Phi_A + \Phi_{\mathrm{ideal}}. \tag{4.5}$$

The quantity $\mathcal{E}_A$ introduced in Eq. (4.5) will be referred as the *integral off-diagonal permittivity excess*, because it describes the difference between the integral off-diagonal permittivity of the real and step-like profiles, i.e.

$$\mathcal{E}_A = \mathcal{E} - \varepsilon_1^{(\mathrm{fm})}t^{(\mathrm{fm})} = \int_{\mathrm{MO\ active\ region}} \varepsilon_1(\tau)\,\mathrm{d}\tau - \varepsilon_1^{(\mathrm{fm})}t^{(\mathrm{fm})}. \tag{4.6}$$

(c) In the third case, the off-diagonal permittivity $\varepsilon_1(\tau)$ is described by a function depending on the position across the sandwich structure [see Fig. 4.1(c)]. In this case, the integral off-diagonal permittivity $\mathcal{E}$ is a general function of $t^{(\mathrm{fm})}$. Although the function has an arbitrary form, it can be approximated by an expression similar to Eq. (4.5), i.e.

$$\mathcal{E}(t^{(\mathrm{fm})}) = \int_{\mathrm{MO\ active\ region}} \varepsilon_1(\tau,\,t^{(\mathrm{fm})})\,\mathrm{d}\tau \approx \mathcal{E}'_A + \varepsilon_1'^{(\mathrm{fm})}t^{(\mathrm{fm})}, \tag{4.7}$$

where $\varepsilon_1'^{(\mathrm{fm})}$ and $\mathcal{E}'_A$ are some effective values of the off-diagonal permittivity and its corresponding integral excess.

In the following we will consider the *case (b) of a profile composed of three parts* [Fig. 4.1(b)]. For comparing the theoretical [Eq. (4.5)] and experimental [Eq. (4.1)] dependences of the PMOKE on the FM layer thickness up to the linear term, it is convenient to consider the following ratio between coefficients of Eq. (4.1):

$$\frac{A}{B} = \frac{\mathcal{E}_A}{\varepsilon_1^{(\mathrm{fm})}} \tag{4.8}$$

This expression shows that the experimentally measured ratio A/B is directly related to the deviation of the integral off-diagonal permittivity (described by $\mathcal{E}_A$) from the ideal step-like permittivity profile. This is the *key point* of the proposed method to analyze the MO interface contributions.

I list below the predicted advantages of the use of the A/B ratio for investigating interfaces:

(i) It is directly determined from the experimental FM thickness dependence of PMOKE.

(ii) From the definition of $\mathcal{E}_A$ given by Eq. (4.6), it follows that the A/B ratio is independent on the exact profile of the off-diagonal permittivity distribution $\varepsilon_1(\tau)$ across the interface region. Its value is given by the difference between the integral off-diagonal permittivity of the real and step-like profiles, provided that the ultrathin FM film approximation is fulfilled.

(iii) In the ultrathin FM film approximation, this A/B ratio describes the MO properties of the FM/non-FM interface. It does *not* depend on the incidence angle and on the polarization state of the probing light. It is also invariant with respect to other characteristics of the studied structures, such as the thickness and optical parameters of the non-FM sandwiching layers.

(iv) Although Eq. (4.8) was derived for a sandwich structure containing only a single ultrathin FM layer, it should be emphasized that it is also valid for stacks of *identical* ultrathin FM layers embedded in the same non-FM material, providing that the thickness of all FM layers *together* fulfills the ultrathin FM film approximation. We will extend this result to a bilayer FM structure. Because of its additive character, the measured MOKE is a sum of contributions originating from both FM layers, i.e.

$$\Phi = \Phi_1 + \Phi_2 = \tilde{\chi}_1 \mathcal{E}_1 + \tilde{\chi}_2 \mathcal{E}_2. \tag{4.9}$$

If the layer thickness and magnetic properties of both FM layers are identical, i.e. $\mathcal{E}_1 = \mathcal{E}_2 = \mathcal{E}$, the total MOKE is the product of the integral off-diagonal permittivity $\mathcal{E}$ by the effective optical term $\tilde{\chi}'$, given itself by the sum of the individual optical terms $\tilde{\chi}_1$ and $\tilde{\chi}_2$, i.e.

$$\Phi = \tilde{\chi}' \mathcal{E}, \qquad \tilde{\chi}' = \tilde{\chi}_1 + \tilde{\chi}_2. \tag{4.10}$$

From an experimental point of view, for this particular kind of FM bilayer, the dependence of the total MOKE on the individual FM layer thickness can be again described by an equation analogous to Eq. (4.1):

$$\Phi = A' + B' t^{(\mathrm{fm})} + C' \left(t^{(\mathrm{fm})} \right)^2. \tag{4.11}$$

Similarly as for Equation (4.8), the comparison of Eq. (4.10) and (4.11) results in the equality between the experimentally obtained value of A'/B' and the ratio $\mathcal{E}_A/\varepsilon_1^{(\mathrm{fm})}$, where $\mathcal{E}_A$ is calculated as in Eq. (4.6).

(v) The approach described above can also be used for ultrathin FM layer structures with in-plane magnetization. In this case, the off-diagonal permittivity is given by $\varepsilon_1^{(\mathrm{fm})} = -i\varepsilon_{xz}^{(\mathrm{fm})} = i\varepsilon_{zx}^{(\mathrm{fm})}$. The longitudinal MOKE (LMOKE) is proportional to the ratio between the off-diagonal and diagonal permittivities of the ultrathin FM film [Eq. (3.42)], i.e.

$$\Phi_{\mathrm{lon},\mathbf{s/p}} = \pm\chi Q V_{\mathbf{s/p}} N_y N^{(\mathrm{nf})} t^{(\mathrm{fm})} \left(\frac{\varepsilon_1^{(\mathrm{fm})}}{\varepsilon_0^{(\mathrm{fm})}}\right), \tag{4.12}$$

where plus and minus correspond to $\mathbf{s}$ and $\mathbf{p}$-LMOKE respectively. Parameters equivalent to $\mathcal{E}$ and $\mathcal{E}_A$ can be defined in the longitudinal case by

$$\begin{aligned} \mathcal{E}_{\mathrm{lon}} &= \int \frac{\varepsilon_1(\tau)}{\varepsilon_0(\tau)}\,\mathrm{d}\tau, \\ \mathcal{E}_{A,\mathrm{lon}} &= \int \frac{\varepsilon_1(\tau)}{\varepsilon_0(\tau)}\,\mathrm{d}\tau - \frac{\varepsilon_1^{(\mathrm{fm})}}{\varepsilon_0^{(\mathrm{fm})}} t^{(\mathrm{fm})}, \end{aligned} \tag{4.13}$$

and thus the ratio $(A/B)_{\mathrm{lon}}$ can be written as

$$\left(\frac{A}{B}\right)_{\mathrm{lon}} = \mathcal{E}_{A,\mathrm{lon}} \frac{\varepsilon_0^{(\mathrm{fm})}}{\varepsilon_1^{(\mathrm{fm})}}. \tag{4.14}$$

(vi) The equations (4.4) and (4.6) show that the interface contribution to the total MOKE can be quantified by the integral off-diagonal permittivity excess $\mathcal{E}_A$. In order to include the interface contributions into the multilayer model (Section 3.2 or ref. [46, 41]), one can introduce additional ultrathin transition interface layers located at all FM/non-FM interfaces. These interface layers have to be chosen so that they must include the total integrated permittivity excess $\mathcal{E}_A$. To demonstrate our predictions, it is practical to use very simple interface structures. A reasonable choice is to consider two identical interface layers having the diagonal permittivity of the FM layer. These interlayers have an equivalent thickness $t^{(\mathrm{in})}$ [for example $t^{(\mathrm{in})} = 1\,\mathrm{AL}$ (Atomic Layer)] and are located at both sides of the FM layer (see Figure 4.2). For
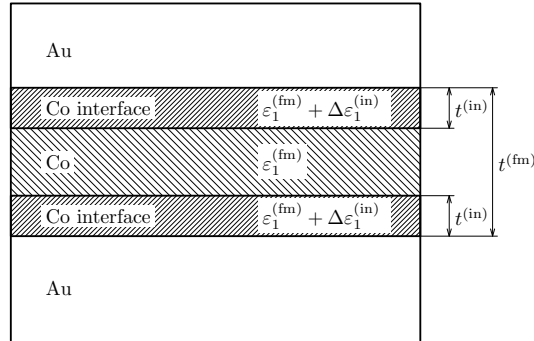
Figure 4.2: Sketch of interface layers of thickness $t^{(\mathrm{in})}$ located at both sides of the FM layer.

these interlayers, the off-diagonal permittivity $\varepsilon_1^{(\text{in})}$ differs from zero by a quantity

$$\Delta\varepsilon_1^{(\text{in})} = \frac{\mathcal{E}_A}{2\,t^{(\text{in})}}. \tag{4.15}$$

The factor 2 is introduced at the denominator to distribute the total excess between the two interface layers. Because the integral off-diagonal permittivity excess $\mathcal{E}_A$ is related to the ratio A/B through Equation (4.8), one obtains

$$\Delta\varepsilon_1^{(\text{in})} = \frac{\varepsilon_1^{(\text{fm})}}{2\,t^{(\text{in})}}\frac{A}{B}. \tag{4.16}$$

With these interlayers one can reproduce the experimental data down to the limit of $t^{(\text{fm})}$, for which the part 2 in Fig. 4.1(b) disappears.

4.4   Preparation and properties of Co/Au(111) samples

4.4.1   Elaboration

The studied Co/Au(111) ultrathin film structures were prepared by thermal evaporation in an ultra-high vacuum chamber (10^{-10} Torr range), either at the "Institut d'Optique" (D. Renard) or at the "Institut d'Electronique Fondamentale" (P. Beauvillain).

First, a 24 nm-thick Au(111) textured *fcc* polycrystalline buffer layer was deposited at room temperature on a float glass substrate at a rate of 0.2 nm/s and subsequently annealed at 175°C. After this thermal treatment, the average lateral crystallite size of the buffer layer was 100 nm and the atomically flat terraces, separated by monoatomic steps, had a 30 nm average width. The average rms roughness of the Au(111) surface, measured by Atomic Force Microscopy over a 10 μm×10 μm area, was about 0.5 nm (2 AL), confirmed by low-angle X-ray diffractometry on the entire surface of the sample [72]. Onto this annealed buffer, a 3 nm thick Au layer was deposited at room temperature. Low-angle X-ray diffractometry showed that this additional Au layer has the same *fcc* crystallographic structure as the annealed buffer layer. This last Au layer provides a long range smoothing of the surface, and suppresses in part imperfections due to grain boundaries. However, as we shall see later, we have not found any clear difference between the A/B ratios measured for specimens either covered or not by this additional Au layer.

On the high-quality Au(111) buffer layers, the Co layer is grown at room temperature at a deposition rate of 0.005 nm/s. Due to the large misfit between the Au and Co lattices (14%), the Co film grows initially in a double-layer mode. The Co film becomes continuous for $t^{(\text{Co})} = 2 - 3$ AL ($0.4 - 0.6$ nm). No variation of the Co surface roughness has been observed up to 15 AL (3 nm) [72]. These results are coherent with resistivity measurements on our samples during the Co layer growth [73] and consistent with previous STM studies of the Co growth mode on a reconstructed Au(111) surface [74].

The Co film exhibits a (0001) hexagonal close-packed (hcp) structure, as checked on a few-nm-thick Co film by TEM and by ^{59}Co nuclear magnetic resonance [75]. 80-85% of the Au-Co interface misfit is relaxed, while remaining 20-15% give strains [76]. Finally, the Co film was covered by an ultrathin gold overlayer, grown at room temperature at a deposition rate of 0.05 nm/s. The rms roughness of the top Au-Co interface is estimated to 3 AL (0.6 nm), the Co crystallites having a mean lateral size of about 7 nm [72]. These results agree with the data of cross-section TEM of Au-Co interfaces [77]. Note that a clear demixing between Au and Co was previously evidenced [78].

4.4.2 Details of the investigated samples

MO experiments were carried on three Au/Co structures with stepped-wedge Co layers. The samples are referred as the "sandwich X", "sandwich Y" and "Co bilayer Z" and their structure presented on Table 4.1.

sample notation	sample structure	thicknesses of Co layers $t^{(\mathrm{Co})}$
sandwich X	$\mathrm{Au}(5\,\mathrm{nm})/\mathrm{Co}(t^{(\mathrm{Co})})/\mathrm{Au}(27\,\mathrm{nm})/\mathrm{float}$ glass substrate	0.4, 0.6, 0.7, 0.8, ..., 1.5, 1.6 nm
sandwich Y	$\mathrm{Au}(7.5\,\mathrm{nm})/\mathrm{Co}(t^{(\mathrm{Co})})/\mathrm{Au}(28\,\mathrm{nm})/\mathrm{float}$ glass substrate	0.7, 0.8, 0.9, 1.0, 1.1, 1.2 nm
Co bilayer Z	$\mathrm{Au}(5\,\mathrm{nm})/\mathrm{Co}(t^{(\mathrm{Co})})/\mathrm{Au}(1.3\,\mathrm{nm})/$ $\mathrm{Co}(t^{(\mathrm{Co})})/\mathrm{Au}(27\,\mathrm{nm})/\mathrm{float}$ glass substrate	0.34, 0.7, 0.9, 1.1, 1.3, 1.5, 1.9 nm

Table 4.1: Structures of the studied Au/Co samples.

For sandwiches X and Y, each Co layer step on the wedge has a width of 3 mm; it was 4 mm for the Co bilayer Z. The samples X and Z were prepared by the procedure described in the previous Section 4.4. The sample Y was prepared in a different UHV chamber by a very similar procedure [78], but without an additional thin layer (3 nm) of Au on the standard annealed Au buffer.

4.4.3 Magnetic properties of the Co/Au(111) system

The magnetic properties of the Co/Au(111) system are the following: when increasing the Co layer thickness, the magnetic anisotropy is reduced so that the magnetization exhibits a reorientation transition from out-of-plane to in-plane for a Co thickness close to 2 nm at room temperature [75, 79]. Its exact value depends on the film quality and on the roughness of the Au/Co interface. It was shown that this transition is due to the coexistence of both out-of-plane and in-plane magnetized domains, and not to a pure canted state of the magnetization vector [80]. Furthermore, the room temperature coercive field H_c decreases when increasing the Co thickness [81], as a consequence of weaker domain wall pinning.

For a double Co-layer structure, Au/Co/Au/Co/Au(111), the oscillatory coupling between the Co layers is either FM or anti-FM depending upon the thickness of the Au spacer. An anti-FM coupling is present for Au thicknesses between 4 to 6 AL (1 to 1.5 nm) and 9 to 12 AL (2.25 to 3 nm) [79].

4.5 Experimental procedures and results

4.5.1 Procedures

In order to obtain informations about Co/Au(111) interfaces, reliable to our formal description, we measured MOKE spectra to deduce the spectral dependence of the A/B ratio. The PMOKE spectra of the Co/Au(111) system were previously studied [32, 42]. The PMOKE dependence on the incidence angle was reported in [82].

Spectroscopic PMOKE measurements have been performed by two equivalent methods. Samples X and Z were investigated in Praha by a MO set-up using Faraday rotators with a feedback compensation (Section 2.4.3). The sandwich Y was investigated at the Institute d'Electronique Fondamentale, Orsay, by a MO set-up based on the modulation of the polarization state of the light by a photoelastic modulator (Section 2.4.1). The precision of both techniques was of the order of 10^{-4} deg.

The PMOKE measurements ($\boldsymbol{H} \parallel \hat{z}$) were performed in the following geometries (Table 4.2), in a magnetic field of 0.15 T after pre-magnetizing it at saturation with a pulse of field of 0.56 T, applied during 1 s. The PMOKE value was deduced from the difference between MO signals for two opposite orientations of the magnetic field.

sample	s-MOKE	p-MOKE	φ
sandwich X	no	yes	$7°$, $60°$, $80°$
sandwich Y	no	yes	$5°$
Co bilayer Z	yes	yes	$7°$, $60°$, $70°$, $80°$

Table 4.2: Kerr configurations and angle of incidence φ used to study the different samples.

The small Au diamagnetic MO contribution was measured separately on a part of the specimen where $t^{(\mathrm{Co})} = 0$ nm, and subtracted from the experimental PMOKE for nonzero $t^{(\mathrm{Co})}$ values.

4.5.2 Experimental results and fitting of the A/B ratio

Single FM layer: Typical variations of the PMOKE rotation and ellipticity data with cobalt layer thickness $t^{(\mathrm{Co})}$ in Au/Co($t^{(\mathrm{Co})}$)/Au(111) sandwiches are shown in Fig. 4.3.
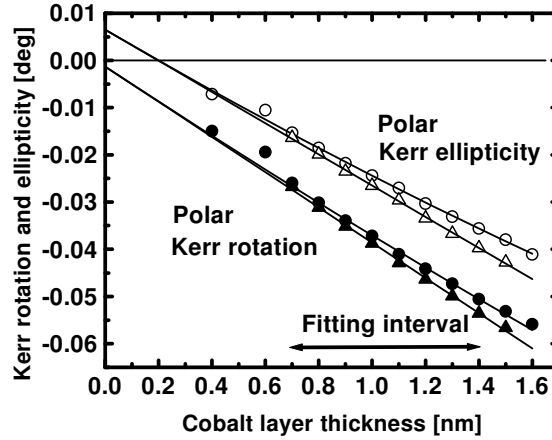
Figure 4.3: Typical experimental variation of the p-PMOKE rotation (full circles) and ellipticity (open circles) data with the thickness of the Co layer in the sample X, measured at a photon energy of 3.45 eV, at nearly normal incidence ($\varphi = 7°$). The data used for the linear fitting procedure after subtraction of the non-linear contribution, as described in the text, are plotted by full or open triangles.

The dependence on $t^{(\mathrm{Co})}$ is generally better described by a parabolic function [Eq. (4.1)]. In spite of the low value of the C coefficient, the introduction of the quadratic term
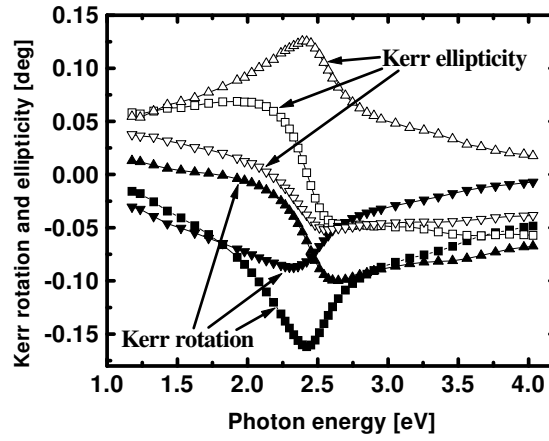
Figure 4.4: Experimental spectra of the PMOKE for the sample Z with two identical Co layers of thickness $t^{(Co)} = 1.3\,$nm. The spectra are represented for incidence angles $\varphi = 7°$ (squares) and $\varphi = 70°$, where s-MOKE Φ_s and p-MOKE Φ_p are displayed by triangles and inverted triangles, respectively.

$C(t^{(fm)})^2$ in Eq. (4.1) improves the accuracy on the deduced values of the A and B coefficients. This correction is introduced to obtain an accurate data analysis. The fitting procedure was carried out for cobalt layer thickness in the range of 0.7–1.4 nm (i.e. 3.5–7 AL) over which the surface morphology of the Co film remains quite identical. For thinner cobalt layers, the experimental data exhibit quite large deviation from the quasi-linear dependence of Φ on $t^{(Co)}$ [72]. This deviation comes mainly from the fact that the magnetic anisotropy changes sign for $t^{(fm)} \geq 7\,$AL and a large field is required to reach saturation of the sample magnetization [83]. For the used applied magnetic field, the magnetic saturation can not be completely reached for $t^{(fm)} \geq 7\,$AL. As a consequence, the Co films exhibit a smaller PMOKE (a larger curvature in Fig. 4.3) than expected for a saturated sample. For Co thickness smaller than 7 AL, best fits are obtained using a non-linear term $C\left(t^{(Co)}\right)^2$ [Eq. (4.1)] estimated theoretically from the optical multilayer model (Section 3.2). For this calculation, the optical data of Au [42] and Co [84] were used and the MO coefficient for Co deduced from the experimental PMOKE measured on thick Co films [85]. The coefficients A and B were then determined from the experimental data, after subtracting the calculated non-linear term $C\left(t^{(Co)}\right)^2$. In other words, the data $\Phi - C\left(t^{(Co)}\right)^2$ has been fitted by the linear function $A + B\,t^{(Co)}$.

FM bilayers: Figure 4.4 shows typical experimental spectra of PMOKE rotation and ellipticity obtained for the bilayer Z with $t^{(Co)} = 1.3\,$nm. As expected, the spectra exhibit clear spectroscopic structures near 2.5 eV, associated with the gold plasma edge. This is a well-known effect induced by the optical properties of the buffer layer, which was first evidenced by Katayama et al. in the Fe/Cu system [86]. For the present Au/Co system, PMOKE was initially analyzed by Š. Višňovský *et al.* [32, 42].

When PMOKE Φ_s and Φ_p spectra obtained at nearly normal incidence, $\varphi = 7°$, are compared with PMOKE spectra for larger angles of incidence (e.g., for $\varphi = 70°$, as shown in Fig. 4.4), a significant qualitative difference is observed. Such a difference results from the angular dependence of the Fresnel reflection coefficients, especially in the vicinity of the
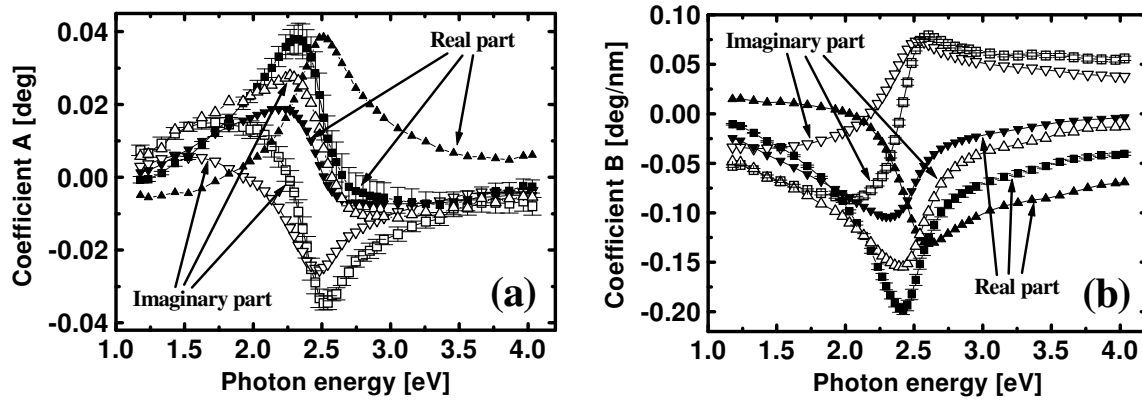
Figure 4.5: Experimental spectra of the coefficients A (a) and B (b) obtained from the data of PMOKE measured on the specimen Z, examples of which are shown in Fig. 4.4. The spectra are displayed for the angles of incidence $\varphi = 7°$ (squares) and $\varphi = 70°$ (triangles for Φ_s and inverted triangles for Φ_p). The typical error bars are shown for the angle of incidence $\varphi = 7°$ and correspond to the standard deviation of the linear fit, as described in Sec. 4.5. The error bars for the other curves have similar magnitude and were omitted.

total reflection angle of incidence. It should also be noted that qualitatively, the PMOKE spectra are proportional to the cobalt layer thickness $t^{(Co)}$. We do not observe any clear features associated with the presence of quantum well states in the FM Co layer, as already reported in other systems [87]. Note that the Au protective layer is thick enough, so that the contributions of quantum well states to PMOKE can be neglected in this Co layer [88].

A linear regression analysis of the PMOKE variation with $t^{(Co)}$, performed after the subtraction of the quadratic contribution, provides spectra of the A and B coefficients [Figures 4.5(a)(b)]. As expected from the theoretical background reported in Sec. 4.3, the spectra of the A coefficient should vary significantly with the angle of incidence and with the polarization state of the incident light in the vicinity of the Brewster angle. This is due to the fact that A is proportional to $\tilde{\chi}$, as expected from the comparison of Eqs. (4.1) and (4.5). Indeed, such large variations are clearly observable in Fig. 4.5(a). The spectra of the B coefficient have nearly the same shape as those of PMOKE in the same geometry. This is due to the fact that the term $B\,t^{(Co)}$ in Eq. (4.1) dominates the PMOKE.

Figure 4.6 shows the spectra of the ratio A/B, determined from the analysis of the experimental data obtained on the bilayer Z, for different angles of incidence φ and two incident polarizations. The larger experimental errors on the A/B ratio for large photon energies are due to smaller absolute values of the A and B coefficients at these energies. The ratio A/B exhibits only a weak (within the error bars) dependence on the angle of incidence φ, as predicted in Section 4.3. On the other hand, a slight difference between the values corresponding to s and p polarized incident light is evidenced. This difference is especially clear for photon energies higher than 3 eV. In order to explain the origin of the difference between the values corresponding to s and p polarized incident light (Figure 4.6), numerical analysis of the A/B ratio deduced from the Φ_p and Φ_s observables was performed. The experimental data were simulated by a model using interface interlayers, as described in Sec.4.3. In the simulation, the polarization dependence of the A/B ratio was found to be much smaller than that shown in Fig. 4.6. This points out that the observed difference does not originate from the ultrathin FM film approximation employed
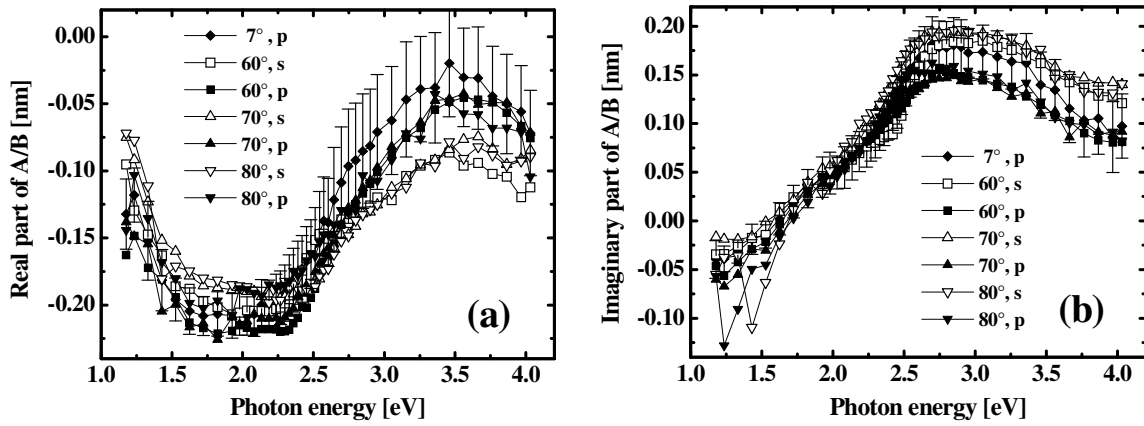
Figure 4.6: Real (a) and imaginary (b) parts of the A/B ratio obtained from s-MOKE Φ_s (empty symbols), p-MOKE Φ_p (filled symbols) measured on the Co bilayer Z at different angles of incidence. The error bars display typical standard deviations, as obtained from the linear regression procedure described in Sec. 4.5.
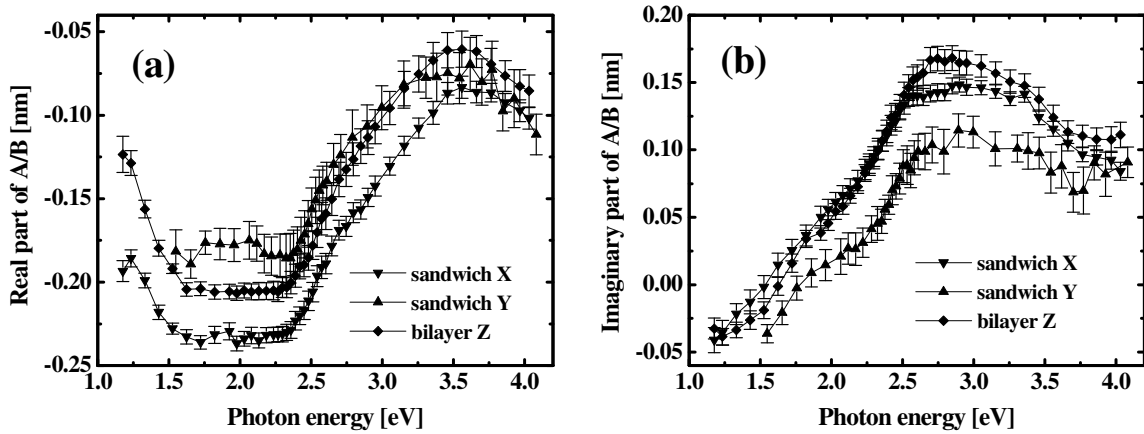
Figure 4.7: Real (a) and imaginary (b) parts of the experimental ratio A/B for all three studied Au/Co specimens. Each curve was obtained as an average of all experimental spectra of the A/B ratio available for each specimen.
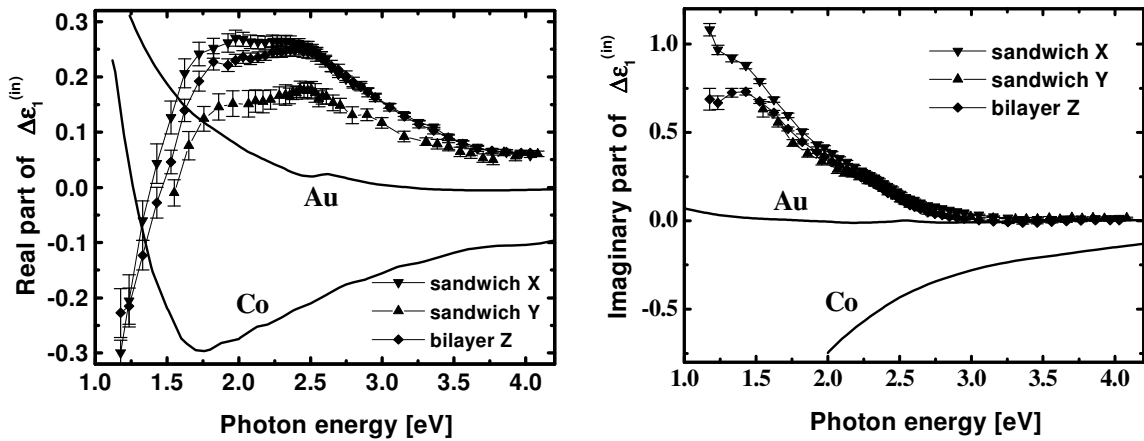
Figure 4.8: Real (a) and imaginary (b) parts of the quantity $\Delta\varepsilon_1^{(in)}$ acquired from all studied Au/Co structures. They are compared with the bulk values of the off-diagonal permittivity of Co and Au (solid lines). The Au/Co interface interlayer was assumed to have a thickness $t^{(in)} = 1\,\text{AL}$ (0.2 nm).

here to analyze the data. Note that for this sample, the thickness of the Au interlayer separating the two Co layers is only 6.5 AL (1.3 nm); this value is not so far from the end of the decay length of the oscillatory exchange coupling in the Au/Co/Au/Co/Au(111) system [79]. One can therefore expect that there will be still a weak MOKE contribution of the spin-polarized quantum well states in this Au layer [89, 90] which can be sensitive to the incident polarization. Because we do not have a precise microscopic model of the interface, we cannot assign the origin of this difference. Another possible reason for this discrepancy could be a small systematic error between the experimental data measured for both polarizations.

Comparison of all samples: Figure 4.7 compares the spectra of the A/B ratios for the Au/Co interface contributions obtained for all studied samples. The resulting data are averages of all A/B ratios obtained for all specimens. Their spectra show very similar features. The A/B ratio exhibits a significant change in slope near 2.5 eV, i.e. around the plasma edge of gold. This change is not an artifact of processing of the experimental PMOKE spectra, but is more related to a characteristic spectroscopic structure in this energy region. It shows that the MO characteristics of the Au/Co interface are influenced by the optical properties of gold.

It should be emphasized that Figure 4.7 contains valuable experimental results. These results can be compared with theoretical calculations which provide the complex MO observables, i.e. the PMOKE rotation and ellipticity. To obtain the A/B ratio, it is enough to consider a similar procedure to that used for the treatment of our experimental data.

From the experimental A/B data and using Eq. (4.16), the spectral variation of the quantity $\Delta\varepsilon_1^{(in)}$ defined as the permittivity excess for the interface layer in Eq. (4.15), is obtained (Figure 4.8). In the calculation, one assumes $t^{(in)} = 1$ AL (0.2 nm).

4.6 Modeling of the Au/Co interface and discussion

We have already separated the contribution of the FM/non-FM interfaces from the total PMOKE. Let us now discuss its possible origins. As it has been mentioned in the introduction, there are several effects which can be responsible for the MO interface contributions. The most interesting one is that related to the hybridization of the electronic wavefunctions of neighboring Au and Co monoatomic layers at the Au/Co interface [42]. In a simple macroscopic formalism one of course cannot evaluate this interface contribution. From the theoretical side, and to our knowledge, up to now there is no available *ab-initio* calculation of the effect of the Co/Au interface hybridization on optical properties. Other possible mechanisms can also contribute to the interface MO term in real samples and cannot be *a-priori* neglected. In this Section, we show how they can be included in the general formalism and compared with the experimental data of the A/B ratio spectra (Fig. 4.9).

4.6.1 Disorder at the interfaces

In the absence of any universal optical and MO theory in the presence of rough interfaces, we consider a simple interpretation of the Au/Co/Au data. It is well known that Co and Au do not intermix together (Sec. 4.5 or [78]). Thus, from a structural point of view, only
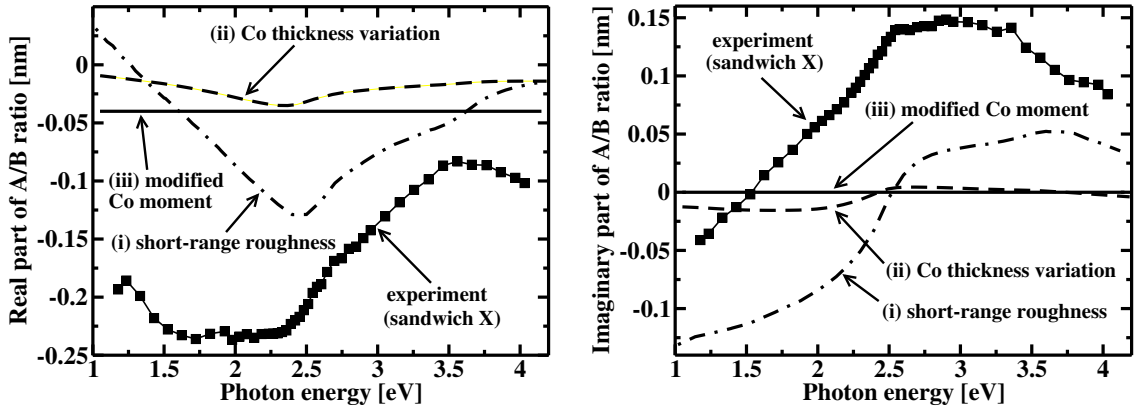
Figure 4.9: Real (a) and imaginary (b) parts of the A/B ratio calculated for (i) the short range roughness contribution of the Co layer surface (over the thickness $t^{(in)} = 0.4\,nm$), computed by using the Effective Medium Approximation (EMA), (ii) the contribution of the Co thickness variation $\sigma^{(fm)} = 0.6\,nm$, and (iii) the modified magnetic moment $m^{(in)} = 0.9$ of one Co monolayer of thickness $t^{(in)} = 0.2\,nm$.

the interface roughness has to be considered. There is a significant difference between the nature of the two involved Au/Co interfaces (Section 4.4). The top one is locally more perturbed (short and long range disorder) than the deeper one, which is rough only over large distances. So, in order to model both interfaces, we distinguish between short and long range roughness. The short range roughness (upper Au/Co interface) takes place at the range of few atomic distances and can be modeled in the framework of the Bruggeman Effective Medium Approximation (EMA) [91, 92]. In spite of its different origin, the calculation will be the same as for a real Co-Au intermixing. In counterpart, the effect due to roughness at a longer range may be estimated independently, and accounts for both interfaces through the spatial variation of the Co layer thickness. The thickness variation of the Au overlayer and the roughness of the air/Au interface give negligible MO contributions.

Short range roughness: Consider the interfacial contribution due to the short range roughness. It can be described within the Effective Medium Approximation. Let the parameter x be a volume ratio of cobalt in the mixture. Then, the permittivity deviation is $\Delta\varepsilon_1^{(in)} = \varepsilon_1^{(mix)} - x\varepsilon_1^{(fm)}$. By using Eq. (4.16), the A/B ratio can be expressed as

$$\left(\frac{A}{B}\right)_{mix} = 2\,t^{(in)}\left(\frac{\varepsilon_1^{(mix)}}{\varepsilon_1^{(fm)}} - x\right), \tag{4.17}$$

where $\varepsilon_1^{(mix)}$ is the off-diagonal permittivity of the mixture.

The short range roughness effect was calculated assuming an interface thickness $t^{(in)} = 2\,AL$ (0.4 nm) that corresponds to the local peak to peak roughness of the upper Au/Co interface. The MO effects due to this contribution are depicted in Fig. 4.9, assuming a hypothetical $Au_{0.5}Co_{0.5}$ interface layer. When changing interlayer concentration by ±20%, the spectral variation of the A/B ratio does not change significantly. The calculated spectral variation of the A/B ratio has some similarities to the experimental data, but its magnitude is smaller than that observed. Thus, this contribution alone is unable to explain the main part of the interface MO contribution.

Variation of the Co layer thickness due to long range roughness: The most important effect due to the long range roughness is related to the variation of the Co layer thickness. This model assumes that the interfaces of the Co layer are not ideally flat, but consist of flat areas (terraces) separated by steps. In our case, the terraces are quite large (tens of nanometers), but are much shorter than the light wavelength. Then, the specimen can be modeled as an assembly of close microscopic structures with different Co thickness.

The distribution $g^{(i)}$ $(\sum g^{(i)} = 1)$ of cobalt layer thickness is determined by the mean value of the cobalt thickness $t^{(\mathrm{fm})} = \sum t^{(i)} g^{(i)}$ and by its mean square deviation $\sigma^{(\mathrm{fm})} = \left(\sum g^{(i)} (t^{(i)} - t^{(\mathrm{fm})})^2 \right)^{1/2}$. The macroscopic reflection coefficients (and thus PMOKE $\Phi_{\mathrm{s}} = -r_{\mathrm{sp}}/r_{\mathrm{ss}}$, $\Phi_{\mathrm{p}} = r_{\mathrm{ps}}/r_{\mathrm{pp}}$) are determined as a weighted average of the reflection coefficients which are calculated for different cobalt layer thicknesses $r_{uv} = \sum g^{(i)} r_{uv}^{(i)}$, (the subscripts u, v stand for $\mathtt{s}$ or $\mathtt{p}$ polarization).

The dependence of the A term (or of the A/B ratio) on the total roughness is quadratic $(A \sim \sigma^{(\mathrm{fm})^2})$ [82]. The quadratic increase of this contribution with $\sigma^{(\mathrm{fm})}$ is obvious because the linear terms cancel after averaging. Moreover, if both Au/Co interfaces display uncorrelated roughness σ_1 and σ_2, then the Co layer thickness variation is $\sigma^{(\mathrm{fm})} = (\sigma_1^2 + \sigma_2^2)^{1/2}$. On the other hand, if both interfaces have identical and fully correlated roughness, then $\sigma^{(\mathrm{fm})} = 0$. In our samples, both Au/Co interfaces exhibit long-range rms roughness of about 2 to 3 AL and we can assume that they are partly correlated. We estimate that the maximum peak to peak Co terraces thickness variation is not larger than $\sigma^{(\mathrm{fm})} = 3\,\mathrm{AL}$ (0.6 nm). This "long range roughness" contribution to the A/B ratio is plotted in Figure 4.9 for a Au(5 nm)/Co($t^{(\mathrm{Co})}$)/Au film. The shape of the calculated A/B spectra is close to that calculated by EMA. However, as shown Figure 4.9, this last mechanism contributes much less than the previous "short range roughness" term.

In principle, there could be also long range surface roughness contributions of the Au buffer and overlayer. These effects were evaluated and found to be negligible (1% of the contribution of the Co thickness variation).

4.6.2   Modified magnetic moment of Co atoms at the interface

This model assumes that the cobalt atoms which are in contact with the gold layer have a magnetic moment different from those in the inner part of the Co layer. This can be accounted for by considering that a part of the Co layer, with thickness $t^{(\mathrm{in})}$, has a normalized magnetization $m^{(\mathrm{in})} \neq 1$. Consequently, $\Delta \varepsilon_1^{(\mathrm{in})} = (m^{(\mathrm{in})} - 1) \varepsilon_1^{(\mathrm{Co})}$ and Equation (4.16) implies that

$$\left(\frac{A}{B} \right)_{\mathrm{Co}} = 2 \left(m^{(\mathrm{in})} - 1 \right) t^{(\mathrm{in})}. \tag{4.18}$$

This contribution, invariant with respect to the photon energy, affects only the real part of the A/B ratio. Figure 4.9 presents this contribution for one monolayer of Co atoms $(t^{(\mathrm{in})} = 0.2\,\mathrm{nm})$ with a reasonable reduction of the magnetic moment by 10% $(m^{(\mathrm{in})} = 0.9)$ at the Au/Co interface. Because this contribution is a real number, it cannot explain the presence of an imaginary part in the experimental A/B ratio and their spectral variation. If it is present, this mechanism would have only a tiny effect.

Up to now, neither the interface disorder nor the reduction of the Co moment can account for the experimental MO contribution of the Co/Au interface.

4.6.3   Au-Co electronic hybridization

Our results suggest that the most important part of the interface contribution arises from intrinsic properties of the interface itself, i.e. from the Au-Co electronic hybridization. From this hybridization, one could expect that it changes the off-diagonal permittivity of one monoatomic interface layer by a value which is of the same order of magnitude as the off-diagonal permittivity of cobalt $\varepsilon_1^{(Co)}$.

The suggested representation of interface effects by an integral permittivity excess is very general and can be compared with any type of permittivity tensor profile determined theoretically, especially with results of *ab-initio* calculations of the layer-resolved permittivity tensor [26].

It would be very useful to extract the net contribution of the electronic interface hybridization from the experimental data. This should be possible for systems where the film grows pseudomorphically layer by layer, giving rise to very flat FM/non-FM interfaces. In such a case the presence of interlayers, described within the EMA, can be excluded. Then, real space studies of surface morphology would provide structural parameters to account for roughness effects, and the intrinsic electronic contribution could be determined.

In the case of our Au/Co/Au(111) structures, the situation is somewhat more complicated. Although the bottom interface of the Co layer is planar at a microscopic scale, the top Au/Co interface has a complex topology and the electronic interaction at the top interface is probably affected by the non uniform configuration of the nearest neighbors along the interface plane. Consequently, the electronic contribution will also depend on these interface properties. Therefore, it will not be possible to separate *exactly* the contribution of effective intermixing at interfaces from that due to the electronic hybridization at the flat Au/Co interface. However, the lower interface is flat at a fraction of nanometers and the top Au/Co interface is reasonably flat on the surface of Co islands. Therefore, to our opinion, the *approximate* separation of these two contributions is certainly valid and the present experimental data on the interface MO contributions may be compared with future *ab-initio* calculations of the effect of electronic hybridization at flat Au(111)/Co interfaces.

4.7   Conclusion of Chapter 4

By using analytical expressions of the Polar Magneto-Optical Kerr Effect (PMOKE) in simple ultrathin FM structures, we have developed an original procedure to extract the linear magneto-optical parameters of interfaces between FM and non-FM metals. The experimental variation of the complex MOKE with the FM layer thickness $t^{(fm)}$ is expressed using a linear approximation, $\Phi \approx A + B\,t^{(fm)}$. Then, the interface contributions are expressed as the ratio A/B. The advantage of this representation is that the A/B ratio is independent of the experimental conditions (i.e. the angle of incidence and the polarization state of the incident light), as well as of the optical properties and thickness of sandwiching layers. This kind of analysis allows to link experimental data to theoretical calculations of electronic interactions at the FM/non-FM interfaces.

This treatment is applied to three Au/Co/Au(111) polycrystalline structures with perpendicular magnetic anisotropy. For the first time, the procedure allows to extract the interface-related information from standard MO experiments, at different angles of incidence and on different specimens. It also provides reliable physical data relevant to

the interface-induced contributions to the MO observables. This also proves that the interface effects can be accounted for by macroscopic optical approaches and described by the variation of the local optical permittivity tensor inside interfacial regions. The off-diagonal permittivity excess $\Delta\varepsilon_1^{(\mathrm{in})}$ can be calculated directly from the experimental value of the A/B ratio, under the condition that the off-diagonal permittivity of the inner part of the FM layer is known.

Various attempts were tried in order to reproduce the experimental interface contributions in Au/Co/Au systems. Models taking into account the short range film roughness and the variation of Co layer thickness provide interface contributions which have spectroscopic features similar to the experimental data. However, those structural effects are smaller than the observed MO interface effects. Therefore, another new contribution has to be emphasized. We suggest that this comes from the Au-Co electronic hybridization at the Au/Co interfaces. *Ab-initio* calculations of the layer-resolved permittivity tensor are welcome to provide a deeper understanding on this problem.

Chapter 5

In-depth resolution of the Magneto-optical Kerr effect

I shall try to answer to the general question: How to determine the magnetization state corresponding to each ferromagnetic (FM) layer located at a given depth in FM/non-FM multilayer structures by MOKE? The previously proposed solutions for structures with two FM layers [93, 94, 95, 96] are discussed here within a new unified formalism. For a system with three or more FM layers, two new approaches (the Parallel Kerr vector and Cascade numerical projection methods) are proposed to extract selectively the MOKE signals originating from each individual FM layer. Furthermore, we show how to straightforwardly determine the in-depth location of a FM layer corresponding to a given MOKE hysteresis loop. All these techniques are checked experimentally with success on several simple multilayer structures. Most of the results presented in this Chapter were published recently by J. Hamrle *et al.* [97].

5.1 Introduction

High quality multilayers are now commonly produced. Since the amount of material concerned by interfaces tends to be comparable to that involved in the layers themselves, the properties of the multilayers are strongly dependent upon their intimate structure. For example, the breaking of symmetry at interfaces induces new properties such as the interface-induced magnetic anisotropy [58], the giant magnetoresistance [98], the oscillatory magnetic coupling between FM layers [93, 79], etc.

In order to understand these phenomena, it is necessary to develop new techniques, which can study both local structural and magnetic properties. The knowledge of the in-depth profile of the magnetization, a selective determination of the magnetization state of all involved FM layers, and the link between the magnetic domain structure in neighbouring layers is of particular importance in FM layer stacks. I believe that magneto-optics is a privileged technique to answer to these questions.

Before showing how MOKE can be used to check selectively the magnetism of buried FM layers, i.e. to discuss on the in-depth resolution of this optical technique, I wish to review other techniques allowing to be magnetically in-depth sensitive.

- Using polarized neutron reflectometry, the profile of magnetic moments can be de-

termined from the fit of the angular dependence of the reflected neutron intensity [99]. The advantage of this method is that it can give the vectorial profile of the magnetic moment, up to large depths $\approx$100 nm. However, the in-depth resolution is rather poor, dynamic measurements are almost impossible, and this technique does not provide good lateral resolution.

• Mössbauer spectroscopy gives information about local modification of the hyperfine electronic structure. The electronic structure can be probed by means of an isotope nuclei (e.g. ^{197}Au, ^{119}Sn, ^{57}Fe). The in-depth variation of the hyperfine structure can be deduced if isotopes are placed successively at different depths in the multilayer structure. Thus, the in-depth profile of the magnetic polarization can be indirectly probed [100, 101]. This technique can reach an atomic resolution, but is time consuming and needs a large set of comparable samples with ultrathin isotope layers located at many different depths.

• The most used ways to check the in-depth profile of the magnetization are based on optical methods, namely MOKE or X-ray magnetic circular dichroism (XMCD).

  – The X-ray magnetic circular dichroism (XMCD) can provide chemical selectivity by choosing appropriate absorption edges of the atoms constituing the layers. Scaning the incoming photon energy (of the order of some keV) and reversing their polarization, one can probe selectively FM layers or even interfaces consisting of different materials. For example, it was used to image selectively layers and interfaces in the $LaFeO_3$/Co [102] or Co/NiO [103] structures. XMCD has been applied for studing the dynamic behavior of the magnetization of different FM layers, for example, in NiO/Co [104] or Co/X/NiFe (X=Al_2O_3 and Cu) bilayers [105].

  – The pioneering work on the in-depth dependence of MOKE was introduced first by Hubert *et al.* [48, 49]. This property was elegantly used to demonstrate the existence of a biquadratic coupling between the two FM layers in the Fe/Cr/Fe structure. The beauty of this study is that the coupling was directly checked from the selective magnetic domain LMOKE visualization in the two Fe layers [24]. The MOKE in-depth magnetization sensitivity has been also demonstrated in the Co/Au system with perpendicular anisotropy [94, 95].

  To our knowledge, among the various mentioned techniques, only MOKE was used to select the magnetic properties of FM bilayer structures *made of the same material*. Others techniques are either based on their chemical selectivity (XMCD) or they investigate static magnetic state (Mössbauer spectroscopy, polarized neutron reflection). However, our treatment presented in this Chapter could be applied in the future to XMCD in the ultraviolet range.

5.2   Generalities

Before treating the in-depth resolution of MOKE, let us first recall some results of Section 2.2.3 concerning the MOKE representation as a Kerr vector in a complex $\theta\epsilon$-plane [Fig. 2.4(a)(b)]:

 (i) The MOKE value $\Phi = \theta + i\epsilon = \Omega \exp[i\xi]$ is a complex number and thus it can be represented by a Kerr vector in the complex $\theta\epsilon$-plane. Real and imaginary axes

of the $\theta\epsilon$-plane correspond to Kerr rotation θ and ellipticity ϵ, respectively. The length and azimuth of the Kerr vector correspond to the Kerr amplitude Ω and Kerr phase ξ, respectively.

(ii) The additivity of MOKE for different FM layers or different contributions (e.g. polar & longitudinal) can be presented as a sum of Kerr vectors in the $\theta\epsilon$-plane.

(iii) A magneto-optical set-up measures a *Kerr signal s*, which is a projection of the Kerr vector onto a projection axis making a projection angle ψ with the real axis, i.e. $s = \Re(\Phi \exp[-i\psi])$ [Fig. 2.4(b) and Eq. (2.18)]. Experimentally, the continuous variation of ψ can be realized with a Babinet-Soleil compensator – see Section 2.4.2 for details.

5.3 Separation of polar, longitudinal and transverse Kerr effects

The determination of the in-depth profile of the magnetization vector in a multilayer structure require two successive steps. Starting from a general MOKE signal, the polar, longitudinal and transverse components of the magnetization have to be first separated. Then, the magnetization components *of each FM layer* must be determined. This procedure is required, if, for example, one wishes to investigate the dynamical behavior of the magnetization reversal for several uncoupled or coupled FM layers in a given structure.

The polar MOKE (PMOKE) and longitudinal MOKE (LMOKE) are related to the out-of-plane $m_z^{(i)}$ and in-plane $m_y^{(i)}$ magnetization components of the i-th FM layers, respectively (Section 2.2.1). For an oblique incidence angle, MO set-ups always measure the sum of the PMOKE $s_{\text{pol}}^{(\text{tot})}$ and LMOKE $s_{\text{lon}}^{(\text{tot})}$ signals. These two signals can be separated by reversing the incidence angle from φ to $-\varphi$. Since PMOKE is even with φ, and LMOKE odd with φ, $s_{\text{pol}}^{(\text{tot})}$ can be deduced from the sum of the Kerr signals $s^{(\text{tot})}(\varphi)+s^{(\text{tot})}(-\varphi)$ and $s_{\text{lon}}^{(\text{tot})}$ from their difference [see Eqs. (3.46) or [80]]. Another differentiation can be obtained from $\mathbf{s}$ and $\mathbf{p}$ Kerr signals, $s_{\mathbf{s}}^{(\text{tot})}$, $s_{\mathbf{p}}^{(\text{tot})}$ measured at small incidence angles ($\varphi \lesssim 30°$). In this case, $V_{\mathbf{s}} \approx V_{\mathbf{p}}$ and [Eqs. (3.46)]

$$\Phi_{\text{pol},\mathbf{s}}^{(i)} \approx \Phi_{\text{pol},\mathbf{p}}^{(i)} \qquad \Phi_{\text{lon},\mathbf{s}}^{(i)} \approx -\Phi_{\text{lon},\mathbf{p}}^{(i)}. \tag{5.1}$$

Hence, $s_{\text{pol}}^{(\text{tot})}$ can be obtained from the sum $(s_{\mathbf{s}}^{(\text{tot})} + s_{\mathbf{p}}^{(\text{tot})})$, and $s_{\text{lon}}^{(\text{tot})}$ from their difference.

The transverse m_x component of the magnetization can be measured by the transverse MOKE (TMOKE) (introduced in Section 2.2.1), or by rotating the sample and the magnet by 90° around the z-axis to measure m_x by LMOKE. Another way to measure both LMOKE and TMOKE at the same time is to use a rotating analyzer, as proposed by F. Ott [106]. Once the PMOKE, LMOKE and TMOKE contributions are separated, the Kerr signals $s_{\text{pol}}^{(\text{tot})}$, $s_{\text{lon}}^{(\text{tot})}$, $s_{\text{tra}}^{(\text{tot})}$ depend on the in-depth MO response, related to $m_z^{(i)}$, $m_y^{(i)}$, $m_x^{(i)}$ magnetization components, respectively. Then, the magnetization components of each FM layer can be deduced through the procedures discussed in the following Sections.

In conclusion, the separation between polar, longitudinal and transverse Kerr signals and the determination of their in-depths profiles are different problems. Hence, MOKE[1]

---

[1]In the following, MOKE can be PMOKE, LMOKE or TMOKE.

and depth sensitivity functions related to polar and longitudinal magnetizations are treated separately .

5.4   Depth sensitivity function of PMOKE and LMOKE

The depth sensitivity function describes the difference between MOKE $\Phi^{(i)}$ effects originating from different FM layers (i) located at different depths $d^{(i)}$. The definition of the depth sensitivity function has been first proposed by Hubert *et al.* [48] for bulk materials. Here, we generalize it to multilayer structures and define the polar or longitudinal depth sensitivity functions[2], $q_{\text{pol}}^{\langle i,1\rangle}$ or $q_{\text{lon}}^{\langle i,1\rangle}$, as the ratio of PMOKE or LMOKE, respectively, originating from the i-th FM and 1st FM layer:

$$
\begin{aligned}
q_{\text{pol}}^{\langle i,1\rangle} &= \frac{\Phi_{\text{pol}}^{(i)}}{\Phi_{\text{pol}}^{(1)}} = \frac{\Omega_{\text{pol}}^{(i)}}{\Omega_{\text{pol}}^{(1)}} e^{i\Delta\xi_{\text{pol}}^{\langle i,1\rangle}} \\
q_{\text{lon}}^{\langle i,1\rangle} &= \frac{\Phi_{\text{lon}}^{(i)}}{\Phi_{\text{lon}}^{(1)}} = \frac{\Omega_{\text{lon}}^{(i)}}{\Omega_{\text{lon}}^{(1)}} e^{i\Delta\xi_{\text{lon}}^{\langle i,1\rangle}} .
\end{aligned}
\tag{5.2}
$$

The depth sensitivity function q can be visualized in the $\theta\epsilon$-plane as follows: $\arg(q^{\langle i,1\rangle}) = \xi^{(i)} - \xi^{(1)} \equiv \Delta\xi^{\langle i,1\rangle}$ is the angle between the i-th and the 1-st Kerr vectors, and thus expresses the difference between Kerr phases $\xi^{(i)}$ originating from the i-th and the 1st FM layer. The modulus of the depth sensitivity function, $|q^{\langle i,1\rangle}| = \Omega^{(i)}/\Omega^{(1)}$, gives the ratio between Kerr amplitudes for the i-th and the 1st FM layer.

5.4.1   Depth sensitivity function in the ultrathin FM layer approximation

If all FM layers are ultrathin, the polar $q_{\text{pol}}^{\langle i,1\rangle} = \Phi_{\text{pol}}^{(i)}/\Phi_{\text{pol}}^{(1)}$ and longitudinal $q_{\text{lon}}^{\langle i,1\rangle} = \Phi_{\text{lon}}^{(i)}/\Phi_{\text{lon}}^{(1)}$ depth sensitivity functions are analytically expressed from Eqs. (3.46) [48, 49]

$$
q_{\text{pol}}^{\langle i,1\rangle} = \frac{t^{(i)}}{t^{(1)}} \frac{\varepsilon_1^{(i)}}{\varepsilon_1^{(1)}} Q(\Delta d^{\langle i,1\rangle}),
\tag{5.3}
$$

and

$$
q_{\text{lon}}^{\langle i,1\rangle} = \frac{t^{(i)}}{t^{(1)}} \frac{\varepsilon_1^{(i)}\varepsilon_0^{(1)}}{\varepsilon_1^{(1)}\varepsilon_0^{(i)}} Q(\Delta d^{\langle i,1\rangle}),
\tag{5.4}
$$

where $\Delta d^{\langle i,1\rangle} = d^{(i)} - d^{(1)}$ is the distance between the i-th and 1st FM layer. The only difference between polar and longitudinal depth sensitivity functions comes from the multiplicative $\varepsilon_0^{(1)}/\varepsilon_0^{(i)}$ term. The coefficient Q [Eq. (3.41)]

$$
Q(\Delta d^{\langle i,1\rangle}) = \exp[4\pi i N_z^{(\text{nf})}\Delta d^{\langle i,1\rangle}/\lambda^{(\omega)}]
\tag{5.5}
$$

---

[2]The superscript $^{\langle i,j\rangle}$ means "between the i-th and j-th FM layer". For example, $\Delta d^{\langle i,1\rangle} \equiv d^{(i)} - d^{(1)}$, means the distance between the i-th and 1-st FM layer. $\Delta\xi^{\langle i,1\rangle} \equiv \xi^{(i)} - \xi^{(1)}$ denotes the difference of Kerr phases originating from the i-th and 1st FM layer.

describes the attenuation of MOKE with the increasing in-depth position of the considered FM layer. Recall that $\lambda^{(\omega)}$ is the wavelength in vacuum, and $N_z^{(\mathrm{nf})}$ the z-component of the normalized wavevector in the non-FM media [Eq. (3.9)].

Both depth sensitivity functions $q_{\mathrm{pol}}^{\langle i,1\rangle}$, $q_{\mathrm{lon}}^{\langle i,i\rangle}$ [Eqs. (5.3) and (5.4)] are products of the three quantities:

- the ratio between FM layers thicknesses $t^{(i)}/t^{(1)}$. This is a constant for a given film structure.

- the quotient between the permittivities $\varepsilon_1^{(i)}/\varepsilon_1^{(1)}$ for $q_{\mathrm{pol}}^{\langle i,1\rangle}$ and $(\varepsilon_0^{(1)}\varepsilon_1^{(i)})/(\varepsilon_0^{(i)}\varepsilon_1^{(1)})$ for $q_{\mathrm{lon}}^{\langle i,1\rangle}$; this term differs from unity only if FM layers are made of different materials. In that case, the value of this contribution can only be changed by varying the photon energy. This term provides a sort of "chemical" contrast in the depth sensitivity functions.

- the contribution $Q(\Delta d^{\langle i,1\rangle})$ describes the optical influence of the non-FM spacer layers. This term provides a "phase" contrast in the depth sensitivity function, linked to the optical distance between FM layers.

The angle between the i-th and the 1-st Kerr vector (i.e. the difference between Kerr phases) $\Delta\xi^{\langle i,1\rangle} \equiv \xi^{(i)} - \xi^{(1)}$, introduced by non-FM spacer layers *increases* with the spacer thickness [Eq. (3.41)], so that:

$$\arg\left(q^{\langle i,1\rangle}\right)_{\mathrm{spacer}} = \left(\Delta\xi^{\langle i,1\rangle}\right)_{\mathrm{spacer}} = \arg\left[Q(\Delta d^{\langle i,1\rangle})\right] = 4\pi\,\Re(N_z^{(\mathrm{nf})})\frac{\Delta d^{\langle i,1\rangle}}{\lambda^{(\omega)}}, \quad (5.6)$$

where $\Re(N_z^{(\mathrm{nf})}) > 0$. Similarly, an absorbing spacer material attenuates the i-th Kerr amplitude $\Omega^{(i)}$ by

$$|q^{\langle i,1\rangle}|_{\mathrm{spacer}} = |Q(\Delta d^{\langle i,1\rangle})| = \exp\left[-4\pi\Im(N_z^{(\mathrm{nf})})\frac{\Delta d^{\langle i,1\rangle}}{\lambda^{(\omega)}}\right], \quad (5.7)$$

where, as follows from our time convention [Appendix A], $\Im(N_z^{(\mathrm{nf})}) > 0$. If FM layers are made of the same material, the Kerr phase $\xi^{(i)}$ increases monotonously with i, i.e. with the in-depth location of the FM layer. At the same time, the normalized Kerr amplitude $\Omega^{(i)}/t^{(i)}$ decreases monotonously. The physical reason is that if the FM layer is located deeper, the optical path for reaching the FM layer is longer (it increases ξ) and the light is more absorbed (it decreases Ω). These statements will be used in Sections 5.5.1 and 5.5.2 to associate a given MOKE contribution to a selected FM layer in the structure.

As an example, the evolution of the polar Kerr vector in the $\theta\epsilon$-plane, when increasing the thickness $d^{(1)}$ of the Au overlayer in the $\mathrm{Au}(d^{(1)})/\mathrm{Co}(1\mathrm{nm})/\mathrm{Au}$ structure (the Co layer being perpendicularly magnetized) is calculated for $\varphi = 0°$ and $E = 3$ eV (Fig. 5.1). As the FM layer is located deeper in the multilayer stack, the Kerr vector rotates anti-clock-wise and its length decreases.

As any of the three products involved in the q expression [Eqs. (5.3)(5.4)] does not depend on the polarization state of the incident light beam, the depth sensitivity function q
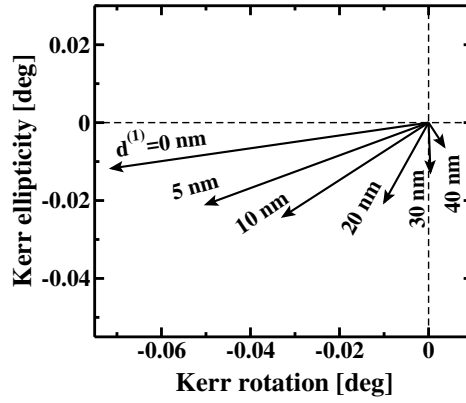
Figure 5.1: Variation of the Kerr vector with increasing the overlayer thickness $d^{(1)}$ for the Au($d^{(1)}$)/Co(1 nm)/Au system, calculated for $\varphi = 0°$, $E = 3$ eV.

does not vary with polarization in the ultrathin FM film approximation. For a given structure, *q depends only on the incidence angle φ and photon energy E.*

In conclusion, the depth sensitivity function q consists of both "chemical" and "phase" contrast contributions. The first contribution exists if FM layers consist of different materials, and the second is associated to the optical distance between FM layers. Obviously, in case of very thin spacer layers and FM layers of different composition, the chemical contrast provides a larger contribution to the depth sensitivity function than the phase difference. In the following, we will focus on the case of FM layers consisting of the same material.

5.4.2   Depth sensitivity function for ultrathin FM layers consisting of the same material

If ultrathin FM layers are made of the same material, the depth sensitivity function q expression is simplified, and remains the same for both PMOKE and LMOKE [see Eqs. (5.3)(5.4)]:

$$q_{\text{pol}}^{\langle i,1 \rangle} = q_{\text{lon}}^{\langle i,1 \rangle} = \frac{t^{(i)}}{t^{(1)}} Q(\Delta d^{\langle i,1 \rangle}). \tag{5.8}$$

Hence, q can be modified only by varying Q, which can be monitored only by the spacer thickness $\Delta d^{\langle i,1 \rangle}$, the spacer refractive index $N^{(\text{nf})}$, the photon energy E or the incidence angle φ.

Later, we will show that to distinguish MO signals coming from:

(i) two FM layers, the argument of $q^{\langle 2,1 \rangle}$ has to be non-zero (Section 5.6).

(ii) three or more FM layers, the value of q must be tunable (Section 5.7).

Thus, to understand and optimize the sensitivity of in-depth investigations, spectral and angular dependences of Q (and thus of q) have to be studied in detail.
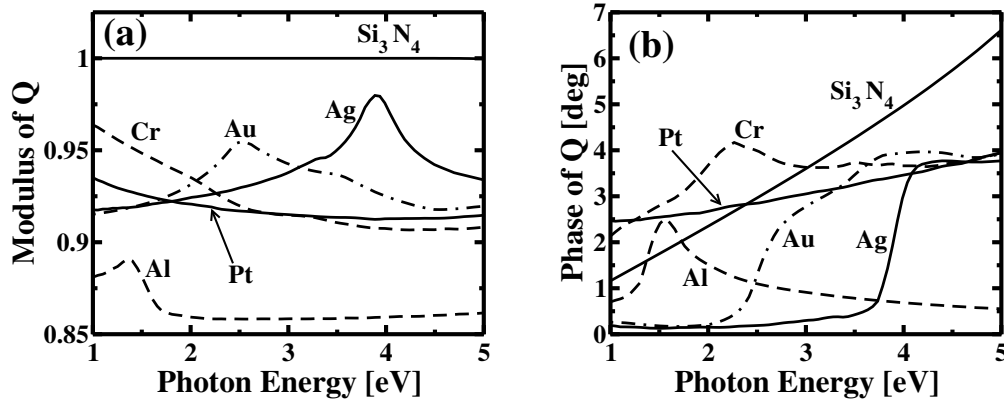
Figure 5.2: Photon energy dependence of (a) the modulus and (b) the phase of Q [defined in Eq. (3.41)] in the case of a 1 nm thick spacer layer of different materials.

Spectral dependence of Q: The spectral dependence of Q, for a 1 nm thick spacer layer[3], is depicted in Fig. 5.2(a)(b) for several common metals and Si_3N_4. As expected:

(i) there is no damping [$|Q| = 1$] for transparent materials, such as Si_3N_4. Noble metals cause a decrease of the Kerr amplitude by about 7% per nm of spacer thickness [$|Q| \approx 0.93$]. Because noble metals are more transparent [i.e. their $\Im(N^{(\mathrm{nf})})$ is smaller] in the vicinity of their plasma edge, the modulus $|Q|$ is larger here, as follows from Eq. (5.7). This can be seen in Fig. 5.2(a) for Au at 2.5 eV and Ag at 3.8 eV.

(ii) Fig. 5.2(b) shows that the variation of the Kerr phase, $\Delta\xi_{\mathrm{spacer}} = \arg(Q)$, depends strongly on the photon energy and can vary up to 4° per nm of spacer thickness. Noble metals exhibit very small Kerr phase shift ξ for photon energies below the plasma edge, as the consequence of both a longer wavelength for smaller photon energies E, and a smaller refractive index $\Re(N^{(\mathrm{nf})})$ in this region.

Dependence of Q on the incidence angle φ: An example of the calculated dependence of Q with the incidence angle φ is shown on Figure 5.3 for 1 nm of Au spacer and for several photon energies (the light is assumed to come from vacuum, i.e. $N^{(0)} = 1$). We can see that the angular dependence of Q is weaker than its spectral variation. A variation of the incidence angle φ from 0 to 90°, e.g. at a fixed photon energy $E = 4\ eV$, changes the modulus $|Q|$ by about 0.5% and the phase $\arg(Q)$ by about 0.3°.

Thus, as Q depends rather weakly on the incidence angle φ, it is convenient to define the renormalized quantity

$$p^{\langle i,1\rangle}(\varphi) = \frac{Q(\varphi, \Delta d^{\langle i,1\rangle})}{Q(\varphi = 0, \Delta d^{\langle i,1\rangle})} \approx 1 - 2\pi i \frac{(N^{(0)})^2}{N^{(\mathrm{nf})}} \frac{\Delta d^{\langle i,1\rangle}}{\lambda^{(\omega)}} \sin^2 \varphi, \tag{5.9}$$

---

[3]The value of Q for different spacer thickness $d^{\langle i,j\rangle}$ can be determined easily since [Eq. (5.5)]:

$$|Q(d^{\langle i,j\rangle}\ [\mathrm{nm}])| = |Q(d^{\langle i,j\rangle}{=}1\ [\mathrm{nm}])|^{d^{\langle i,j\rangle}}$$
$$\arg(Q(d^{\langle i,j\rangle}\ [\mathrm{nm}])) = d^{\langle i,j\rangle}\arg(Q(d^{\langle i,j\rangle}{=}1\ [\mathrm{nm}])).$$
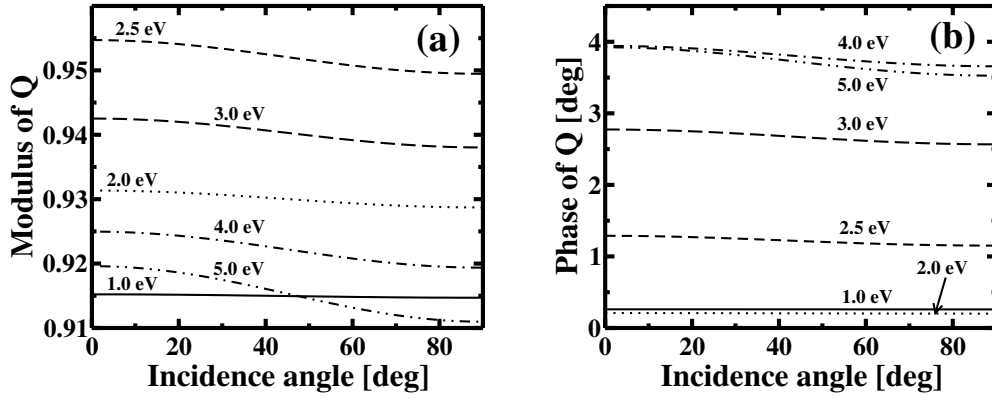
Figure 5.3: Incidence angle φ dependence of (a) the modulus and (b) the phase of Q [Eq. (3.41)] in the case of a 1 nm thick Au spacer layer for several photon energies. The light is assumed to come from the vacuum side, i.e. $N^{(0)} = 1$.

which better expresses the angular dependence of Q. In this analytical derivation, the approximation $N_z^{(\mathrm{nf})} \approx N^{(\mathrm{nf})} - N^{(0)2}/(2N^{(\mathrm{nf})}) \sin^2 \varphi$ was used. Equation (5.9) points out that the angular dependence of Q is given by $\sin^2 \varphi$, as shown on Figure 5.3. The spectral variation of p at $\varphi = 70°$ for a 1 nm thick spacer layer is depicted in Fig. 5.4(a)(b) for several materials, and for a probing light coming from vacuum ($N^{(0)} = 1$).
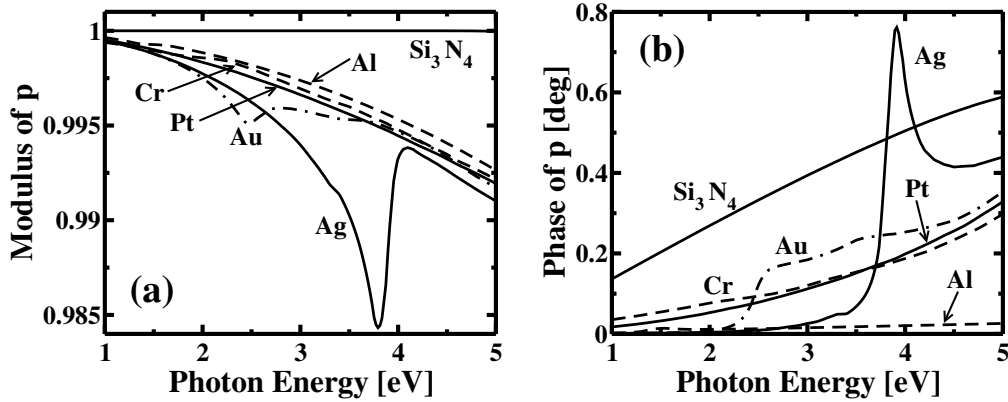
Figure 5.4: Photon energy dependence of (a) the modulus and (b) the phase of $p = Q(70°)/Q(0°)$ defined by Eq. (5.9), in the case of a 1 nm thick spacer layer of different materials.

Then, some comments can be done:

(i) As it can be seen from comparison between Figs. 5.2 and 5.4, the dependence of Q with the incidence angle is in general approximately 10 times weaker than that found when changing the photon energy. The associated physical reason is that Q depends on the incidence angle φ only through the variation of $N_z(\varphi)$, which is quite weak (about 10% between $\varphi = 0$ and $\varphi = 90°$). This reflects the fact that metals are optically denser materials than vacuum, and consequently the light is always refracted in the multilayer in a direction close to the film normal.

(ii) Larger values of p are reached for higher photon energies.

(iii) As can be seen from Eq.(5.9), p depends quadratically on $N^{(0)}$. Hence, the dependence of $q_{\text{pol/lon}}$ on φ can be enhanced if the incident light comes from an optically denser medium, for example, using a half-cylinder glass coupler contacted optically to the sample by an immersion liquid. For a coupling with $N^{(0)} = 1.8$, the variation of $q_{\text{pol/lon}}$ with the incidence angle increases by about three times $[(N^{(0)})^2 \approx 3]$. The disadvantage of a smaller sensitivity of q with the angle of incidence φ is balanced by the fact that it is linked here to only one set of optical and MO parameters at a fixed photon energy.

In conclusion, if ultrathin FM layers are build with the same material, the coefficient Q (describing the attenuation or phase shift linked to the spacer) is the only quantity sensitive to the difference between MOKE contributions originating from different FM layers located at different depths. The other parameters, χ [Eq. (3.43)], $V_{\mathbf{s(p)}}$ [Eq. (3.44)], that describe the spectral and incidence angle variations of MOKE [Eq. (3.46)] are *the same* for *all* concerned FM layers. For example, the change of the incidence angle φ pronouncedly modifies all Kerr vectors in the $\theta\epsilon$-plane, but in a *similar* fashion. This is demonstrated on Fig. 5.5(a)(b), which gives the calculated variation of Kerr vectors in the Au(5nm)/Co(1nm)/Au(5nm)/Co(1nm)/Au(bulk) film structure for different photon energies [Fig. 5.5(a)] and incidence angles [Fig. 5.5(b)].
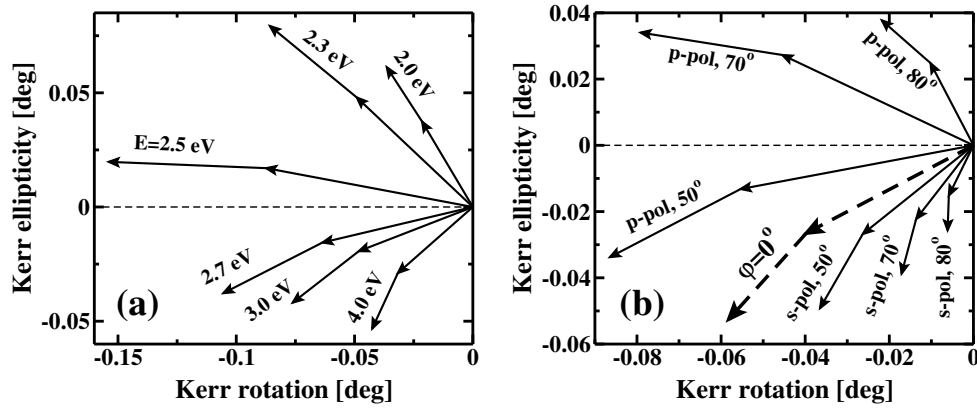
Figure 5.5: Calculated variation of the MOKE in the $\theta\epsilon$-plane originating from both FM layers in the Au(5nm)/Co(1nm)/Au(5nm)/Co(1nm)/Au(bulk) system. (a) Variation of Kerr vectors at different photon energies for $\varphi = 0$. (b) Variation of Kerr vectors for different incidence angles for both **s** and **p**-MOKE at $E = 3$ eV. Notice, that an increase of the incidence angle gives an anti-clock-wise rotation of the **s**-MOKE, while it gives an a clock-wise rotation of the **p**-MOKE. Kerr vectors from both FM layers vary with E and φ in the $\theta\epsilon$-plane in a very similar way.

Here we can immediately see that although the spectral and angular variation of Kerr vectors are important, their *relative variation* remains rather weak. This explains why the separation of Kerr signals originating from a given FM layer in a stack of several FM layers is not a trivial task, and why the inspection of the depth sensitivity function q is so important.

The value of the depth sensitivity function q can be modified (and thus, the depth resolution of more than two FM layers achieved):

(i) by varying the photon energy, with the advantages of a higher in-depth resolution and the use of a fixed experimental set-up geometry. This is the solution we have

(a)

non–FM	Au	5 nm
FM 1	Co	1.2 nm
non–FM	Au	3 nm
FM 2	Co	0.8 nm
non–FM	Au	

(b)

$4\times$
Si_3N_4	67 nm
$[Tb(0.8\,nm)/Fe(1.1\,nm)]_{10}$	19 nm
Si_3N_4	10.5 nm
glass	

(c)

non–FM	Au	5 nm
FM 1	Co	0.6 nm
non–FM	Au	5 nm
FM 2	Co	1.0 nm
non–FM	Au	5 nm
FM 3	Co	1.4 nm
non–FM	Au	
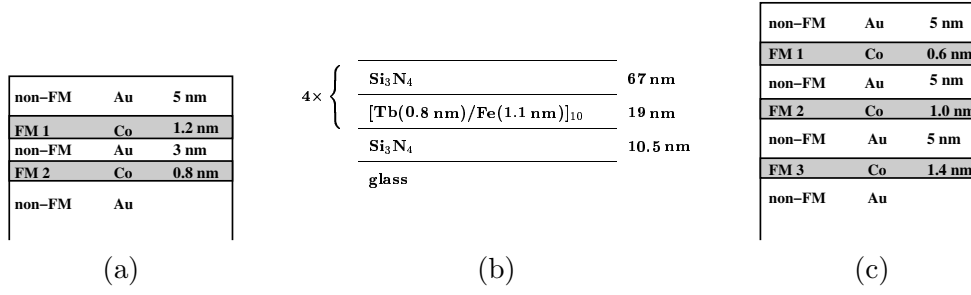
Figure 5.6: Sketches of studied sample structures (a) $(Au/Co)_2$ (b) $(TbFe/Si_3N_4)_4$ and (c) $(Au/Co)_3$.

adopted in following.

(ii) if one does not dispose of a spectroscopic equipment, but of a laser source, magnetic in-depth measurements require to vary φ over a large range.

5.4.3 Experimental determination of the polar depth sensitivity function q_{pol} for the $(Au/Co)_2$ system

This Section deals with the experimental determination of the polar depth sensitivity function q_{pol} of a $(Au/Co)_2$ FM bilayer system and its comparison to calculations based on the analytical formula (5.3) and on the 4×4 matrix formalism (Chapter 3 or [32, 46]).

The studied structure is $Au(5nm)/Co(1.2nm)/Au(3nm)/Co(0.8nm)/Au(25\ nm)$ deposited on float glass [Fig. 5.6(a)]. The sample preparation and structural characteristics are reported in Section 4.4 and in the references therein. Both Co layers have here a perpendicular magnetic anisotropy and exhibit square hysteresis loops; their thickness differ in order to fix different coercive fields [79, 81, 107]. Consequently, in this case, it is easy to deduce the s or p-PMOKE loops up to saturation corresponding either to the 0.8 or the 1.2 nm thick Co layers. These PMOKE hysteresis loops are obtained by applying the
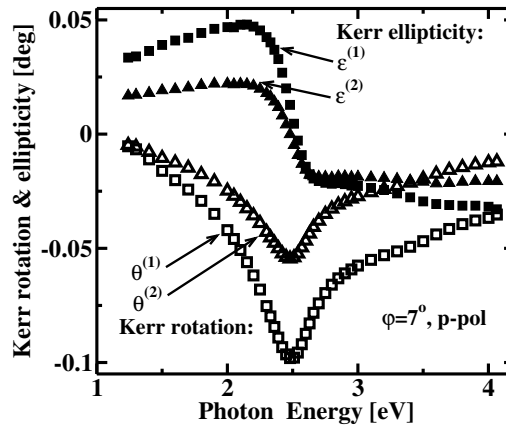
Figure 5.7: Experimental p-PMOKE rotation and ellipticity spectra of each Co layer ($t^{(1)} = 1.2\,nm$ $t^{(2)} = 0.8\,nm$) in the $(Au/Co)_2$ structure. The p-PMOKE measurements were performed at nearly normal incidence ($\varphi = 7°$).

magnetic field along the easy anisotropy axis ($\boldsymbol{H} \parallel \hat{z}$). The spectral dependence of the PMOKE rotation and ellipticity at saturation are represented in Fig. 5.7 for each Co layer.

Because of the small thickness of the Au spacer ($\Delta d^{\langle 2,1 \rangle} = 3$ nm), the two experimental PMOKE spectra look quite similar within a scaling factor related to the relative Co layer thicknesses. From the experimental PMOKE values $\Phi^{(1)}$ and $\Phi^{(2)}$, the depth sensitivity $q_{\text{pol}}^{\langle 2,1 \rangle}$ is deduced by Eq. (5.2) and presented in Fig. 5.8 in the complex form $|q| \exp[i \Delta \xi]$.
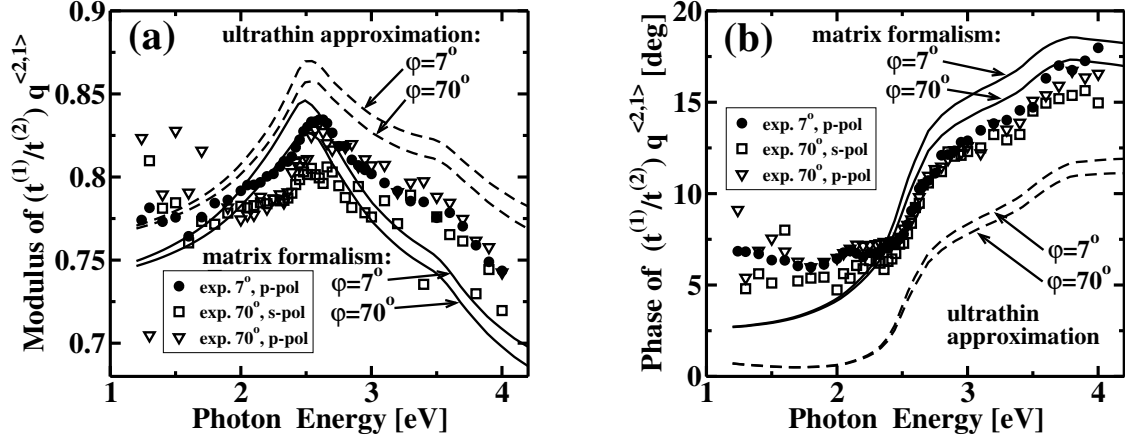
Figure 5.8: Experimental values of the normalized PMOKE depth sensitivity $\frac{t^{(1)}}{t^{(2)}} q^{\langle 2,1 \rangle} = \frac{t^{(1)}}{t^{(2)}} \frac{\Phi^{(2)}}{\Phi^{(1)}}$ as a function of the photon energy for $(\mathrm{Au}/\mathrm{Co})_2$ at $\varphi = 0$ and $\varphi = 70°$ incidence angles. In the ultrathin Co layer approximation, it should correspond to Q defined by Eq. (3.41) whose variation is represented by a dashed line. The full line shows the normalized depth sensitivity calculated from $\Phi^{(1)}$, $\Phi^{(2)}$ determined from the matrix formalism [46].

We prefer to plot the normalized quantity $(t^{(1)}/t^{(2)}) q_{\text{pol}}^{\langle 2,1 \rangle}$, that is comparable to calculations performed by the analytical formula (5.6)(5.7), using $\Delta d^{\langle 2,1 \rangle} = t^{(\mathrm{Au})} = 3$ nm. Fig. 5.8 shows the $(t^{(1)}/t^{(2)}) q_{\text{pol}}^{\langle 2,1 \rangle} = (\Phi^{(2)} t^{(1)})/(\Phi^{(1)} t^{(2)})$ variation, where $\Phi^{(1)}$ and $\Phi^{(2)}$ are calculated from the usual 4×4 matrix formalism.

On a real structure, we demonstrate that the modulus and phase of $(t^{(1)}/t^{(2)}) q_{\text{pol}}^{\langle 2,1 \rangle}$ depend weakly on the incidence angle φ and is independent on the polarization of the incident light (Fig. 5.8). As expected, the agreement between $(t^{(2)}/t^{(1)}) q_{\text{pol}}^{\langle 2,1 \rangle}$, calculated from the 4×4 matrix formalism and experimental data is nearly perfect. The analytical formulae (5.6)(5.7) well describe the experimental variation of q_{pol}. The weak difference between experimental data and analytical calculations comes from additional damping and phase shifts originating from Co layers, that are neglected in our simple treatment. This explains why the ultrathin FM film approximation predicts a smaller damping (i.e. a larger value of $|q|$) and a smaller phase shift.

5.4.4 Transverse Kerr effect (TMOKE)

Let us discuss now briefly the depth sensitivity of transverse MOKE (TMOKE), introduced in Section 2.2.1. Recall that TMOKE is only sensitive to the transverse component m_x of the magnetization. TMOKE is a different type of observable than PMOKE and LMOKE, because it is not measured by a polarimetric method, but by the variation of the reflected light intensity for p-polarized incident light at oblique incidence (i.e. $\varphi \neq 0$).

Similarly to the MOKE additivity [Section 3.3.3], the total reflection coefficient $r_{\text{pp}}^{(\text{tot})}$ writes as a linear expansion of the reflection coefficients r_{pp} with respect to the transverse magnetization components $m_x^{(i)}$ in all FM layers (i) [Table 3.1]:

$$r_{\text{pp}}^{(\text{tot})} = r_{\text{pp}}^{(0)} + \sum_i r_{\text{pp}}^{(i,\text{mag})} \, m_x^{(i)}, \tag{5.10}$$

where r_{pp} is independent on the sample magnetization and $r_{\text{pp}}^{(i,\text{mag})}$ represents the contribution of the magnetized i-th FM layer. The $r_{\text{pp}}^{(i,\text{mag})}$ coefficient can be expressed as

$$r_{\text{pp}}^{(i,\text{mag})} = q_{\text{tra}}^{\langle i,1 \rangle} r_{\text{pp,mag}}^{(1)}, \tag{5.11}$$

where $q_{\text{tra}}^{\langle i,1 \rangle}$ is the associated transverse depth sensitivity function.

In the ultrathin FM layer approximation, the magnetic reflection coefficients $r_{\text{pp}}^{(i,\text{mag})}$ are expressed as [Table 3.1, Eq. (3.45)]

$$r_{\text{pp}}^{(i,\text{mag})} = \frac{-4ik_0^{(\omega)}(N^{(}\text{nf}))^2 N_y N_z^{(\text{nf})} N^{(0)} \cos\varphi}{\left[N^{(0)} N_z^{(\text{nf})} + (N^{(\text{nf})})^2 \cos\varphi \right]^2} \frac{\varepsilon_1^{(i)}}{\varepsilon_0^{(i)}} Q(d^{(i)}) \, t^{(i)} \, m_x^{(i)}, \tag{5.12}$$

where $\varepsilon_1^{(i)}$, $\varepsilon_0^{(i)}$ are the off-diagonal, diagonal permittivity tensor elements of the i-th FM layer, respectively. $t^{(i)}$ is the i-th FM layer thickness and $d^{(i)}$ is the distance between FM layer and the top of the sample [Figure 3.3(b)]. The remaining coefficients are defined in Section 3.3.1.

Expressing the transverse depth sensitivity function $q_{\text{tra}}^{\langle i,1 \rangle} = r_{\text{pp}}^{(i,\text{mag})}/r_{\text{pp}}^{(1,\text{mag})}$ in the ultrathin approximation of the FM layer, we find that it has exactly the same form as the longitudinal one, i.e. $q_{\text{tra}}^{\langle i,1 \rangle} = q_{\text{lon}}^{\langle i,1 \rangle}$ [Eq. (5.4)], and thus discussion related with longitudinal depth sensitivity function is valid for transverse one as well.

Because the $r_{\text{pp}}^{(i,\text{mag})}$ magnetic contribution is much smaller than $r_{\text{pp}}^{(0)}$, the reflected p-polarized light intensity $I_\text{p} \sim |r_{\text{pp}}|^2$ can be written as

$$I_\text{p} = I_\text{p}^{(0)} + \sum_i I_\text{p}^{(i,\text{mag})} \sim |r_{\text{pp}}^{(0)}|^2 \left(1 + s_{\text{tra}}^{(\text{tot})} \right). \tag{5.13}$$

Here, $s_{\text{tra}}^{(\text{tot})}$ represents the total transverse Kerr signal, which expresses as

$$s_{\text{tra}}^{(\text{tot})} = \sum_i s_{\text{tra}}^{(i)} = 2 \sum_i \Re \left(q_{\text{tra}}^{\langle i,1 \rangle} \frac{r_{\text{pp}}^{(1,\text{mag})}}{r_{\text{pp}}^{(0)}} \right) m_x^{(i)} = 2 \sum_i \Re \left(q_{\text{tra}}^{\langle i,1 \rangle} \tilde{\Phi}^{(1)} \right) m_x^{(i)}, \tag{5.14}$$

where $\tilde{\Phi}^{(1)} \equiv r_{\text{pp}}^{(1,\text{mag})}/r_{\text{pp}}^{(0)}$ [Eq. (2.15)]. Eq. (5.13) can be compared with PMOKE/LMOKE signals $s_{\text{pol/lon}}^{(i)} = \sum_i \Re(q_{\text{pol/lon}}^{\langle i,1 \rangle} \Phi_{\text{pol/lon}}^{(1)} m_{z/y}^{(i)} e^{i\psi})$ [Eqs. (2.17)(2.18)(5.2)]. Thus, the transverse Kerr signal $s_{\text{tra}}^{(i)}$ can give the same depth sensitive information than previously discussed for polar $s_{\text{pol}}^{(i)}$ and longitudinal $s_{\text{lon}}^{(i)}$ Kerr signals. The only difference is that, in the case of TMOKE, it is not possible to tune the projection angle ψ by means of a compensator (Section 2.4.2, Figure 2.4), and consequently the projection angle is fixed to $\psi = 0$.

5.5 Assignment of the MOKE contribution for a selected FM layer

5.5.1 Generalities

Let us consider the case of a multilayer structure composed of several ultrathin FM layers of the same material, each providing nearly square magnetic hysteresis loops, and separated by non-FM spacer layers [Fig. 3.3(b)]. An open question is often to assign each loop to a particular FM layer located at a given depth $d^{(i)}$. To solve this problem, let us recall the results extracted from the examination of Eqs. (5.6)(5.7) (Figure 5.1):

(i) The Kerr phase $\xi^{(i)}$ increases *monotonously* when increasing the in-depth position $d^{(i)}$.

(ii) For absorbing spacer materials, $\Im(N_z^{(\mathrm{nf})}) > 0$, the normalized Kerr amplitude $\Omega^{(i)}/t^{(i)}$ decreases monotonously when increasing $d^{(i)}$.

Consequently, the procedure for determining the in-depth position of a FM layer is the following:

(i) Hysteresis loops in Kerr rotation $\theta^{(\mathrm{tot})}$ and Kerr ellipticity $\epsilon^{(\mathrm{tot})}$ are measured at the same photon energy E and incidence angle φ.

(ii) The value of MOKE at saturation, $\Phi^{(i)} = \theta^{(i)} + i\epsilon^{(i)} = \Omega^{(i)} e^{i\xi^{(i)}}$ is determined experimentally for each FM layer; this is an easy procedure when the coercive field differs for each FM layer.

(iii) The Kerr phase, $\xi^{(i)} = \arg(\Phi^{(i)})$, is determined, and the $\xi^{(i)}$ values are classified in a decreasing order. Then, the largest value of $\xi^{(i)}$ corresponds to the deepest FM layer.

(iv) The in-depth location of the FM layers can be confirmed from the normalized Kerr amplitudes $\Omega^{(i)}/t^{(i)}$, which must decrease with $d^{(i)}$.

This analysis is valid for a large number of FM layers. The main limitation is when some FM layers exhibit the same coercive field or when the applied field is not large enough to saturate the magnetization in a FM layer. In such a case, a calculation involving all informations about optical and magneto-optical parameters (e.g. the 4×4 matrix formalism) must be used.

If the FM layers are not constituted with the same FM material, then the MOKE contributions $\Phi^{(i)}$ have to be renormalized by $\varepsilon_1^{(i)}$ for PMOKE and by $\varepsilon_1^{(i)}/\varepsilon_0^{(i)}$ for LMOKE. Then, the influence of different FM materials is avoided, as can be found from Eqs. (3.46).

In the case of thick spacer layers, the same rules are valid as well. The only problem is that the deduced value of the Kerr phase $\xi^{(i)}$ can be underestimated by a factor 2π, which can generate difficulties to classify the Kerr phases $\xi^{(i)}$. This is overcome when considering the normalized Kerr amplitude $\Omega^{(i)}/t^{(i)}$, or knowing the angular or spectral dependence of $\xi^{(i)}$. Since

$$\xi^{(i)} = \xi^{(1)} + \Delta\xi^{\langle i,1\rangle}, \tag{5.15}$$

$\Delta\xi^{\langle i,1\rangle}$, in the ultrathin FM approximation, writes

$$\Delta\xi^{\langle i,1\rangle} = \frac{4\pi}{\lambda^{(\omega)}}\Delta d^{\langle i,1\rangle}\Re\left(N_z^{(\mathrm{nf})}\right) > 0. \tag{5.16}$$

The deepest FM layer has the largest $\Delta d^{\langle i,1 \rangle}$, and consequently the largest slope in the plots of $\xi^{(i)}$ with the photon energy or the incidence angle. This will be illustrated for the spectral dependence of the Kerr phase $\xi^{(i)}$ of the TbFe/Si$_3$N$_4$ system, where the deepest reachable (the third) FM stack has the largest slope in the $\xi^{(i)}(E)$ dependence (Section 5.7.2).

To illustrate this Section, the MOKE determination of the in-depth position of FM layers involved in a (Au/Co)$_3$ multilayer structure is reported in the next Section 5.5.2.

5.5.2 Application to the (Au/Co)$_3$ film structure

The Au(5nm)/Co(0.6nm)/Au(5nm)/Co(1nm)/Au(5nm)/Co(1.4nm)/Au(24nm)/glass film structure is considered in this subsection. The sample is presented in Figure 5.6(c) and its preparation and characterization have been reported previously in Section 4.4. Because the thicker Co layer has the smaller coercive field [107, 81], it is possible to pre-assign each PMOKE loop contribution to one of the three Co layers. Hysteresis loops are measured by both p-PMOKE rotation and ellipticity at nearly normal incidence ($\varphi = 7°$, $E = 3.8$ eV), in a magnetic field applied along the normal of the film ($\boldsymbol{H} \parallel \hat{z}$) (Figure 5.9).
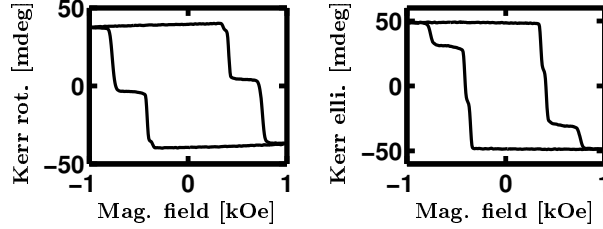
Figure 5.9: p-PMOKE ($\varphi = 7°$) rotation and ellipticity hysteresis loops measured on the (Au/Co)$_3$ system at $E = 3.8$ eV.

The light enters in the sample from the Au(5 nm) overlayer side. The values of individual coercive fields and Kerr rotations and ellipticities corresponding to each FM layer are given in Table 5.1.

	H_c[Oe]	$\theta^{(i)}$[mdeg]	$\epsilon^{(i)}$[mdeg]	$\Omega^{(i)}$[mdeg]	$\xi^{(i)}$[deg]	$t^{(i)}$[nm]	$\Omega^{(i)}/t^{(i)}$[mdeg/nm]
$\Phi^{(1)}$	770	-21.0	-9.0	22.9	203°	0.6	38.2
$\Phi^{(2)}$	420	-15.8	-21.4	26.6	233°	1.0	26.6
$\Phi^{(3)}$	360	-2.1	-18.0	18.1	263°	1.4	12.9

Table 5.1: PMOKE rotation and ellipticity at saturation and coercive field for each FM layer in the (Au/Co)$_3$ system [Figure 5.6(c)]. Note that values of $\theta^{(i)}$ and $\epsilon^{(i)}$ do not vary consistently with (i), i.e. with the depth of the FM layer. The pertinent quantities are here $\xi^{(i)}$ and $\Omega^{(i)}/t^{(i)}$.

From another side, it is possible to assign independently the different PMOKE contributions from their values for each FM layer. As expected, the value of $\xi^{(i)}$ increases continuously with i, while the ratio $\Omega^{(i)}/t^{(i)}$ decreases, proving that the in-depth location of the considered FM layer increases with i. Because both Au spacer layers have the same thickness $\Delta d^{\langle 2,1 \rangle} = \Delta d^{\langle 3,2 \rangle} = 5$ nm, the difference of Kerr phases are obviously equal $\Delta \xi^{\langle 2,1 \rangle} = \Delta \xi^{\langle 3,2 \rangle} = 30°$. The ratio between normalized Kerr amplitudes

$(\Omega^{(2)}/t^{(2)})/(\Omega^{(1)}/t^{(1)}) = 0.69$, $(\Omega^{(3)}/t^{(3)})/(\Omega^{(2)}/t^{(2)}) = 0.49$ should be the same. They differ from each other certainly because the interface contributions to PMOKE are neglected [Chapter 4 or [57]]. Since normalized Kerr amplitudes, calculated by the 4×4 matrix formalism, are $(\Omega^{(2)}/t^{(2)})/(\Omega^{(1)}/t^{(1)}) = 0.62$, $(\Omega^{(3)}/t^{(3)})/(\Omega^{(2)}/t^{(2)}) = 0.60$, the influence of the Co thickness itself can not explain the above discrepancy.

5.6   Separation of Kerr signals in a FM bilayer structure

This Section proposes ways to separate the Kerr signals, $s^{(1)}$ and $s^{(2)}$, of each FM layer in a structure consisting of two FM layers separated by a non-FM spacer layer. In other words, we solve the problem of finding particular MO arrangements to cancel either the Kerr signal contribution coming from one or the other FM layer. Using the representation of MOKE in the complex $\theta\epsilon$-plane (Section 2.2.3), the contribution of the 1-st or 2-nd FM layer cancels ($s^{(1)}$ or $s^{(2)} = 0$) if the Kerr vector $\Phi^{(1)}$ or $\Phi^{(2)}$ is *perpendicular* to the projection axis. This situation is schematically depicted in Fig. 5.10(a) for canceling the MOKE contribution of the 1-st FM layer.
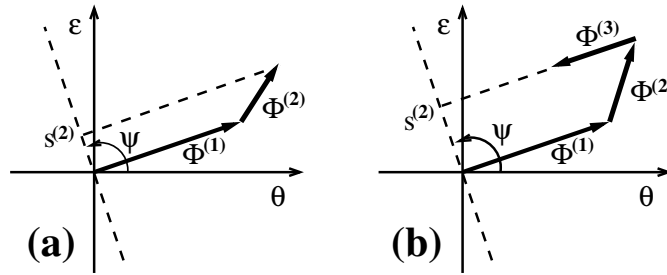
Figure 5.10: Sketch of Kerr vectors and projection axis in the $\theta\epsilon$-plane to obtain a Kerr signal coming from only one FM layer in a system consisting of (a) two and (b) three FM layers.

The angle between the Kerr vector $\Phi^{(i)}$ and the projection axis is $\arg(\Phi^{(i)}) - \psi = \xi^{(i)} - \psi$. It can be tuned by several ways:

- For a fixed projection angle ψ, the orientation of the Kerr vectors can be modified by varying the photon energy E [Fig. 5.5(a)] [94] or the angle of incidence φ [Fig. 5.5(b)] [96]. An example of the Kerr vector variations with E or φ in the complex $\theta\epsilon$-plane is reported in Fig. 5.5 for a Au/Co/Au/Co/Au structure. It shows how it is possible to find values of E or φ that gives either $\theta^{(i)} = 0$ or $\epsilon^{(i)} = 0$, selectively for each of the two FM layers.

- For fixed Kerr vectors in the complex $\theta\epsilon$-plane (i.e. for given values of E and φ), the projection angle ψ can be tuned, for example with a Babinet-Soleil compensator (Section 2.4.2, [95]). Note that this elegant technique has been used in its microscopy mode to prove unambiguously the existence of a biquadratic coupling between Fe layers separated by a Cr spacer layer [93].

- In principle, it is not necessary to tune experimentally the projection angle ψ, because the decomposition can be done numerically. From the knowledge of two Kerr signals s_a and s_b, measured in different experimental conditions (for example Kerr

rotation and ellipticity or two Kerr signals measured at two different photon energies or incidence angles), it is possible to deduce the Kerr signal $s^{(i)}$ which originates from each FM layer ($i = \{1, 2\}$):

$$s^{(i)} = s_a \cos \psi^{(i)} + s_b \sin \psi^{(i)}, \tag{5.17}$$

where the weight of the linear combination of experimental Kerr signals s_a and s_b is parametrized by the numerical projection angle $\psi^{(i)}$. A similar approach has been suggested in ref. [108].

5.6.1   LMOKE case: application to the GaMnAs bilayer structure

Here, we will show how the above technique can be used to separate LMOKE signals coming from two FM GaMnAs layers separated by a double tunnel junction.

When the GaAs semiconductor is weakly doped by Mn ions, the resulting $Ga_{1-x}Mn_xAs$ compound exhibits ferromagnetism at finite temperature [109]. For example, for a Mn ion concentration of only $x = 5\%$, its Curie temperature may be as high as 110 K [110]. This value does not depend directly on x, but more on the number of carriers (holes) by which the exchange interaction is mediated. This compound belongs to the very attractive new class of Dilute Magnetic Semiconductors (DMS) which are promising materials in spin-electronics since GaMnAs grows epitaxially on GaAs.

For a GaMnAs(001) (300 nm) thick layer, G. Moore *et al.* [111] have shown that in-plane fourfold axes of [100]-type act as easy anisotropy axes. Thus, the in-plane magnetic field-induced magnetization reversal occurs by successive jumps between the four equivalent [100] directions. The reversal process is simple if the field is rigorously applied along high symmetry [100] or [110] directions: the hysteresis loop is highly square for $\boldsymbol{H} \parallel$ [110] and $\boldsymbol{H} \parallel$ [100], while it shows two jumps, for any other field orientation.

In this work, we have performed LMOKE measurements on a DMS double tunnel junction structure in order to determine the easy anisotropy directions. This is important for applications since large magnetoresistance may be only obtained for simple spin configurations. The investigated sample is $Ga_{94.7}Mn_{5.3}As(30\,nm)/GaAs(1\,nm)/AlAs(1.7\,nm)/GaAs(1\,nm)/Ga_{95.3}Mn_{4.7}As(300\,nm)/GaAs(3\,nm)$ deposited on a GaAs(001) substrate. It was grown by MBE and provided to us by J.-M. George and R. Mattana (Thales, Orsay). Both GaMnAs layers are FM at low enough temperature. We do not present here details on the sample preparation and structural properties.
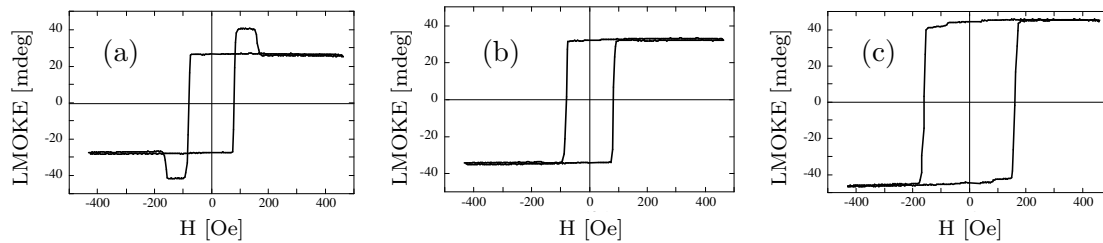
Figure 5.11: LMOKE hysteresis loops of a double GaMnAs tunnel junction (see Section 5.6.1 for details), measured with $\boldsymbol{H}$ applied parallel along the [110] high symmetry axis at $T = 1.8$ K, $\varphi = 45°$ and photon energy E=1.55 eV. The projection angle ψ is tuned by means of a Babinet-Soleil compensator. (a) Pure Kerr rotation hysteresis loop obtained for $\psi = 0$ (b); $\psi = 8°$, providing a LMOKE signal associated only to the second (deeper) GaMnAs(300 nm) FM layer; (c) $\psi = 97°$, providing a LMOKE signal associated only to the first GaMnAs(30 nm) layer.

We checked first the magnetization reversal from low temperature ($T = 1.8$ K) LMOKE loops measured with light penetrating the sample from the $Ga_{94.7}Mn_{5.3}As(30$ nm$)$ top side, under an incidence angle of $\varphi = 45°$ at light wavelength $\lambda^{(\omega)} = 801$ nm (photon energy $E = 1.55$ eV). This photon energy close to the GaAs band energy, was chosen to obtain a very large MOKE since GaMnAs is known to exhibit here a huge spin polarization splitting of about 0.2 eV. The large dispersion of the extinction and refractive index in this energy range favor the in-depth resolution for separating the MO contributions of the two GaMnAs layers. When $\boldsymbol{H}$ is applied along one of the [110]-type of fourfold axes, the superposition of two square loops (Fig. 5.11) with significantly different coercive fields, $H_{c1} = 70$ Oe and $H_{c2} = 140$ Oe, is observed.

In order to know if each loop corresponds to one of the two GaMnAs layers, we separated them using the proposed in-depth sensitive LMOKE experiment. The variation of the Kerr signal at saturation for the two square loops with the projection angle ψ, scanned by means of a Babinet-Soleil compensator, is reported in Fig. 5.12.
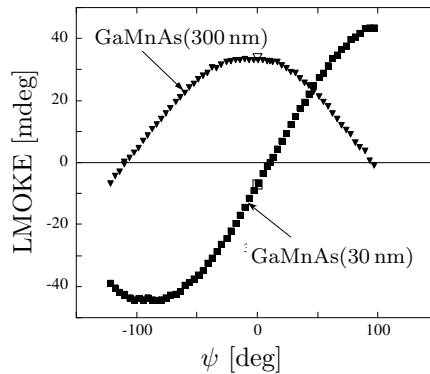
Figure 5.12: Variation of the LMOKE signals, originating form the first and the second FM layer, with the projection angle ψ. The sample and experimental conditions are the same as for Fig. 5.11.

We find that the LMOKE signal, associated with the upper and deeper GaMnAs layer, cancel for $\psi_1 = 8°$ and $\psi_2 = 97°$, respectively. The difference $(\psi_2 - \psi_1)$ is really huge here considering that the separation between the two FM layers is only 3.7 nm. This is a consequence of the very thick (300 nm) bottom (second) FM layer, providing a large optical distance between the centers of the FM layers. Thus, we are able to easily decompose the initial double loop into two distinct ones corresponding to each GaMnAs layer. For $\psi_1 = 8°$, the hysteresis loop of the deeper $Ga_{95.3}Mn_{4.7}As(300$ nm$)$ layer is obtained [Fig. 5.11(b)], while for $\psi_1 = 97°$ one has access to the $Ga_{94.7}Mn_{5.3}As(30$ nm$)$ upper layer [Fig. 5.11(c)].

From experiments performed on a similar layer, described in Ref. [111], it has been shown unambiguously that the easy anisotropy axes are of the [100]-type. Here we confirm this property for both GaMnAs layers. Moreover, the upper $Ga_{94.7}Mn_{5.3}As(30$ nm$)$ layer has a coercive field two times larger than the deeper one. I have not developed calculations in this case since the magneto-optical coefficients are not well known.

We have confirmed our MO analysis in a more complex case. For example, for an arbitrary orientation of the applied magnetic field, one expects the superposition of four loops, two of them coming from the upper FM layer and the two others associated to the deeper FM layer. This is found experimentally. Now, keeping the previous values for ψ_1 and ψ_2, we have measured selectively the two set of complex loops corresponding to each

FM layer. So, we proved that ψ_1 and ψ_2 do not depend on the in-plane field orientation.

5.7   Separation of Kerr signals in a FM trilayer structure

In this Section, we present two new "Parallel Kerr vectors" and "Cascade numerical projection" methods, allowing to separate the Kerr signal coming from one given FM layer in a multilayer structure consisting of three FM layer.

5.7.1   The "Parallel Kerr vectors" method

As it has been discussed in Section 5.6, the MOKE of the i-th layer can always be canceled if the corresponding Kerr vector $\Phi^{(i)}$ becomes perpendicular to the projection axis. Thus, for a FM trilayer structure, if one succeeds to set-up two Kerr vectors $\Phi^{(i)}$ and $\Phi^{(j)}$ parallel to each other and perpendicular to the projection axis, the measured Kerr signal will depend only on the magnetization state of the remaining FM layer. This situation is schematically presented in Figure 5.10(b), where Kerr signals from the 1-st and 3-rd FM layers are canceled simultaneously and, consequently, only the Kerr signal coming from the 2-nd FM layer is detected. We call this procedure the "Parallel Kerr vectors" method. More generally, the i-th and j-th Kerr vectors are parallel, if

$$\Delta\xi^{\langle i,j\rangle} = \xi^{(i)} - \xi^{(j)} = \arg(q^{\langle i,j\rangle}) = n\pi, \tag{5.18}$$

where n is an integer. Considering PMOKE, the angle between two Kerr vectors is analytically expressed by [Eq. (5.3)]

$$\Delta\xi^{\langle i,j\rangle} = \frac{4\pi}{\lambda^{(\omega)}}\Delta d^{\langle i,j\rangle}\Re\left(N_z^{(\mathrm{nf})}\right) + \arg\left(\frac{\varepsilon_1^{(i)}}{\varepsilon_1^{(j)}}\right). \tag{5.19}$$

Just note that in the case of LMOKE, the second term in Equation (5.19) becomes $\arg[(\varepsilon_1^{(i)}\varepsilon_0^{(j)})/(\varepsilon_1^{(j)}\varepsilon_0^{(i)})]$. Consequently, both terms appearing in Eq.(5.19) can be tuned to set-up simultaneously two Kerr vectors parallel (i.e. $\Delta\xi^{\langle i,j\rangle} = n\pi$)

(i) when the two FM layers consist of different materials and if the distance $\Delta d^{\langle i,j\rangle}$ between these FM layers is small; then, the main contribution to $\Delta\xi^{\langle i,j\rangle}$ comes from the second term, $\arg(\varepsilon_1^{(i)}/\varepsilon_1^{(j)})$, whose value can only be tuned by the photon energy.

(ii) when both the i-th and j-th FM layers are made of the same material; the only non-zero contribution to $\Delta\xi^{\langle i,j\rangle}$ comes from the first term of Eq.(5.19), requiring a certain distance $\Delta d^{\langle i,j\rangle}$ between the FM layers to realize $\Delta\xi^{\langle i,j\rangle} = n\pi$. For typical values of the photon energy and refractive index of the non-FM spacer layers ($E = 3$ eV, $N^{(\mathrm{nf})} = 2.5$), the minimum distance between FM layers required to get a parallel Kerr vectors configuration is as large as $\Delta d^{\langle i,j\rangle} \approx 40$ nm. However, using higher photon energies of the order of ten to hundreds eV (XMCD in the ultra-violet range, on interband transitions), a phase shift of $n\pi$ can be obtained for $\Delta d^{\langle i,j\rangle}$ of the order of few nm.

5.7.2 Application to the $(TbFe/Si_3N_4)_4$ structure

The "Parallel Kerr vectors" method is particularly suitable for checking the individual single layer magnetizations in a multilayer structure of three FM layer, when:

(i) FM layers are made of different materials.

(ii) FM layers are made of the same material but they are separated by thick ($d^{\langle i,j \rangle} \approx n\lambda^{(\omega)}/[4\Re(N_z^{(\mathrm{nf})})]$, n is integer) non-FM spacer layers. This case is treated below for a typical magneto-optical recording $(TbFe/Si_3N_4)_4$ multilayer sample.

By adjusting the photon energy, we demonstrate how to separate individual Kerr signals originating from each FM layer in a FM trilayer structure.

The sample under investigation was $(Si_3N_4/TbFe)_4/Si_3N_4(10.5\ nm)/glass$ where TbFe represents a single $[Tb(0.8\ nm)/Fe(1.1\ nm)]_{10}$ multilayer stack. TbFe stacks are separated by 67 nm of Si_3N_4 [Fig. 5.6(b)]. Informations on this sputtered sample are reported elsewhere [112, 113]. Each TbFe stack displays perpendicular magnetic anisotropy. All p-PMOKE measurements have been performed at nearly normal incidence ($\varphi = 7°$), in a magnetic field applied along the normal of the film ($\boldsymbol{H} \parallel \hat{z}$). As it is commonly observed [114, 115], in spite of the same thickness, the TbFe stacks usually exhibit slightly different coercive fields.

Although the sample consists of *four* stacks of TbFe, carrying out PMOKE measurements from the upper Si_3N_4 side, we showed that the fourth (deepest) TbFe stack is screened and exhibits a negligible MO contribution over the main spectral range. Thus, PMOKE practically probes here only the three first FM stacks in the multilayer, allowing us to demonstrate how to separate Kerr signals coming from an equivalent *three* FM layer structure.

The first problem is to find photon energies for which two individual Kerr vectors become parallel. Thus, the MOKE spectra have been measured in Praha on a set-up
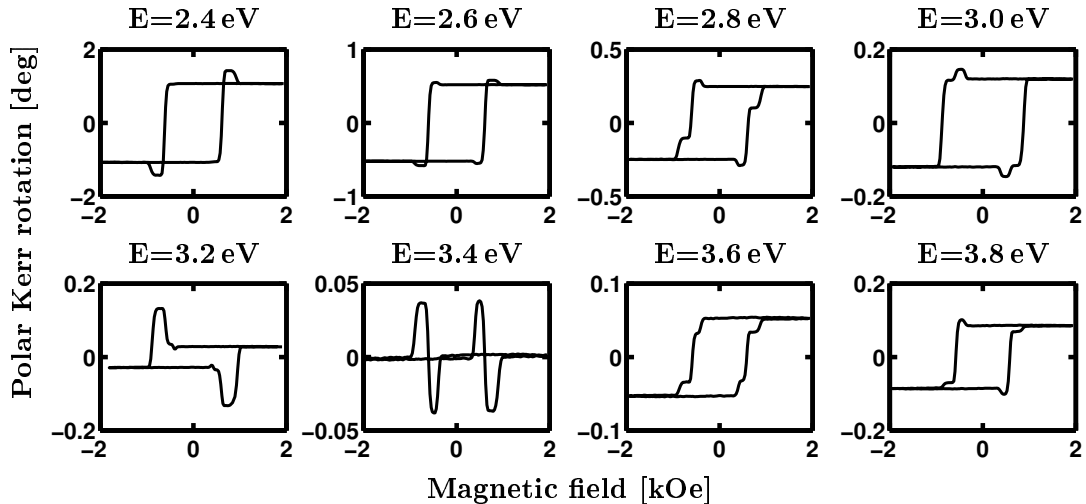
Figure 5.13: Example of PMOKE rotation hysteresis loops measured at several photon energies E on the $(TbFe/Si_3N_4)_4$ sample. Each jump in the hysteresis loop indentifies a given TbFe stack.

described in Section 2.4.3. The hysteresis loops of the sample were measured for both Kerr rotation and Kerr ellipticity over the 1.2 - 4.2 eV spectral range. Some of the Kerr rotation hysteresis loops, measured at different photon energies E, are presented in Figure 5.13.

Since individual loops are square and exhibit different coercivities, it is straightforward to determine the maximum Kerr rotation and Kerr ellipticity for each of the three TbFe stacks of interest. On the entire photon energy range, the corresponding Kerr amplitudes $\Omega^{(i)}$ and Kerr phases $\xi^{(i)}$ are then deduced and ploted as a function of E in Figure 5.14(a)(b).
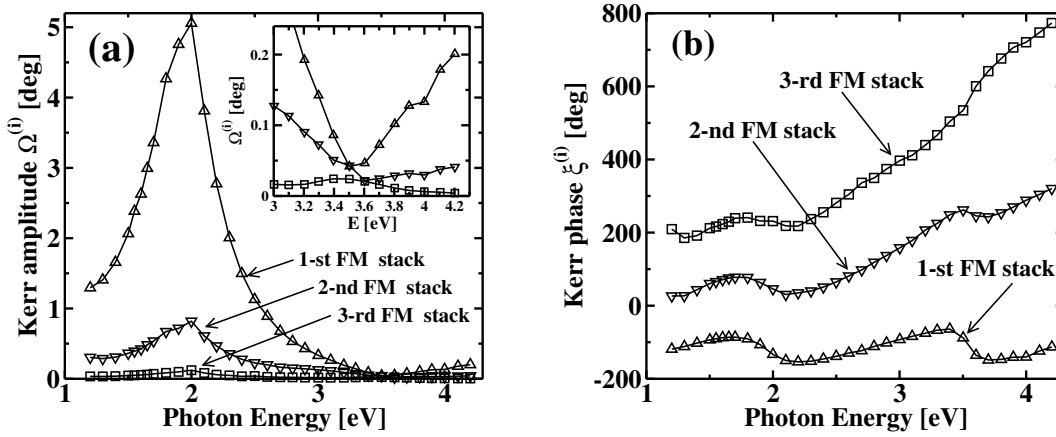
Figure 5.14: Experimental PMOKE spectra (a) Kerr amplitude $\Omega^{(i)}$, (b) Kerr phase $\xi^{(i)}$ of each FM stack in the $(TbFe/Si_3N_4)_4$ system.

As expected, the deepest FM stack shows the smallest normalized Kerr amplitude $\Omega^{(i)}/t^{(i)}$ and exhibits the largest slope in the spectral $\xi^{(i)}(E)$ variation. The spectra of Kerr amplitudes $\Omega^{(i)}(E)$ [Fig. 5.14(a)], show two interesting features: firstly, a pronounced maximum at 2.0 eV and secondly, the TbFe stacks become more transparent near 3.5 eV, giving weaker and comparable Kerr amplitudes $\Omega^{(i)}$ [see inset of Fig. 5.14(a)].

The PMOKE spectra can be as well represented in the complex $\theta\epsilon$-plane. This representation is given in Fig. 5.15(a) over the $3.1 - 3.9$ eV limited spectral range. For photon energy data represented by dashed lines, two Kerr vectors become nearly parallel to each other. To determine more precisely the photon energies at which two Kerr vectors become parallel, I have plotted the spectral dependence of the difference between Kerr phases $\Delta\xi^{\langle i,j \rangle}$ as a function of the photon energy [see Fig. 5.15(b)].

The Kerr vectors from the i-th and j-th TbFe stacks are obviously parallel if $\Delta\xi^{\langle i,j \rangle} = n\pi$. This condition is fulfilled for photon energies $E = 3.32$ eV ($\Delta\xi^{\langle 3,1 \rangle} = 540°$), $E = 3.53$ eV ($\Delta\xi^{\langle 2,1 \rangle} = 360°$) and $E = 3.62$ eV ($\Delta\xi^{\langle 3,2 \rangle} = 360°$). Since in our sample the spacer layer thicknesses $\Delta d^{\langle 2,1 \rangle} = \Delta d^{\langle 3,2 \rangle} = 67$ nm are equal, $\Delta\xi^{\langle 3,2 \rangle}$ is obviously found experimentally close to $\Delta\xi^{\langle 2,1 \rangle}$ [Fig. 5.15(b)]. Note that this is not exactly true in the vicinity of 3.5 eV where the TbFe stacks are more transparent and thus the fourth TbFe stack slightly influences the $\Delta\xi^{\langle 3,2 \rangle}$ value.

Thus, we have chosen photon energies that provide parallelism between two Kerr vectors. We tuned the projection angle ψ by a Babinet-Soleil compensator (as discussed in Section 2.4.2) to set the projection axis perpendicular to the two parallel Kerr vectors.
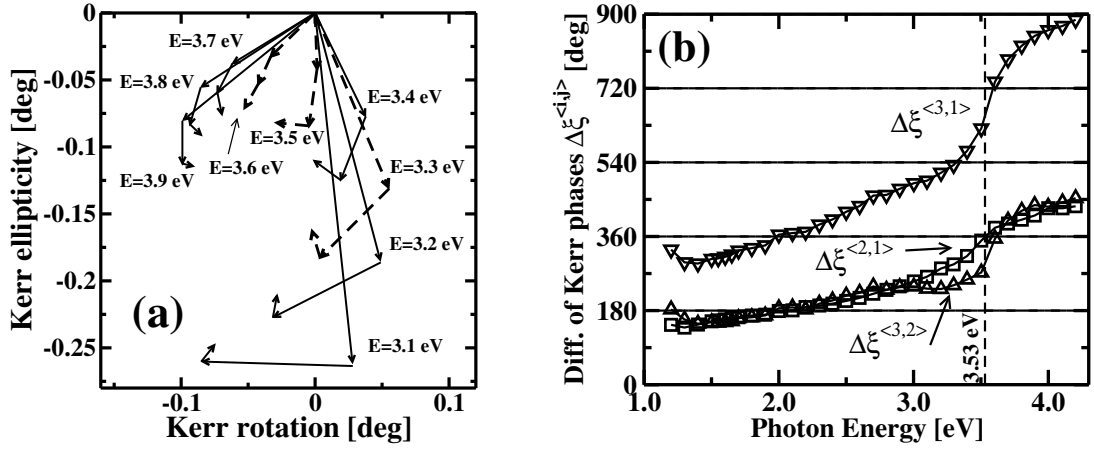
Figure 5.15: (a) experimental PMOKE originating from each FM stack in the $(TbFe/Si_3N_4)_4$ system, for several photon energies. (b) differences between Kerr phases $\Delta\xi^{\langle i,j\rangle}$ as a function of the photon energy. If $\Delta\xi^{\langle i,j\rangle} = n\,180°$, the i-th and j-th Kerr vectors are parallel.
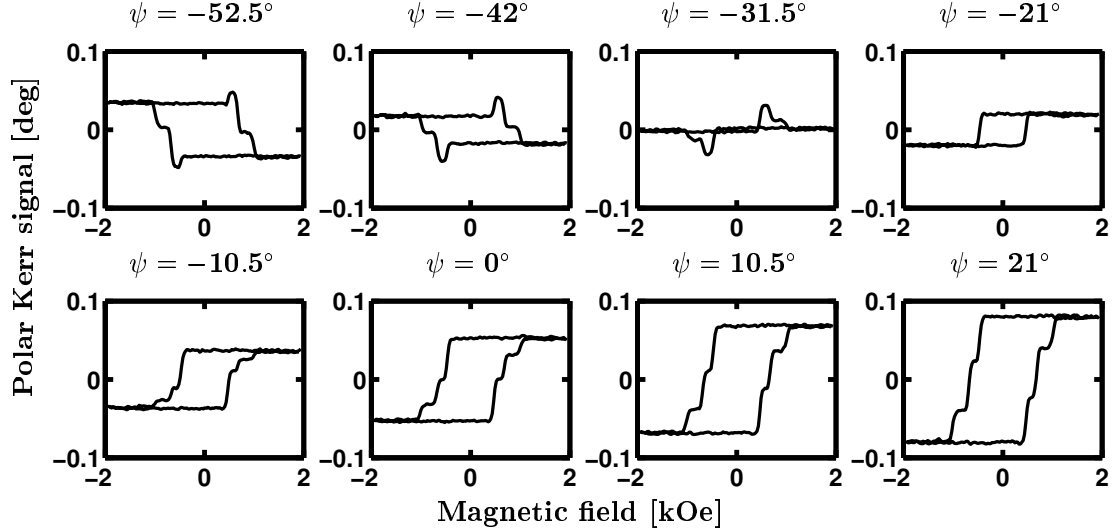
Figure 5.16: PMOKE hysteresis loops for several values of the projection angle ψ and for the $(TbFe/Si_3N_4)_4$ system. The photon energy ($E = 3.53$ eV) is chosen so that Kerr vectors $\Phi^{(1)}$ and $\Phi^{(2)}$ are parallel. Consequently, there is a projection angle ψ (here $\psi = -21°$) for which the measured Kerr signal depends only on the magnetization state of the third FM layer.

As example, at a given photon energy $E = 3.53$ eV, large modifications in hysteresis loop shape are observed when changing the projection angle ψ (Fig. 5.16).

Hysteresis loops are combinations of the three individual MOKE loops. However, the hysteresis loop measured for $\psi = -21°$ corresponds only to the third TbFe stack and Kerr contributions coming from the first and the second TbFe stacks cancel together. Hence, choosing well the photon energy E and the projection angle ψ, we succeeded to separate the hysteresis loops coming from each FM stack.
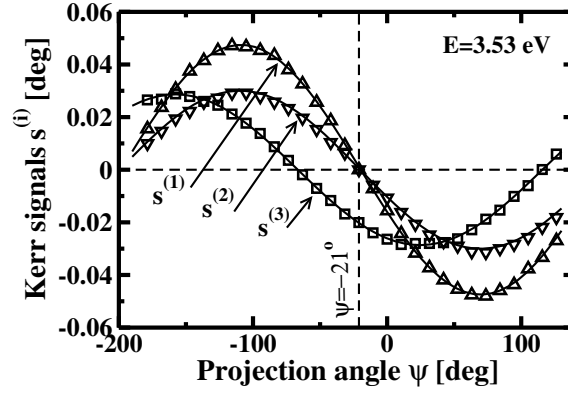
Figure 5.17: Experimental variation of PMOKE signals $s^{(i)}$, measured at $E = 3.53$ eV, as a function of the projection angle ψ, for each FM stack in the $(\text{TbFe}/\text{Si}_3\text{N}_4)_4$ system. These curves were obtained from hysteresis loops presented in Fig. 5.16. For $\psi = -21°$, $s^{(1)}$, $s^{(2)}$ cancel simultaneously and the PMOKE signal, measured at $E = 3.53$ eV and $\psi = -21°$, comes only from the third FM stack. The full lines are sinusoidal fits.

From loops presented in Fig. 5.16, we are even able to follow the variation of Kerr signals $s^{(i)}$ coming from each TbFe stack with the projection angle ψ (Fig. 5.17). As expected from Eq. (2.18), $s^{(i)} = \Re[\Phi^{(i)} \exp(i\psi)]$, the dependence of $s^{(i)}(\psi)$ is sinusoidal [95]. Sinusoidal full lines fit perfectly the experimental data (Fig. 5.17). Furthermore, one can verify that two Kerr signals $s^{(1)}$, $s^{(2)}$ cancel simultaneously for $\psi = -21°$. This explains why only the Kerr signal originating from the third TbFe stack is measured at this particular photon energy and projection angle.

The resulting three simple PMOKE hysteresis loops depending only on the magnetization state of the first, second and third TbFe stacks were measured independently by choosing appropriate couples of E and ψ values (Fig. 5.18).
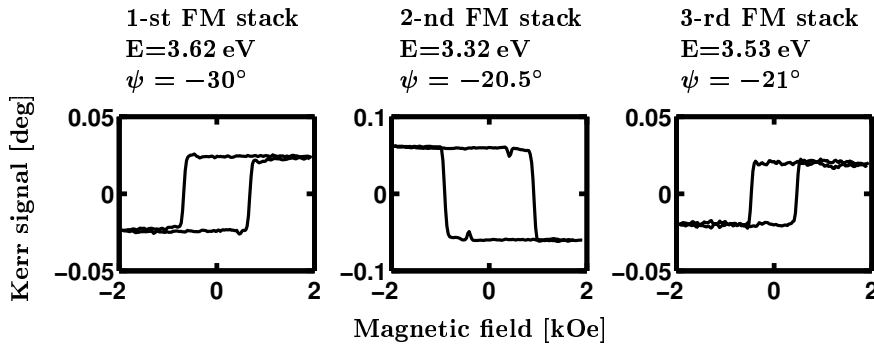
Figure 5.18: Individual PMOKE hysteresis loops of each TbFe stack in the $(\text{TbFe}/\text{Si}_3\text{N}_4)_4$ system, obtained when choosing E and ψ to cancel Kerr signals of two TbFe stacks. Values of E, ψ are indicated above each loop.

5.8   Large number of magnetic layers: "Cascade numerical projection" method

5.8.1   General formalism

Considering the case of more than three FM layers and thin non-FM spacer layers, it is generally not possible to separate the MO contributions by the "Parallel Kerr vectors" method. This is only possible for specially engineered structures, as described later in Section 5.9. This subsection treats the present problem from another point of view: the total MOKE is measured in different experimental conditions to get a set of independent total Kerr signals, from which we deduce the Kerr signal coming from each FM layer. This numerical approach can be extended to a large number of FM layers.

Separation of total polar, longitudinal and transverse Kerr signals, $s_{\text{pol}}^{(\text{tot})}$, $s_{\text{lon}}^{(\text{tot})}$, $s_{\text{tra}}^{(\text{tot})}$ has been already discussed in Section 5.3. Once separated, each Kerr signal depends on the profile of only one magnetization component $m_j^{(i)}$, $j = x$ or y or z. Thus, in the following, we assume that measured Kerr signals s are only function of the m_z component. m_x, m_y components can be obtained analogously.

Let us consider a system with a number N of FM layers having polar magnetizations $m_z^{(i)}$, $i = 1 \ldots N$. Furthermore let us assume that L polar Kerr signals $s_w^{(\text{tot})}$, $w = 1 \ldots L$, $L \geq N$ are measured in independent experimental conditions. Independent means that experiments have to be carried out at different photon energies, different incidence angles, or different projection angles. The measured Kerr signals $s_w^{(\text{tot})}$ are given by a sum of Kerr contributions $s_w^{(i)}$ from the i-th FM layer weighted by the corresponding polar FM layer magnetization $m_z^{(i)}$. This relationship between $s_w^{(\text{tot})}$ and $m_z^{(i)}$ can be written through a **W**-matrix [116]

$$
\begin{bmatrix} s_1^{(\text{tot})} \\ s_2^{(\text{tot})} \\ \vdots \\ s_L^{(\text{tot})} \end{bmatrix} = \begin{bmatrix} s_1^{(1)} & s_1^{(2)} & \cdots & s_1^{(N)} \\ s_2^{(1)} & s_2^{(2)} & \cdots & s_2^{(N)} \\ \vdots & \vdots & \ddots & \vdots \\ s_L^{(1)} & s_L^{(2)} & \cdots & s_L^{(N)} \end{bmatrix} \cdot \begin{bmatrix} m_z^{(1)} \\ m_z^{(2)} \\ \vdots \\ m_z^{(N)} \end{bmatrix}
$$

$$
\boldsymbol{s}^{(\text{tot})} = \mathbf{W} \cdot \boldsymbol{\Upsilon}. \tag{5.20}
$$

Consequently, the FM layer magnetizations $m_z^{(i)}$ can be straightforwardly deduced by inversion (for $L = N$) or pseudo-inversion (for $L > N$) of the **W**-matrix

$$
\boldsymbol{\Upsilon} = \widetilde{\text{inv}}(\mathbf{W}) \cdot \boldsymbol{s}^{(\text{tot})}. \tag{5.21}
$$

The pseudo-inversion of **W** means that the equation (5.20) is solved to minimize the mean square error, i.e. $||\boldsymbol{s}^{(\text{tot})} - \mathbf{W} \cdot \boldsymbol{\Upsilon}||$ [117].

Two principal problems occur in practical implementation of Eq. (5.21):

(i) Under which conditions the inversion or the pseudo-inversion of the **W**-matrix exists? We have to deal with independent experimental conditions $w = 1 \ldots L$, so that the **W**-matrix does not contain linearly dependent columns.

(ii) How to determine $\widetilde{\mathrm{inv}}(\mathbf{W})$ experimentally? In principle, the $\mathbf{W}$-matrix and its inversion or pseudo-inversion can be calculated. But, in practice, the agreement between experiment and theory is not always sufficient.

These two problems are discussed below.

5.8.2   Existence of the $\widetilde{\mathrm{inv}}(\mathbf{W})$ matrix

Considering the complex representation of MOKE in polar coordinates $\Phi_w^{(i)} = \Omega_w^{(i)} \exp[i\xi_w^{(i)}]$, the definition of the Kerr signal $s_w^{(i)} = \Re[\Phi_w^{(i)} \exp(-i\psi_w)] = \Re[\Omega_w^{(i)} \exp(i\xi_w^{(i)} - i\psi_w)]$ [Eq. (2.18)] and of the depth sensitivity function $q_w^{\langle i,1 \rangle} = \Phi_w^{(i)}/\Phi_w^{(1)} = |q_w^{\langle i,1 \rangle}| \exp[i\Delta\xi_w^{\langle i,1 \rangle}]$ [Eq. (5.2)], the components of the $\mathbf{W}$-matrix express as

$$s_w^{(i)} = \Omega_w^{(1)} |q_w^{\langle i,1 \rangle}| \sin(\xi_w^{(1)} + \Delta\xi_w^{\langle i,1 \rangle} - \psi_w). \tag{5.22}$$

Now, let us discuss the conditions under which the $\mathbf{W}$-matrix has linearly independent columns. Because the term $\Omega_w^{(1)}$ is just a multiplicative constant of each $\mathbf{W}$-matrix line, it does not play any role in the following discussion.

In the case of a $(L \times 2)$ $\mathbf{W}$-matrix (for two FM layers), one only needs to have $\psi_1 \neq \psi_2$, or $\xi_1^{(1)} \neq \xi_2^{(1)}$, or $q_1^{\langle i,1 \rangle} \neq q_2^{\langle i,1 \rangle}$. This is a sufficient condition for the existence of $\widetilde{\mathrm{inv}}(\mathbf{W})$.

In the case of a $(L \times N)$ $\mathbf{W}$-matrix; $N \geq 3$ (for three or more FM layers), the conditions of existence of $\widetilde{\mathrm{inv}}(\mathbf{W})$ are not as straightforward as in the previous case and it is shown that the depth sensitivity function q has to vary with some parameters. Let us consider first the case of L experimental configurations ($L \geq N$), which differ only by the projection angle $\psi_k \neq \psi_l$, ($k \neq l$) or by the Kerr phase of the first FM layer $\xi_k^{(1)} \neq \xi_l^{(1)}$, *keeping* the depth sensitivity function $q_l^{\langle i,1 \rangle} = q_k^{\langle i,1 \rangle} = |q^{\langle i,j \rangle}| \exp[i\Delta\xi^{\langle i,1 \rangle}]$ constant. Then, the $\widetilde{\mathrm{inv}}(X)$ is only possible if the matrix with components

$$\hat{s}_w^{(i)} = |q^{\langle i,1 \rangle}| \sin(\xi_w^{(1)} + \Delta\xi^{\langle i,1 \rangle} - \psi_w) \tag{5.23}$$

has linearly independent columns. Because the components ψ_w, $\xi_w^{(1)}$ are the same for all terms in each line, and terms $|q^{\langle i,1 \rangle}|$, $\Delta\xi^{\langle i,1 \rangle}$ are the same for all terms in each column, it can be shown that such a matrix (and consequently the $\mathbf{W}$-matrix) has *always* linearly dependent columns.

Consequently, in the case of three or more FM layers, to select Kerr signals coming from each FM layer, it is not sufficient to perform MO experiments at different projection angles ψ_w. All Kerr vectors have to change independently, which is a situation that is not fulfilled when $\Omega_w^{(1)}$, $\xi_w^{(1)}$ are varied while keeping $q_w^{\langle i,1 \rangle}$ constant. Hence, it is necessary to choose experimental conditions giving different depth sensitivity function $q_w^{\langle i,1 \rangle}$. In conclusion, for $N \geq 3$, different Kerr signals s_w have to be measured at several photon energies or incidence angles, otherwise the $\mathbf{W}$-matrix has linearly dependent columns.

5.8.3   Inversion of the W-matrix

In this subsection we discuss how the Eq. (5.20), $\boldsymbol{s}^{(\mathrm{tot})} = \mathbf{W} \cdot \boldsymbol{\Upsilon}$, can be solved if the elements of the $\mathbf{W}$-matrix are not *a-priori* known. In other words, we wish to find how to tune the linear combination of several $s_w^{(\mathrm{tot})}$ to obtain a Kerr signal $s^{(i)}$ providing information about the magnetization state of a single FM layer in the multilayer structure. In principle,

the $\widetilde{\mathrm{inv}}(\mathbf{W})$ can be calculated theoretically, but due to the inaccuracy of optical and MO parameters, layer thicknesses and additional interface contributions, it can happen that the reliability of these calculations is not good enough.

The key idea of $\widetilde{\mathrm{inv}}(\mathbf{W})$ tuning is a generalization of the numerical projection method introduced earlier for a two FM layers structure [Eq. (5.17)]: $s^{(\bar{i})} = s_1 \cos \psi^{(\bar{i})} + s_2 \sin \psi^{(\bar{i})}$, where s_1, s_2 are two different Kerr signals determined experimentally. For a given tuned projection angle $\psi^{(\bar{i})}$, one cancels the Kerr signal due to the i-th FM layer, and consequently $s^{(\bar{i})}$ measures only the magnetization of the second FM layer. Applying this algorithm recursively, one can successively cancel the Kerr signal from other FM layers. From an algebraic point of view, this algorithm is similar to the Gaussian elimination method.

This tuning procedure, based on successive cancellation of signals from all layers in the multilayer structure, except for one, requires the knowledge of at least the approximate shape of hysteresis loops for individual layers. It is necessary to decide whether the observed hysteresis loop is a superposition of many contributions. This is quite easy in the simple case of square hysteresis loops with different coercive fields. If the tuning procedure cannot be performed, the $\widetilde{\mathrm{inv}}(\mathbf{W})$ matrix should be calculated theoretically with carefully selected optical and MO parameters for all layers. Combination of both methods is possible as well: approximate values of projection angles can be calculated through Eq. (5.28) from the $\mathbf{W}$-matrix, and smoothly tuned afterwards.

As an example of tuning procedure, let us take a three-FM-layers structure, on which three different Kerr signals $s_1^{(\mathrm{tot})}$, $s_2^{(\mathrm{tot})}$, $s_3^{(\mathrm{tot})}$ are measured. These Kerr signals $s_i^{(\mathrm{tot})}$ are superposition of different Kerr contributions originating from all three FM layers. As an example, let us show how to separate Kerr contributions originating only from the first and the second FM layer. Two independent projections between $s_1^{(\mathrm{tot})}$, $s_2^{(\mathrm{tot})}$ and between $s_1^{(\mathrm{tot})}$ and $s_3^{(\mathrm{tot})}$ can cancel the Kerr contribution coming from the third FM layer

$$s_{1,2}^{(\bar{3})} = s_1^{(\mathrm{tot})} \cos \psi_{1,2}^{(\bar{3})} + s_2^{(\mathrm{tot})} \sin \psi_{1,2}^{(\bar{3})} \tag{5.24}$$

$$s_{1,3}^{(\bar{3})} = s_1^{(\mathrm{tot})} \cos \psi_{1,3}^{(\bar{3})} + s_3^{(\mathrm{tot})} \sin \psi_{1,3}^{(\bar{3})}, \tag{5.25}$$

and thus the Kerr signals $s_{1,2}^{(\bar{3})}$ and $s_{1,3}^{(\bar{3})}$ are different and depend only on effects coming from the first and the second FM layers. Then, we can apply again the projection procedure to separate Kerr signals coming from the first or second FM layer

$$s^{(1)} = s_{1,2}^{(\bar{3})} \cos \psi^{(1,\bar{3})} + s_{1,3}^{(\bar{3})} \sin \psi^{(1,\bar{3})} \tag{5.26}$$

$$s^{(2)} = s_{1,2}^{(\bar{3})} \cos \psi^{(2,\bar{3})} + s_{1,3}^{(\bar{3})} \sin \psi^{(2,\bar{3})}. \tag{5.27}$$

Hence, in a system composed of three FM layers ($N = 3$, $L = 3$), to be selective to only one FM layer, one has to tune subsequently three projection angles ψ. To deduce MOKE hysteresis loops of all three FM layers, seven projection angles have to be tuned. Similarly, for four FM layers ($N = 4$, $L = 4$), six projection angles have to be tuned to separate the Kerr signal coming from one FM layer. For separating MOKE hysteresis loops of all four FM layers, 16 projection angles are required.

If the Kerr signal values originating from the i-th FM layer, $s_1^{(i)}$, $s_2^{(i)}$ are known, the

projection angle $\psi_{1,2}^{(\bar{i})}$, which cancels the Kerr signal of the i-th FM layer is [Eq. (5.17)]

$$\tan \psi_{1,2}^{(\bar{i})} = -\frac{s_1^{(i)}}{s_2^{(i)}}. \tag{5.28}$$

When values of $s_w^{(i)}$ are known, but not with sufficient accuracy, the derived values of $\psi^{(\bar{i})}$ can be used as starting points for the projection tuning.

5.8.4   Application to the $(Au/Co)_3$ film structure

The "Cascade numerical projection" method allows to separate the Kerr signals originating from each FM layer through linear combinations of several experimental Kerr measurements, each consisting of a sum of contributions issued from the different FM layers. It is based on subsequent (i.e. cascade) numerical Kerr signals cancellation from arbitrary FM layer, up to obtain a Kerr signal only related to the considered FM layer.

This technique has been applied here to the Au(5nm)/Co(0.6nm)/Au(5nm)/Co(1nm)/Au(5nm)/Co(1.4nm)/Au(24nm)/glass multilayer [Fig. 5.6(c)] which was already studied in Section 5.5.2. The sample preparation and characterization are described in Section 4.4. All Co layers display perpendicular magnetic anisotropy and provide square PMOKE hysteresis loops. Since the Co layer thickness varies from layer to layer in this structure, the associated coercive field decreases when increasing the thickness [107, 81].

As it has been discussed in Section 5.8.2, Kerr signals have to be measured at least for two different values of the depth sensitivity function q_w. So, we measured both Kerr rotation and ellipticity hysteresis loops at two photon energies 2.5 eV and 3.8 eV. p-PMOKE measurements are performed at nearly normal incidence ($\varphi = 7°$), and the measured loops are presented on the left side of Fig. 5.19. The shown loop at 2.5 eV is measured for a projection angle $\psi = 33°$, but the particular value of this projection angle has no special meaning.

Each experimental loop is due to contributions of all three Co layers, resulting in three step loops. For a given linear combination, weighted by projection angle ψ, of the two original loops s_1 and s_2, one can cancel out the contribution from a given Co layer: $s = s_1 \cos \psi + s_2 \sin \psi$. Then, the resulting signal s depends on the magnetization state of only two Co layers. The projection angle ψ can be determined just by tuning it up to remove the Kerr signal coming from the targeted Co layer. By this first projection one gets two hysteresis loop curves depending only on Kerr contributions coming from the 1-st and 3-rd Co layer and two from the 1-st and 2-nd Co layer (Fig. 5.19).

After this first projection, one obtains pairs of *different* MOKE hysteresis loops both depending, for example, on magnetization of the 1-st and the 3-rd Co layer. Hence, the subsequent second projection can cancel out the Kerr signal coming from one more Co layer and the Kerr signal originating from only one Co layer may be separated (Fig. 5.19). Thus, we succeeded to separate Kerr signals coming from each FM layer.

Let us comment on the reduction of the Signal to Noise Ratio (SNR) at each projection stage. The noise amplitude of the projected Kerr signal is determined by the sum of the noise corresponding to each hysteresis loop. On the other hand, for each projection, the amplitude of the Kerr signal itself is decreased. After the first projection, shown in Fig. 5.19, the SNR is reduced by a factor $2\sqrt{2}$. After the second projection, the SNR is
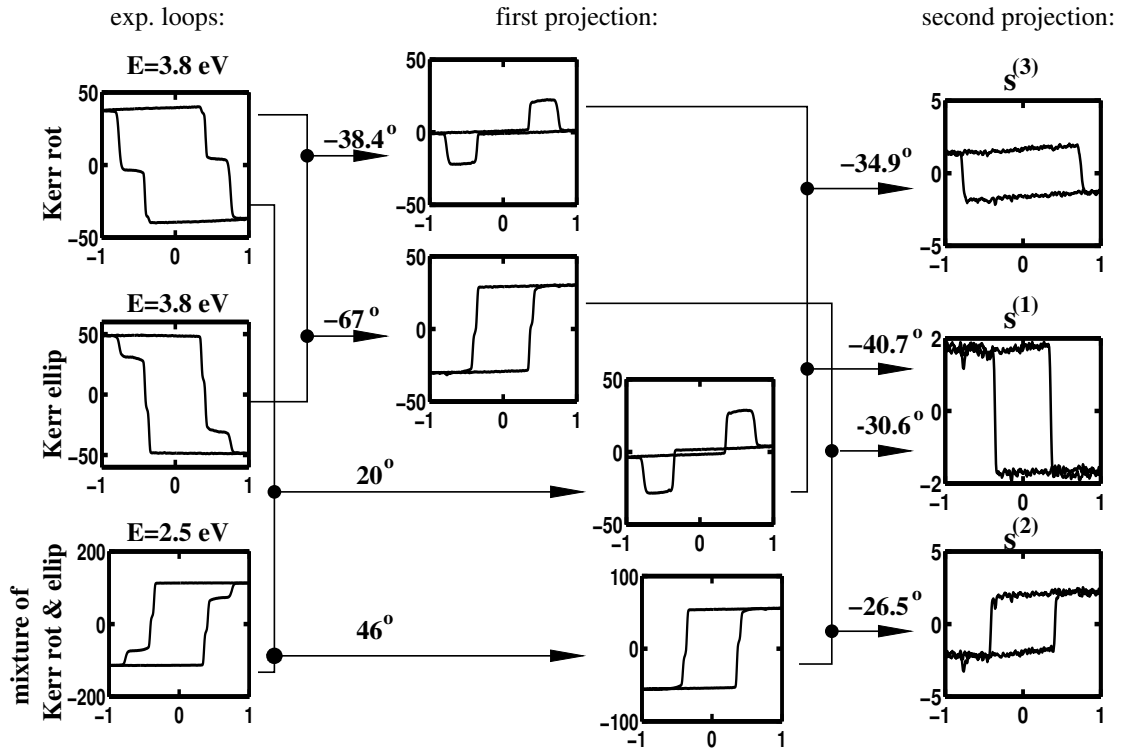
Figure 5.19: Demonstration of the "Cascade numerical projection" procedure for the $(Au/Co)_3$ sample. The three experimental PMOKE hysteresis loops on the left side depend on the magnetization state of all three Co layers. By two subsequent projections with angles ψ, the Kerr signal depending on the magnetization state of only one Co layer is separated. The projection angle ψ values used for linear combination of given pair of hysteresis loops are given for each stage. The Kerr signal and external magnetic field units are mdeg and kOe, respectively.

reduced again approximately by a factor $10\sqrt{2}$. This large decrease of the SNR at this second stage is due to the close-to-one value of the depth sensitivity q. We estimate, that the furthercoming projection will decrease the SNR approximately by a factor 5 to 10. The reduction of SNR at each projection stage is obviously more significant for thinner spacer layer. The SNR decreasing rate with the number of projection stages depends upon the linear independence of columns in the **W**-matrix [Eq. (5.20)], which is determined by the change of the depth sensitivity function q_w corresponding to particular experimental conditions w.

5.9 Possible applications: volume MO recording for four storage layers

The question raised here is: how to realize a convenient four-storage-layer magneto-optical perpendicular recording media by thin film engineering? The properties of depth-sensitive MO readout from the $(FM/non\text{-}FM)_4$ proposed structure are the following:

(i) the MO readout can be done at a single photon energy,

(ii) each FM layer is perpendicularly magnetized and exhibits a polar square hysteresis loop.

(iii) the PMOKE rotation signal carries information about the magnetization state of two FM layers and PMOKE ellipticity gives information about the magnetization state of the two remaining FM layers.

(iv) the magnetization states of each pair of two FM layers are distinguished by the so-called four level MO readout procedure [116, 114]. This means that FM layers provide Kerr signals with different amplitudes and, consequently, for two opposite magnetization states in each FM layer, four Kerr signal levels are measured.
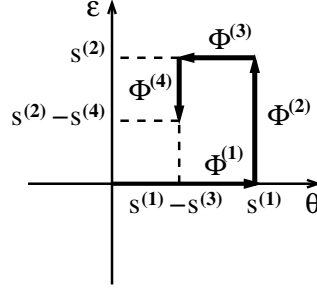
Figure 5.20: Kerr vector configuration used for volume MO readout with four FM recording layers. See Section 5.9 for details.

These conditions may be fulfilled if the four FM layers lead to the following Kerr vector configuration (see Fig. 5.20):

(i) Kerr vectors $\Phi^{(1)}$, $\Phi^{(3)}$ are parallel to the Kerr rotation axis θ, and $\Phi^{(2)}$, $\Phi^{(4)}$ are parallel to the Kerr ellipticity axis ϵ.

(ii) For each pair of parallel Kerr vectors, one of them must be about twice larger than the other $(\Omega^{(1)}/\Omega^{(3)} \approx 2, \Omega^{(2)}/\Omega^{(4)} \approx 2)$.

Thus, the PMOKE rotation (ellipticity) measurements provide four possible levels

$$
\begin{aligned}
\theta &= \Omega^{(1)} m_z^{(1)} + \Omega^{(3)} m_z^{(3)} = \{-\Omega^{(1)} - \Omega^{(3)}, -\Omega^{(1)} + \Omega^{(3)}, \Omega^{(1)} - \Omega^{(3)}, \Omega^{(1)} + \Omega^{(3)}\} \\
\epsilon &= \Omega^{(2)} m_z^{(2)} + \Omega^{(4)} m_z^{(4)} = \{-\Omega^{(2)} - \Omega^{(4)}, -\Omega^{(2)} + \Omega^{(4)}, \Omega^{(2)} - \Omega^{(4)}, \Omega^{(2)} + \Omega^{(4)}\},
\end{aligned}
\tag{5.29}
$$

so that the magnetization state of each FM layer can be determined.

In conclusion, readout of both PMOKE rotation and PMOKE ellipticity at a *single* photon energy gives access to the magnetization state of all *four* buried FM layers in conveniently engineered structures. This solution combines the advantages of readout by both Kerr rotation and ellipticity [116] and four level MO readout [114].

5.10   Conclusion of Chapter 5

In this Chapter, I propose solutions to determine the magnetization state of each FM layer in a multilayer structure by MOKE.

Firstly, the variation between MOKE contributions originating from FM layers located at different depths is described by the sensitivity function q. This function is expressed analytically and advantageously presented in the complex $\theta\epsilon$-plane.

Then, I show, both theoretically and experimentally on simple model systems, how to straightforwardly determine the in-depth location of a FM layer, if the saturated MOKE is known for each FM layer. A consistent approach is developed, providing the separation of Kerr signals coming from each FM layer in a FM bilayer structure, by varying either the photon energy, the incidence angle or the compensator phase shift. I show how to separate polar, longitudinal and transverse components of the magnetization, in order to handle in-depth magnetometry measurements of all the three magnetization components.

To be selective to the magnetization state of each FM layer, I propose and demonstrate the power of two new approaches: the "Parallel Kerr vectors" and "Cascade numerical projection" methods. The "Parallel Kerr vectors" method is based on the tuning of some parameters (for example the photon energy and the compensator phase shift). On the other hand, the "Cascade numerical projection" method allows to separate Kerr signals originating from each individual FM layer by means of well chosen linear combinations of MOKE hysteresis loops measured in different experimental conditions. For that purpose it is shown that MOKE hysteresis loops have to be measured for, at least, two different photon energies.

Each method has been satisfactorily checked experimentally on Co/Au, TbFe/Si$_3$O$_4$ multilayer structures and on double tunnel junction involving diluted FM semiconductors.

Finally, I propose a suitable Kerr vectors configuration that can be realized in an engineered film structure for providing a volume magneto-optical reading solution in four storage layers.

". . . Quand l'oiseau arrive
s'il arrive
observer le plus profond silence
attendre que l'oiseau entre dans la cage
et quand il est entré
fermer doucement la porte avec le pinceau
puis
effacer un à un tous les barreaux
en ayant soin de ne toucher aucune des plumes de l'oiseau . . ."

Chapter 6

Vicinal Induced Surface Magneto-Optical Kerr Effect (VISMOKE)

In this Chapter, I analytically derive and experimentally evidence a novel Magneto-optical Kerr effect for an ultrathin FM layer deposited on a vicinal surface. We call it Vicinal-Induced Surface Magneto-Optical Kerr Effect (VISMOKE).

Vicinal surfaces attract physicists, either as a template to fabricate self-organized structures [118, 119, 120], or as a way to well control the magnetic anisotropy of FM films grown on them, e.g. by varying the miscut angle [121, 122]. Vicinal interfaces can also be used to drive non-isotropic magnetic domain wall propagation [123].

I show that VISMOKE originates from both magnetic and structural perturbations, the later being induced by the low-symmetry of the interface. Such a situation prevails, for example, for FM layers deposited on a vicinal single crystal surface. Since MOKE is often used to investigate thin-film magnetism, VISMOKE will be of prime importance for future investigations of vicinal structures. VISMOKE is found to be linear with in-plane magnetization. Contrarily to PMOKE and LMOKE, VISMOKE is present in a transverse field at zero angle of incidence ($\varphi = 0$), whereas no linear MOKE was expected in this MO configuration. Note that, this effect was recently predicted by A.V. Petukhov et al. [124] for low symmetry interfaces and qualitatively mentioned for vicinal interfaces.

Here, we have experimentally evidenced and studied VISMOKE and differential reflectivity on a system consisting of an ultrathin Co layer deposited on a Au(322) vicinal surface. Furthermore, I have developed a phenomenological electromagnetic model to explain VISMOKE originating from modified boundary conditions at the vicinal interface.

This work has been done in the frame of a collaboration with the team "Nanostructures et Microscopie à Effet Tunnel" (S. Rousset) of the "Groupe de Physique des Solides" of the University Paris VII. Experimental results presented here have been obtained by G. Baudot during his Ph.D. A large part of the results presented in this Chapter is under publication (J. Hamrle *et al.* [125]).

6.1 MOKE theory for FM layers deposited on vicinal surfaces

6.1.1 Used Cartesian referential

As far as the studied samples are not invariant upon rotation around the sample normal $\hat{z}$, we must use two Cartesian referentials, that for light $(\hat{x}, \hat{y}, \hat{z})$ and that associated to the sample $(\hat{X}, \hat{Y}, \hat{z})$, as shown on Figure 6.1. For the light referential $(\hat{x}, \hat{y}, \hat{z})$, in agreement with Appendix A, $\hat{y}\hat{z}$ defines the plane of incidence and $\hat{z}$ is the sample normal. In the sample referential, $(\hat{X}, \hat{Y}, \hat{z})$, $\hat{X}$ is perpendicular to the step edges, and thus the $\hat{X}\hat{z}$ plane is the only mirror plane of the vicinal interface. When rotating the sample around $\hat{z}$, the rotation of vicinal steps with respect to the light referential is determined by the angle $\alpha = (\hat{x}, \hat{X})$. The direction of the sample magnetization is given by the angles β, γ in the *light* referential [see Fig. 6.1(c)], so that the normalized magnetization is $\boldsymbol{m} = [\cos\gamma\cos\beta, \cos\gamma\sin\beta, \sin\gamma]$.
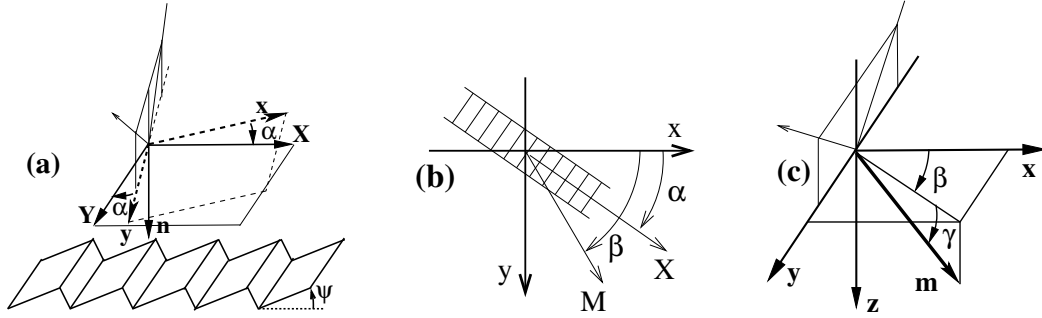
Figure 6.1: Definition of light $(\hat{x}, \hat{y}, \hat{z})$ and sample $(\hat{X}, \hat{Y}, \hat{z})$ Cartesian systems. The $\hat{y}\hat{z}$-plane is the plane of incidence. α is the sample rotation angle around the $\hat{z}$-axis referenced with respect to $\hat{x}$. The direction of the normalized magnetization $\boldsymbol{m}$ is determined by the angles β and γ in the *light* referential.

6.1.2 Permittivity tensor of the FM layer near the vicinal interface

The optical and magneto-optical properties of a FM layer deposited on a low-symmetry surface are described by a permittivity tensor $\boldsymbol{\varepsilon}$, which can be decomposed into a structural part $\boldsymbol{\varepsilon}_{\mathrm{str}}$, due to the broken structural symmetry, and in a magnetic part $\boldsymbol{\varepsilon}_{\mathrm{mag}}$, induced by the FM layer magnetization.

Structural part of the permittivity tensor: Later it will be shown that a media exhibiting VISMOKE has to provide non-zero off-diagonal permittivity elements (ε_{xz}, ε_{zy}, ε_{yz} or ε_{zx}) associated with a *structural* symmetry breaking. As follows from Onsager relations of reciprocity [17, 38, 126], the permittivity tensor is always symmetric, so that $\varepsilon_{ij} = \varepsilon_{ji}$ in the absence of any external magnetic field. Consequently, from symmetry arguments [38], the media must belong to the following point symmetry groups[1] 1, $\bar{1}$, 2, $\bar{2}$, $2/m$, to provide non-zero off-diagonal permittivity coefficients, and hence VISMOKE. The only possible symmetry operations are *one* mirror plane and inversion.

In the close vicinity of the vicinal interface the medium has a symmetry m, and in the bulk of the layer, a "vicinal bulk" symmetry $2/m$. Thus, for $\alpha = 0$, i.e. $\hat{x} \parallel \hat{X}$ (Figure 6.1),

---

[1]The overbar indicates the existence of inversion.

the structural part of the permittivity tensor near the vicinal interface has the form

$$\boldsymbol{\varepsilon}_{\mathrm{str}}(\alpha=0) = \begin{bmatrix} \varepsilon_{xx} & 0 & \varepsilon_s \\ 0 & \varepsilon_{yy} & 0 \\ \varepsilon_s & 0 & \varepsilon_{zz} \end{bmatrix}. \tag{6.1}$$

The off-diagonal structural perturbation ε_s is non-zero only in the vicinity of the vicinal interface, i.e. over a *memory depth* t_s, which is, in general, smaller than the thickness of the FM layer thickness $t^{(\mathrm{fm})}$.

When rotating the sample by an angle α around the $\hat{z}$-axis, $\boldsymbol{\varepsilon}_{\mathrm{str}}(\alpha)$ takes the form

$$\boldsymbol{\varepsilon}_{\mathrm{str}}(\alpha) = (\mathbf{R}_\alpha)^{-1}\boldsymbol{\varepsilon}_{\mathrm{str}}(\alpha=0)\mathbf{R}_\alpha = \begin{bmatrix} \varepsilon_{11}\cos^2\alpha + \varepsilon_{22}\sin^2\alpha & \frac{1}{2}(\varepsilon_{11}-\varepsilon_{22})\sin 2\alpha & \varepsilon_s\cos\alpha \\ \frac{1}{2}(\varepsilon_{11}-\varepsilon_{22})\sin 2\alpha & \varepsilon_{22}\cos^2\alpha + \varepsilon_{11}\sin^2\alpha & \varepsilon_s\sin\alpha \\ \varepsilon_s\cos\alpha & \varepsilon_s\sin\alpha & \varepsilon_{33} \end{bmatrix}, \tag{6.2}$$

where $\mathbf{R}_\alpha$ is the associated rotation matrix

$$\mathbf{R}_\alpha = \begin{bmatrix} \cos\alpha & \sin\alpha & 0 \\ -\sin\alpha & \cos\alpha & 0 \\ 0 & 0 & 1 \end{bmatrix}. \tag{6.3}$$

Magnetic part of the permittivity tensor: Considering $\boldsymbol{m} = [\cos\gamma\cos\beta, \cos\gamma\sin\beta, \sin\gamma]$ [Figure 6.1(c)], the magnetic part of the permittivity tensor has the form [see Eq. (3.45)]

$$\boldsymbol{\varepsilon}_{\mathrm{mag}} = \begin{bmatrix} 0 & \varepsilon_m\sin\gamma & -\varepsilon_m\cos\gamma\sin\beta \\ -\varepsilon_m\sin\gamma & 0 & \varepsilon_m\cos\gamma\cos\beta \\ \varepsilon_m\cos\gamma\cos\beta & -\varepsilon_m\cos\gamma\cos\beta & 0 \end{bmatrix}. \tag{6.4}$$

This form is only valid for isotropic, cubic or hexagonal materials. Although the medium near a vicinal interface has a lower symmetry, we suppose that both structural and magnetic perturbations are small and independent from each other. Thus, we assume that the magnetic part of the permittivity tensor is the same as for an isotropic material, as described by Equation (6.4).

Permittivity tensor of the FM layer at a vicinal interface: If both structural and magnetic perturbations are small, the permittivity tensor $\boldsymbol{\varepsilon}$ in the vicinity of the FM interface, i.e. over a thickness t_s, is determined by the sum of structural [Eq. (6.2)] and magnetic contributions [Eq. (6.4)],

$$\boldsymbol{\varepsilon} = \boldsymbol{\varepsilon}_{\mathrm{str}} + \boldsymbol{\varepsilon}_{\mathrm{mag}}. \tag{6.5}$$

All components of the resulting permittivity tensor $\boldsymbol{\varepsilon}$, in the most general case, are reported on Table 6.1. There are two kinds of the off-diagonal structural elements. It will be shown [Eq. (6.6)] that VISMOKE arises only from the off-diagonal element ε_s, which is present only in systems having a very low symmetry (one mirror plane). Other off-diagonal structural elements, $\varepsilon_{xy} = \varepsilon_{yx} = (1/2)(\varepsilon_{xx} - \varepsilon_{yy})\sin 2\alpha$ arise only from the non-equality between diagonal permittivity elements, when rotating the sample around $\hat{z}$ and they do not give rise to VISMOKE.

	structural contribution $\varepsilon_{\mathrm{str}}$ [over a thickness t_s]	magnetic contribution $\boldsymbol{\varepsilon}_{\mathrm{mag}}$ [over a thickness $t^{(\mathrm{fm})}$]
ε_{xx}; $\begin{pmatrix} \bullet & \cdot & \cdot \\ \cdot & \cdot & \cdot \\ \cdot & \cdot & \cdot \end{pmatrix}$	$\varepsilon_{xx}\cos^2\alpha + \varepsilon_{yy}\sin^2\alpha$	0
ε_{yy}; $\begin{pmatrix} \cdot & \cdot & \cdot \\ \cdot & \bullet & \cdot \\ \cdot & \cdot & \cdot \end{pmatrix}$	$\varepsilon_{yy}\cos^2\alpha + \varepsilon_{xx}\sin^2\alpha$	0
ε_{zz}; $\begin{pmatrix} \cdot & \cdot & \cdot \\ \cdot & \cdot & \cdot \\ \cdot & \cdot & \bullet \end{pmatrix}$	ε_{zz}	0
ε_{xy}; $\begin{pmatrix} \cdot & \bullet & \cdot \\ \cdot & \cdot & \cdot \\ \cdot & \cdot & \cdot \end{pmatrix}$	$\frac{1}{2}(\varepsilon_{xx}-\varepsilon_{yy})\sin 2\alpha$	$\varepsilon_m \sin\gamma$
ε_{yx}; $\begin{pmatrix} \cdot & \cdot & \cdot \\ \bullet & \cdot & \cdot \\ \cdot & \cdot & \cdot \end{pmatrix}$	$\frac{1}{2}(\varepsilon_{xx}-\varepsilon_{yy})\sin 2\alpha$	$-\varepsilon_m \sin\gamma$
ε_{xz}; $\begin{pmatrix} \cdot & \cdot & \bullet \\ \cdot & \cdot & \cdot \\ \cdot & \cdot & \cdot \end{pmatrix}$	$\varepsilon_s \cos\alpha$	$-\varepsilon_m \cos\gamma\sin\beta$
ε_{zx}; $\begin{pmatrix} \cdot & \cdot & \cdot \\ \cdot & \cdot & \cdot \\ \bullet & \cdot & \cdot \end{pmatrix}$	$\varepsilon_s \cos\alpha$	$\varepsilon_m \cos\gamma\sin\beta$
ε_{yz}; $\begin{pmatrix} \cdot & \cdot & \cdot \\ \cdot & \cdot & \bullet \\ \cdot & \cdot & \cdot \end{pmatrix}$	$\varepsilon_s \sin\alpha$	$\varepsilon_m \cos\gamma\cos\beta$
ε_{zy}; $\begin{pmatrix} \cdot & \cdot & \cdot \\ \cdot & \cdot & \cdot \\ \cdot & \bullet & \cdot \end{pmatrix}$	$\varepsilon_s \sin\alpha$	$-\varepsilon_m \cos\gamma\cos\beta$

Table 6.1: Permittivity tensor $\boldsymbol{\varepsilon}$ elements for a magnetized layer deposited on a vicinal surface for a sample rotation α and a magnetization orientation defined by β and γ angles (Figure 6.1).

6.1.3 MO response from a magnetized vicinal interface

The MO response of an ultrathin FM layer of thickness $t^{(\text{fm})}$ sandwiched between an infinite buffer and an overlayer has been determined in Section 3.3.2 for the most general permittivity tensor form of the FM layer. More precisely, this permittivity tensor [Eq. (3.38)] is assumed to have arbitrary off-diagonal elements, but all diagonal elements are supposed to be the same, $\varepsilon_{xx} = \varepsilon_{yy} = \varepsilon_{zz} = \varepsilon_0^{(\text{fm})}$. The s or p-MOKE originating from such an ultrathin FM layer is [Eq. (3.42)]

$$
\begin{aligned}
\Phi_{\mathsf{s}} &\equiv -\frac{r_{\mathsf{ps}}}{r_{\mathsf{ss}}} = \chi\, Q\, V_{\mathsf{s}}\, t^{(\text{fm})} \left(i\varepsilon_{yx} \frac{N_z^{(\text{nf})}}{N^{(\text{nf})}} + \frac{iN_y N^{(\text{nf})}\varepsilon_{zx}}{\varepsilon_0^{(\text{fm})}} - i\frac{\varepsilon_{zx}\varepsilon_{yz}N_z^{(\text{nf})}}{\varepsilon_0^{(\text{fm})} N^{(\text{nf})}} \right) \\
\Phi_{\mathsf{p}} &\equiv \frac{r_{\mathsf{sp}}}{r_{\mathsf{pp}}} = \chi\, Q\, V_{\mathsf{p}}\, t^{(\text{fm})} \left(-i\varepsilon_{xy} \frac{N_z^{(\text{nf})}}{N^{(\text{nf})}} + \frac{iN_y N^{(\text{nf})}\varepsilon_{xz}}{\varepsilon_0^{(\text{fm})}} + i\frac{\varepsilon_{xz}\varepsilon_{zy}N_z^{(\text{nf})}}{\varepsilon_0^{(\text{fm})} N^{(\text{nf})}} \right).
\end{aligned}
\tag{6.6}
$$

Recall that the first and second terms of Eq. (6.6) represent the generalized PMOKE, LMOKE contributions to the measured MOKE. The third term gives rise to VISMOKE.

We consider the permittivity tensor form near a vicinal interface, as given in Table 6.1. Recall that the structural off-diagonal permittivity element ε_s is assumed to be efficient only over a memory depth t_s, but the magnetic off-diagonal permittivity element ε_m is constant over the full FM layer thickness $t^{(\text{fm})}$ (see Section 6.1.2).

Then, we find that s or p-MOKE depend on of different contributions reported in Table 6.2.

		normalized s-MOKE $\dfrac{\Phi_{\mathsf{s}}}{\chi V_{\mathsf{s}} Q}$	normalized p-MOKE $\dfrac{\Phi_{\mathsf{p}}}{\chi V_{\mathsf{p}} Q}$
magnetic	PMOKE	$-\mathsf{A}\, t^{(\text{fm})} \varepsilon_m \sin\gamma$	$-\mathsf{A}\, t^{(\text{fm})} \varepsilon_m \sin\gamma$
	VISMOKE	$-\mathsf{A}\, t_s \dfrac{\varepsilon_s \varepsilon_m}{\varepsilon_0^{(\text{fm})}} \cos\gamma \cos(\alpha - \beta)$	$-\mathsf{A}\, t_s \dfrac{\varepsilon_s \varepsilon_m}{\varepsilon_0^{(\text{fm})}} \cos\gamma \cos(\alpha - \beta)$
	LMOKE	$\mathsf{B}\, t^{(\text{fm})} \varepsilon_m \cos\gamma \sin\beta$	$-\mathsf{B}\, t^{(\text{fm})} \varepsilon_m \cos\gamma \sin\beta$
structural	PMOKE	$\mathsf{A}\, t_s \frac{1}{2}(\varepsilon_{xx} - \varepsilon_{yy}) \sin 2\alpha$	$-\mathsf{A}\, t_s \frac{1}{2}(\varepsilon_{xx} - \varepsilon_{yy}) \sin 2\alpha$
	VISMOKE	$-\mathsf{A}\, t_s \dfrac{\varepsilon_s^2}{2\varepsilon_0^{(\text{fm})}} \sin 2\alpha$	$\mathsf{A}\, t_s \dfrac{\varepsilon_s^2}{2\varepsilon_0^{(\text{fm})}} \sin 2\alpha$
	LMOKE	$\mathsf{B}\, t_s \varepsilon_s \cos\alpha$	$\mathsf{B}\, t_s \varepsilon_s \cos\alpha$

Table 6.2: Generalized structural and magnetic contributions to MOKE arising from an ultrathin FM layer deposited on a vicinal surface and capped by an overlayer. The coefficients A and B are defined by Eq. (6.7).

The newly introduced coefficients A, B are defined by

$$\mathsf{A} = \frac{iN_z^{(\mathrm{nf})}}{N^{(\mathrm{nf})}}, \qquad \mathsf{B} = \frac{iN_y N^{(\mathrm{nf})}}{\varepsilon_0^{(\mathrm{fm})}}. \tag{6.7}$$

The coefficients χ, $V_{\mathrm{s/p}}$, Q describe the influence of the infinite buffer, the angle of the incidence and the overlayer, respectively. These coefficients are already defined and discussed in Section 3.3.2. We distinguish "structural" and "magnetic" contributions, depending or not on the FM layer magnetization. The second order magnetic contributions, proportional to ε_m^2, are neglected.

Here, we do not discuss in detail the structural (i.e. non-magnetic) contributions to MOKE, described in Table 6.2. Their determination can be useful if we wish to measure directly ε_s by sample rotation α. However, in Section 6.3 we have used a more accurate approach to determine the value of ε_s from reflectivity measurements.

Some comments concerning the magnetic terms in Table. 6.2 have to be addressed and will be useful later.

- The contributions called "magnetic PMOKE" and "magnetic LMOKE" are nothing more than the classical PMOKE and LMOKE.

- The new "magnetic VISMOKE" originates from both the structural ε_s and magnetic ε_m off-diagonal permittivities. Later we call this effect simply "VISMOKE".

- Both (magnetic) PMOKE and VISMOKE are present at normal incidence ($\varphi = 0$) and have the same dependence on φ. Thus, the separation between these two contributions can only be obtained from sample rotation α around its normal axis (see Table 6.2).

- The (magnetic) VISMOKE varies as $\cos(\alpha - \beta)$. Thus,

  (i) it is zero for $\alpha - \beta = \pm\pi/2$, i.e. when the magnetization is parallel to vicinal steps. As shown later, this is an easy magnetization axis for the Co/Au(322) system. Thus, in this system, no VISMOKE is expected at remnant state.

  (ii) for a fixed magnetization orientation with respect to the light referential (β, γ fixed), the VISMOKE has a periodicity 2π when rotating the sample around the normal film axis ($\hat{z}$-axis). This means an inversion of the sign of the VISMOKE for a sample rotation of π, i.e. $\alpha \to \alpha + 180°$.

- The coefficients $V_{\mathrm{s,p}}$, Q and A (and hence PMOKE and VISMOKE) are even function of the incidence angle φ and quasi-constant in the range $\langle -30°; 30° \rangle$. The coefficient B (and hence LMOKE) is odd with φ and varies quasi-linearly with φ in the range $\langle -30°; 30° \rangle$.

6.2 Experimental data for Co deposited on a Au(322) vicinal surface

We have already described the structural and magnetic properties of a non-vicinal Au/Co/Au structure (Section 4.4). For Co layer deposited on a Au(322) vicinal surface, the magnetization reorients continuously from the out-of-plane to the in-plane direction when increasing the Co thickness $t^{(Co)}$ between 2 AL and 5 AL. These results, obtained in the frame of a collaboration between our group and the "Groupe de Physique des Solides" at the University Paris VII, will be discussed in details in the thesis of G. Baudot.

Hence, to study VISMOKE, a Au(7 AL)/Co(5 AL)/Au(322) film structure was selected in order to get a large enough in-plane anisotropy and a negligible remnant out-of-plane component of the magnetization. All MOKE measurements presented in this Chapter are obtained on this Co(5 AL) sample and they were performed with a MO set-up using a photoelastic modulator (Section 2.4.1).

6.2.1 Preparation and structure of Co/Au(322) structure

The Au(322) single crystal studied here is a 2 mm thick disk of 4 mm in diameter, polished to get a mirror-like surface. The surface is prepared in-situ in an ultra-high-vacuum (UHV) chamber, with a base pressure of 3×10^{-11} mbar, by repeated cycles of Ar^+ sputtering at 900 eV and annealing at 800 K. The obtained morphology, shown in Fig. 6.2(a), displays regularly spaced steps with experimental terraces width distribution with an averaged value of 1.2 nm. The purity of the initial surface is checked by Auger Electron Spectroscopy. Intrinsically, the Au(322) vicinal surface is misoriented by an angle $\psi = 11.4°$ from the [111] direction, and is ideally made of 1.17 nm terraces widths. All steps are monoatomic, i.e. 0.235 nm high [118].

(a)   (b)
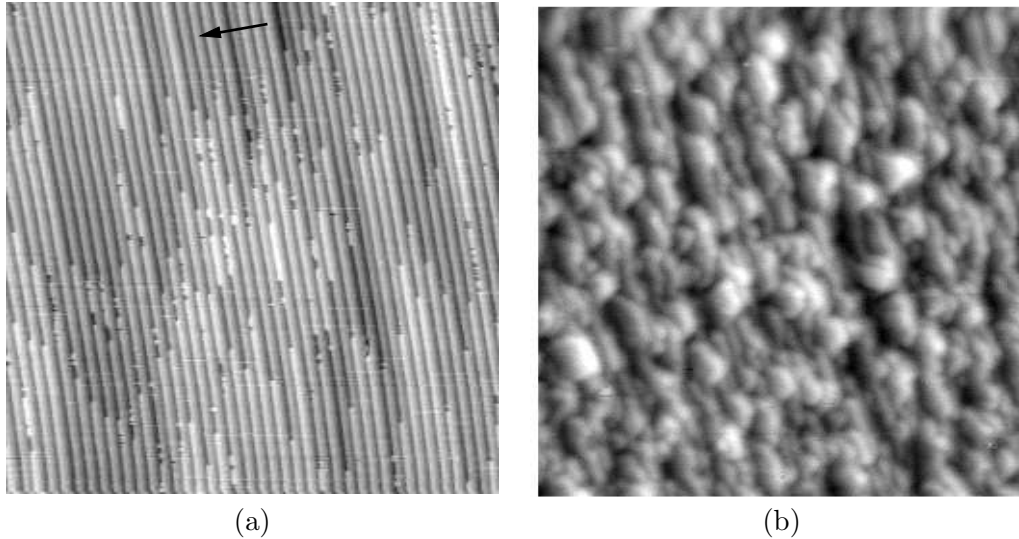
Figure 6.2: STM images (50 nm×50 nm) of (a) a Au(322) vicinal surface (b) a Co(4 AL) layer deposited on this Au(322) surface. The arrow indicates the $[2\bar{1}\bar{1}]$ descending step direction. Both images have the same orientation and were courteously taken from [118].

Cobalt evaporation is done using a 2 mm diameter cobalt rod directly heated by electron bombardment (I_{em}=12 mA, U=900 V). The pressure during the evaporation

is always below 2×10^{-10} mbar. The morphology of the top Co interface is shown on Fig. 6.2(b), evidencing that the Co growth is not pseudomorph on a Au(322) substrate. Although it is still possible to distinguish reminiscence of the vicinal staircase, the Co surface is rough and much more isotropic than the initial Au(322) surface. This is due to the fact that Co does not grow layer-by-layer as it has a larger surface energy than Au. For this reason, we consider only the Co/Au(322) interface as a symmetry breaking source for the VISMOKE calculations. This justifies the introduction of memory depth t_s in Section (6.1.2) and Table 6.2. Finally, the 5 AL Co layer is capped with a 7 AL Au overlayer for ex-situ magneto-optic measurements. The flux rate of the Co and Au deposition is about $\frac{1}{2}$ AL/min and the layer thickness is measured in-situ by a quartz microbalance calibrated by Rutherford Backscattering Spectrometry [118].

6.2.2   PMOKE loops in polar configuration ($H \parallel \hat{z}$)

The Figure 6.3 presents the PMOKE hysteresis loop of the Au(7AL)/Co(5AL)/Au(322) sample measured in polar geometry (i.e. $H \parallel \hat{z}$), at zero angle of incidence ($\varphi = 0$). In this configuration, we only measure PMOKE, i.e. the m_z component of the magnetization. The LMOKE is also zero, because $\varphi = 0$. No VISMOKE is present, because, as shown later, the remnant in-plane magnetization orients along the Au(322) steps (i.e. $\alpha - \beta = \pm\pi/2$).
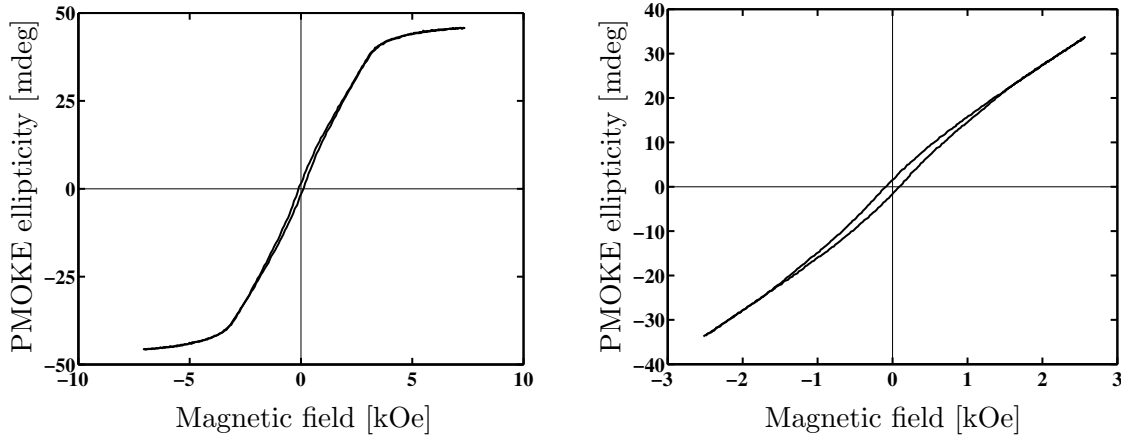
Figure 6.3: PMOKE ($H \parallel \hat{z}$) ellipticity hysteresis loop of the Au(7AL)/Co(5AL)/Au(322) sample measured at 1.95 eV. The left loop shows the full hysteresis loop and the right one the minor loop.

The shape of the PMOKE loop indicates that spins lie nearly in-plane. However, there is a weakly open hysteresis loop with a non-zero value for the remnant state (Fig. 6.3). This means that the easy anisotropy axis is not exactly oriented in-plane, but this slightly tilted away from it by an angle $\gamma_0 = 1.4°$. This value is determined from the ratio of PMOKE in the remnant state and at saturation, which is equal to $\sin\gamma_0$.

6.2.3   MOKE loops in transverse field ($H \parallel \hat{x}$)

Here, we discuss on MOKE hysteresis loops measured in transverse field $H \parallel \hat{x}$. This configuration has not to be confused with the transverse MOKE measuring the variation of the r_{pp} reflection coefficient with m_x, which is zero here for $\varphi = 0$ (see Section 2.2.1).

Transverse means here that the external magnetic field $\boldsymbol{H}$ is applied perpendicularly ($\varphi = 0$) to the light wavevector of the incident and reflected beams.

The MOKE loops for $\varphi = 0$ are presented on Figure 6.4 for a transverse in-plane applied field ($\boldsymbol{H} \parallel \hat{x}$) for several sample rotation angle values α. Figure 6.4 shows that ideal square loops are obtained for $\alpha = \pm 90°$ (i.e. when $\boldsymbol{H} \parallel \hat{Y}$, which is the vicinal step direction). The squareness of these loops clearly demonstrates that the easy magnetic anisotropy axis lies in the step edge direction which corresponds to $\hat{Y}$. These square loops are linked only to PMOKE since both LMOKE ($\varphi = 0$) and VISMOKE ($\beta = 0$ at saturation, and hence $\cos(\alpha - \beta) = 0$) are zero in this configuration (see Table 6.2). For $\alpha = 90°$, the weak observed PMOKE signal arises from a slight out-of-plane tilt of the easy axis by an angle $\gamma_0 = 1.4°$ (see previous Section 6.2.2 and Figure 6.3). As expected, the value of the PMOKE remnant ellipticity (1.1mdeg) in the transverse field configuration corresponds exactly to the tilt angle $\gamma_0 = 1.4°$ determined previously from PMOKE in $\boldsymbol{H} \parallel \hat{z}$ field.
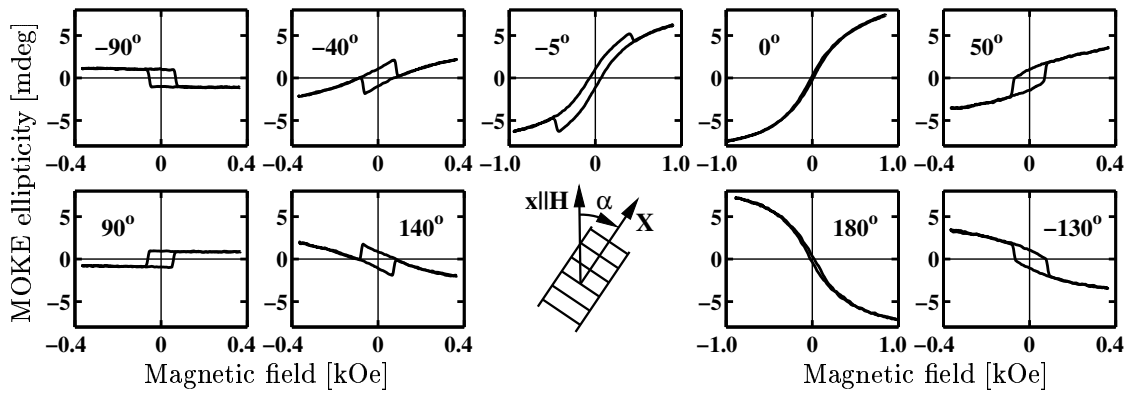
Figure 6.4: MOKE ellipticity hysteresis loops measured on Au(7AL)/Co(5AL)/Au(322) for several sample rotation angles $\alpha = (\hat{x}, \hat{X})$. The measurements were performed at zero angle of incidence, the external magnetic field was applied in the transverse direction ($\boldsymbol{H} \parallel \hat{x}$).
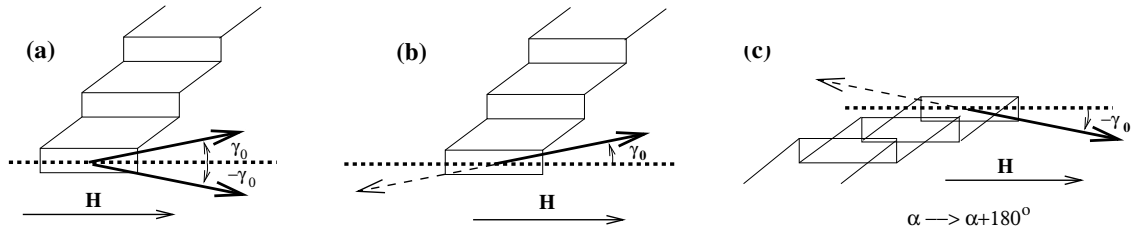
Figure 6.5: (a) Easy magnetization axis directions for a 5 AL thick Co film deposited on a Au(322) a vicinal interface, as follows from a pure mirror symmetry. (b) Experimentally observed unique easy magnetization axis direction, the mirror symmetry has been removed as probably due to atomic 'kinks' on the Au(322) surface (see Fig. 6.2). (c) Same situation as in case (b), but the sample is rotated around $\hat{z}$ by 180°. Thus, if only one easy axis direction is present, a sample rotation $\alpha \to \alpha + 180°$ reverses the magnetization tilt angle (i.e. $\gamma_0 \to -\gamma_0$).

Nevertheless, following symmetry arguments for a pure mirror, the PMOKE in a transversal field is expected to cancel due to the presence of two equivalent anisotropy axes, oriented at $\gamma_0 = \pm 1.4°$ [Figure 6.5(a)]. However, in our case, another small structural perturbation

lifts this degeneracy, making one of the axis preferable [Figure 6.5(b)]. The STM image of the Au(322) vicinal surface (Figure 6.2) shows that the sample is slightly disoriented in azimuth with respect to the $[2\bar{1}\bar{1}]$ direction and therefore it displays atomic kinks always oriented in the same direction. This effect explains such an additional symmetry breaking. The absence of an second easy axis was confirmed by loops measurements, when transversal external magnetic field $\boldsymbol{H}$ is slightly tilted out-of-plane, providing similar hysteresis loops.

The MOKE hysteresis loops, measured in transverse field geometry ($\boldsymbol{H} \parallel \hat{x}$), at $\varphi = 0$ (Figure 6.4), can be decomposed into square and S-shape contributions. The dependence of the amplitudes of the square and S-shape contributions on the rotation angle α are represented on Figure 6.6. Recall that square contribution originates from PMOKE. The PMOKE amplitude at saturation (Fig. 6.6, triangles) does not depend much on the sample rotation α, but it changes sign when α crosses 0 or 180°. This is in agreement with the presence of only one easy anisotropy axis, as shown on Figure 6.5(b) and (c). When the sample is rotated from α to ($\alpha + 180°$) the loop is inverted, i.e. the angle γ_0 changes sign.
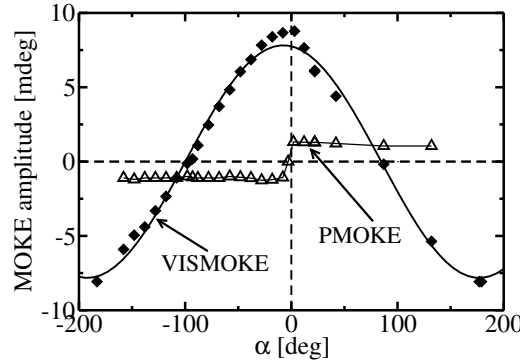
Figure 6.6: Dependence of the **s**-MOKE ellipticity amplitudes of both square loop ($\triangle$) and S-shape ($\blacklozenge$) MOKE contributions on sample rotation α, as determined from hysteresis loops presented on Figure 6.4. The S-shape contribution is fitted by a cosine function.

The second MOKE ellipticity contribution is the S-shape field-induced VISMOKE (Figure 6.6, diamond). It reaches a maximum, far greater then the square loop amplitude when magnetization is perpendicular to the step edges, i.e. for ($\alpha - \beta$) = 0 or 180°. This maximum VISMOKE signal is reached for hysteresis loops measured for $\alpha = 0$ or 180° (Figure 6.4). As predicted theoretically (Table 6.2), for $\beta = 0$, VISMOKE depends on α as $\cos \alpha$. So, the low mirror symmetry of vicinal steps fixes a 2π periodicity for VISMOKE, i.e. it reverses sign when rotating the sample by 180°. To our knowledge, this unusual behaviour has never been experimentally reported for ultrathin FM films grown on a vicinal surface.

Figure 6.7 shows the dependence of the in-plane coercive field H_c of the PMOKE ellipticity (square) signal with the sample rotation α. This gives the main proof that the anisotropy axis lies in the step edge plane. In agreement with the uniaxial anisotropy model [127], the coercive field varies as $H_c = H_{c0}/\sin \alpha$, and thus diverges for $\alpha = 0, 180°$, i.e. when $\boldsymbol{H}$ become perpendicular to step edges. In another words, the model predicts that the projection of the coercive field $\boldsymbol{H}_c$ onto the easy axis direction is kept constant, i.e. $\boldsymbol{H}_c \cdot \hat{Y} = H_{c0}$ =const., $\hat{Y}$ being the easy axis direction.
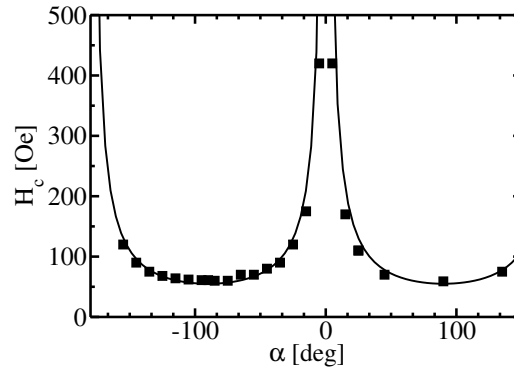
Figure 6.7: Variation of the in-plane coercive field with the sample rotation angle α. The origin $\alpha = 0$ corresponds to $\boldsymbol{H} \parallel \hat{X}$. The full line shows a fit of the data by the $H_c = H_{c0}/|\sin\alpha|$ function, with $H_{c0} = 55$ Oe.

6.2.4 MOKE loop in high transverse field

Here arises the question: Can VISMOKE be confused with a mistakenly measured PMOKE signal? This can be checked for an in-plane magnetically saturated film. Indeed, the out-of-plane component of the magnetization cancels (i.e. $\gamma \to 0$) in large enough in-plane applied field, giving finally no PMOKE contribution. Thus, at normal incidence ($\varphi = 0$) and for $\alpha = 0$ or $180°$, only VISMOKE is expected to survive at saturation. On the other hand, for $\alpha = \pm 90°$, there should be no VISMOKE and PMOKE in high transverse field. Unfortunately, we could not test this idea on the original sample, since it was destroyed before. Thus, in order to perform high field measurements, a new sample was fabricated. For this new Co layer deposited on the same Au(322) vicinal surface, the tilt angle γ_0 was about $3°$.

We measured hysteresis loops up to $2.5\,\mathrm{kOe}$ for $\boldsymbol{H} \parallel \hat{x}$. As expected from the previous discussion, for $\alpha = \pm 90°$, the MOKE ellipticity vanish at high field. For $\alpha = 0$, when increasing the field, the MOKE field-induced curve shows an S-shape at low field, reaches a maximum around $1.2\,\mathrm{kOe}$, and tends to decrease a little at higher field to finally saturate. This loop is presented on Figure 6.8. This final decrease of the MOKE signal in high field comes from the reduction of the small PMOKE component, which tends finally to zero
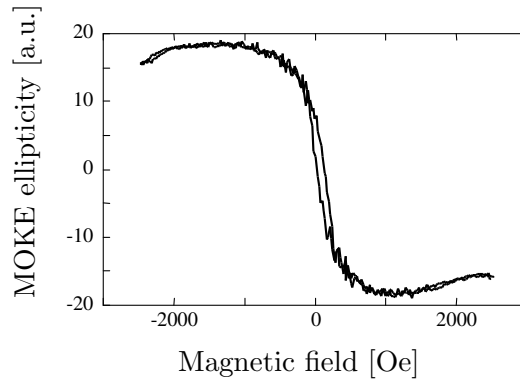
Figure 6.8: MOKE ellipticity hysteresis loop of the new Au(5AL)/Co(5AL)/Au(322) sample for $\boldsymbol{H} \parallel \hat{x}$ and at $\varphi = 0$, measured in a rather high field. The rotation angle was $\alpha \approx 0$.

($\gamma \to 0$). Only the VISMOKE contribution is then present at high field. As expected, this high field MOKE change is nearly equal to PMOKE measured for $\alpha = 0$ or $180°$. Thus, this is another proof that the measured VISMOKE signal is not mistakenly coming from a PMOKE signal.

6.2.5   MOKE at oblique angle of incidence

As shown above, the field-induced MOKE ($\boldsymbol{H} \parallel \hat{y}$) hysteresis curves may be decomposed into S-shape and square loop contributions. The dependence of the S-shape (for $\alpha = \pm 90°$) and square loop (for $\alpha = 0, 180°$) contributions with the incidence angle φ are presented in Fig. 6.9. Recall that here for $\boldsymbol{H} \parallel \hat{y}$, the larger S-shape signal is obtained for $\alpha = \pm 90°$. As expected from Table 6.2, PMOKE and VISMOKE are quasi-constant while LMOKE varies quasi-linearly with φ in the $\langle -30°, 30° \rangle$ range. Since LMOKE is zero at $\varphi = 0$, we can extract the PMOKE and VISMOKE effects from the square loop and S-shape amplitudes, respectively for $\varphi = 0$. As expected, the variation $\Im[d(\text{MOKE})/d\varphi] = -0.078$ mdeg/deg is found to be identical in all cases (Fig. 6.9).
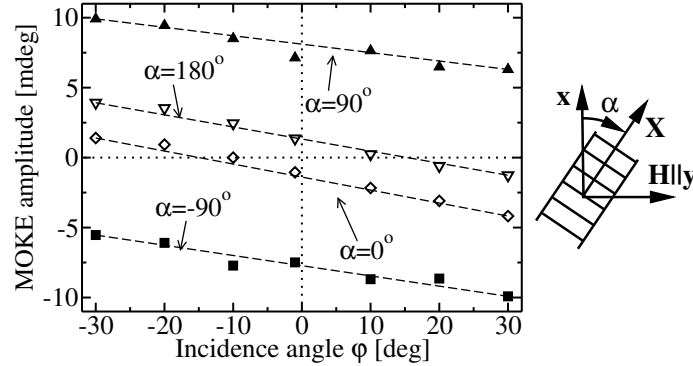
Figure 6.9: Variation of the MOKE ellipticity amplitude of the square loop ($\alpha = 0°$ and $180°$) and S-shape ($\alpha = \pm 90°$) contributions with the incidence angle φ for $\boldsymbol{H} \parallel \hat{y}$. Note that here $\boldsymbol{H}$ is applied along $\hat{y}$, i.e. at $90°$ from previous situations.

6.2.6   Determination of ε_s from MOKE measurements

The VISMOKE measured at photon energy $E = 1.95\,\text{eV}$, for $\varphi = 0$, is found to be equal to $(0 - 9i)$ mdeg at saturation. The saturated PMOKE for $\boldsymbol{H} \parallel \hat{z}$ ($\gamma = 90°$) is $(-23 + 48i)$ mdeg. Comparing the analytical expressions of s-PMOKE ($A\chi V_{\mathsf{s}} Q\, t^{(\text{Co})}\varepsilon_m$) with that of s-VISMOKE ($A\chi V_{\mathsf{s}} Q\, t_s \varepsilon_s \varepsilon_m / \varepsilon_0^{(\text{fm})}$), the value of ε_s can be estimated from the VISMOKE/PMOKE ratio. Thus, we deduce $\varepsilon_s t_s / \varepsilon_d t^{(\text{Co})} = (-0.15 + 0.07i) \pm 0.02$ mdeg. Assuming a memory thickness $t_s = 2$ AL, and using the diagonal Co permittivity $\varepsilon_0^{(\text{fm})} = -12.6 + 18.5i$ (ref. [84]), we deduce a rather large value for the off-diagonal structural coefficient, $\varepsilon_s = 1.42 - 9.38i$. It has to be compared with $\varepsilon_0^{(\text{nf})} = -13.47 + 1.27i$ for the Au and $\varepsilon_0^{(\text{fm})} = -12.56 + 18.53i$ for the Co layer.

6.3 Optical determination of ε_s

As the structural off-diagonal element ε_s has a pure optical origin, we can determine its value from "structural" (non-magnetic) measurements. For example, ε_s can be determined from the experimental dependence of the MOKE signal with sample rotation, i.e. $\Phi^{(\mathrm{struc})}(\alpha)$ (Table 6.2).

In order to get the best accuracy on ε_s, we prefered to keep the sample fixed and rotate all optical elements by an angle μ. By this way, the reflected light beam is surely fixed in position through all optical elements and the light spot always checks the same sample area. We used an optical set-up with the following arrangement: laser – polarizer(p) – sample – photoelastic modulator($0°$) – analyzer($45°$) – detector. As shown in Section 2.4.1, the signal detected at the modulator frequency f, and for $\mu = 0$, is proportional to $S = \Im(r_{\mathrm{sp}}/r_{\mathrm{pp}})$ [Eq. (2.24)]. When optical elements are rotated by an angle μ, the coefficients of the usual reflection matrix are replaced by their effective counterparts r'_{ij}, $i, j = \{\mathrm{s}, \mathrm{p}\}$

$$\mathbf{R'} = \begin{bmatrix} r'_{\mathrm{ss}} & r'_{\mathrm{sp}} \\ r'_{\mathrm{ps}} & r'_{\mathrm{pp}} \end{bmatrix} = \mathbf{K}(\mu)\mathbf{R}\mathbf{K}(\mu)$$

$$= \begin{bmatrix} c^2 r_{\mathrm{ss}} - s^2 r_{\mathrm{pp}} + cs(r_{\mathrm{ps}} - r_{\mathrm{sp}}) & c^2 r_{\mathrm{sp}} + s^2 r_{\mathrm{ps}} + cs(r_{\mathrm{pp}} + r_{\mathrm{ss}}) \\ c^2 r_{\mathrm{ps}} + s^2 r_{\mathrm{sp}} - cs(r_{\mathrm{pp}} + r_{\mathrm{ss}}) & c^2 r_{\mathrm{pp}} - s^2 r_{\mathrm{ss}} + cs(-r_{\mathrm{sp}} + r_{\mathrm{ps}}) \end{bmatrix},$$

(6.8)

where c, s are shortcuts for $\cos\mu$, $\sin\mu$, respectively, $\mathbf{K}(\mu)$ being the rotation 2×2 matrix. As can be seen from Eq. (6.8), the large contribution to the reflectivity signal, $S(\mu) = \Im(r'_{\mathrm{sp}}/r'_{\mathrm{pp}})$, is not linked to ε_s, but to the sum of the reflection coefficients $r_{\mathrm{ss}} + r_{\mathrm{pp}}$ at oblique incidence angle. Note that for $\varphi = 0$, $r_{\mathrm{ss}} = -r_{\mathrm{pp}}$ (see Tab. 2.1 or Tab. 3.1). Thus, this contribution must be canceled out by subtracting two successive measurements performed for $\alpha = 0$ and $\alpha = 90°$. Taking into account that $\Delta S = (S_{\alpha=90°} - S_{\alpha=0})$ does not depends much on r_{sp} and r_{ps} in our experimental conditions, i.e. for $\varphi = 10°$, the dependence of ΔS on ε_s is mainly related to $\rho_{\mathrm{ss}}^{(2)}$, $\rho_{\mathrm{pp}}^{(2)}$, leading to

$$\Delta S(\mu) \approx \frac{\rho_{\mathrm{pp}}^{(2)} - \rho_{\mathrm{ss}}^{(2)}}{r_{\mathrm{pp}}^{(0)} - r_{\mathrm{ss}}^{(0)}} \varepsilon_s^2 \, t_s \, \sin 2\mu,$$

(6.9)

where $r_{\mathrm{ss}}^{(0)}$, $r_{\mathrm{pp}}^{(0)}$ and $\rho_{\mathrm{pp}}^{(2)}$, $\rho_{\mathrm{ss}}^{(2)}$ are the zeroth and second-order diagonal reflection coefficients in ε_{ij}, with $i \neq j$, respectively. These coefficients are defined in Table 3.1 and their numerical values are reported in Appendix 6.7. Note that $\Delta S \sim \varepsilon_s^2$.

The experimental data relative to the $S(\mu)$ variation for a sample in its remnant state, for $\varphi = 10°$, $\alpha = 0°$ and $90°$, and of their difference $\Delta S(\mu)$ are represented on Fig. 6.10. The experimental data fit quite well the theoretical $S(\mu)$ curve. The deduced differential curve $\Delta S(\mu)$ [Fig. 6.10(b)] exhibits a $C \sin 2\mu$ dependence with $C = 40$ mdeg. In counterpart, substituting to Equation (6.9) the complex value of ε_s, obtained from MOKE measurements and assuming $t_s = 2$ AL, we deduce $C = 15$ mdeg. So, since $\Delta S(\mu) \sim \varepsilon_s^2$, the present reflectivity measurements lead here to a larger value of ε_s by a factor 1.6 than that deduced before from the VISMOKE/PMOKE ratio. However, one has to consider that the measurements and calibration errors could be about 20%.

This can not explain the discrepancy between MOKE and reflectivity determinations of ε_s. A reason for this discrepancy is more behind our too simplified model which assumes a step profile along z for both ε_s (over a thickness t_s) and ε_m (over a thickness $t^{(\mathrm{fm})}$).
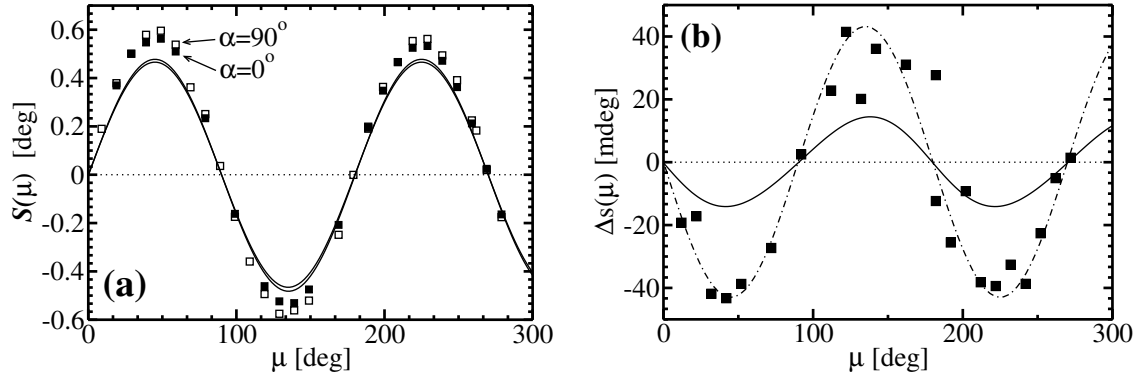
Figure 6.10: (a) Variation of the differential optical reflectivity $S = \Im(r'_{\rm sp}/r'_{\rm pp})$, measured for $\varphi = 10°$ and $\alpha = 0°$ ($\square$) or $\alpha = 90°$ ($\blacksquare$) as a function of the orientation angle μ of the optical elements with respect to the sample [see Eq. (6.8)]. The calculated $S(\mu) \sim \sin 2\mu$ curves are represented by lines. (b) The difference $\Delta S(\mu) = S_{\alpha=90°}(\mu) - S_{\alpha=0°}(\mu)$ is related to ε_s^2. The full line shows a plot of the $\Delta S(\mu)$ value calculated by the 4×4 matrix formalism, substituting the ε_s value found from the VISMOKE/PMOKE ratio. The dash-dotted line gives the plot of the $-\sin 2\mu$ variation and stands as a guide for the eye.

Taking into account of the profiles for $\varepsilon_s(z)$ and $\varepsilon_m(z)$, our measurements are sensitive to different integral quantities, since VISMOKE is proportional to $\int \varepsilon_s(z)\varepsilon_m(z)\mathrm{d}z$, PMOKE to $\int \varepsilon_m(z)\mathrm{d}z$ and $\Delta S \sim \int \varepsilon_s^2(z)\mathrm{d}z$ (see Chapter 4 or ref. [57]). So, in the absence of well known profiles for ε_s and ε_m, it is unreasonable to give any interpretation on the origin of the discrepancy between the optical and MO determination of ε_s. On the other hand, such measurements can give more informations about in-depth profiles of ε_s or ε_m.

6.4 Phenomenological model for ε_s

The microscopic origin of the opto-structural perturbation ε_s is certainly associated in part to the difference between electronic band structures for vicinal and non-vicinal planar interfaces. As already discussed in Chapter 4, the evaluation of this contribution requires the use of sophisticated *ab-initio* calculations. Another contribution comes from the different boundary conditions of the electrical field at vicinal and planar interfaces. In this Section, we present a simple phenomenological model for interpreting ε_s as a consequence of modified boundary conditions at the vicinal interface.

The classical planar boundary relation (conservation of tangential $\boldsymbol{E}$ and normal $\boldsymbol{D}$ components) found in any textbook of electromagnetism, between two isotropic media [denoted by (a) and (b)] can be expressed as

$$\Delta \boldsymbol{D}^{(\mathrm{pln})} = \boldsymbol{D}^{(b,\mathrm{pln})} - \boldsymbol{D}^{(a,\mathrm{pln})} = (\varepsilon_0^{(b)} - \varepsilon_0^{(a)}) \begin{bmatrix} E_x^{(a)} \\ E_y^{(a)} \\ 0 \end{bmatrix} = (\varepsilon_0^{(b)} - \varepsilon_0^{(a)}) \begin{bmatrix} E_x^{(b)} \\ E_y^{(b)} \\ 0 \end{bmatrix}, \qquad (6.10)$$

where the superscript "pln" refers to the planar interface [Figure 6.11(a)]. Since we assume that the interface separates two isotropic media, $\boldsymbol{D}^{(j,\mathrm{pln})} = \boldsymbol{\varepsilon}^{(j,\mathrm{iso})} \boldsymbol{E}^{(j,\mathrm{pln})}$, where $j = \{a, b\}$ relates to the medium and $\boldsymbol{\varepsilon}^{(j,\mathrm{iso})} = \varepsilon_0^{(j)} \delta_{mn}$ is the isotropic permittivity, δ_{mn} is the Kronecker symbol. Note, that $\Delta D_z^{(\mathrm{pln})} = 0$ in Eq.(6.10) expresses the conservation of the normal components for $\boldsymbol{D}$ over the interface.
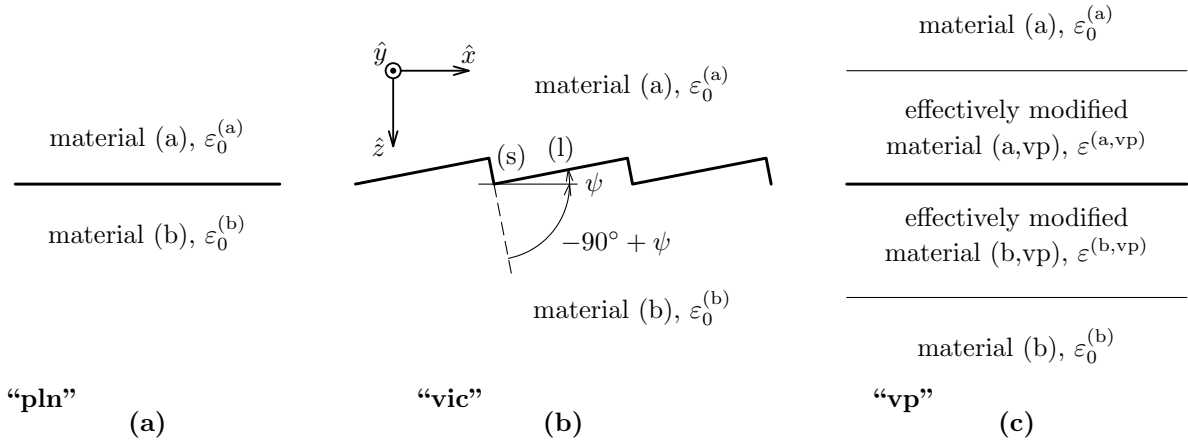
Figure 6.11: (a) Planar interface ("pln") fulfilling planar boundary conditions [Eq. (6.10)] (b) vicinal interface ("vic"), where planar boundary conditions are assumed to be fulfilled on the extended [larger (l)] steps of the vicinal interface [Eq. (6.11)] (c) vicinal interface ("vp"), but vicinal boundary conditions are described by a modification of the permittivity tensor in the vicinity of the vicinal interface, keeping planar boundary conditions valid [Eqs. (6.12)(6.15)].

Let us assume that the planar boundary conditions, expressed by Eq. (6.10), are valid on the extended flat parts [denoted as large (l) on Figure 6.11(b)] of the vicinal interface steps, which are misoriented by a miscut angle ψ with respect to the mean optical plane. Thus, rotating the planar boundary conditions by an angle $-\psi$ around the $\hat{x}$ axis, the vicinal boundary conditions can be written

$$
\Delta \boldsymbol{D}^{(\text{vic})} = \boldsymbol{D}^{(b,\text{vic})} - \boldsymbol{D}^{(a,\text{vic})} \;=\; \left(\varepsilon_0^{(b)} - \varepsilon_0^{(a)} \right)
\begin{bmatrix}
E_x^{(a,\text{vic})} \cos^2 \psi + \frac{1}{2} E_z^{(a,\text{vic})} \sin 2\psi \\
E_y^{(a,\text{vic})} \\
\frac{1}{2} E_x^{(a,\text{vic})} \sin 2\psi + E_z^{(a,\text{vic})} \sin^2 \psi
\end{bmatrix}
$$

$$
= \left(\varepsilon_0^{(b)} - \varepsilon_0^{(a)} \right)
\begin{bmatrix}
E_x^{(b,\text{vic})} \cos^2 \psi + \frac{1}{2} E_z^{(b,\text{vic})} \sin 2\psi \\
E_y^{(b,\text{vic})} \\
\frac{1}{2} E_x^{(b,\text{vic})} \sin 2\psi + E_z^{(b,\text{vic})} \sin^2 \psi
\end{bmatrix},
$$

$$(6.11)$$

where the superscript "vic" denotes that the variables and boundary conditions belong to each extended step (l) of the vicinal interface. Again, the vicinal interface is assumed to separate two isotropic media, i.e. $\boldsymbol{D}^{(j,\text{vic})} = \varepsilon^{(j,\text{iso})} \boldsymbol{E}^{(j,\text{vic})}$.

Most formalisms treating of the light propagation inside a multilayer structure assume that planar boundary conditions are fulfilled. Thus, we want to introduce here a model for vicinal interfaces in which:

(i) planar boundary conditions [Eq. (6.10)] are valid

(ii) vicinal boundary conditions [Eq. (6.11)] modify the form of the permittivity tensor in the vicinity of the vicinal interface[2].

Introducing a new superscript "vp" related to a vicinal interface which fulfills planar boundary conditions [Figure 6.11(c)], the new relationship between $\boldsymbol{D}^{(\text{vp})}$ and $\boldsymbol{E}^{(\text{vp})}$ at

---

[2]Another way to treat modified boundary conditions is to introduce the surface polarization on the vicinal interface [124].

the vicinal interface writes

$$\boldsymbol{D}^{(j,\mathrm{vp})} = \boldsymbol{\varepsilon}^{(j,\mathrm{vp})} \boldsymbol{E}^{(j,\mathrm{vp})}. \tag{6.12}$$

To find solutions of Eq.(6.12), we need to relate the independent "pln", "vic" and "vp" systems. This relation can be established through a common variable $\boldsymbol{A}$. Hence, the variation of electric fields $\boldsymbol{E}^{(j,\mathrm{pln})}(\boldsymbol{A})$, $\boldsymbol{E}^{(j,\mathrm{vic})}(\boldsymbol{A})$, $\boldsymbol{E}^{(j,\mathrm{vp})}(\boldsymbol{A})$, and inductions $\boldsymbol{D}^{(j,\mathrm{pln})}(\boldsymbol{A})$, $\boldsymbol{D}^{(j,\mathrm{vic})}(\boldsymbol{A})$ $\boldsymbol{D}^{(j,\mathrm{vp})}(\boldsymbol{A})$ has to be found. Because the choice of $\boldsymbol{A}$ is arbitrary, the easiest way is to set up this common variable by equalizing the electric fields for all cases, i.e. $\boldsymbol{A} = \boldsymbol{E}^{(a,\mathrm{pln})} = \boldsymbol{E}^{(a,\mathrm{vic})} = \boldsymbol{E}^{(a,\mathrm{vp})} \equiv \boldsymbol{E}^{(a)}$, or $\boldsymbol{A} = \boldsymbol{E}^{(b,\mathrm{pln})} = \boldsymbol{E}^{(b,\mathrm{vic})} = \boldsymbol{E}^{(b,\mathrm{vp})} \equiv \boldsymbol{E}^{(b)}$. Then, the difference between planar and vicinal boundary conditions $\Delta\Delta\boldsymbol{D}$, expressed through newly defined common variables $\boldsymbol{E}^{(a)}$ or $\boldsymbol{E}^{(b)}$ becomes

$$
\begin{aligned}
\Delta\Delta\boldsymbol{D} = \Delta\boldsymbol{D}^{(\mathrm{vic})} - \Delta\boldsymbol{D}^{(\mathrm{pln})} = & \left(\varepsilon_0^{(b)} - \varepsilon_0^{(a)}\right) \begin{bmatrix} -E_x^{(a)} \sin^2\psi + \frac{1}{2} E_z^{(a)} \sin 2\psi \\ 0 \\ \frac{1}{2} E_x^{(a)} \sin 2\psi + E_z^{(a)} \sin^2\psi \end{bmatrix} \\
= & \left(\varepsilon_0^{(b)} - \varepsilon_0^{(a)}\right) \begin{bmatrix} -E_x^{(b)} \sin^2\psi + \frac{1}{2} E_z^{(b)} \sin 2\psi \\ 0 \\ \frac{1}{2} E_x^{(b)} \sin 2\psi + E_z^{(b)} \sin^2\psi \end{bmatrix}.
\end{aligned}
\tag{6.13}
$$

This difference between boundary conditions gives the modification of $\boldsymbol{\varepsilon}^{(j,\mathrm{vp})}$. We assume that this difference is equally distributed into both media at interfaces, i.e. between both $\boldsymbol{\varepsilon}^{(a,\mathrm{vp})}$ and $\boldsymbol{\varepsilon}^{(b,\mathrm{vp})}$ permittivity tensors. Since the common variable $\boldsymbol{A}$ for "pln", "vic" and "vp" systems is arbitrary, it is convenient to choose $\boldsymbol{E}^{(a)}$ and $\boldsymbol{E}^{(b)}$ to determine $\boldsymbol{\varepsilon}^{(a,\mathrm{vp})}$ and $\boldsymbol{\varepsilon}^{(b,\mathrm{vp})}$, respectively. Hence, the relationship between electric inductions are

$$
\begin{aligned}
\boldsymbol{D}^{(a,\mathrm{vic})}(\boldsymbol{E}^{(a)}) &= \boldsymbol{D}^{(a,\mathrm{vp})}(\boldsymbol{E}^{(a)}) - \Delta\Delta\boldsymbol{D}(\boldsymbol{E}^{(a)})/2 \\
\boldsymbol{D}^{(b,\mathrm{vic})}(\boldsymbol{E}^{(b)}) &= \boldsymbol{D}^{(b,\mathrm{vp})}(\boldsymbol{E}^{(b)}) + \Delta\Delta\boldsymbol{D}(\boldsymbol{E}^{(b)})/2.
\end{aligned}
\tag{6.14}
$$

This is the crucial step of our analysis. Equation (6.14) justifies that planar and vicinal boundary conditions of $\Delta\boldsymbol{D}^{(\mathrm{vp})} = \Delta\boldsymbol{D}^{(\mathrm{pln})}$ and of $\boldsymbol{D}^{(\mathrm{vic})}$ are fulfilled and their difference is $\Delta\Delta\boldsymbol{D}$. Taking into account that $\boldsymbol{D}^{(j,\mathrm{vic})} = \boldsymbol{\varepsilon}^{(j,\mathrm{iso})} \boldsymbol{E}^{(j,\mathrm{vic})}$, we obtain

$$
\boldsymbol{\varepsilon}^{(j,\mathrm{vp})} = \begin{bmatrix} \varepsilon_0^{(j)} - \varepsilon_t^{(j)} & 0 & \varepsilon_s^{(j)} \\ 0 & \varepsilon_0^{(j)} & 0 \\ \varepsilon_s^{(j)} & 0 & \varepsilon_0^{(j)} + \varepsilon_t^{(j)} \end{bmatrix},
\tag{6.15}
$$

where $\varepsilon_s^{(a)}$, $\varepsilon_s^{(b)}$, $\varepsilon_t^{(a)}$, $\varepsilon_t^{(b)}$ have the following form

$$\varepsilon_s^{(a)} = \frac{1}{4}\left(\varepsilon_0^{(b)} - \varepsilon_0^{(a)}\right)\sin 2\psi \qquad \varepsilon_s^{(b)} = \frac{1}{4}\left(\varepsilon_0^{(a)} - \varepsilon_0^{(b)}\right)\sin 2\psi \tag{6.16}$$

$$\varepsilon_t^{(a)} = -\frac{1}{2}\left(\varepsilon_0^{(b)} - \varepsilon_0^{(a)}\right)\sin^2\psi \qquad \varepsilon_t^{(b)} = -\frac{1}{2}\left(\varepsilon_0^{(a)} - \varepsilon_0^{(b)}\right)\sin^2\psi. \tag{6.17}$$

This result can be applied to both types of large (l) and small (s) parts of the vicinal interface [Figure 6.11(a)], having orientations ψ and $(\psi - 90°)$, respectively. Substituting these angles into Eq. (6.16), we found that these contributions (per unit area) give opposite

sign for ε_s. Thus, summing the weighted contributions for small (s) and large (l) steps, we arrive to

$$\varepsilon_s^{(a)} = \frac{1}{4}(\varepsilon_0^{(b)} - \varepsilon_0^{(a)})\left(\cos^2\psi - \sin^2\psi\right)\sin 2\psi. \tag{6.18}$$

In the case of a small miscut angle ψ, the area of (l) type steps is much larger than that of (s) type steps, and thus this last contribution can be neglected. Hence, ε_s expresses by Eq. (6.16). In the hypothetical case of $\psi = 45°$, Eq. (6.18) leads to $\varepsilon_s = 0$, as expected when a new mirror plane symmetry is added.

6.4.1 Numerical calculation of ε_s for a Co/Au(322) interface

Figure 6.12 shows the calculated spectral dependence of ε_s inside the Co layer in the vicinity of a Co/Au(322) interface (miscut angle $\psi = 11.4°$), as expressed by Eq. (6.16). In particular, for $E = 1.95$ eV, the value of the structural off-diagonal coefficient is calculated to be $\varepsilon_s = 0.09 + 1.67i$. It can be compared with the experimental value determined from MOKE measurements, giving $\varepsilon_s = 1.42 - 9.38i$. Thus, the theoretical value is only 18% of the experimental one, which is determined in Section 6.2.6 from the VISMOKE/PMOKE ratio, and about 30% of the value obtained from reflectivity measurements. Thus, to get a more quantitative agreement, refined calculations on the influence of the modified boundary conditions and the perturbation of the electronic band structure at the interface are required. From an experimental point of view, the spectral dependence of ε_s can give some insight into the processes involved at the vicinal interface.
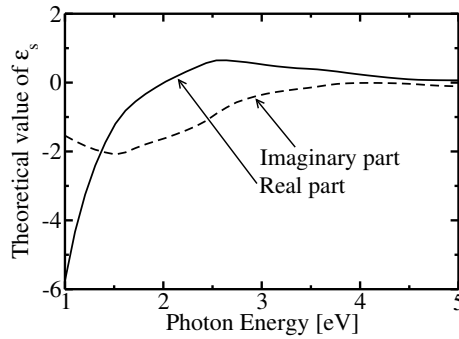
Figure 6.12: Calculated real (full line) and imaginary (dashed line) parts of the spectral dependence of ε_s related to the Co/Au(322) interface (miscut angle $\psi = 11.4°$), using Eq. (6.16).

6.5 Conclusion and perspectives of Chapter 6

In this Chapter the Vicinal Interface Sensitive Magneto-Optical Kerr Effect (VISMOKE) was analytically predicted, and for the first time experimentally evidenced on a Co layer deposited on a Au(322) vicinal surface. VISMOKE appears when FM layers are deposited on very low-symmetry surfaces (i.e. on surfaces providing at most one mirror symmetry plane). Obviously, VISMOKE cannot be evidenced from a FM layer grown on high symmetry surfaces, such as Au(111). VISMOKE comes from the coupling between the opto-structural perturbation ε_s, induced by the low interface symmetry, and the usual

magneto-optical perturbation ε_m. It is linear with in-plane magnetization and characterized by a 2π symmetry behavior when rotating the film around its normal axis. I developed a phenomenological model for interpreting ε_s as a consequence of modified boundary conditions at the vicinal interface. As experimentally demonstrated, VISMOKE has to be considered in all MOKE studies concerning FM films deposited on vicinal surfaces.

It would be very interesting to determine the spectral dependence of ε_s, since there is not many ways for performing spectroscopy of FM/non-FM buried metal interfaces. Other possible methods could be:

(i) Magneto-Optical Second Harmonic Generation, but the actual accessible spectral range is rather limited for the moment.

(ii) a technique presented here in Chapter 4 (or reference [57]) which determines the interface contribution from the dependence of MOKE on the FM layer thickness, $\Phi(t^{(\mathrm{fm})})$.

From an experimental point of view, ε_s can be determined by several ways; either from the VISMOKE/PMOKE ratio, or from optical reflectivity measurements. All these results would be interesting for testing phenomenological models or *ab-initio* calculations in simple model film structures with known sharp interfaces.

6.6   Appendix I of Chapter 6

angle of incidence	φ	
sample rotation	α	
magnetization orientation	$\beta,\ \gamma$	
photon energy	E	1.95 eV
wavelength	λ	634 nm
refractive index of air	$N^{(0)}$	1
Au diagonal permittivity	$\varepsilon_0^{(\mathrm{nf})} \equiv \varepsilon_0^{(\mathrm{Au})}$	-13.47 + 1.27i
refractive index of Au	$N^{(\mathrm{nf})} = N^{(\mathrm{Au})} = \sqrt{\varepsilon_0^{(\mathrm{Au})}}$	0.17 + 3.67i
Co diagonal permittivity	$\varepsilon_0^{(\mathrm{fm})} \equiv \varepsilon_0^{(\mathrm{Co})}$	-12.56 +18.53i
refractive index of Co	$\sqrt{\varepsilon_0^{(\mathrm{Co})}}$	2.22 + 4.18i
Co off-diagonal mag. permitt.	$\varepsilon_m \equiv -i\varepsilon_1^{(\mathrm{Co})}$	0.75 + 0.21i
Co off-diagonal struc. permitt.	ε_s	1.42-9.38i *
Co layer thickness	$t^{(\mathrm{fm})} \equiv t^{(\mathrm{Co})}$	5 AL$\hat{=}$1 nm
Au overlayer thickness	$d^{(\mathrm{nf},1)} \equiv d^{(\mathrm{Au},1)}$	7 AL$\hat{=}$1.8 nm
wavevector in vacuum	$k_0^{(\omega)}$	$9.90\times10^{-3}\,\mathrm{nm}^{-1}$

Table 6.2: Numerical values of some coefficients used in present Chapter 6.

* This value of ε_s is determined from the VISMOKE/PMOKE ratio.

6.7 Appendix II of Chapter 6

	$\varphi = 0°$	$\varphi = 30°$	$\varphi = 70°$
N_y	0	0.50	0.94
$N_z^{(\mathrm{nf})}$	0.17 + 3.67i	0.17 + 3.71i	0.17 + 3.79i
Q	0.9030 + 0.0043i	0.9022 + 0.0043i	0.9001 + 0.0042i
$r_{\mathrm{ss}}^{(0)}$	-0.84 - 0.49i	-0.88 - 0.43i	-0.98 - 0.18i
$r_{\mathrm{pp}}^{(0)}$	0.84 + 0.49i	0.80 + 0.56i	0.19 + 0.93i
$\rho_{\mathrm{ss}}^{(0,t^{(\mathrm{fm})})} \, [\mathrm{nm}^{-1}]$	$(0.018 + 0.011i)$	$(0.0159 + 0.0086i)$	$(0.0070 + 0.0016i)$
$\rho_{\mathrm{pp}}^{(0,t^{(\mathrm{fm})})} \, [\mathrm{nm}^{-1}]$	$(-0.018 - 0.011i)$	$(-0.019 - 0.015i)$	$(-0.0064 - 0.0408i)$
$\rho_{\mathrm{pp}}^{(1)} \, [\mathrm{nm}^{-1}]$	0	$(0.0068 - 0.1117i)10^{-3}$	$(0.25 - 0.25i)10^{-3}$
$\rho_{\mathrm{ss}}^{(2)} \, [\mathrm{nm}^{-1}]$	$(0.537 + 0.015i)10^{-4}$	$(0.466 - 0.021i)10^{-4}$	$(0.177 - 0.059i)10^{-4}$
$\rho_{\mathrm{pp}}^{(2)} \, [\mathrm{nm}^{-1}]$	$(-0.537 - 0.015i)10^{-4}$	$(-0.610 - 0.067i)10^{-4}$	$(-0.696 - 0.780i)10^{-4}$

Table 6.3: Values of some coefficients for the Au(7AL)/Co(5AL)/Au structure, at a photon energy E=1.95 eV. All these coefficients have been defined in Table 3.1.

Chapter 7

Second Harmonic Generation (SHG) from a multilayer structure

The Second Harmonic Generation (SHG) defined in Section 2.2.2, also called non-linear MO, is especially suitable for studying surfaces and *buried* interfaces in usual multilayer structures (for an overview see, e.g. [1, 2]). Furthermore, the SHG signal depends linearly on magnetization, and thus can provide information about the magnetization state of surface or interfaces. In this case, it is called Magneto-Optical SHG (MOSHG). As we shall see below, this technique is complementary to the in-depth Kerr effect investigated previously in Chapter 5. The basic properties of MOSHG, compared to linear MO, are the following:

- No SHG or MOSHG is generated from bulk centrosymmetric media. Thus, in most metallic multilayers, the *MOSHG originates from surface and interfaces*, where the symmetry inversion is broken. Thus, MOSHG is here selectively sensitive to the magnetization of interfaces. This is far different for MOKE which is determined by an integration over the thickness of all FM layers present in the multilayer structure.

- As for MOKE, MOSHG performed in different configurations, checks different magnetization components (discussed later in Section 8.3). For example, `ss` and `pp` configurations (defined below) are only sensitive to longitudinal or transverse components of the magnetization, respectively. As we shall see later, contrarily to PMOKE, the MOSHG is never related to the polar magnetization alone.

- In the case of MOKE, the contributions from different FM layers are simply additive [45]. In counterpart, MOSHG contributions issued from different interfaces interfere with each other, leading to more complex behavior. Since the phase of the SHG signal is opposite when reversing the order of the metals at the interface [1], an ultrathin FM layer sandwiched between non-magnetic layers of the same composition will give rise only to a weak MOSHG effect. For example, in the Au/Co/Au structure having a very thin Co thickness, the total contribution from both Au/Co interfaces is much smaller than the MOSHG signal due to only one interface [128].

  Furthermore, it is easier to determine the depth of a FM layer with MOKE since it contains the phase information (see Section 5.5). In the case of MOSHG, the

situation is not so straightforward because one usually measures the light intensity, i.e. phase information is removed.

The aim of this Chapter is to develop a new formalism, allowing to calculate SHG and MOSHG from any multilayer structure. In fact, one of the motivations was the absence of a general SHG and MOSHG formalism providing the description of samples, with a lateral distribution of properties at their interface (periodic magnetic domains, irradiated samples etc.).

The originality of our approach is based on the description of the SHG phenomenon by means of an *electric point dipole radiation* which modifies the boundary conditions at its location, i.e. for the tangential components of $\boldsymbol{E}^{(2\omega)}$, $\boldsymbol{H}^{(2\omega)}$. This allows to calculate the radiated intensity provided by any dipole distributions. These dipoles can be assumed to radiate either coherently or non-coherently. Furthermore, the proposed formalism is suitable to treat the case of optically anisotropic multilayers.

The previous formalism, proposed by Wierenga *et al.* [4], assumed that SHG was generated by a homogeneously polarized sheet. However, they have not derived the modified boundary conditions in the presence of this polarized sheet. The rigorous determination of these boundary conditions in the $\boldsymbol{r}$-space was proposed recently by R. Atkinson and N.F. Kubrakov [129]. The analytical formulas for MOSHG at a single air/FM interface was derived by A.K. Zvezdin and N.F. Kubrakov [130].

The formalism presented in this Chapter is recently submitted for publication (J. Hamrle *et al.* [131]).

7.1 Sketch of the developed SHG formalism

The SHG formalism presented here involves several stages. Some of them, in particular mathematical considerations, are already presented in Chapter 3 and Appendices C, D and E. The sketch of the SHG formalism is presented on Figure 7.1.

- The determination of the electric field intensity at the ν-th interface at the fundamental (ω) frequency, $\boldsymbol{E}_\nu^{(\omega)}$, has been already solved in Section 3.2.5. It is expressed in the matrix form by $\boldsymbol{E}_\nu^{(\omega)} = \mathbf{X}_\nu^{(\omega)} \boldsymbol{J}_{0,+}^{(\omega)}$ [Eq. (3.33)], where $\mathbf{X}_\nu^{(\omega)}$ is the matrix of incoming generalized Fresnel coefficients, and $\boldsymbol{J}_{0,+}^{(\omega)} = [\mathcal{E}_{0,\mathrm{s},-}^{(\omega)}, \mathcal{E}_{0,\mathrm{p},-}^{(\omega)}]^{\mathrm{T}}$ the Jones vector of the incoming light.

- The determination of the complex moment of an electric point dipole located on the ν-th interface, $\boldsymbol{\mu}_\nu^{(2\omega)} = \chi_\nu \otimes \boldsymbol{E}_\nu^{(\omega)} \boldsymbol{E}_\nu^{(\omega)}$, where χ_ν is the third-rank susceptibility tensor (sometimes called non-linear susceptibility tensor, second-order susceptibility tensor or χ-tensor), is discussed in the following Section 7.2 and its symmetry detailed in Section 8.1.2.

  Recall that χ is non-zero solely for media where the symmetry inversion *is* broken. In most metallic multilayers, this condition is fulfilled only on surface and interfaces. Thus we assume that SHG and MOSHG radiation originate only from surface and interfaces [1].

- The presence of the radiating point dipole $\boldsymbol{\mu}_\nu^{(2\omega)}$ implies modified boundary conditions, which have to be derived first (Appendix D). For this task, it was necessary to

Definition of the q-space (Section 3.1) + its mathematical properties (Appendix C)

Solution of Maxwell equations in the q-space for (Appendix D)
$\rho^{(2\omega)} = -\boldsymbol{\mu}_\nu^{(2\omega)} \cdot \nabla \delta(\boldsymbol{r} - \boldsymbol{r}_\nu)$,
$\boldsymbol{j}^{(2\omega)} = -i(2\omega)\boldsymbol{\mu}_\nu^{(2\omega)}\delta(\boldsymbol{r} - \boldsymbol{r}_\nu)$

Incoming Jones vector at ω
$$\boldsymbol{J}_{0,+}^{(\omega)} = \left[\mathcal{E}_{0,\mathbf{s},+}^{(\omega)}, \mathcal{E}_{0,\mathbf{p},+}^{(\omega)} \right]^{\mathrm{T}}$$

incoming Fresnel matrix $\mathbf{X}_\nu^{(\omega)}$ (Section 3.2.5)

Electric field at ω at each ν-th interface
$$\boldsymbol{E}_\nu^{(\omega)} = \mathbf{X}_\nu^{(\omega)} \boldsymbol{J}_{0,+}^{(\omega)}$$

third rank susceptibility tensor χ_ν (Section 7.2)

Single electric dipole of moment $\boldsymbol{\mu}_\nu^{(2\omega)}$ located on an ultrathin vacuum sheet at the ν-th interface
$$\boldsymbol{\mu}_\nu^{(2\omega)} = \chi_\nu \otimes \boldsymbol{E}_\nu^{(\omega)} \boldsymbol{E}_\nu^{(\omega)}$$

Modification of the boundary conditions
$$\Delta \mathcal{E}_{\nu,\mathbf{s},\pm}^\mu, \Delta \mathcal{E}_{\nu,\mathbf{p},\pm}^\mu$$

outcoming Fresnel matrix $\mathbf{Y}_\nu^{(2\omega)}$ or $\mathbf{Z}_\nu^{(2\omega)}$ (Section 7.3)

Modal amplitudes emitted by single point dipole and outcoming multilayer structure
$$\boldsymbol{A}_{\nu,\mathrm{spd}}^{(2\omega)} = \left[\mathcal{E}_{M+1,\mathbf{s},+,\mathrm{spd}}^{(2\omega)}, \mathcal{E}_{0,\mathbf{s},-,\mathrm{spd}}^{(2\omega)}, \mathcal{E}_{M+1,\mathbf{p},+,\mathrm{spd}}^{(2\omega)}, \mathcal{E}_{0,\mathbf{p},-,\mathrm{spd}}^{(2\omega)} \right]^{\mathrm{T}} = \mathbf{Y}_\nu^{(2\omega)} \boldsymbol{\mu}_\nu^{(2\omega)}$$
$$\text{or} \quad \boldsymbol{J}_{\nu,d,\mathrm{spd}}^{(2\omega)} = \left[\mathcal{E}_{\nu,\mathbf{s},d,\mathrm{spd}}^{(2\omega)}, \mathcal{E}_{\nu,\mathbf{p},d,\mathrm{spd}}^{(2\omega)} \right]^{\mathrm{T}} = \mathbf{Z}_{\nu,d}^{(2\omega)} \boldsymbol{\mu}_\nu^{(2\omega)}$$

$\iint$ over interface (Section 7.4)

Modal amplitudes emitted by each interface outcoming multilayer structure
$$\boldsymbol{A}_{\nu,\mathrm{iface}}^{(2\omega)} = \left[\mathcal{E}_{M+1,\mathbf{s},+,\mathrm{iface}}^{(2\omega)}, \mathcal{E}_{0,\mathbf{s},-,\mathrm{iface}}^{(2\omega)}, \mathcal{E}_{M+1,\mathbf{p},+,\mathrm{iface}}^{(2\omega)}, \mathcal{E}_{0,\mathbf{p},-,\mathrm{iface}}^{(2\omega)} \right]^{\mathrm{T}}$$

$\sum$ over all interfaces (Section 7.4)

Modal amplitudes emitted by all interfaces outcoming multilayer structure
$$\boldsymbol{A}_{\nu,\mathrm{ml}}^{(2\omega)} = \left[\mathcal{E}_{M+1,\mathbf{s},+,\mathrm{ml}}^{(2\omega)}, \mathcal{E}_{0,\mathbf{s},-,\mathrm{ml}}^{(2\omega)}, \mathcal{E}_{M+1,\mathbf{p},+,\mathrm{ml}}^{(2\omega)}, \mathcal{E}_{0,\mathbf{p},-,\mathrm{ml}}^{(2\omega)} \right]^{\mathrm{T}}$$

total radiated light intensity (Section 7.5)

Total radiated light intensity
$$I_j^{(2\omega)} = \frac{1}{2\eta_0} \frac{(2\pi k_0^{(2\omega)})^2}{(2\pi k_0^u)^4} \frac{N_j^{(2\omega)} |N_{z,j}^{(2\omega)}|^2}{r^2} \left(|\mathcal{E}_{j,\mathbf{s},d,\mathrm{ml}}^{(2\omega)}|^2 + |\mathcal{E}_{j,\mathbf{p},d,\mathrm{ml}}^{(2\omega)}|^2 \right)$$

Figure 7.1: Sketch of the developed SHG formalism. For details see Section 7.1.

come back to mathematical aspects. Thus, I propose and define a new $\boldsymbol{q}$-space (Section 3.1), in which the electric point dipole radiation is described by a non-diverging function. It is not the case in the $\boldsymbol{k}$-space (for details see Appendix E).

- These modified boundary conditions were incorporated into the 4×4 matrix formalism in order to determine the outcoming radiated modal amplitudes (Section 7.3). The relation between radiated modal amplitudes and the dipole moment is then expressed in a matrix form: $\boldsymbol{A}^{(2\omega)}_{\nu,\mathrm{spd}} = \mathbf{Y}^{(2\omega)}_{\nu} \boldsymbol{\mu}^{(\omega)}_{\nu}$ or by $\boldsymbol{J}^{(2\omega)}_{\nu,d,\mathrm{spd}} = \mathbf{Z}^{(2\omega)}_{\nu,d} \boldsymbol{\mu}^{(2\omega)}_{\nu}$, where $\mathbf{Y}^{(2\omega)}_{\nu}$, $\mathbf{Z}^{(2\omega)}_{\nu,d}$ are the generalized outcoming Fresnel matrices.

- The resulting vector of radiated modal amplitudes $\boldsymbol{A}^{(2\omega)}_{\mathrm{ml}}$ is then determined by integration over all radiating dipoles located on each interface and by summing over all interfaces (Section 7.4).

- Finally, I express the total radiated light intensity in far field. This is not a trivial task, since modal amplitudes are expressed in the $\boldsymbol{q}$-space, and thus the light intensity is not simply given by the square of the modal amplitude coming out from the structure (Section 7.5).

Let us now examine the different stages which have not been treated so far.

7.2   SHG as radiation of an electric point dipole

In most publications and textbooks concerning the SHG and MOSHG in multilayers (e.g. [4]), the source of SHG is described by an infinitely thin polarization sheet located at the interface. In the dipole approximation, the polarization of the sheet $\boldsymbol{P}^{(2\omega)}$ is quadratically dependent on the electric field at the interface $\boldsymbol{E}^{(\omega)}$ by:

$$\boldsymbol{P}^{(2\omega)} = \tilde{\chi} \otimes \boldsymbol{E}^{(\omega)} \boldsymbol{E}^{(\omega)} \tag{7.1}$$

through the 3-rd rank susceptibility tensor $\tilde{\chi}$, which phenomenologically describes the origin of the electromagnetic field at 2ω. The polarization sheet is assumed homogeneous and coherent. The sheet polarization $\boldsymbol{P}^{(2\omega)}$ is incorporated into the Maxwell equations considering the relation $\boldsymbol{D}^{(2\omega)} = \varepsilon_0 \boldsymbol{E}^{(2\omega)} + \boldsymbol{P}^{(2\omega)}$. Consequently, this causes a discontinuity of $\boldsymbol{E}$ and $\boldsymbol{H}$ fields through the sheet (or interface) [129].

In the presented new formalism, I reconsider this problem from a different point of view: I assume that each electric *point* dipole, oscillating at frequency 2ω is a source of SHG. Thus, the total radiated intensity in the multilayer structure is given by summing all radiating dipole contributions (over one entire interface and over all interfaces). The complex moment $\boldsymbol{\mu}^{(2\omega)}$ of an electric point dipole can be expressed similarly to Eq. (7.1)

$$\boldsymbol{\mu}^{(2\omega)} = \chi \otimes \boldsymbol{E}^{(\omega)} \boldsymbol{E}^{(\omega)}, \tag{7.2}$$

where χ and $\tilde{\chi}$ have the same symmetry, discussed in detail in Section 8.1.2. The electric point dipole moment $\boldsymbol{\mu}^{(2\omega)}$ is incorporated into the Maxwell equations through non-zero sources $\rho^{(2\omega)}$, $\boldsymbol{j}^{(2\omega)}$, as described in Appendix D.2.

Of course, the point dipole approach give finally the same results as the more traditional one, when treating an uniform and isotropic problem.

Finally notes that the form of Eqs. (7.1)(7.2) suggests that different electric point dipoles are coherent, as the phase of $\boldsymbol{\mu}^{(2\omega)}$ is related to the phase of $\boldsymbol{E}^{(\omega)}$.

7.3   Incorporation of a radiating electric point dipole into the multilayer structure

In this Section, the dipole radiation is incorporated into a multilayer structure and the modal amplitudes outcoming the multilayer structure are determined.

Firstly, important assumptions of our model that incorporates dipoles into multilayer structure must be defined. The dipole of complex moment $\boldsymbol{\mu}_\nu^{(2\omega)}$ is assumed to be located inside an *infinitesimally thin vacuum sheet*, which is located on the ν-th interface [Figure 7.2].
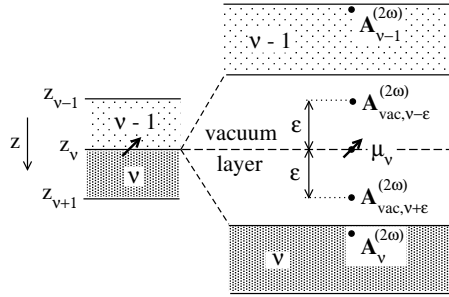
Figure 7.2: Sketch of the electric point dipole located inside the ultrathin vacuum layer located at each interface.

The justifications and objectives of the presence this ultrathin vacuum sheet are the following [2, 4]:

(i) In the derivation of the electric point dipole radiation (Appendix D), we assume that dipole is situated inside an ultrathin sheet located at the ν-th interface. However the value of the interface permittivity $\overline{\varepsilon}_\nu^{(2\omega)}$ of the sheet is unfortunately unknown. Thus, instead of supposing that the interface permittivity is some sort of "average" of permittivities surrounding it, we suppose that $\overline{\varepsilon}_\nu^{(2\omega)}$ of this sheet has the vacuum permittivity.

(ii) This approach is justified [2] since this arbitrary choice of interface permittivity value $\overline{\varepsilon}_\nu^{(2\omega)}$ does not prevent the calculations to be general. The relation between the outcoming Jones vector $\boldsymbol{J}_{\nu,d}^{(2\omega)}$ and the electrical field on the interface $\boldsymbol{E}_\nu^{(\omega)}$ can be obtained independently from the knowledge of $\overline{\varepsilon}_\nu^{(2\omega)}$. This is only related to the renormalization of χ-tensor elements accordingly to the value of $\overline{\varepsilon}_\nu^{(2\omega)}$. In other words, we define new χ-tensor elements that are renormalized with respect to this assumed vacuum interface sheet.

(iii) In counterpart, we suppose that the electric field $\boldsymbol{E}_\nu^{(\omega)}$ at the interface is just the average of its values just above and under the interface [Eq. (3.32)]. This is not contradictory with this ultrathin vacuum sheet, inside which the emitting dipole is located.

The presence of a radiating dipole relaxes the conservation rule on the tangential components of modal amplitudes $\mathcal{E}_{\nu,\mathrm{s/p},\pm}^{(2\omega)}$ inside the ultrathin vacuum sheet. Thus, the

jump of the modal amplitudes at interfaces is [Eq. (D.27)]:

$$\mathcal{E}^{(2\omega)}_{\nu+\epsilon,\mathbf{s},\pm} - \mathcal{E}^{(2\omega)}_{\nu-\epsilon,\mathbf{s},\pm} = \Delta\mathcal{E}^{\mu}_{\nu,\mathbf{s},\pm} = \frac{i(k_0^u)^2}{2\varepsilon_0} \frac{k_0^{(2\omega)}}{\pm N_{z,\mathrm{vac}}^{(2\omega)}} (\boldsymbol{\mu}_\nu^{(2\omega)} \cdot \hat{e}^{(2\omega)}_{\mathrm{vac},\mathbf{s},\pm}) \exp[-i\boldsymbol{q}^{(2\omega)} \cdot \boldsymbol{\rho}_\nu],$$

$$\mathcal{E}^{(2\omega)}_{\nu+\epsilon,\mathbf{p},\pm} - \mathcal{E}^{(2\omega)}_{\nu-\epsilon,\mathbf{p},\pm} = \Delta\mathcal{E}^{\mu}_{\nu,\mathbf{p},\pm} = \frac{i(k_0^u)^2}{2\varepsilon_0} \frac{k_0^{(2\omega)}}{\pm N_{z,\mathrm{vac}}^{(2\omega)}} (\boldsymbol{\mu}_\nu^{(2\omega)} \cdot \hat{e}^{(2\omega)}_{\mathrm{vac},\mathbf{p},\pm}) \exp[-i\boldsymbol{q}^{(2\omega)} \cdot \boldsymbol{\rho}_\nu],$$

$$(7.3)$$

where $\mathcal{E}^{(2\omega)}_{\nu+\epsilon,\mathbf{s}/\mathbf{p},\pm}$ and $\mathcal{E}^{(2\omega)}_{\nu-\epsilon,\mathbf{s}/\mathbf{p},\pm}$ are $\mathbf{s}$ and $\mathbf{p}$ modal amplitudes located inside the ultrathin vacuum sheet at positions $z_\nu + \epsilon$ and $z_\nu - \epsilon$, for $\epsilon \to 0$, respectively, i.e. just above and just under the dipole placed at the position z_ν. The modal polarizations $\hat{e}^{(2\omega)}_{\mathrm{vac},\mathbf{s}/\mathbf{p},\pm}$ characterize the $\mathbf{s}$ and $\mathbf{p}$ polarization directions inside this vacuum sheet [see Eq. (3.19)]. For a given material and at a fixed frequency, $\boldsymbol{q}^{(2\omega)} \equiv [k_x^{(2\omega)}, k_y^{(2\omega)}]$ defines the propagation direction of a radiation mode. $\boldsymbol{\rho}_\nu \equiv [x_\nu, y_\nu]$ gives the lateral dipole position on the ν-th interface. $k^{(2\omega)} = 2\omega/c$ is the vacuum wavevector and c the light velocity in vacuum. k_0^u is a normalization factor in m^{-1} units, appearing when equalizing the units between the electric field expressed in the real space [i.e. $\boldsymbol{E}(\boldsymbol{r})$] and in the Fourier $\boldsymbol{q}$-space [i.e. $\boldsymbol{\mathcal{E}}(\boldsymbol{q})$]. For numerical calculations we set $k_0^u = k_0^{(\omega)}$. For the definition of the $\boldsymbol{q}$-space, see Eq. (3.4), and for the Fourier transformation, consider Eqs. (A.2-A.3). ε_0 is the absolute permittivity in vacuum and $N_{z,\mathrm{vac}}^{(2\omega)}$ represents the z-component of the reduced wavevector inside the infinitesimally thin vacuum sheet, i.e. $\boldsymbol{N}_{\mathrm{vac}}^{(2\omega)} = \boldsymbol{k}_{\mathrm{vac}}^{(2\omega)}/k_0^{(2\omega)} = [N_x^{(2\omega)}, N_y^{(2\omega)}, N_{z,\mathrm{vac}}^{(2\omega)}]$, where $N_{z,\mathrm{vac}}^{(2\omega)} = \sqrt{\varepsilon_{\mathrm{vac}} - (N_x^{(2\omega)})^2 - (N_y^{(2\omega)})^2}$, being $\varepsilon_{\mathrm{vac}} = 1$. Note that when the fundamental light beam is coming from the air, then $N_{z,\mathrm{vac}}^{(2\omega)} = \cos\varphi$ where φ is incidence angle.

Starting from Eq. (7.3), the modal amplitudes of the radiating point dipole can be introduced into the 4×4 matrix formalism (Section 3.2). Firstly, we define

$$\Delta\boldsymbol{A}_\nu^{(2\omega)} \equiv [\Delta\mathcal{E}^{\mu}_{\nu,\mathbf{s},+}, \Delta\mathcal{E}^{\mu}_{\nu,\mathbf{s},-}, \Delta\mathcal{E}^{\mu}_{\nu,\mathbf{p},+}, \Delta\mathcal{E}^{\mu}_{\nu,\mathbf{p},-}]^{\mathrm{T}} = \boldsymbol{A}_{\nu+\epsilon,\mathrm{vac}}^{(2\omega)} - \boldsymbol{A}_{\nu-\epsilon,\mathrm{vac}}^{(2\omega)}, \qquad (7.4)$$

which expresses the difference between vectors of modal amplitudes $\boldsymbol{A}_{\nu\pm\epsilon,\mathrm{vac}}^{(2\omega)}$ just above and under the radiating point dipole located inside the infinitesimally thin vacuum sheet. The superscript $^{\mathrm{T}}$ denotes the vector transposition.

The $\boldsymbol{A}_{\nu\pm\epsilon,\mathrm{vac}}^{(2\omega)}$ vectors are connected with vectors of modal amplitudes inside the superstrate $\boldsymbol{A}_0^{(2\omega)}$ and the substrate $\boldsymbol{A}_{M+1}^{(2\omega)}$ [Eqs.(3.16)(3.18)] so that:

$$\boldsymbol{A}_0^{(2\omega)} = \mathbf{L}_\nu^{(2\omega)}[\mathbf{D}_\nu^{(2\omega)}]^{(-1)}\mathbf{D}_{\mathrm{vac}}^{(2\omega)}\boldsymbol{A}_{\nu-\epsilon,\mathrm{vac}}^{(2\omega)} \qquad (7.5)$$

$$\boldsymbol{A}_{\nu+\epsilon,\mathrm{vac}}^{(2\omega)} = [\mathbf{D}_{\mathrm{vac}}^{(2\omega)}]^{-1}\mathbf{D}_\nu^{(2\omega)}[\mathbf{L}_\nu^{(2\omega)}]^{-1}\mathbf{L}_{M+1}^{(2\omega)}A_{M+1}^{(2\omega)}, \qquad (7.6)$$

where the matrix $\mathbf{L}_\nu^{(2\omega)}$ is defined by Eq.(3.17). The matrix products $[\mathbf{D}_{\mathrm{vac}}^{(2\omega)}]^{-1}\mathbf{D}_\nu^{(2\omega)}$ and $[\mathbf{D}_\nu^{(2\omega)}]^{(-1)}\mathbf{D}_{\mathrm{vac}}^{(2\omega)}$ ensure that $\boldsymbol{A}_{\nu\pm\epsilon,\mathrm{vac}}^{(2\omega)}$ are modal amplitudes inside the vacuum sheet and not in the ν-th layer.

Considering Equations (7.4)(7.5)(7.6), we arrive to the expression

$$\boldsymbol{A}_0^{(2\omega)} = \mathbf{L}_{M+1}^{(2\omega)} \cdot \boldsymbol{A}_{M+1}^{(2\omega)} - \mathbf{L}_\nu^{(2\omega)}[\mathbf{D}_\nu^{(2\omega)}]^{-1}\mathbf{D}_{\mathrm{vac}}^{(2\omega)} \cdot \Delta\boldsymbol{A}_\nu^{(2\omega)}, \qquad (7.7)$$

relating the outcoming vectors of modal amplitudes $\boldsymbol{A}_0^{(2\omega)}$, $\boldsymbol{A}_{M+1}^{(2\omega)}$, to the jump of modal amplitudes $\Delta\boldsymbol{A}_\nu^{(2\omega)}$, appearing at the position of the radiating point dipole.

Because the SHG light comes out from the structure, the vectors of modal amplitudes in the superstrate and substrate have the form

$$\boldsymbol{A}_0^{(2\omega)} = [0, \mathcal{E}_{0,\mathbf{s},-}^{(2\omega)}, 0, \mathcal{E}_{0,\mathbf{p},-}^{(2\omega)}]^{\mathrm{T}} \tag{7.8}$$

$$\boldsymbol{A}_{M+1}^{(2\omega)} = [\mathcal{E}_{M+1,\mathbf{s},+}^{(2\omega)}, 0, \mathcal{E}_{M+1,\mathbf{p},+}^{(2\omega)}, 0]^{\mathrm{T}} \tag{7.9}$$

Thus, the relation between the outcoming modal amplitudes and the discontinuity created by the radiating point dipole is:

$$\boldsymbol{A}_{\nu,\mathrm{spd}}^{(2\omega)} = \begin{bmatrix} \mathcal{E}_{M+1,s,+}^{(2\omega)} \\ \mathcal{E}_{0,s,-}^{(2\omega)} \\ \mathcal{E}_{M+1,p,+}^{(2\omega)} \\ \mathcal{E}_{0,p,-}^{(2\omega)} \end{bmatrix} = [\mathbf{K}_{M+1}^{(2\omega)}]^{-1}\mathbf{L}_\nu^{(2\omega)}[\mathbf{D}_\nu^{(2\omega)}]^{-1}\mathbf{D}_{\mathrm{vac}}^{(2\omega)} \cdot \Delta\boldsymbol{A}_\nu^{(2\omega)} \tag{7.10}$$

where the subscript "spd" represents the outcoming SHG radiation generated by the *single point dipole*. $\mathbf{K}_{M+1}^{(2\omega)}$ is defined by

$$\mathbf{K}_{M+1}^{(2\omega)} = \begin{bmatrix} L_{11,M+1}^{(2\omega)} & 0 & L_{13,M+1}^{(2\omega)} & 0 \\ L_{21,M+1}^{(2\omega)} & -1 & L_{23,M+1}^{(2\omega)} & 0 \\ L_{31,M+1}^{(2\omega)} & 0 & L_{33,M+1}^{(2\omega)} & 0 \\ L_{41,M+1}^{(2\omega)} & 0 & L_{43,M+1}^{(2\omega)} & -1 \end{bmatrix}, \tag{7.11}$$

where $L_{ij,M+1}^{(2\omega)}$ are the i, j components of the $\mathbf{L}_{M+1}^{(2\omega)}$ matrix elements. Eq. (7.10) determines the Jones vector of the SHG field propagating in the superstrate $[\mathcal{E}_{0,\mathbf{s},-}^{(2\omega)}, \mathcal{E}_{0,\mathbf{p},-}^{(2\omega)}]$ and the substrate $[\mathcal{E}_{M+1,\mathbf{s},+}^{(2\omega)}, \mathcal{E}_{M+1,\mathbf{p},+}^{(2\omega)}]$, radiated by a single point dipole with complex dipole moment $\boldsymbol{\mu}_\nu^{(2\omega)}$.

Equation (7.10) gives the relation between the jump of the vector of modal amplitudes $\Delta\boldsymbol{A}_\nu^{(2\omega)}$ induced by a single point dipole $\boldsymbol{\mu}_\nu^{(2\omega)}$ and the vector of modal amplitudes $\boldsymbol{A}_{\nu,\mathrm{spd}}^{(2\omega)}$ coming out from the multilayer structure. This result can be summarized into the simple matrix product

$$\boldsymbol{A}_{\nu,\mathrm{spd}}^{(2\omega)} = \mathbf{Y}_\nu^{(2\omega)}\boldsymbol{\mu}_\nu^{(2\omega)}\exp[-i\boldsymbol{q}^{(2\omega)} \cdot \boldsymbol{\rho}_\nu] \tag{7.12}$$

where $\mathbf{Y}_\nu^{(2\omega)}$ is a 4×3 matrix of *outcoming generalized Fresnel coefficients*, which gives directly the relation between the dipole moment $\boldsymbol{\mu}_\nu^{(2\omega)}$ located at the ν-th interface and the radiated far-field vector of modal amplitudes $\boldsymbol{A}_{\nu,\mathrm{spd}}^{(2\omega)}$. Taking into account Eqs. (7.3)(7.4)(7.10), the $\mathbf{Y}_\nu^{(2\omega)}$ matrix is expressed by

$$\mathbf{Y}_\nu^{(2\omega)} = \frac{i(k_0^u)^2}{2\varepsilon_0}\frac{k_0^{(2\omega)}}{N_{z,\mathrm{vac}}}[\mathbf{K}_{M+1}^{(2\omega)}]^{-1}\mathbf{L}_\nu^{(2\omega)}[\mathbf{D}_\nu^{(2\omega)}]^{-1}\mathbf{D}_{\mathrm{vac}}^{(2\omega)}\mathbf{V}^{(2\omega)}, \tag{7.13}$$

where $\mathbf{V}^{(2\omega)}$ is

$$
\mathbf{V}^{(2\omega)} =
\begin{bmatrix}
+\hat{e}^{(2\omega)}_{\text{vac,s},+} \cdot \hat{x} & +\hat{e}^{(2\omega)}_{\text{vac,s},+} \cdot \hat{y} & +\hat{e}^{(2\omega)}_{\text{vac,s},+} \cdot \hat{z} \\
-\hat{e}^{(2\omega)}_{\text{vac,s},-} \cdot \hat{x} & -\hat{e}^{(2\omega)}_{\text{vac,s},-} \cdot \hat{y} & -\hat{e}^{(2\omega)}_{\text{vac,s},-} \cdot \hat{z} \\
+\hat{e}^{(2\omega)}_{\text{vac,p},+} \cdot \hat{x} & +\hat{e}^{(2\omega)}_{\text{vac,p},+} \cdot \hat{y} & +\hat{e}^{(2\omega)}_{\text{vac,p},+} \cdot \hat{z} \\
-\hat{e}^{(2\omega)}_{\text{vac,p},-} \cdot \hat{x} & -\hat{e}^{(2\omega)}_{\text{vac,p},-} \cdot \hat{y} & -\hat{e}^{(2\omega)}_{\text{vac,p},-} \cdot \hat{z}
\end{bmatrix}
=
\begin{bmatrix}
1 & 0 & 0 \\
-1 & 0 & 0 \\
0 & N^{(2\omega)}_{z,\text{vac}}/N^{(2\omega)}_{\text{vac}} & -N^{(2\omega)}_{y,\text{vac}}/N^{(2\omega)}_{\text{vac}} \\
0 & -N^{(2\omega)}_{z,\text{vac}}/N^{(2\omega)}_{\text{vac}} & N^{(2\omega)}_{y,\text{vac}}/N^{(2\omega)}_{\text{vac}}
\end{bmatrix},
$$

$$(7.14)$$

as follows from the scalar product in Eq. (7.3).

The exponential factor in Eqs. (7.3)(7.12) simply describes the variation of the phase of the outcoming modal amplitudes with the lateral position of the radiating point dipole. This factor becomes important in the following Section 7.4, where the total radiation by all dipoles is considered. Since this exponential factor is not included into the $\mathbf{Y}^{(2\omega)}_\nu$ matrix, $\mathbf{Y}^{(2\omega)}_\nu$ matrix does not depend on the lateral position of the point dipole, and is determined only by properties of the multilayer structure (i.e. by the thickness and optical constants of each layer and of the surrounding media) and by the propagation direction $\boldsymbol{q}^{(2\omega)}$ of the radiated light mode.

7.4   SHG in far-field

In the previous Section, I expressed the SHG radiation emitted by a single point dipole placed on the ν-th interface of the multilayer system [Eq. (7.12)]. In this Section, I derive the expressions of the far-field SHG given by dipoles distributed over the entire interface, and finally by all interfaces of the multilayer system.

Firstly, let us express the vector of modal amplitudes $\boldsymbol{A}^{(2\omega)}_{\nu,\text{iface}} = [\mathcal{E}^{(2\omega)}_{M+1,\text{s},+,\text{iface}}, \mathcal{E}^{(2\omega)}_{0,\text{s},-,\text{iface}},$ $\mathcal{E}^{(2\omega)}_{M+1,\text{p},+,\text{iface}}, \mathcal{E}^{(2\omega)}_{0,\text{p},-,\text{iface}}]^{\text{T}}$ radiated by entire ν-th interface in *far-field* ($|\boldsymbol{r}| \gg \lambda^{(2\omega)}$) into the superstrate and the substrate. $\boldsymbol{A}^{(2\omega)}_{\nu,\text{iface}}$ is simply given by a summation over all radiating dipoles

$$
\boldsymbol{A}^{(2\omega)}_{\nu,\text{iface}} = \iint \mathrm{d}\boldsymbol{\rho}_\nu \, \boldsymbol{A}^{(2\omega)}_{\nu,\text{spd}}(\boldsymbol{\rho}_\nu).
\tag{7.15}
$$

Expressing $\boldsymbol{A}^{(2\omega)}_{\nu,\text{spd}}$ by Eq. (7.12), we arrive to:

$$
\boldsymbol{A}^{(2\omega)}_{\nu,\text{iface}} = \iint \mathrm{d}\boldsymbol{\rho}_\nu \, \mathbf{Y}^{(2\omega)} \boldsymbol{\mu}^{(2\omega)}(\boldsymbol{\rho}_\nu) \exp[-i\boldsymbol{\rho}_\nu \cdot \boldsymbol{q}^{(2\omega)}].
\tag{7.16}
$$

The exponential factor in Eq. (7.16) means that sources located at different lateral positions contribute with different phases, i.e. the point dipole located at the $\boldsymbol{\rho}_\nu \equiv [x_\nu, y_\nu]$ position exhibits a phase shift $\delta\phi^{(2\omega)} = -\boldsymbol{\rho}_\nu \cdot \boldsymbol{q}^{(2\omega)}$ with respect to the contribution of the same dipole located at position $\boldsymbol{\rho}_\nu = [0,0]$.

The complex dipole moment $\boldsymbol{\mu}^{(2\omega)}_\nu$ is defined by Eq. (7.2), $\boldsymbol{\mu}^{(2\omega)}_\nu(\boldsymbol{\rho}_\nu, \boldsymbol{q}^{(\omega)}) = \boldsymbol{\chi}(\boldsymbol{\rho}_\nu) \otimes$ $\boldsymbol{E}^{(\omega)}_\nu(\boldsymbol{\rho}_\nu, \boldsymbol{q}^{(\omega)}) \boldsymbol{E}^{(\omega)}(\boldsymbol{\rho}_\nu, \boldsymbol{q}^{(\omega)})$. As it was shown in Section 3.2.5, Eq. (3.33), the electric field at the ν-th interface $\boldsymbol{E}^{(\omega)}_\nu$ can be expressed in a compact matrix form

$$
\boldsymbol{E}^{(\omega)}_\nu(\boldsymbol{\rho}_\nu, \boldsymbol{q}^{(\omega)}) = \exp[i\boldsymbol{\rho}_\nu \cdot \boldsymbol{q}^{(\omega)}]\mathbf{X}^{(\omega)}_\nu \boldsymbol{J}^{(\omega)}_{0,+}
\tag{7.17}
$$

where the incoming Jones vector $\boldsymbol{J}_{0,+}^{(\omega)} = [\mathcal{E}_{0,\mathsf{s},+}^{(\omega)}, \mathcal{E}_{0,\mathsf{p},+}^{(\omega)}]^{\mathrm{T}}$ contains the modal amplitudes of the incident light at frequency ω. The 3×2 incoming Fresnel matrix $\mathbf{X}_{\nu}^{(\omega)}$ is defined by Eq. (3.34).

Combining Eqs. (7.16) and (7.17), the vector of modal amplitudes $\boldsymbol{A}_{\nu,\mathrm{iface}}^{(2\omega)}$ generated by entire ν-th interface writes:

$$\boldsymbol{A}_{\nu,\mathrm{iface}}^{(2\omega)} = \mathbf{Y}_{\nu}^{(2\omega)} \left[\iint \mathrm{d}\boldsymbol{\rho}_{\nu}\, \chi(\boldsymbol{\rho}_{\nu}) \exp[2i\boldsymbol{\rho}_{\nu} \cdot \boldsymbol{q}^{(\omega)} - i\boldsymbol{\rho}_{\nu} \cdot \boldsymbol{q}^{(2\omega)}] \right] \otimes \left(\mathbf{X}_{\nu}^{(\omega)} \boldsymbol{J}_{0,+}^{(\omega)} \right)^2 . \quad (7.18)$$

This equation gives a relation between the outcoming far-field light state,

$$\boldsymbol{A}_{\nu,\mathrm{iface}} = [\mathcal{E}_{M+1,\mathsf{s},+,\mathrm{iface}}^{(2\omega)}, \mathcal{E}_{0,\mathsf{s},-,\mathrm{iface}}^{(2\omega)}, \mathcal{E}_{M+1,\mathsf{p},+,\mathrm{iface}}^{(2\omega)} \cdot \mathcal{E}_{0,\mathsf{p},-,\mathrm{iface}}^{(2\omega)}]^T, \quad (7.19)$$

generated by entire ν-th interface and the incoming Jones vector $\boldsymbol{J}_{0,+}^{(\omega)} = [\mathcal{E}_{0,\mathsf{s},+}^{(\omega)}, \mathcal{E}_{0,\mathsf{p},+}^{(\omega)}]^{\mathrm{T}}$. The Eq. (7.18) shows that the angular dependence of the radiated field $\boldsymbol{A}_{\nu,\mathrm{iface}}^{(2\omega)}$ is determined by

(i) the angular dependence of the generalized Fresnel coefficients, i.e the components of the matrices $\mathbf{X}_{\nu}^{(\omega)}$, $\mathbf{Y}_{\nu}^{(2\omega)}$ matrices.

(ii) the 2D Fourier transform of the spatial dependence of $\chi(\boldsymbol{\rho}_{\nu})$. This is very similar to the Fraunhofer diffraction, where the angular dependence of the diffracted light is determined by the 2D Fourier transform of the diffraction pattern [19, 132].

If Eq. (7.18) is solved assuming that χ varies only in the y direction, then both the radiated and incident light are located in the plane of incidence (yz-plane). On the other hand, when Eq. (7.18) is solved for a general $\chi(\boldsymbol{\rho})$ distribution, it gives rise to light radiated in all directions, i.e. $N_x^{(2\omega)} \neq 0$, $N_y^{(2\omega)} \neq 0$. Mathematically speaking, if χ varies with the x-coordinate, $N_x^{(2\omega)}$ is non-zero any more, contrarily to what was assumed in Section 3.2.1, where the 4×4 matrix formalism is expressed for $N_x = 0$. For treating the case of radiation emitted by a 2D distribution of $\chi(\boldsymbol{\rho})$, the 4×4 matrix formalism has to be generalized to $N_x \neq 0$. This generalization is trivial from a physical point of view, but rather ugly from a mathematical point of view. On the other hand, the boundary conditions we determine presence of a radiating point dipole are always valid even for $N_x^{(2\omega)} \neq 0$ [Eq. (7.3)].

If the spatial properties of the interface are optically uniform (isotropic), then $\chi(\boldsymbol{\rho}_{\nu})$ is constant. Hence, the integration of Eq. (7.18) gives

$$\boldsymbol{A}_{\nu,\mathrm{iface}}^{(2\omega)} = 2\pi \mathbf{Y}_{\nu}^{(2\omega)} \chi \otimes \left(\mathbf{X}_{\nu}^{(\omega)} \boldsymbol{J}_{0,+}^{(\omega)} \right) \delta(2\boldsymbol{q}^{(\omega)} - \boldsymbol{q}^{(2\omega)}) \quad (7.20)$$

Taking into that account $2k_0^{(\omega)} \equiv k_0^{(2\omega)} = 2\omega/c$, then $\delta(2\boldsymbol{q}^{(\omega)} - \boldsymbol{q}^{(2\omega)}) = (1/k_0^{(\omega)})^2 \delta(N_y^{(\omega)} - N_y^{(2\omega)}) \delta(N_x^{(2\omega)} - N_x^{(\omega)})$. Thus, both $N_x^{(\omega)} = N_x^{(2\omega)}$ and $N_y^{(\omega)} = N_y^{(2\omega)}$ are the same for an incident (ω) and a radiated (2ω) light. In other words, the emitted SHG light follows the Snell law. This corresponds to the well know property that the incidence angle of the fundamental field (at ω) is opposite to the emission angle of the SHG field radiated at 2ω [3, 133, 134] with respect to the sample normal, if one assumes that the superstrate has no dispersion $\varepsilon_{ij,0}^{(\omega)} = \varepsilon_{ij,0}^{(2\omega)}$.

Another important consequence of Eq. (7.20) is that the modal amplitudes radiated by the entire uniform interface can be expressed (within a scaling factor 2π), as a radiation

of a single point dipole radiating in the direction determined by vector $2\boldsymbol{q}^{(\omega)} = \boldsymbol{q}^{(2\omega)}$, i.e. when $[N_x^{(2\omega)}, N_y^{(2\omega)}] = [N_x^{(\omega)}, N_y^{(\omega)}]$.

Note that the influence of the finite size of the light spot can be straightforwardly incorporated in Eq. (7.18). In that case the incoming Jones vector $\boldsymbol{J}_{0,+}^{(\omega)}$ is a lateral function of $\boldsymbol{\rho}_\nu$, which can be incorporated before the integration of Eq. (7.18).

The far-field SHG radiated vector of modal amplitudes $\boldsymbol{A}_{\mathrm{ml}}^{(2\omega)}$ is simply given by summing all interfaces contributions in the multilayer (ml) structure

$$\boldsymbol{A}_{\mathrm{ml}}^{(2\omega)} = \sum_{\nu=1}^{M+1} \boldsymbol{A}_{\nu,\mathrm{iface}}^{(2\omega)}. \tag{7.21}$$

Recall that radiation emitted by dipoles located on various interfaces is assumed to be coherent. In a similar way, as for the vector $\boldsymbol{A}_{\nu,\mathrm{iface}}^{(2\omega)}$, the elements of the $\boldsymbol{A}_{\mathrm{ml}}^{(2\omega)}$ vector are defined by

$$\boldsymbol{A}_{\mathrm{ml}}^{(2\omega)} \equiv [\mathcal{E}_{M+1,\mathrm{s},+,\mathrm{ml}}^{(2\omega)}, \mathcal{E}_{0,\mathrm{s},-,\mathrm{ml}}^{(2\omega)}, \mathcal{E}_{M+1,\mathrm{p},+,\mathrm{ml}}^{(2\omega)}, \mathcal{E}_{0,\mathrm{p},-,\mathrm{ml}}^{(2\omega)}]^{\mathrm{T}}. \tag{7.22}$$

They represent the magnitudes of the $\mathtt{s}$ and $\mathtt{p}$ polarised modes propagating in the superstrate (subscript 0) and in the substrate (subscript $M+1$) in a direction defined by $\boldsymbol{q}^{(2\omega)} = k_0^{(2\omega)}[0, N_y^{(2\omega)}]$, and originating from the entire multilayer structure.

7.5   SHG light intensity in far-field

In this Section, I calculate the total SHG light intensity $I_j^{(2\omega)}$ outcoming from the multilayer structure (i.e. in the superstrate or in the substrate) as a function of the modal amplitudes $\mathcal{E}_{j,\Pi,d,\mathrm{ml}}^{(2\omega)}$ originating from the entire multilayer structure [Eq. (7.22)]. The subscripts j and d refer to the superstrate ($j = 0$, $d = -$) or to the substrate ($j = M+1$, $d = +$). Recall that the superscript Π denotes the polarization state ($\mathtt{s}$ or $\mathtt{p}$) of the outcoming light.

The in-depth (z) dependence of the modal amplitude $\mathcal{E}_{j,\Pi,d,\mathrm{ml}}^{(2\omega)}(\boldsymbol{q}, z)$ propagating in a superstrate or a substrate writes [Eq.(3.10)]

$$\mathcal{E}_{j,\Pi,d,\mathrm{ml}}^{(2\omega)}(\boldsymbol{q}, z) = \mathcal{E}_{j,\Pi,d,\mathrm{ml}}^{(2\omega)}(\boldsymbol{q}, z_j) \exp[i k_{z,j,d}^{(2\omega)}(z - z_j)], \tag{7.23}$$

where $\mathcal{E}^{(2\omega)}(\boldsymbol{q}, z_j)^{(2\omega)}$ is the modal amplitude at $z = z_j$, where z_j is the position of either the first ($j = 1$) or the last ($j = M+1$) interface with superstate or substrate, respectively. In the derivation of Eq.(7.23), I consider that in the substrate (superstrate) the 2ω wave propagates only in the plus (minus) direction. The substrate or superstrate, in which the ligth intensity can be measured, are assumed to be isotropic, i.e. $k_{z,j,\mathrm{s},d}^{(2\omega)} = k_{z,j,\mathrm{p},d}^{(2\omega)} \equiv k_{z,j,d}^{(2\omega)}$.

Let us find the relation between the electric field $\boldsymbol{E}^{(2\omega)}(\boldsymbol{r})$ in *far field* and the modal amplitudes $\mathcal{E}_{j,\Pi,d,\mathrm{ml}}^{(2\omega)}$. This relation comes from the definition of the $\boldsymbol{q}$-space [Eq.(3.4)], where the transformation between the electric field in the $\boldsymbol{r}$ and $\boldsymbol{q}$-space is expressed. Substituting Eq. (7.23) into Eq.(3.4), we arrive to:

$$\boldsymbol{E}_{j,\Sigma,d,\mathrm{ml}}^{(2\omega)}(\boldsymbol{r}) = \frac{1}{(2\pi k_0^u)^2} \iint \boldsymbol{\mathcal{E}}_{j,\Sigma,d,\mathrm{ml}}^{(2\omega)} \exp[i\boldsymbol{\rho} \cdot \boldsymbol{q} + i k_{z,j,d}^{(2\omega)} z] \, \mathrm{d}\boldsymbol{q}, \tag{7.24}$$

where the vector of modal amplitudes is expressed by $\boldsymbol{\mathcal{E}}^{(2\omega)}_{j,\Sigma,d,\mathrm{ml}} = \mathcal{E}^{(2\omega)}_{j,\mathbf{s},d,\mathrm{ml}}\hat{\boldsymbol{e}}^{(2\omega)}_{j,\mathbf{s},d} + \mathcal{E}^{(2\omega)}_{j,\mathbf{p},d,\mathrm{ml}}\hat{\boldsymbol{e}}^{(2\omega)}_{j,\mathbf{p},d}$, where $\mathcal{E}^{(2\omega)}_{j,\mathbf{s}/\mathbf{p},d,\mathrm{ml}}$ are the outcoming modal amplitudes from the multilayer structure, as defined by Eq. (7.22).

As already said, I want to express the electric field $\boldsymbol{E}^{(2\omega)}_{j,\Sigma,d,\mathrm{ml}}(\boldsymbol{r})$ in far-field. To determine the quantitative relation between $\boldsymbol{E}^{(2\omega)}_{j,\Sigma,d,\mathrm{ml}}(\boldsymbol{r})$ and $\boldsymbol{\mathcal{E}}^{(2\omega)}_{j,\Sigma,d,\mathrm{ml}}$, it is convenient to proceed at the integration of Eq. (7.24) in polar coordinates,

$$\begin{bmatrix} x \\ y \\ z \end{bmatrix} = \begin{bmatrix} r\sin\theta_r\cos\varphi_r \\ r\sin\theta_r\sin\varphi_r \\ r\cos\theta_r \end{bmatrix} \qquad \begin{bmatrix} k_x \\ k_y \\ k_z \end{bmatrix} = \begin{bmatrix} k_j^{(2\omega)}\sin\theta_k\cos\varphi_k \\ k_j^{(2\omega)}\sin\theta_k\sin\varphi_k \\ k_j^{(2\omega)}\cos\theta_k \end{bmatrix}, \qquad (7.25)$$

where θ_r and φ_r are the polar angles of the $\boldsymbol{r}$-vector and θ_k and φ_k those of the $\boldsymbol{k}_j^{(2\omega)}$-vector. Consequently, the phase factor ϕ in Eq. (7.24) becomes

$$\phi = i\boldsymbol{\rho}\cdot\boldsymbol{q} + ik^{(2\omega)}_{z,j,d}z \equiv i\boldsymbol{k}_j^{(2\omega)}\cdot\boldsymbol{r} = irk_j^{(2\omega)}[\cos(\theta_r-\theta_k)+[\cos(\varphi_r-\varphi_k)-1]\sin\theta_r\sin\theta_k] \tag{7.26}$$

and the differencial quantity $\mathrm{d}\boldsymbol{q} \equiv \mathrm{d}k_x\mathrm{d}k_y$ writes

$$\mathrm{d}k_x\mathrm{d}k_y = (k^{(2\omega)})^2\cos\theta_k\sin\theta_k\mathrm{d}\theta_k\mathrm{d}\varphi_k. \tag{7.27}$$

The integration can be done after substitution of previous two Eqs. (7.26)(7.27) into Eq. (7.24). However, the integration is not trivial and several tricks are used:

(i) when integrating a function like $I = \int \mathrm{d}w\, g(w)\exp[af(w)]$, for $a \gg 1$, if $f(w)$ is a maximum for $w = w_0$, the exponential factor has maximum for $w = w_0$ as well. When a is very large, $\exp[af(w)]$ has somewhat the character of a Dirac δ-fuction, i.e. it is nearly zero except at $w = w_0$, for which the exponential function is very large. In other words, the exponential function "amplifies" the $f(w)$ maximum. Hence, if $g(w)$ is a slowly varying function, it can be factorised out infront of the integral, so that $I \approx g(w_0)\int \mathrm{d}w\,\exp[af(w)]$.

(ii) Since the maximum of a smooth function can always be approximed by a parabola, $f(w) \approx f(w_0) + (1/2)b(w - w_0)^2$ with $b = \partial f/\partial w_{(w=w_0)}$, the integration can be proceeded, leading to $I = g(w_0)\exp[af(w_0)](2\pi/ab)^{(1/2)}$.

(iii) Although properties (i) and (ii) are valid for $a > 0$, the same results hold for a pure imaginary number $a = ic$, as $a = ic + \epsilon$ with $\epsilon \to 0$.

Considering the properties (i) – (iii), the integration in Eq. (7.24) can be proceeded. Thus, in far-field approximation, we find the relation between the electric fields expressed in the $\boldsymbol{q}$-space and $\boldsymbol{r}$-space

$$\boldsymbol{E}^{(2\omega)}(\boldsymbol{r}) = \frac{2\pi}{(2\pi k_0^u)^2}\frac{k^{(2\omega)}}{ir}\frac{N_z^{(2\omega)}}{N^{(2\omega)}}\,\boldsymbol{\mathcal{E}}^{(2\omega)}_{j,\Sigma,d,\mathrm{ml}}. \tag{7.28}$$

where $N_z^{(2\omega)}/N^{(2\omega)} = \cos\theta_k$ and $\boldsymbol{\mathcal{E}}^{(2\omega)}_{j,\Sigma,d,\mathrm{ml}}$ is the modal vector amplitude of the ligth mode which is described by a $\boldsymbol{q}$-vector, for which $\boldsymbol{k}_{j,d}^{(2\omega)} = [\boldsymbol{q}, k_{z,j,d}^{(2\omega)}]$ is parallel to $\boldsymbol{r}$ associated

with the position of the far-field detector. Thus, in conclusion, the only contribution to $\boldsymbol{E}_{j,\Sigma,d,\mathrm{ml}}^{(2\omega)}(\boldsymbol{r})$ is determined by one plane wave for which $\boldsymbol{k}_{j,d}^{(2\omega)}$ is parallel to $\boldsymbol{r}$.

Note, that our above approach is analogous to the "method of stationary phase": the electric field in the far-field approximation is only obtained for the $\boldsymbol{k}$-vector, where the $\boldsymbol{k}$-gradient of the phase is zero, [19, 132]

$$\nabla_{\boldsymbol{k}}\phi(\boldsymbol{q}) \equiv \begin{bmatrix} \frac{\partial}{\partial k_x}\phi \\ \frac{\partial}{\partial k_y}\phi \\ \frac{\partial}{\partial k_z}\phi \end{bmatrix} = 0, \tag{7.29}$$

where ϕ is the phase in the exponent of Eq. (7.24).

Substituting the result of Eq. (7.28) into the light intensity expression [17], we find

$$\begin{aligned} I_j^{(2\omega)}(\theta,\varphi) = \quad & I_j^{(2\omega)}(\boldsymbol{r}) = |\langle \boldsymbol{S}_j(\boldsymbol{r}) \rangle| = \frac{1}{2}|\boldsymbol{E}_j^{(2\omega)}(\boldsymbol{r}) \times \boldsymbol{H}_j^{(2\omega)}(\boldsymbol{r})| = \frac{1}{2\eta_0} N_j^{(2\omega)} |\boldsymbol{E}_j^{(2\omega)}(\boldsymbol{r})|^2 \\ \\ = \quad & \frac{1}{2\eta_0} \frac{(2\pi k_0^{(2\omega)})^2}{(2\pi k_0^u)^4} \frac{N_j^{(2\omega)}|N_{z,j}^{(2\omega)}|^2}{r^2} |\boldsymbol{\mathcal{E}}_{j,\Sigma,d,\mathrm{ml}}^{(2\omega)}(\boldsymbol{q})|^2 \\ \\ = \quad & \frac{1}{2\eta_0} \frac{(2\pi k_0^{(2\omega)})^2}{(2\pi k_0^u)^4} \frac{N_j^{(2\omega)}|N_{z,j}^{(2\omega)}|^2}{r^2} \left(|\mathcal{E}_{j,\mathrm{s},d,\mathrm{ml}}^{(2\omega)}|^2 + |\mathcal{E}_{j,\mathrm{p},d,\mathrm{ml}}^{(2\omega)}|^2 \right), \end{aligned} \tag{7.30}$$

where $\eta_0 = \sqrt{\mu_0/\varepsilon_0}$ is the vacuum impedance and $|\langle \boldsymbol{S}_j(\boldsymbol{r}) \rangle|$ the time average of the Poynting vector. Eq. (7.30) is the final result of this Section, expressing the radiated light intensity $I_j^{(2\omega)}$ from the modal vector amplitude $\boldsymbol{\mathcal{E}}_{j,\Sigma,d,\mathrm{ml}}^{(2\omega)} = \mathcal{E}_{j,\mathrm{s},d\mathrm{ml}}^{(2\omega)}\hat{e}_{j,\mathrm{s},d}^{(2\omega)} + \mathcal{E}_{j,\mathrm{p},d\mathrm{ml}}^{(2\omega)}\hat{e}_{j,\mathrm{p},d}^{(2\omega)}$ in $\boldsymbol{q}$-space [Eq. (3.8)]. Together with our previous extended 4×4 matrix formalism, this expression gives a *quantitative* relation between the complex dipole moment $\boldsymbol{\mu}^{(2\omega)}$ of the radiating point dipole and the measured light intensity $I_j^{(2\omega)}(\theta_j,\varphi_j)$. Several comments about Eq. (7.30) can be done:

- Let us express the emitted light intensity by a single point dipole in an unbound media. It can be expressed by substituting the modification of boundary conditions in the presence of a point dipole $\Delta\mathcal{E}_{\nu,\mathrm{s}/\mathrm{p},\pm}^{\mu}$ [Eq. (7.3)] into the far-field expression of the light intensity [Eq. (7.30)]

$$I(\boldsymbol{r}) = |\langle \boldsymbol{S}_j(\boldsymbol{r}) \rangle| = \frac{(k_0^{(\omega_0)})^4 N_j}{32\pi^2 \eta_0 (\epsilon_0)^2} \frac{(|\boldsymbol{\mu}^{(2\omega)}|\cos\theta_j)^2}{r^2}, \tag{7.31}$$

  where θ_j is the angle between the dipole direction and the direction of observation, i.e. $\cos\theta_j = \boldsymbol{\mu}^{(2\omega)} \cdot \boldsymbol{k}_j^{(2\omega)}/(|\boldsymbol{\mu}^{(2\omega)}||\boldsymbol{k}_j^{(2\omega)}|)$. Eq. (7.31) is in perfect agreement with textbook fomula [17, 135].

  From the Eq. (7.31), it follows that two identical dipoles $\boldsymbol{\mu}$ embedded in two different infinite materials with refractive indices N_a and N_b, emit light intensities so that their ratio is $I_a/I_b = N_a/N_b$, when measured in a direction perpendicular to $\boldsymbol{\mu}$. However, for radiating dipoles located at the interface between two semi-infinite materials, having refractive indices N_a, N_b, this intensity ratio becomes [Eq. (7.30)] $I_a/I_b = (N_a/N_b)^3$ [131].

- The most important point originating from Eq. (7.30) is that the measured light intensity has different expressions, depending on the space in which the calculations have been performed. For modal amplitudes coming form the $\boldsymbol{k}$-space, people find that the ligth intensity is proportional to $|\mathcal{E}_{\boldsymbol{k},j}^{(2\omega)}|^2$ [19, 17]. In the $\boldsymbol{q}$-space, in which I developed the SHG formalism, the light intensity is proportional to $|N_{z,j}^{(2\omega)}\mathcal{E}_{\boldsymbol{q},j}^{(2\omega)}|^2$. The presence of $N_{z,j}^{(2\omega)}$ is necessary, otherwise the angular dependence of the radiated light is expressed incorrectly.

- The modifications of boundary conditions in the presence of a radiating dipole $\Delta\mathcal{E}_{\nu,\mathtt{s}/\mathtt{p},\pm}^{\mu}$ [Eq.(7.3)] are proportional to the factor $(k_0^u)^2$, which equalizes units between the electric field expressed in the $\boldsymbol{r}$, $\boldsymbol{q}$ and $\boldsymbol{k}$ spaces [Eqs. (3.2)(3.4)]. Thus, the modal amplitudes $\mathcal{E}_{j,\mathtt{s}/\mathtt{p},d,\mathrm{ml}}^{(2\omega)}$ outcoming from the structure are proportional to $(k_0^u)^2$ as well. Furthermore, $I_j^{(2\omega)}$ in Eq. (7.30) is proportional to $1/(k_0^u)^4$. Thus, the final relation between the light intensity $I_j^{(2\omega)}$ and the dipole moment $\boldsymbol{\mu}_\nu^{(2\omega)}$ does not depend on the factor k_0^u. This is expected since k_0^u can have any arbitrary value and light intensity is an observable, which must be independent on such a "free parameter".

7.6 Conclusion of Chapter 7

In this Section, I introduce a very general and new formalism which allows to calculate the Second Harmonic Generation from an arbitrary magnetized or non-magnetized multilayer structure, which can consist of optically anisotropic layers. Starting from an electric point dipole radiation, the resulting outcoming SHG intensity is then given by the integration over all radiating dipoles. This gives also a possibility to calculate the SHG response of any set of coherent or non-coherent radiating dipoles. For example, our formalism may be applied to SHG and MOSHG of stacks of non-homogenously magnetized layers. This formalism has been implemented numerically (for numerical examples see either the next Chapter 8, or our article [131]).

Since our formalism is designed to be general, further extensions could be done:

(i) It would be usefull to express modified boundary conditions in the presence of other radiating sources, e.g. magnetic point dipoles or electric point quadrupoles, as symmetry arguments allows such sources to exist even in bulk material. These sources can contribute to SHG radiation [1, 2, 136]. Modified boundary conditions in the presence of such sources can be determined by my formalism, as developed in Appendix D.

(ii) To have a better insight about SHG radiation, it would be convenient to express simplified analytical expressions for SHG radiation (analogously to the ultrathin FM film approximation).

(iii) Extending my numerical implementation of SHG radiation to the case of any 2D-distribution of point dipoles, laterally inhomogenous system could be investigated.

In-depth sensitivity of SHG radiation

In the previous Chapter, I have introduced the Second Harmonic Generation (SHG) of light emitted by an electric point dipole, allowing to calculate the SHG radiation from a multilayer structure. In this Chapter, I have used this formalism to discuss about the in-depth sensitivity of the SHG radiation, i.e. on its selectivity to buried interfaces located at different in-depths in the multilayer structure.

In a multilayer magnetic structure, two main questions arise about the depth sensitivity of SHG and MOSHG:

- what is the probing depth of MOSHG and SHG radiation at each interface, depending on the associated third-rank susceptibility tensor χ elements?

  As it has been already discussed, in the electric dipole approximation, the SHG is intrinsically generated in media where space inversion is broken. Thus, in the case of a multilayer structure built with centrosymmetric materials (such as metals), the SHG is dominantly generated around interfaces. However, symmetry arguments alone do not predict what is the "active depth" from which the SHG originates.

  As was shown by A.V. Pethukov and A. Liebsch [137] on an Al(111) surface, the SHG radiated by a normal current (i.e. by a normal dipole components $\mu_z^{(2\omega)}$) is more surface sensitive than SHG radiated by tangential currents (i.e. by tangential dipole components $\mu_x^{(2\omega)}$ or $\mu_y^{(2\omega)}$). They found that χ_{zzz} arises from an ultrathin region of thickness $\sim 0.1\,\mathrm{nm}$ localized at the interface, although χ_{xxx} originates from a much thicker region ($\sim 2\,\mathrm{nm}$). Both elements rely to different modifications of the electronic structure near the interface, χ_{zzz} being sensitive to the surface charging and not to interface corrugation, while χ_{xxx} being more sensitive to electronic scattering and interface corrugation [137].

  These predictions were confirmed by J. Güdde *et al.* [138, 139] for ultrathin FM films (Co and Ni) deposited on Cu(001).

- How can SHG be selective to a particular interface or to the surface in a multilayer structure? In another words, which SHG configurations are more selective to a given interface?

In this Chapter, I will try to answer this question considering generalized incoming and outcoming Fresnel elements. Incoming Fresnel elements (elements of the $\mathbf{X}_\nu^{(\omega)}$ matrix) relate the incoming Jones vector to the electric field at each interface [Eq. (3.33)]. On the other hand, outcoming Fresnel elements (elements of the $\mathbf{Y}_\nu^{(2\omega)}$ matrix [Eq. (7.12)] or of the later defined $\mathbf{Z}_{\nu,d}^{(2\omega)}$ matrix [Eq. (8.8)]) relate the dipole moment components $\mu_{j,\nu}^{(2\omega)}$, $j = \{x, y, z\}$ to the outcoming Jones vector of the emitted SHG light. To my knowledge, no general treatment including Fresnel elements has been investigated so far.

On a one hand, A. Kirilyuk *et al.* have determined the values of some second order susceptibility elements χ_{ijk} for the air/Pt and Pt/CoNi interfaces in the Pt/CoNi/Pt film structure by fitting the measured angular dependence of the SHG intensity for several samples having different CoNi thickness [3]. On the other hand, for example, Y.Z. Wu *et al.*, when interpreting the MOSHG data in Ni/Cu structures [140], have neglected the influence of Fresnel elements.

The MOSHG experiments presented in this Chapter have been performed by L. Sampaio during his visiting stay in our group at Orsay, on an experimental setup located at the Laboratoire Charles Fabry at the Institut d'Optique, Orsay. In this Chapter, I develop theoretical calculations giving some insight into their interpretation.

8.1   MOSHG setup, configurations and related χ-tensor elements

8.1.1   MOSHG setup

The sketch of the used MOSHG setup is presented on Figure 8.1. The light source is a pulsed Ti-sapphire laser emitting light at 800 nm (E=1.55 eV) with a pulse length of 100 fs, a repeat rate of 86 MHz and an average power of 20-100 mW. The laser light is
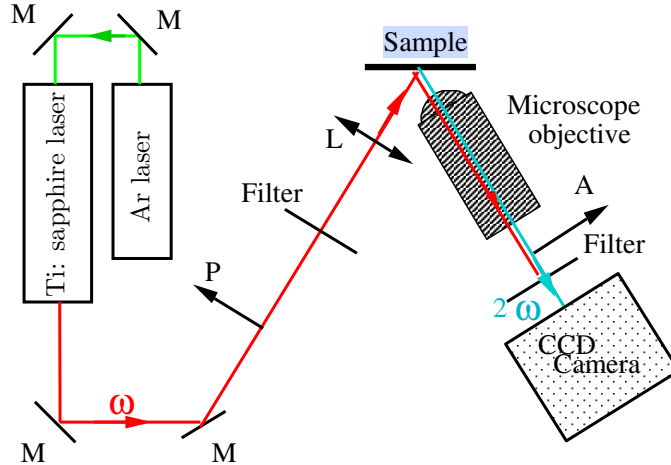
Figure 8.1: Sketch of the MOSHG setup.

linearly `s` or `p` polarized by a Glan polarizer P. After, the light passes through a filter blocking the spurious second harmonic light generated by all optical elements. Then, the light penetrates into the sample, which emits SHG field. It should be mentioned that although the light frequency is doubled, radiation still follows the Snell law [see Eq. (7.20)]. Thus, both reflected fundamental (at ω) and emitted (2ω) SHG light passes through a new set of filters, blocking light at ω frequency. The used filter has a high selectivity so that it insures a total extinction ratio of about 10^{-15}. Then, the light passes through an analyzer A, usually oriented along either the `s` or the `p`-direction. Finally, the light intensity is detected by a N_2-cooled CCD camera.

Within this experimental setup, it is also possible to measure LMOKE in the same experimental conditions, particularly to keep the same heating conditions. For LMOKE, the filters are obviously interchanged to detect light at ω frequency.

The polarization of the incident light beam at ω and the polarization state before detection define the basic configurations of SHG and MOSHG. They are called `pp`, `ps`, `sp` or `ss` configurations. For example, `sp` means that the incident beam is `s` polarized (at ω) and the analyzer transmits `p` polarized light (at 2ω).

8.1.2 Non-linear susceptibility tensor χ and its dependence on magnetization

In this Section, I discuss on the form of the non-linear susceptibility tensor χ and on its dependence on the interface magnetization. In the following, I limit myself to interfaces having 4-fold, 6-fold and ∞-fold symmetry, and to SHG allowed by electric dipole transitions. I do not consider less efficient contributions to SHG, due to electric quadrupole and magnetic dipole mechanisms. Furthermore, I assume that the multilayer structure is made of optically isotropic layers and interfaces.

The electric point dipole moment $\boldsymbol{\mu}_\nu^{(2\omega)} = \chi_\nu \otimes \boldsymbol{E}_\nu^{(\omega)} \boldsymbol{E}_\nu^{(\omega)}$ is determined for each interface of the multilayer structure (Section 7.2). It can be expressed in the matrix form:

$$\begin{bmatrix} \mu_x^{(2\omega)} \\ \mu_y^{(2\omega)} \\ \mu_z^{(2\omega)} \end{bmatrix} = \begin{bmatrix} \chi_{xxx} & \chi_{xyy} & \chi_{xzz} & \chi_{xyz} & \chi_{xxz} & \chi_{xxy} \\ \chi_{yxx} & \chi_{yyy} & \chi_{yzz} & \chi_{yyz} & \chi_{yxz} & \chi_{yxy} \\ \chi_{zxx} & \chi_{zyy} & \chi_{zzz} & \chi_{zyz} & \chi_{zxz} & \chi_{zxy} \end{bmatrix} \cdot \begin{bmatrix} (E_x^{(\omega)})^2 \\ (E_y^{(\omega)})^2 \\ (E_z^{(\omega)})^2 \\ E_z^{(\omega)} E_y^{(\omega)} \\ E_z^{(\omega)} E_x^{(\omega)} \\ E_x^{(\omega)} E_y^{(\omega)} \end{bmatrix}, \qquad (8.1)$$

where the non-linear susceptibility tensor χ of rank 3 is expressed by a 3×6 matrix.

The tensor χ can be separated into two parts, odd and even in magnetization. Its development will be limited to linear terms in magnetization [141]. Odd terms are linear in magnetization and are labeled by the superscript $^{(m)}$. Furthermore, the terms even in magnetization are assumed to be constant (non-magnetic); the superscript $^{(nm)}$ will be used. Thus, the non-linear susceptibility can be decomposed into:

$$\chi = \chi^{(nm)} + \chi^{(m)}. \qquad (8.2)$$

As reported in most of the articles concerning MOSHG [1, 2, 142], or by considering symmetry arguments [38], the susceptibility tensor $\chi^{(\mathrm{tra})}$ for an in-plane transversally

magnetized interface, $M||x$, has the form[1]:

$$\chi^{(\text{tra})} = \begin{bmatrix} 0 & 0 & 0 & 0 & \chi_{xzx}^{(nm)} & \chi_{xxy}^{(m)} \\ \chi_{yxx}^{(m)} & \chi_{yyy}^{(m)} & \chi_{yzz}^{(m)} & \chi_{yzy}^{(nm)} & 0 & 0 \\ \chi_{zxx}^{(nm)} & \chi_{zyy}^{(nm)} & \chi_{zzz}^{(nm)} & \chi_{zzy}^{(m)} & 0 & 0 \end{bmatrix}, \tag{8.3}$$

where the elements $\chi_{ijk}^{(m)}$ are linear with magnetization, and $\chi_{ijk}^{(nm)}$ independent on it. Similarly, for a longitudinally magnetized interface, $M||y$,

$$\chi^{(\text{lon})} = \begin{bmatrix} \chi_{xxx}^{(m)} & \chi_{xyy}^{(m)} & \chi_{xzz}^{(m)} & 0 & \chi_{xzx}^{(nm)} & 0 \\ 0 & 0 & 0 & \chi_{yzy}^{(nm)} & 0 & \chi_{yxy}^{(m)} \\ \chi_{zxx}^{(nm)} & \chi_{zyy}^{(nm)} & \chi_{zzz}^{(nm)} & 0 & \chi_{zzx}^{(m)} & 0 \end{bmatrix} \tag{8.4}$$

and for polar magnetization, $M||z$

$$\chi^{(\text{pol})} = \begin{bmatrix} 0 & 0 & 0 & \chi_{xzy}^{(m)} & \chi_{xzx}^{(nm)} & 0 \\ 0 & 0 & 0 & \chi_{yzy}^{(nm)} & -\chi_{xzy}^{(m)} & 0 \\ \chi_{zxx}^{(nm)} & \chi_{zyy}^{(nm)} & \chi_{zzz}^{(nm)} & 0 & 0 & 0 \end{bmatrix}. \tag{8.5}$$

When rotating the sample by 90° around the z-axis, the transverse magnetization becomes longitudinal. Thus, some χ elements induced by a transverse magnetization are identical to others induced by a longitudinal magnetization, as expected when rotating the tensor χ by 90°. The relations between χ-elements are summarized in Table 8.1 for both magnetic and non-magnetic χ-elements.

	transverse $\to$ longitudinal		
magnetic	$\chi_{yzz}^{(m)}$	$\to$	$-\chi_{xzz}^{(m)}$
	$\chi_{yxx}^{(m)}$	$\to$	$-\chi_{xyy}^{(m)}$
	$\chi_{yyy}^{(m)}$	$\to$	$-\chi_{xxx}^{(m)}$
	$\chi_{zzy}^{(m)}$	$\to$	$-\chi_{zzx}^{(m)}$
	$\chi_{xxy}^{(m)}$	$\to$	$-\chi_{yxy}^{(m)}$
non-mag.	$\chi_{zxx}^{(nm)}$	$\to$	$\chi_{zyy}^{(nm)}$
	$\chi_{yzy}^{(nm)}$	$\to$	$\chi_{xzx}^{(nm)}$

Table 8.1: Relations between some magnetic and non-magnetic non-linear susceptibility tensor elements, resulting from symmetry arguments.

8.2 SHG formalism considering generalized Fresnel elements

In this Section, I summarize first the SHG formalism presented in Chapter 7, introducing the generalized incoming and outcoming Fresnel elements of the $\mathbf{X}_{\nu}^{(\omega)}$ and $\mathbf{Z}_{\nu,d}^{(2\omega)}$ matrices.

---

[1] The axis convention is defined in Appendix A

When these Fresnel matrices are known, the SHG or MOSHG responses of the multilayer structure can be compactly calculated through four steps, defined by the following Eqs.(8.6),(8.7),(8.8) and (8.11).

I still assume that the multilayer structure is made of isotropic layers. This allows to simplify considerably the $\mathbf{X}_\nu^{(\omega)}$ and $\mathbf{Z}_{\nu,d}^{(2\omega)}$ matrices since half of their elements vanishes. This approximation is justified in the case of FM metallic structures, since the optical perturbations induced by the magnetization are usually small. Furthermore, the χ tensors are assumed not to depend on the lateral $[x, y]$ coordinates.

The polarization state and intensity of the incident light beam at frequency ω is described by the incoming Jones vector $\boldsymbol{J}_{0,+}^{(\omega)} = [\mathcal{E}_{0,s,+}^{(\omega)}, \mathcal{E}_{0,p,+}^{(\omega)}]^{\mathrm{T}}$. After penetrating into the multilayer structure, the light beam produce an electric field $\boldsymbol{E}_\nu^{(\omega)} = [E_{x,\nu}^{(\omega)}, E_{y,\nu}^{(\omega)}, E_{z,\nu}^{(\omega)}]^{\mathrm{T}}$ at each ν-th interface. $\boldsymbol{J}_{0,+}^{(\omega)}$ and $\boldsymbol{E}_\nu^{(\omega)}$ are related by the incoming Fresnel matrix $\mathbf{X}_\nu^{(\omega)}$ [Eq. (3.34)]

$$
\begin{bmatrix} E_{x,\nu}^{(\omega)} \\ E_{y,\nu}^{(\omega)} \\ E_{z,\nu}^{(\omega)} \end{bmatrix} = \begin{bmatrix} X_{xs,\nu}^{(\omega)} & 0 \\ 0 & X_{yp,\nu}^{(\omega)} \\ 0 & X_{zp,\nu}^{(\omega)} \end{bmatrix} \cdot \begin{bmatrix} \mathcal{E}_{0,s,+}^{(\omega)} \\ \mathcal{E}_{0,p,+}^{(\omega)} \end{bmatrix}. \tag{8.6}
$$

Because $E_z^{(\omega)}$ is not continuous through the interface, the electric field at the ν-th interface is assumed to be represented by the average of values of the electric field just above and below this interface [Eq. (3.32)], i.e., $\boldsymbol{E}_\nu^{(\omega)} = (\boldsymbol{E}_{\nu+\epsilon}^{(\omega)} + \boldsymbol{E}_{\nu-\epsilon}^{(\omega)})/2$, with $\epsilon \to 0$.

The electric field $\boldsymbol{E}_\nu^{(\omega)}$ creates a radiating dipole on the ν-th interface, oscillating at frequency 2ω and having a complex moment $\boldsymbol{\mu}_\nu^{(2\omega)}$

$$
\begin{bmatrix} \mu_{x,\nu}^{(2\omega)} \\ \mu_{y,\nu}^{(2\omega)} \\ \mu_{z,\nu}^{(2\omega)} \end{bmatrix} = \chi_\nu \cdot \begin{bmatrix} (E_{x,\nu}^{(\omega)})^2 \\ (E_{y,\nu}^{(\omega)})^2 \\ (E_{z,\nu}^{(\omega)})^2 \\ E_{y,\nu}^{(\omega)} E_{z,\nu}^{(\omega)} \\ E_{x,\nu}^{(\omega)} E_{z,\nu}^{(\omega)} \\ E_{x,\nu}^{(\omega)} E_{y,\nu}^{(\omega)} \end{bmatrix} \tag{8.7}
$$

as already expressed by Eq. (8.1) in the most general case. Then, the dipole radiation propagates through the multilayer structure and finally across the superstrate or the substrate. The Jones vector, describing the light radiated by a single point dipole (abbreviated by "spd"), located at the ν-th interface, is $\boldsymbol{J}_{\nu,d,\mathrm{spd}}^{(2\omega)} = [\mathcal{E}_{\nu,s,d,\mathrm{spd}}^{(2\omega)}, \mathcal{E}_{\nu,p,d,\mathrm{spd}}^{(2\omega)}]$, where $(j = 0, d = -)$ stands for light in the superstrate and $(j = M + 1, d = +)$ in the substrate. Recall that the subscript d denotes the direction of the propagation mode and thus $+, -$ indicate the direction of light propagation in the positive or negative z-direction. The outcoming Jones vector $\boldsymbol{J}_{\nu,d,\mathrm{spd}}^{(2\omega)}$ is connected to the complex dipole moment $\boldsymbol{\mu}_\nu^{(2\omega)}$ through the Fresnel outcoming matrix $\mathbf{Z}_{\nu,d}^{(2\omega)}$

$$
\begin{bmatrix} \mathcal{E}_{\nu,s,d,\mathrm{spd}}^{(2\omega)} \\ \mathcal{E}_{\nu,p,d,\mathrm{spd}}^{(2\omega)} \end{bmatrix} = \begin{bmatrix} Z_{sx,\nu,d}^{(2\omega)} & 0 & 0 \\ 0 & Z_{py,\nu,d}^{(2\omega)} & Z_{pz,\nu,d}^{(2\omega)} \end{bmatrix} \cdot \begin{bmatrix} \mu_{x,\nu}^{(2\omega)} \\ \mu_{y,\nu}^{(2\omega)} \\ \mu_{z,\nu}^{(2\omega)} \end{bmatrix}. \tag{8.8}
$$

The form of $\mathbf{Z}_{\nu,d}^{(2\omega)}$ matrix shows that the $\mu_x^{(2\omega)}$ component of the radiating electric dipole gives rise to s-polarized light and the $\mu_y^{(2\omega)}$ and $\mu_z^{(2\omega)}$ components to p-polarized light. This reflects the fact that the orientation of radiated modal vector amplitude $\boldsymbol{\mathcal{E}}^{(2\omega)}$ lies in the plane determined by the moment $\boldsymbol{\mu}^{(2\omega)}$ and vector $\boldsymbol{k}^{(2\omega)} \times (\boldsymbol{k}^{(2\omega)} \times \boldsymbol{\mu}^{(2\omega)})$, i.e. in the plane perpendicular to $\boldsymbol{k}^{(2\omega)}$ and containing $\boldsymbol{\mu}^{(2\omega)}$ [Eq. (E.5)].

Comparing the definition of the outcoming Jones vector $\boldsymbol{J}_{\nu,d,\text{spd}}^{(2\omega)}$ to the vector of modal amplitudes $\boldsymbol{A}_{\nu,\text{spd}}^{(2\omega)}$ [Eq. (7.10)], the elements of the $\mathbf{Z}_{\nu,d}^{(2\omega)}$ matrix are found to be related to elements of the $\mathbf{Y}_{\nu}^{(2\omega)}$ matrix defined in Eq. (7.13). Thus, the $\mathbf{Z}_{\nu,+}^{(2\omega)}$ matrix, describing the radiation state into the substrate has the following form

$$\mathbf{Z}_{\nu,+}^{(2\omega)} = \begin{bmatrix} Y_{11,\nu}^{(2\omega)} & Y_{12,\nu}^{(2\omega)} & Y_{13,\nu}^{(2\omega)} \\ Y_{31,\nu}^{(2\omega)} & Y_{32,\nu}^{(2\omega)} & Y_{33,\nu}^{(2\omega)} \end{bmatrix} \tag{8.9}$$

while the $\mathbf{Z}_{\nu,-}^{(2\omega)}$ into the superstrate writes

$$\mathbf{Z}_{\nu,-}^{(2\omega)} = \begin{bmatrix} Y_{21,\nu}^{(2\omega)} & Y_{22,\nu}^{(2\omega)} & Y_{23,\nu}^{(2\omega)} \\ Y_{41,\nu}^{(2\omega)} & Y_{42,\nu}^{(2\omega)} & Y_{43,\nu}^{(2\omega)} \end{bmatrix}. \tag{8.10}$$

The Eq. (8.8) determines the Jones vector $\boldsymbol{J}_{\nu,d,\text{spd}}^{(2\omega)}$ describing the radiation emitted by a point dipole located on the ν-th interface. Assuming that χ_ν does not depend on the lateral coordinates [$\chi([x,y]) = \text{const.}$], the radiation of all point dipoles, is described by $\boldsymbol{J}_{\nu,d,\text{spd}}^{(2\omega)}$ for light radiated in the $\boldsymbol{q}^{(2\omega)} = k_0^{(2\omega)}[0, N_y^{(2\omega)}]$ direction, where $N_y^{(\omega)} = N_y^{(2\omega)}$ (Section 7.4). This means that the Snell law is still valid for SHG (2ω) light, i.e. the radiated light beam is still located in the plane of incidence, keeping the y-component of the normalized wavevector N_y the same for both ω and 2ω light.

Finally, the outcoming light intensity $I_j^{(2\omega)}$ is given by Eqs. (7.21)(7.30)

$$I_j^{(2\omega)} \sim N_j^{(2\omega)} |N_{z,j}^{(2\omega)}|^2 \left(\left| \sum_{\nu=1}^{M+1} \mathcal{E}_{\nu,\text{s},d,\text{spd}}^{(2\omega)} \right|^2 + \left| \sum_{\nu=1}^{M+1} \mathcal{E}_{\nu,\text{p},d,\text{spd}}^{(2\omega)} \right|^2 \right). \tag{8.11}$$

Recall that ($j = M + 1$, $d = +$) for the substrate and ($j = 0$, $d = -$) for the superstrate. Note again that the incorporation of $N_{z,j}^{(2\omega)}$ into Eq. (8.11) is related to the fact that the calculations has been treated in the $\boldsymbol{q}$-space. The presence of $N_{z,j}^{(2\omega)}$ is required to account for the correct angular dependence of the radiated light intensity.

8.3   MOSHG selection rules

As already discussed in Section 8.1, the MOSHG is usually measured in pp, ps, sp, ss (in-out) configurations.

Different incident polarizations give rise to different components of the electric field $\boldsymbol{E}_\nu^{(\omega)}$ on the interface. Thus, the associated moment $\boldsymbol{\mu}_\nu^{(2\omega)}$ is determined through the non-linear susceptibility tensor χ_ν and $\boldsymbol{E}_\nu^{(\omega)}$. Thus, it is of prime importance to determine the selection rules related to the expression of the $\boldsymbol{\mu}_\nu^{(2\omega)}$ components as a function of the

	polar $M\|z$	longitudinal $M\|y$	transverse $M\|x$	non-magnetic
pp			$\mu_y = \chi_{yyy}^{(m)}E_y^2 + \chi_{yzz}^{(m)}E_z^2$ $\mu_z = \chi_{zzy}^{(m)}E_yE_z$	$\mu_y = \chi_{yzy}^{(nm)}E_zE_y$ $\mu_z = \chi_{zyy}^{(nm)}E_y^2 +$ $\chi_{zzz}^{(nm)}E_z^2$
ps	$\mu_x = \chi_{xzy}^{(m)}E_yE_z$	$\mu_x = \chi_{xyy}^{(m)}E_y^2 + \chi_{xzz}^{(m)}E_z^2$		
sp			$\mu_y = \chi_{yxx}^{(m)}E_x^2$	$\mu_z = \chi_{zxx}^{(nm)}E_x^2$
ss		$\mu_x = \chi_{xxx}^{(m)}E_x^2$		

Table 8.2: Components of the SHG radiated dipole moment $\boldsymbol{\mu}^{(2\omega)}$ generated by the electric field $\boldsymbol{E}_\nu^{(\omega)}$ at the ν-th interface, for various MOSHG configurations and interface magnetizations. To clarify, we don't use the superscripts (ω), (2ω).

incoming electric field components and interface magnetization components (Table 8.2), for different forms of susceptibility tensors χ_ν expressed by Eqs. (8.3–8.5) [1].

Table 8.3 presents the same results as Table 8.2, but accounting of the identity of some χ elements induced by transverse or longitudinal magnetizations (Section 8.1.2 and Table 8.1). Thus, in Table 8.3, the identical χ elements are identified by the same notation, e.g. χ_a, χ_b, etc. Furthermore, Table 8.3 underlines the dominant MOSHG contributions for each MOSHG configuration and magnetization orientation. These contributions will be determined later in Sections 8.8, 8.9, for FeSi/DyFeCo and Co/NiO/FeNi structures.

8.4 MOSHG magnetic signal

As is suggested by the previous Section, there are both magnetic and non-magnetic contributions to the electric point dipole $\boldsymbol{\mu}_\nu^{(2\omega)}$, i.e. to emitted SHG modal amplitudes.

The relations between incident $\mathcal{E}_{0,\mathbf{s},+}^{(\omega)}$, $\mathcal{E}_{0,\mathbf{p},+}^{(\omega)}$ and radiated $\mathcal{E}_{\nu,\mathbf{s},d,\mathrm{spd}}^{(2\omega)}$, $\mathcal{E}_{\nu,\mathbf{p},d,\mathrm{spd}}^{(2\omega)}$ modal amplitudes are expressed quantitatively in Table 8.4. These relations depend on the elements of Fresnel matrices $\mathbf{X}_\nu^{(\omega)}$ and $\mathbf{Z}_{\nu,d}^{(2\omega)}$ [Eqs. (8.6)(8.8)], and on the susceptibility tensor elements, described by Eqs.(8.3-8.5). The final relation is determined for each magnetization orientation and for structural (i.e. non-magnetic) contributions.

Since, in Tables 8.2-8.4, the modal amplitudes originating from 'magnetic' and 'non-magnetic' sources are expressed separately, the summation of the radiated modal amplitudes is provided over all interfaces (labeled "tot") and over both magnetic and non-magnetic contributions.

$$
\begin{aligned}
\mathcal{E}_{\mathrm{tot},\mathbf{s},d,\mathrm{spd}}^{(2\omega,m+nm)} &= \sum_\nu \mathcal{E}_{\nu,\mathbf{s},d,\mathrm{spd}}^{(2\omega,m)} + \sum_\nu \mathcal{E}_{\nu,\mathbf{s},d,\mathrm{spd}}^{(2\omega,nm)} = \mathcal{E}_{\mathrm{tot},\mathbf{s},d,\mathrm{spd}}^{(2\omega,m)} + \mathcal{E}_{\mathrm{tot},\mathbf{s},d,\mathrm{spd}}^{(2\omega,nm)}. \\
\mathcal{E}_{\mathrm{tot},\mathbf{p},d,\mathrm{spd}}^{(2\omega,m+nm)} &= \sum_\nu \mathcal{E}_{\nu,\mathbf{p},d,\mathrm{spd}}^{(2\omega,m)} + \sum_\nu \mathcal{E}_{\nu,\mathbf{p},d,\mathrm{spd}}^{(2\omega,nm)} = \mathcal{E}_{\mathrm{tot},\mathbf{p},d,\mathrm{spd}}^{(2\omega,m)} + \mathcal{E}_{\mathrm{tot},\mathbf{p},d,\mathrm{spd}}^{(2\omega,nm)},
\end{aligned}
\tag{8.12}
$$

where $\mathcal{E}_{\mathrm{tot},\mathbf{s},d,\mathrm{spd}}^{(2\omega,m)}$, $\mathcal{E}_{\mathrm{tot},\mathbf{p},d,\mathrm{spd}}^{(2\omega,m)}$ rely to magnetic contributions radiated from all interfaces.

	polar $M\|z$	longitudinal $M\|y$	transverse $M\|x$	non-magnetic
pp			$\mu_y = \chi_c^{(m)} E_y^2 + \chi_b^{(m)} E_z^2$ $\mu_z = \underline{\chi_{zzy}^{(m)} E_y E_z}$	$\mu_y = \chi_{yzy}^{(nm)} E_z E_y$ $\mu_z = \chi_g^{(nm)} E_y^2 +$ $\chi_{zzz}^{(nm)} E_z^2$
ps	$\mu_x = \underline{\chi_{xzy}^{(m)} E_y E_z}$	$\mu_x = -\underline{\chi_a^{(m)} E_y^2} - \chi_b^{(m)} E_z^2$		
sp			$\mu_y = \underline{\chi_a^{(m)} E_x^2}$	$\mu_z = -\chi_g^{(nm)} E_x^2$
ss		$\mu_x = -\underline{\chi_c^{(m)} E_x^2}$		

denotation in this Table	usual denotation
$\chi_a^{(m)}$ (strong)	$\chi_{yxx}^{(m)} = -\chi_{xyy}^{(m)}$
$\chi_b^{(m)}$ (weak)	$\chi_{yzz}^{(m)} = -\chi_{xzz}^{(m)}$
$\chi_c^{(m)}$ (weak)	$\chi_{yyy}^{(m)} = -\chi_{xxx}^{(m)}$
$\chi_g^{(nm)}$	$\chi_{zyy}^{(nm)} = -\chi_{zxx}^{(m)}$

Table 8.3: Same situation as in Table 8.2, but (i) the dominant magnetic contributions for each configuration and magnetization state are underlined [see Sections 8.8 and 8.9]. (ii) Identical χ elements are labeled by a common variable $\chi_a^{(m)}$, $\chi_b^{(m)}$, $\chi_c^{(m)}$ or $\chi_g^{(nm)}$ (see Table 8.1). To clarify, we don't use the superscripts (ω), (2ω).

Finally, the total radiated light intensity is proportional to the square of total modal amplitudes [Eqs. (7.30)(8.11)]

$$
\begin{aligned}
I_{\text{tot},\mathbf{s},d}^{(2\omega,m+nm)} \quad &\sim N_j^{(2\omega)} |N_{z,j,d}^{(2\omega)} \, \mathcal{E}_{\text{tot},\mathbf{s},d,\text{spd}}^{(2\omega,m+nm)}|^2 \\
&= N_j^{(2\omega)} |N_{z,j,d}^{(2\omega)}|^2 \left[|\mathcal{E}_{\text{tot},\mathbf{s},d,\text{spd}}^{(2\omega,nm)}|^2 + \sum_\nu 2\Re\left(\mathcal{E}_{\nu,\mathbf{s},d,\text{spd}}^{(2\omega,m)} (\mathcal{E}_{\text{tot},\mathbf{s},d,\text{spd}}^{(2\omega,nm)})^\dagger \right) + |\mathcal{E}_{\text{tot},\mathbf{s},d,\text{spd}}^{(2\omega,m)}|^2 \right] \\
&\approx I_{\text{tot},\mathbf{s},d}^{(2\omega,nm)} + \sum_\nu I_{\nu,\mathbf{s},d}^{(2\omega,m)}
\end{aligned}
$$

$$(8.13)$$

and similarly for p-polarized light intensity $I_{\text{tot},\mathbf{p},d}^{(2\omega,m+nm)}$. The term quadratic in magnetic contributions, $|\mathcal{E}_{\text{tot},\mathbf{s},d,\text{spd}}^{(2\omega,m)}|^2$, is neglected since it is usually much smaller than the cross-term $I_{\nu,\mathbf{s},d}^{(2\omega,m)} \sim 2\Re\left(\mathcal{E}_{\nu,\mathbf{s},d,\text{spd}}^{(2\omega,m)} (\mathcal{E}_{\text{tot},\mathbf{s},d,\text{spd}}^{(2\omega,nm)})^\dagger \right)$, which I call *magnetic signal* in the following. The dagger sign † denotes the complex conjugate form. $N_{z,j,d}^{(2\omega)}$ is the z-component of reduced wave vector[2] in the superstrate ($j = 1$, $d = -$) or in the substrate ($j = M + 1$, $d = +$), and $N_j^{(2\omega)}$ stands for the refractive index of the substrate or the superstrate. Eq. (8.13) underlines well-known fact that the magnetization is detected through the product of a magnetic and a non-magnetic cross-term [1]. This means that the presence of

---

[2]Recall that reduced wave vector is defined $\boldsymbol{N}_\nu^{(2\omega)} = \boldsymbol{k}_\nu^{(2\omega)}/k_0^{(2\omega)}$, where $\boldsymbol{k}_\nu^{(2\omega)}$ is the wave vector in the ν-th layer and $k_0^{(2\omega)} = 2\omega/c$ the wave vector at 2ω in vacuum.

non-magnetic	pp	$\mathcal{E}^{(2\omega,nm)}_{\nu,\mathrm{p},d,\mathrm{spd}} = \left[Z^{(2\omega)}_{\mathrm{p}y,\nu,d}\, \chi^{(nm)}_{yzy,\nu}\, X^{(\omega)}_{y\mathrm{p},\nu} X^{(\omega)}_{z\mathrm{p},\nu} + Z^{(2\omega)}_{\mathrm{p}z,\nu,d}\, \chi^{(nm)}_{zyy,\nu}\, (X^{(\omega)}_{y\mathrm{p},\nu})^2 \right.$ $\left. + Z^{(2\omega)}_{\mathrm{p}z,\nu,d}\, \chi^{(nm)}_{zzz,\nu}\, (X^{(\omega)}_{z\mathrm{p},\nu})^2 \right] \left[\mathcal{E}^{(\omega)}_{0,\mathrm{p},+} \right]^2$
	ps	
	sp	$\mathcal{E}^{(2\omega,nm)}_{\nu,\mathrm{p},d,\mathrm{spd}} = \left[Z^{(2\omega)}_{\mathrm{p}z,\nu,d}\, \chi^{(nm)}_{zxx,\nu}\, (X^{(\omega)}_{x\mathrm{s},\nu})^2 \right] \left[\mathcal{E}^{(\omega)}_{0,\mathrm{s},+} \right]^2$
	ss	
polar $M\|z$	pp	
	ps	$\mathcal{E}^{(2\omega,m)}_{\nu,\mathrm{s},d,\mathrm{spd}} = \left[Z_{\mathrm{s}x,\nu,d}\, \chi^{(m)}_{xzy}\, X^{(\omega)}_{y\mathrm{p},\nu} X^{(\omega)}_{z\mathrm{p},\nu} \right] \left[\mathcal{E}^{(\omega)}_{0,\mathrm{p},+} \right]^2$
	sp	
	ss	
longitudinal $M\|y$	pp	
	ps	$\mathcal{E}^{(2\omega,m)}_{\nu,\mathrm{s},d,\mathrm{spd}} = \left[Z^{(2\omega)}_{\mathrm{s}x,\nu,d}\, \chi^{(m)}_{xyy,\nu}\, (X^{(\omega)}_{y\mathrm{p},\nu})^2 + Z^{(2\omega)}_{\mathrm{s}x,\nu,d}\, \chi^{(m)}_{xzz,\nu}\, (X^{(\omega)}_{z\mathrm{p},\nu})^2 \right] \left[\mathcal{E}^{(\omega)}_{0,\mathrm{p},+} \right]^2$
	sp	
	ss	$\mathcal{E}^{(2\omega,m)}_{\nu,\mathrm{s},d,\mathrm{spd}} = \left[Z^{(2\omega)}_{\mathrm{s}x,\nu,d}\, \chi^{(m)}_{xxx,\nu}\, (X^{(\omega)}_{x\mathrm{s},\nu})^2 \right] \left[\mathcal{E}^{(\omega)}_{0,\mathrm{s},+} \right]^2$
transverse $M\|x$	pp	$\mathcal{E}^{(2\omega,m)}_{\nu,\mathrm{p},d,\mathrm{spd}} = \left[Z^{(2\omega)}_{\mathrm{p}y,\nu,d}\, \chi^{(m)}_{yyy,\nu}\, (X^{(\omega)}_{y\mathrm{p},\nu})^2 + Z^{(2\omega)}_{\mathrm{p}y,\nu,d}\, \chi^{(m)}_{yzz,\nu}\, (X^{(\omega)}_{z\mathrm{p},\nu})^2 \right.$ $\left. + Z^{(2\omega)}_{\mathrm{p}z,\nu,d}\, \chi^{(m)}_{zzy,\nu}\, X^{(\omega)}_{y\mathrm{p},\nu} X^{(\omega)}_{z\mathrm{p},\nu} \right] \left[\mathcal{E}^{(\omega)}_{0,\mathrm{p},+} \right]^2$
	ps	
	sp	$\mathcal{E}^{(2\omega,m)}_{\nu,\mathrm{p},d,\mathrm{spd}} = \left[Z^{(2\omega)}_{\mathrm{p}y,\nu,d}\, \chi^{(m)}_{yxx,\nu}\, (X^{(\omega)}_{x\mathrm{s},\nu})^2 \right] \left[\mathcal{E}^{(\omega)}_{0,\mathrm{s},+} \right]^2$
	ss	

Table 8.4: Modal amplitudes $\mathcal{E}^{(2\omega)}_{\nu,\mathrm{s},d,\mathrm{spd}}$, $\mathcal{E}^{(2\omega)}_{\nu,\mathrm{p},d,\mathrm{spd}}$, radiated into the superstrate ($d = -$) or the substrate ($d = +$) by given ν-th interface.

the non-magnetic radiated SHG light from interfaces is necessary to produce a variation of MOSHG with magnetization. Furthermore, the form of magnetic signal $I_{\nu,\mathsf{s},d}^{(2\omega,m)}$ tells that the magnetic signal issued from the ν-th FM interface is given by the product of the 'magnetic' modal amplitude $\mathcal{E}_{\nu,\mathsf{p},d}^{(2\omega,m)}$ and the *total* non-magnetic modal amplitude $\mathcal{E}_{\mathrm{tot},\mathsf{p},d}^{(2\omega,nm)}$ originating from all interfaces, i.e. all magnetic modal amplitudes are referenced by the same non-magnetic wave.

8.4.1   Magnetic contrast

In practical cases, it is convenient to express the magnetic contrast ρ from the ratio between the magnetic and non-magnetic SHG contributions [1]. More precisely, ρ is equal to the ratio between the difference of magnetic SHG intensities (MOSHG) for the two opposite saturated magnetization states and the non-magnetic SHG intensity

$$\rho = \frac{I(M+) - I(M-)}{I(M+) + I(M-)} = \frac{I_{\mathsf{s}/\mathsf{p},\mathrm{tot}}^{(2\omega,m)}}{I_{\mathsf{s}/\mathsf{p},\mathrm{tot}}^{(2\omega,nm)}} = \frac{2\,\Re\left[\mathcal{E}_{\mathrm{tot},\mathsf{s}/\mathsf{p},d}^{(2\omega,nm)}\,(\mathcal{E}_{\mathrm{tot},\mathsf{s}/\mathsf{p},d}^{(2\omega,m)})^{\dagger}\right]}{|\mathcal{E}_{\mathrm{tot},\mathsf{p},d}^{(2\omega,nm)}|^2} = 2\Re\left(\frac{\mathcal{E}_{\mathrm{tot},\mathsf{s}/\mathsf{p},d}^{(2\omega,m)}}{\mathcal{E}_{\mathrm{tot},\mathsf{s}/\mathsf{p},d}^{(2\omega,nm)}}\right)$$
$$(8.14)$$

For example, in the particular case of a `pp` configuration and for a sample with three FM interfaces, all having a transverse magnetizations (Table 8.4):

$$\rho_{\mathsf{pp}} = \frac{I_{\mathrm{tot},\mathsf{p},d}^{(2\omega,m)}}{I_{\mathrm{tot},\mathsf{p},d}^{(2\omega,nm)}} = \frac{2\,\Re\left[\mathcal{E}_{\mathrm{tot},\mathsf{p},d}^{(2\omega,nm)}\,(\mathcal{E}_{\mathrm{tot},\mathsf{p},d}^{(2\omega,m)})^{\dagger}\right]}{|\mathcal{E}_{\mathrm{tot},\mathsf{p},d}^{(2\omega,nm)}|^2} \tag{8.15}$$

where the non-magnetic contribution to the emitted modal amplitude at denominator of Eq. (8.14) is

$$\mathcal{E}_{\mathrm{tot},\mathsf{p},d}^{(2\omega,nm)} = \sum_{\nu=0}^{2} \mathcal{E}_{\nu,\mathsf{p},d}^{(2\omega,nm)} =$$

$$= (\mathcal{E}_{0,\mathsf{p},-}^{(\omega)})^2 \sum_{\nu=0}^{2}\left[Z_{\mathsf{p}y,\nu,d}^{(2\omega)}\chi_{yzy,\nu}^{(nm)}X_{y\mathsf{p},\nu}^{(\omega)}X_{z\mathsf{p},\nu}^{(\omega)} + Z_{\mathsf{p}z,\nu,d}^{(2\omega)}\chi_{zyy,\nu}^{(nm)}(X_{y\mathsf{p},\nu}^{(\omega)})^2 + Z_{\mathsf{p}z,\nu,d}^{(2\omega)}\chi_{zzz,\nu}^{(nm)}(X_{z\mathsf{p},\nu}^{(\omega)})^2\right]$$
$$(8.16)$$

and the magnetic contribution at the numerator

$$\mathcal{E}_{\mathrm{tot},\mathsf{p},d}^{(2\omega,m)} = \sum_{\nu=0}^{2} \mathcal{E}_{\nu,\mathsf{p},d}^{(2\omega,m)} =$$

$$= (\mathcal{E}_{0,\mathsf{p},-}^{(\omega)})^2 \sum_{\nu=0}^{2}\left[Z_{\mathsf{p}y,\nu,d}^{(2\omega)}\chi_{yyy,\nu}^{(m)}(X_{y\mathsf{p},\nu}^{(\omega)})^2 + Z_{\mathsf{p}y,\nu,d}^{(2\omega)}\chi_{yzz,\nu}^{(m)}(X_{z\mathsf{p},\nu}^{(\omega)})^2 + Z_{\mathsf{p}z,\nu,d}^{(2\omega)}\chi_{zzy,\nu}^{(m)}X_{y\mathsf{p},\nu}^{(\omega)}X_{z\mathsf{p},\nu}^{(\omega)}\right]$$
$$(8.17)$$

It shows, that in this particular case of three magnetized interfaces, the magnetic contrast ρ_{pp} is expressed by a ratio of two quantities each involving 18 terms. This shows that even in the case of few interfaces, the total MOSHG signal consists of many terms. Thus, to interpret the experimental data, it is of prime importance first to determine which contributions are negligible and which are dominant. This is discussed in Sections 8.8 and 8.9 for MOSHG on FeSi/DyFeCo and Co/NiO/FeNi structures.

8.4.2 Magnetic signal in ps MOSHG configuration

In the previous Sections, it is pointed out that the SHG field radiated by 'non-magnetic' sources is necessary to measure some MOSHG magnetic signal, and thus a magnetic contrast. However, as it can be found in Table 8.2, the ps and ss configurations do not give rise to any 'non-magnetic' SHG. Thus, to measure a large enough magnetic signal, for example, in a ps configuration, the analyzer A must be slightly misoriented from the s direction by angle ζ_a, in order to transmit a p polarized wave which contains a non-magnetic SHG. Thus, the resulting light intensity I_{ps}, in the so-called ps MOSHG configuration, measured by the detector placed in the superstrate is [Eq. (8.13), Table 8.2 and Appendix B]

$$
\begin{aligned}
I_{\text{ps},-}^{(2\omega)} \ \sim & \ \left| \mathcal{E}_{\text{tot,p},-}^{(2\omega,nm)} \right|^2 \sin^2 \zeta_a + 2\,\Re\left[\mathcal{E}_{\text{tot,s},-}^{(2\omega,m)} \left(\mathcal{E}_{\text{tot,p},-}^{(2\omega,nm)} \right)^\dagger \right] m_y \sin \zeta_a \cos \zeta_a \\
& + 2\,\Re\left[\mathcal{E}_{\text{tot,p},-}^{(2\omega,m)} \left(\mathcal{E}_{\text{tot,p},-}^{(2\omega,nm)} \right)^\dagger \right] m_x \sin^2 \zeta_a + \left| \mathcal{E}_{\text{tot,s},-}^{(2\omega,m)} \right|^2 m_y^2 \cos^2 \zeta_a,
\end{aligned}
\tag{8.18}
$$

where $\mathcal{E}_{\text{tot,s},-}^{(2\omega,m)}$ is the s-polarized emitted magnetic component and $\mathcal{E}_{\text{tot,p},-}^{(2\omega,m)}$, $\mathcal{E}_{\text{tot,p},-}^{(2\omega,nm)}$ are the magnetic, non-magnetic emitted p-polarized components of the SHG field. Eq. (8.18) shows that the dominant contribution to the ps-MOSHG signal is $2\Re[\mathcal{E}_{\text{tot,s},-}^{(2\omega,m)}(\mathcal{E}_{\text{tot,p},-}^{(2\omega,nm)})^\dagger]$ $m_y \sin \zeta_0 \cos \zeta_a$. This is due to the fact that ζ_a is small (usually less than $10°$) and thus $\sin^2 \zeta_a \ll \sin \zeta_a \cos \zeta_a$.

Thus, in the ps configuration, the dominant magnetic signal is related to the m_y magnetization component, but the magnetic signal linear in m_x and quadratic in m_y are present as well. These last two magnetic signals are far to be negligible. These additional components modify the shape of the sp MOSHG hysteresis loop as shown for Co/NiO/FeNi (Section 8.9) or for Pt/Co/Pt [143].

8.5 Basic principles of MOSHG in-depth resolution

As discussed in the previous Chapter 7, or in Section 8.2, the SHG radiation emitted by a given interface, inside a multilayer structure, depends upon the three following factors:

- The in-depth profile of the incoming electric field $\boldsymbol{E}^{(\omega)}$. Its tangential components $E_x^{(\omega)}$, $E_y^{(\omega)}$, are conserved at each interface, i.e. all over the multilayer structure for ultrathin layers. In counterpart, the normal component of the electric induction $D_z^{(\omega)}$ is nearly conserved over the multilayer structure. Thus, the $E_z^{(\omega)}$ component is not conserved and its profile can be estimated from the simple relation

$$
\varepsilon_{0,\nu}^{(\omega)} E_z^{(\omega)} \approx \text{const},
\tag{8.19}
$$

where $\varepsilon_{0,\nu}^{(\omega)}$ is the diagonal permittivity element of the ν-th layer. Consequently, for the incoming light, the dipole excitation by the $E_z^{(\omega)}$ component can differ significantly for different interfaces, contrarily to the excitation by $E_x^{(\omega)}$ and $E_y^{(\omega)}$.

The relation between the incoming Jones vector $\boldsymbol{J}_{0,+}^{(\omega)} = [\mathcal{E}_{0,\text{s},+}^{(\omega)}, \mathcal{E}_{0,\text{p},+}^{(\omega)}]^{\text{T}}$ and the electric field at interfaces $\boldsymbol{E}_\nu^{(\omega)}$ involves the generalized Fresnel elements $X_{x\text{s}}^{(\omega)}$, $X_{y\text{p}}^{(\omega)}$,

$X_{z\mathrm{p}}^{(\omega)}$ [see Eq. (8.6)]. The final radiated SHG light intensity depends on the fourth power of the electric field at the interface.

- Except in rare cases [3], the values of the $\chi_{ijk,\nu}$ elements at each ν-th interface are generally unknown. The radiated SHG intensity depends on the second power of the $\chi_{ijk,\nu}$ elements.

- The light intensity, $I_j^{(2\omega)}$, radiated by an electric point dipole having an unitary moment $|\boldsymbol{\mu}_\nu^{(2\omega)}| = 1$ can be calculated by two subsequent stages. Firstly, the outcoming Jones vector $\boldsymbol{J}_{\nu,d}^{(2\omega)}$ of the emitted light is calculated from the knowledge of the dipole $\boldsymbol{\mu}_\nu^{(2\omega)}$ by means of the outcoming Fresnel matrix $\mathbf{Z}_{\nu,d}^{(2\omega)}$, i.e. $\boldsymbol{J}_{\nu,d}^{(2\omega)} = \mathbf{Z}_{\nu,d}^{(2\omega)} \boldsymbol{\mu}_\nu^{(2\omega)}$. Secondly, from this outcoming Jones vector, the emitted light intensity, $I_j^{(2\omega)}$, is determined by Eq. (8.11). In following Sections, it is demonstrated that the radiation of tangential dipole components $(\mu_x^{(2\omega)}, \mu_y^{(2\omega)})$ *into the air* varies more with the depth position of the radiating dipole than for the normal dipole component $\mu_z^{(2\omega)}$ (Figures 8.3, 8.8, 8.12, 8.18). In the case of radiation into an optically denser material (e.g. into a glass substrate), the situation becomes more complex. As shown later, different behaviors appear when light is radiated at angles larger or smaller than the total reflection angle of the air/glass interface.

8.6 Case of an air/glass interface

Firstly, let us investigate a simple air/glass interface. The in-depth profile of the maximum value of the electric field at a given point in the space, in the vicinity of this interface, is presented on Figure 8.2. Mathematically speaking, Fig. 8.2 gives the profile of absolute values of the electric field components $|E_x^{(\omega)}|$, $|E_y^{(\omega)}|$ and $|E_z^{(\omega)}|$. On the other hand, the profile of the electric field components at a given time t is $\Re(E_j^{(\omega)} \exp[-i\omega t])$, with $j = \{x, y, z\}$ [Eq. (2.3)], but we don't present this profile here. In this Chapter, we show only the profiles of the absolute values of the electric field components, since they determine the strength of the radiating dipoles $\boldsymbol{\mu}_\nu^{(2\omega)}$.

8.6.1 Profile of $\boldsymbol{E}^{(\omega)}$ at the air/glass interface

The in-depth profile of the electric field at the air/glass interface is presented on Figure 8.2. As expected, the tangential components $E_x^{(\omega)}$, $E_y^{(\omega)}$ are continuous through the interfaces. The increase of the electric field into the air is due to the interference between incidence and reflected light waves. The marked step in the $E_z^{(\omega)}$ profile at the interface comes from the continuity condition of the normal component of the electric induction $D_z^{(\omega)} = \varepsilon_{0,\nu}^{(\omega)} E_{z,\nu}^{(\omega)}$ through the interface. Thus, in general, the dipoles located in an optical denser material are more efficiently exited by $E_z^{(\omega)}$ components. The values of $E_z^{(\omega)}$ at each interface determine the SHG efficiency.

- the total radiated (2ω) light intensity depends on the fourth power of the exciting electric field, i.e. $I^{(2\omega)} \sim |E_i^{(\omega)} E_j^{(\omega)}|^2$.
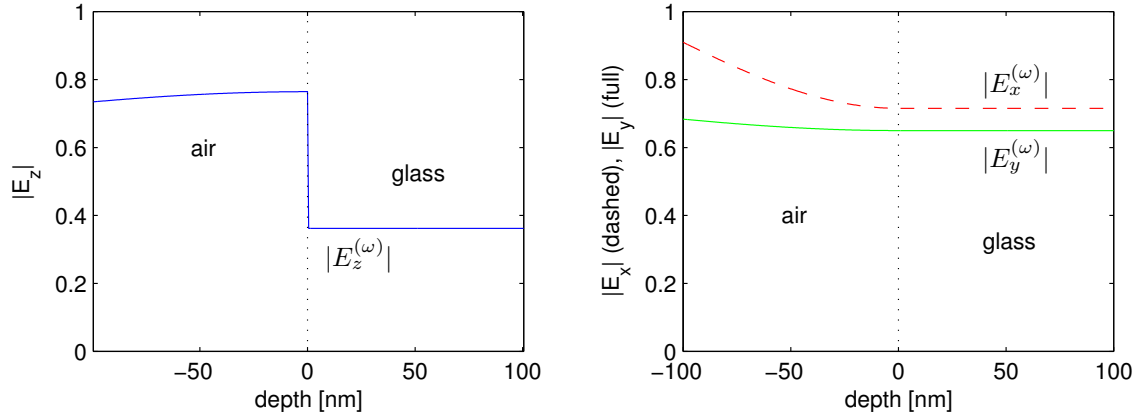
Figure 8.2: In-depth profile of the amplitude of the electric field components, $|E_x^{(\omega)}|$ (for an incident **s** wave) and $|E_y^{(\omega)}|$, $|E_z^{(\omega)}|$ (for an incident **p** wave) through a simple air/glass interface at $E = 1.55\,\text{eV}$. The incidence angle is fixed to $\varphi = 45°$, incident **s** and **p**-polarized waves have an unity amplitude.
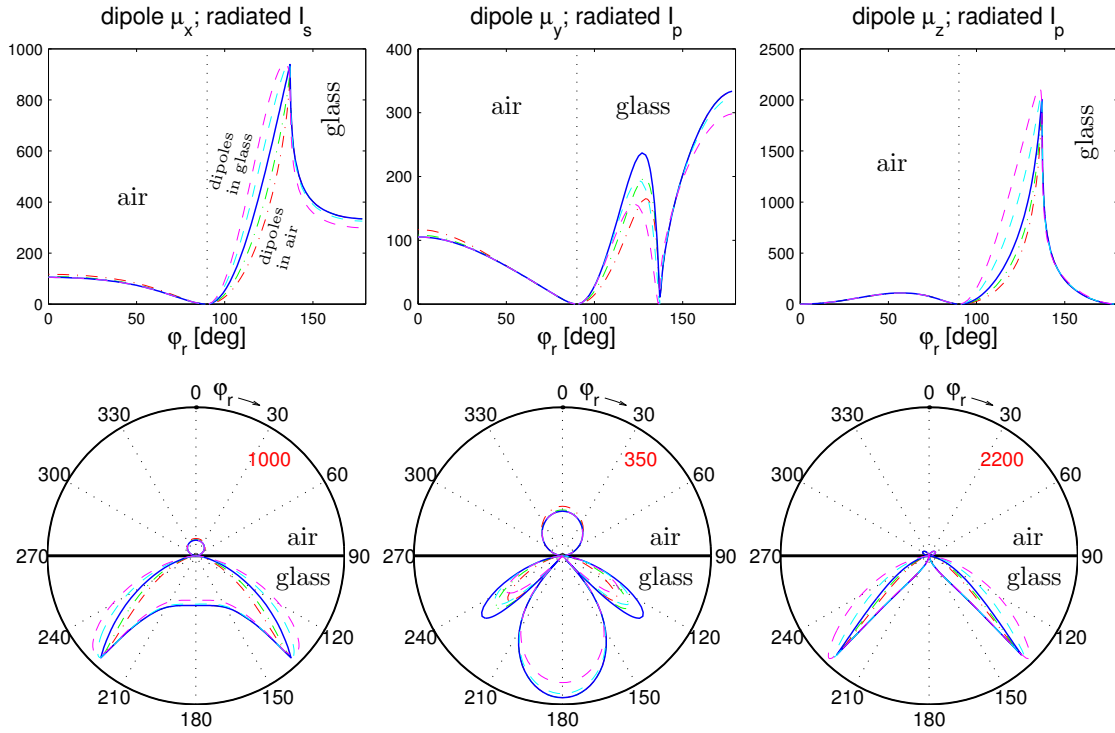
Figure 8.3: Angular dependence of the radiated intensity of **s** and **p** polarized light $I_s^{(2\omega)}$ and $I_p^{(2\omega)}$, emitted by a unity dipole $\boldsymbol{\mu}^{(2\omega)}$, oriented in x, y, z directions for the air/glass structure at $E = 3.1\,\text{eV}$. We present radiation of five dipoles located at different depths. One dipole is located just on the air/glass interface (full blue line), two dipoles are located in air 10 and 20 nm above the interface (green and red dashed-dot lines), and in glass 10 and 20 nm below the interface (bright blue and magenta dashed lines). Both figures in each column contain the same informations, but they are presented either in Cartesian or polar referentials. The light intensity value of the circle terminating the polar graph is denoted by a red number located inside each graph placed on the second row.

- In the case of metallic multilayers, metals can lead to $|\varepsilon_{0,\nu}^{(\omega)}| \simeq 20 - 30$, especially for $E = 1.55\,\mathrm{eV}$ (800 nm), i.e. the typical laser light (at ω) used for SHG, where the optical properties are highly influenced by the Drude tail.

8.6.2   Point dipole radiation from the air/glass interface

The aim of this part is to discuss the variation of the light intensity with the in-depth position of the radiating dipole. The light intensity radiated by different point dipoles, having the same moment and orientation, but located at five different depth near the air/glass interface, is presented in Figure 8.3. One dipole is located on the air/glass interface, two are 10 and 20 nm above into the air, and two 10 and 20 nm below into the glass. The radiation is calculated for unitary dipoles ($|\boldsymbol{\mu}_\nu^{(2\omega)}| = 1$) oriented in the x, y and z directions. Figure 8.3 represents the angular dependence of the radiated light, i.e. with the radiation angle φ_r, defined on Figure 8.4 [53].
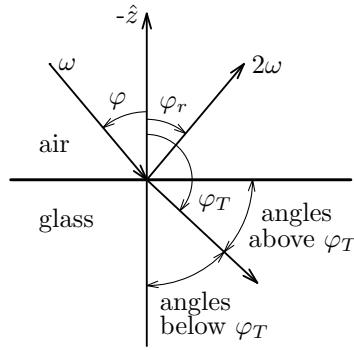
Figure 8.4: Radiation angle φ_r, defined as the angle between the emitted light at 2ω and the sample normal. φ is the incidence angle and φ_T is the total reflection angle of the glass/air interface, expressed as $\varphi_T = 180° - \arcsin(N_{\mathrm{air}}^{(2\omega)}/N_{\mathrm{glass}}^{(2\omega)}) \approx 137°$.

- The radiation into the air does not vary significantly for dipoles located at different depths or different orientations (note that graphs on Figure 8.3 have different scales). The maxima of the radiation emitted by $\mu_x^{(2\omega)}$, $\mu_y^{(2\omega)}$ dipole components occur for $\varphi_r = 0$, i.e. when observing the dipole along the interface normal. On the other hand, the $\mu_z^{(2\omega)}$ component does not radiate for $\varphi_r = 0$, and displays a maximum for $\varphi_r \simeq 60°$.

- The radiation into the glass (i.e. into an optically denser material) is much more efficient than for air. For dipole components $\mu_x^{(2\omega)}$, $\mu_z^{(2\omega)}$, a pronounced maximum of radiation is found in the vicinity of the total reflection angle ϕ_T for the glass/air interface, $\varphi_T = 180° - \arcsin(N_{\mathrm{air}}^{(2\omega)}/N_{\mathrm{glass})}^{(2\omega)}) \approx 137°$.

- The radiation *in air* has nearly the same amplitude wherever the dipole is located in depth. On the other hand, the radiation *in glass* is much more sensitive to the dipole position, particularly above the total reflection angle of the glass/air interface, i.e. for $90° < \varphi_r < 137°$ (Figure 8.3). This can be interpreted considering that in this

range $N_y^{(2\omega)} > 1$, and thus $N_{z,\text{air}}^{(2\omega)}$ in air is purely imaginary, giving an evanescent wave in air. Furthermore, in glass for the same $N_y^{(2\omega)}$, $N_{z,\text{glass}}^{(2\omega)}$ is real, which gives a radiating wave. This can be understood, remarking that there is a "conversion" from the evanescent wave in the air into a radiating wave in the glass.

This evanescent wave is very sensitive for investigating changes in multilayer structures, for example of the distance between the radiating dipole and the interface. Obviously, perturbations of this evanescent wave modify the propagating wave inside the glass as well. The presence of an evanescent wave explains why radiation above the total reflection angle ($90° < \varphi_r < 137°$) depends strongly on the dipole in-depth position, but not below, i.e. for $137° < \varphi_r < 180°$.

Finally, note that the variation of the radiated light intensity with the dipole position is more sensitive for radiation associated with a $\mu_z^{(2\omega)}$ component (Figure 8.3).

8.7 A model system: air/Fe/glass

In this Section, I discuss about a more complicated model system, consisting of 30 nm of Fe deposited on glass. Here I consider four positions for the radiating dipoles, two of them being located on the air/Fe and Fe/glass interfaces and the two others being located in the Fe layer at distances of 5 and 10 nm from the air/Fe interface.

The aim of this Section is to show the influence of an evanescent wave onto the dipole radiation. Hence, two cases are considered for this air/Fe(30 nm)/glass structure. We assume that the imaginary part of the Fe diagonal permittivity, $\Im(\varepsilon_0^{(\omega,2\omega)}) = 0$, is zero (Figures 8.5, 8.6) or non-zero (Figures 8.7, 8.8). For values of optical constants, see Appendix 8.11.

8.7.1 Case of non-absorbing Fe: $\Im(\varepsilon_0) = 0$

The electric field profile in this structure is presented on Figure 8.5. Again, the transversal components of the electric field are continuous throughout the interfaces. The decrease of the electric field in air and Fe is again caused by interference between the incoming and reflected light. As expected, the $E_z^{(\omega)}$ component has a step-like profile and its value stays nearly constant in each layer.

The radiation of all four radiating dipoles defined above is presented on Figure 8.6. The dipole radiation into the air does not depend significantly on their depth location. The radiation of dipoles, which are located near the air/Fe interface and radiating into the glass, display similar features as for the single air/glass interface (Section 8.6). The radiated light intensity depends a lot on the position of dipoles when radiating at angles $\varphi_r > \varphi_T$ ($90° < \varphi_r < 137°$) and not much for $\varphi_r < \varphi_T$ ($137° < \varphi_r < 180°$). The reasons are:

(i) the modes radiating into the glass at angles above φ_T become evanescent into the air.

(ii) the evanescent tail of the dipole radiation depends significantly of the distance from the dipole to the air/Fe interface.
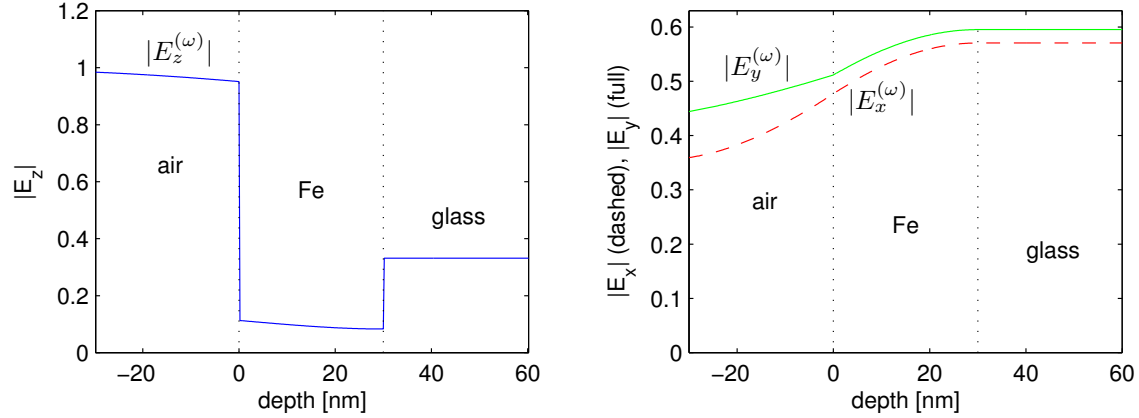
Figure 8.5: In-depth profile of the amplitude of the electric field components $|E_x|$ (incident unitary **s** wave), $|E_y|$, $|E_z|$ (incident unitary **p** wave) for an air/Fe(30 nm)/glass structure, at $E = 1.55$ eV, at a fixed incidence angle $\varphi = 45°$. $\Im(\varepsilon_{0,\mathrm{Fe}}^{(\omega)})$ is assumed to be *zero*.
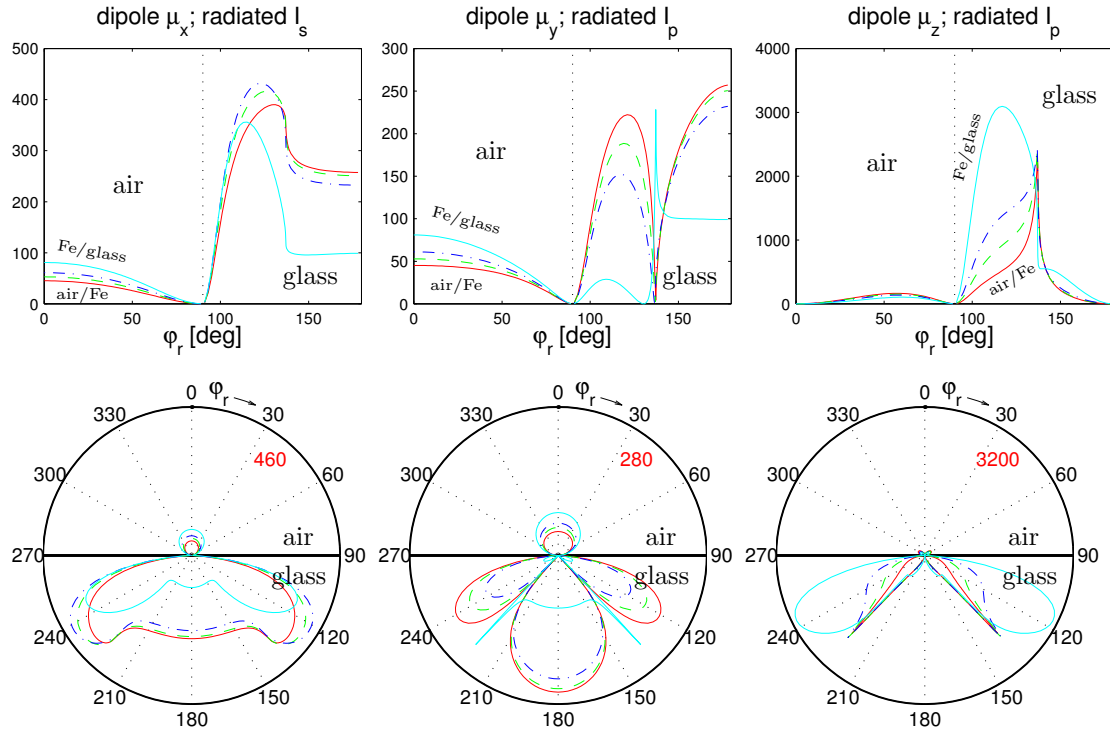
Figure 8.6: Angular dependence of radiated intensity of the **s** and **p** polarized light, $I_\mathbf{s}$, $I_\mathbf{p}$, emitted by unitary dipoles $\boldsymbol{\mu}^{(2\omega)}$ oriented in the x, y and z directions in the air/Fe(30 nm)/glass structure. The radiating dipoles are assumed to be located on the air/Fe interface (red full line), on the Fe/glass interface (bright blue full line) and 5 and 10 nm below the top air/Fe interface (green and blue dashed line). $\Im(\varepsilon_{0,\mathrm{Fe}}^{(2\omega)})$ is assumed to be *zero*.
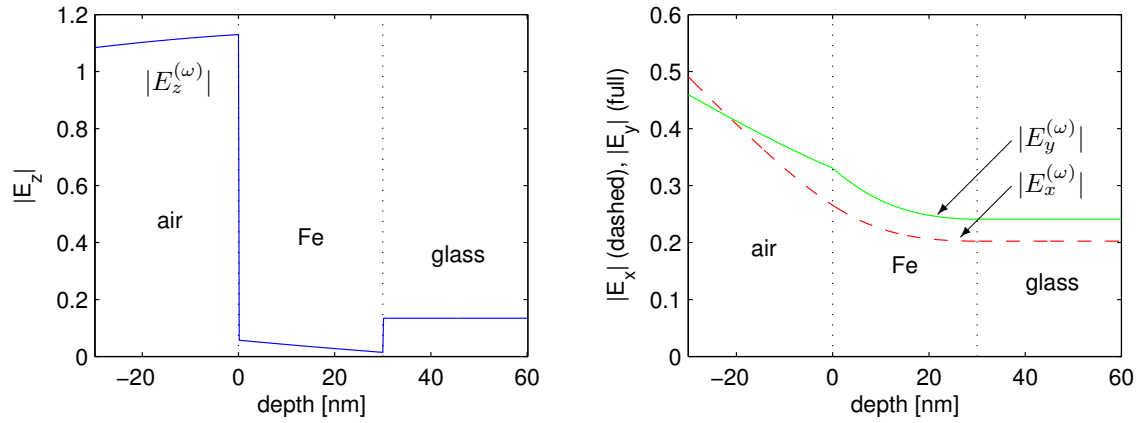
Figure 8.7: In-depth profile of the amplitude of the electric field components $|E_x|$ (incident unitary **s** wave), $|E_y|$, $|E_z|$ (incident unitary **p** wave) for an air/Fe(30 nm)/glass structure, at $E = 1.55$ eV, at a fixed incidence angle $\varphi = 45°$. $\Im(\varepsilon_{0,\text{Fe}}^{(\omega)})$ is assumed to be *non-zero* (Appendix 8.11).
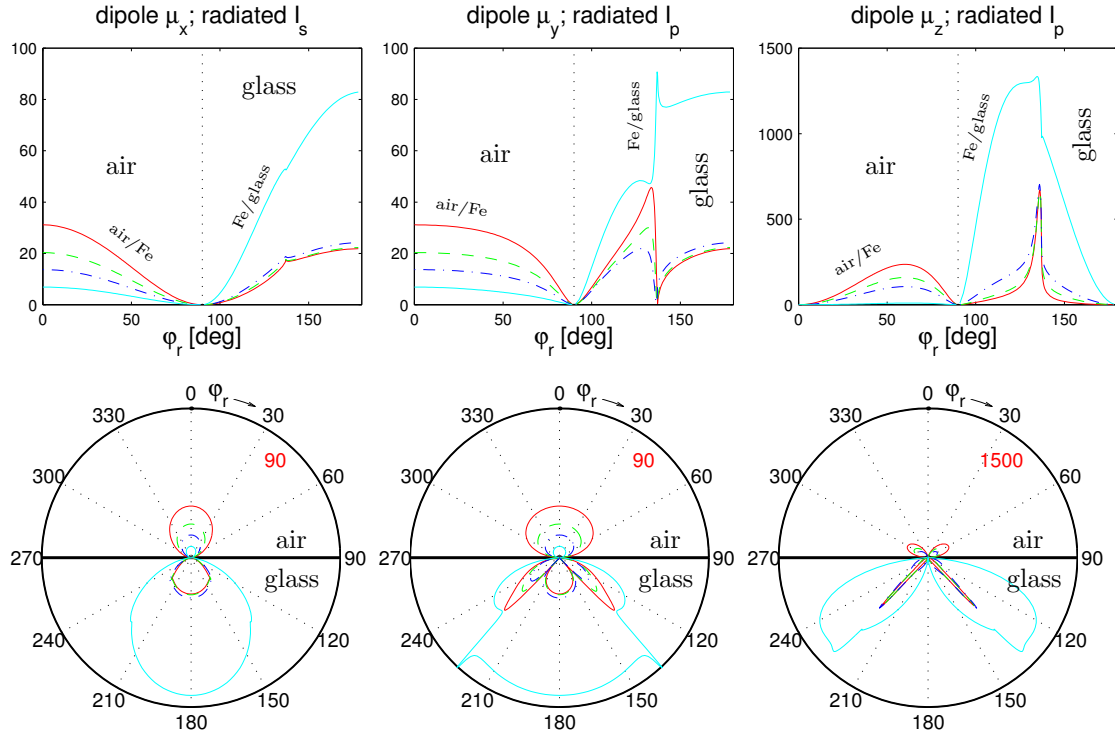
Figure 8.8: Angular dependence of radiated intensity of the **s** and **p** polarized light, I_s, I_p, emitted by unitary dipoles $\boldsymbol{\mu}^{(2\omega)}$ oriented in the x, y and z directions in the air/Fe(30 nm)/glass structure. The radiating dipoles are assumed to be located on the air/Fe interface (red full line), on the Fe/glass interface (bright blue full line) and 5 and 10 nm below the top air/Fe interface (green and blue dashed lines). $\Im(\varepsilon_{0,\text{Fe}}^{(2\omega)})$ is assumed to be *non-zero* (Appendix 8.11).

8.7.2   Case of absorbing Fe: $\Im(\varepsilon_0) \neq 0$

The main difference with above case is that now all waves propagating in Fe are partly evanescent. The profile of the electric field in this situation is presented on Figure 8.7. Again, $E_z^{(\omega)}$ exhibits a step-like profile (Figure 8.5). For tangential components of electric field $E_x^{(\omega)}$, $E_y^{(\omega)}$, the situation differs from Figure 8.5, since the evanescent electric field is decreasing fast inside the Fe layer and that the light is mostly reflected by the air/Fe interface.

The radiation of the four previous dipoles embedded in the air/Fe/glass structure is presented on Figure 8.8. Oppositely to previous cases presented on Figure 8.6, the amplitude of the waves radiating *into the air* are now depth sensitive. This comes from the fact that now *all modes* are evanescent in the Fe layer since $\Im(\varepsilon_0^{(\omega)})$ is finite. Thus, all waves radiated by dipoles embedded in Fe are strongly dependent upon their distance to the air/Fe interface.

In counterpart, Figure 8.8 shows that the radiation of the top three dipoles into the glass does not depend significantly on their in-depth position. This comes from the fact that all these dipoles are too far from the Fe/glass interface, and thus the evanescent wave in Fe is damped before coming out from the glass. This can be proved by a calculation where dipoles are placed into the Fe layer near the Fe/glass interface. In this case, dipoles radiating into the glass are depth sensitive and dipoles radiating into the air are not depth sensitive.

Let us now discussed experimental results obtained in two FM layer structures of interest for applications, FeSi/DyFeCo and Co/NiO/NiFe.

8.8   MOSHG in the FeSi/DyFeCo structure

In this Section MOSHG and LMOKE results on the FeSi/DyFeCo system are presented and discussed. Depth sensitivity of MOSHG by buried interfaces is then evidenced.

8.8.1   Sample properties

The $\text{SiO}_2(10\,\text{nm})/\text{Fe}_{0.96}\text{Si}_{0.04}(5\,\text{nm})/\text{Dy}_{0.30}\text{Fe}_{0.58}\text{Co}_{0.12}(30\,\text{nm})/\text{glass}$ structure [presented on Figure 8.9(a)] was prepared in the group of Prof. Le Gall (Université de Brest). The detailed preparation conditions and structural properties are reported in the thesis of R. Sbiaa [144]. $\text{Dy}_{0.30}\text{Fe}_{0.58}\text{Co}_{0.12}$ is an amorphous ferrimagnet with a Curie temperature $T_c = 200°\text{C}$ and a compensation temperature $T_{\text{comp}} = 60°\text{C}$. DyFeCo shows a high perpendicular anisotropy and a large coercive field. $\text{Fe}_{0.97}\text{Si}_{0.03}$ is a polycrystalline ferromagnet with a large Curie temperature $T_c \approx 700°\text{C}$ that exhibits low coercivity and in-plane anisotropy.

In a FeSi/DyFeCo bilayer, the spins of both FM layers (FeSi and DyFeCo) are coupled together but have competitive in-plane and out-of-plane anisotropies. By LMOKE, we checked that the FeSi anisotropy is nearly isotropic in the film plane. In the FeSi/DyFeCo film structure, one gets a rather square LMOKE hysteresis loop for the FeSi layer [Figure 8.15] with a coercive field of 20 Oe at room temperature. This coercive field is larger than that found in an isolated FeSi layer, for which H_c is only few Oe. This is expected since, in the structure, the FeSi layer is coupled to DyFeCo. In counterpart, an isolated DyFeCo layer does not show any LMOKE signal in low field, confirming its strong perpen-
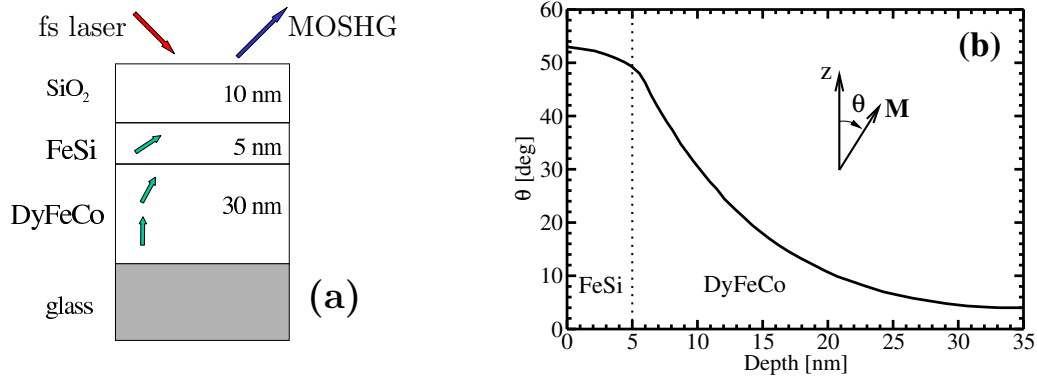
Figure 8.9: (a) Sketch of the studied FeSi/DyFeCo structure. (b) 2D calculations of the in-depth profile of the equilibrium tilt angle between the magnetization and the sample normal.

dicular anisotropy. In perpendicular magnetic field, DyFeCo in the FeSi/DyFeCo structure exhibits a square PMOKE loop with a large coercive field $H_c \approx 2000$ Oe.

In the absence of any in-plane anisotropy, the spin orientation is assumed to be the same inside an horizontal plane, i.e., spins are assumed not to form spiral-like structures for $H = 0$. The 2D-calculation of the in-depth profile of the equilibrium spin state in $H = 0$ is presented on Figure 8.9(b) [145]. In zero field, the magnetization of the top coupled FeSi layer is oriented at $52°$ from the film plane, i.e. far from a complete in-plane-state.

8.8.2 Fresnel elements calculations for the FeSi/DyFeCo structure

The in-depth profile of the electric field in the FeSi/DyFeCo structure is presented on Figure 8.10 for $E = 1.55$ eV and an incidence angle $\varphi = 45°$. As usual, the profile of tangential components $E_x^{(\omega)}$, $E_y^{(\omega)}$ is slightly decreasing through the multilayer structure. The profile of the normal component $E_z^{(\omega)}$ is again step-like and $E_z^{(\omega)}$ has a very low value at the FeSi/DyFeCo interface, since both neighboring layers are metallic with rather large diagonal permittivities values. For the concerned optical constants see Appendix 8.11 of this Chapter.

To be more explicit, the calculated values of the generalized incoming Fresnel elements $X_{x\mathbf{s},\nu}^{(\omega)}$, $X_{y\mathbf{p},\nu}^{(\omega)}$ and $X_{z\mathbf{p},\nu}^{(\omega)}$ are presented on Figure 8.11 in a polar form. This presentation contains also an information about the phase of $\boldsymbol{E}^{(\omega)}$ at the interface (recall, that assuming the incident field amplitude $|\mathcal{E}_{0,\Pi,+}^{(\omega)}| = 1$, the electric fields on the interfaces are $|E_x^{(\omega)}| = |X_{x\mathbf{s},\nu}^{(\omega)}|$, $|E_y^{(\omega)}| = |X_{y\mathbf{p},\nu}^{(\omega)}|$, $|E_z^{(\omega)}| = |X_{z\mathbf{p},\nu}^{(\omega)}|$). Again, we see on Figure 8.11, that when increasing the depth of the interface, the modules and phases of $X_{x\mathbf{s},\nu}^{(\omega)}$, $X_{y\mathbf{p},\nu}^{(\omega)}$ are smoothly decreasing. The largest value of $X_{z\mathbf{p},\nu}^{(\omega)}$ is obviously obtained at the air/SiO$_2$ interface, and it is negligible at deeper FeSi/DyFeCo and DyFeCo/glass interfaces.

The SHG radiation of unitary electric point dipoles located at each interface in the FeSi/DyFeCo structure is presented on Figure 8.12. We can see that the SHG radiation generated by the dipole components $\mu_x^{(2\omega)}$, $\mu_y^{(2\omega)}$ depends rather significantly on their in-depth location (compared to the deeper FeSi/DyFeCo interface, the upper SiO$_2$/FeSi interface radiates more by a factor of 2 for $\mu_x^{(2\omega)}$ and of 1.6 for $\mu_y^{(2\omega)}$). The SHG radiation issued from of the deepest DyFeCo/glass interface is negligible in air, and thus is neglected
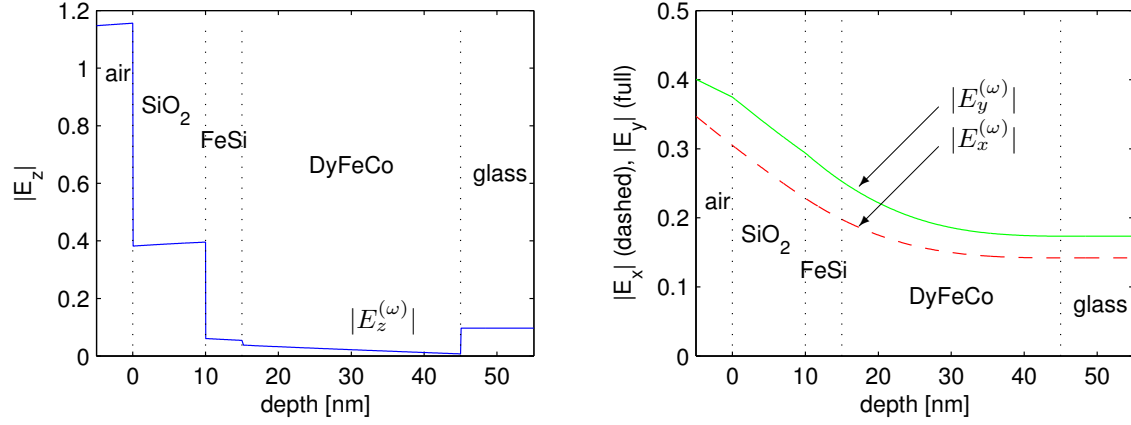
Figure 8.10: In-depth profile of the amplitude of the electric field $|E_x^{(\omega)}|$ (incident unitary **s** wave), $|E_y|$, $|E_z|$ (incident unitary **p** wave) in the air/SiO$_2$(10 nm)/FeSi(5 nm)/DyFeCo(30 nm)/glass structure, at an incidence angle $\varphi = 45°$, and $E = 1.55$ eV.
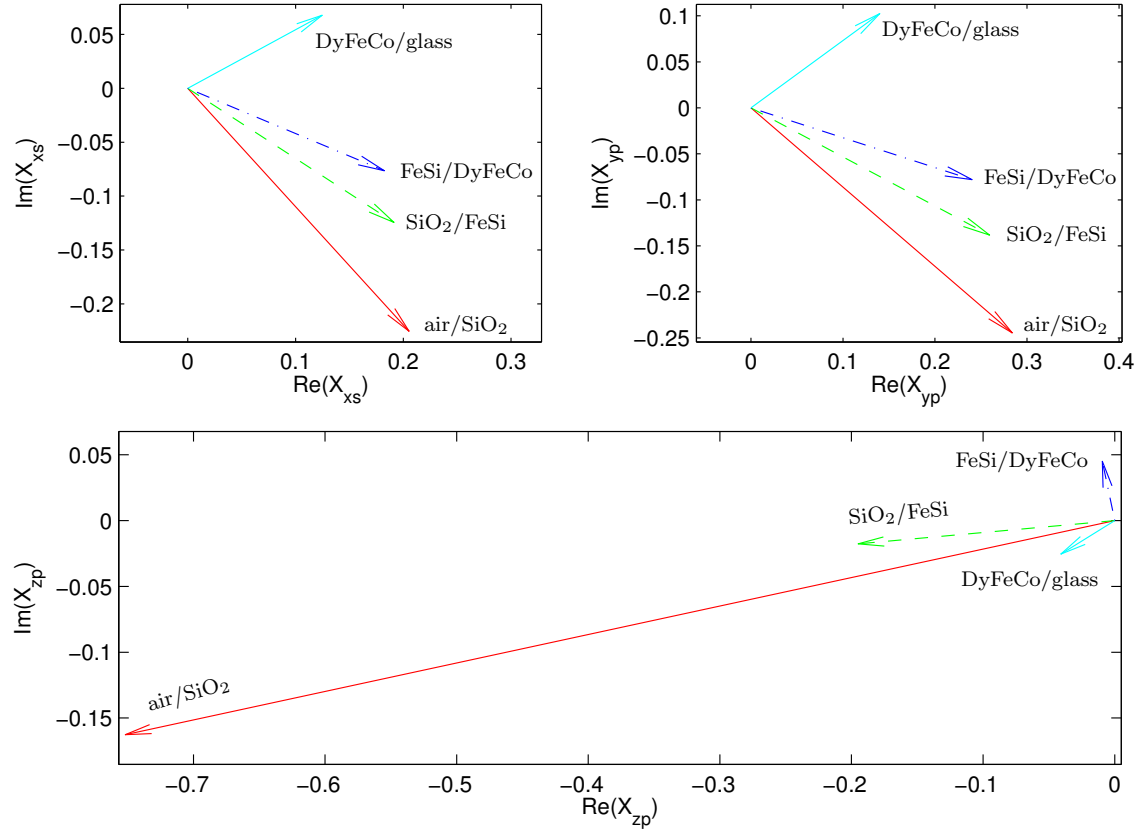
Figure 8.11: Incoming Fresnel elements $X_{xs}^{(\omega)}$, $X_{yp,\nu}^{(\omega)}$ and $X_{zp,\nu}^{(\omega)}$ at each interface, for the air/SiO$_2$(10 nm)/ FeSi(5 nm)/DyFeCo(30 nm)/glass structure, at an incidence angle $\varphi = 45°$, and for $E = 1.55$ eV. $X_{zp,\nu}^{(\omega)}$ is calculated as the average of the two electric fields acting on each side of the interface. Note, that absolute values of the $X_{xs,\nu}^{(\omega)}$, $X_{yp,\nu}^{(\omega)}$ and $X_{zp,\nu}^{(\omega)}$ are identical to electric fields present on the interfaces, as presented in Fig.8.10.
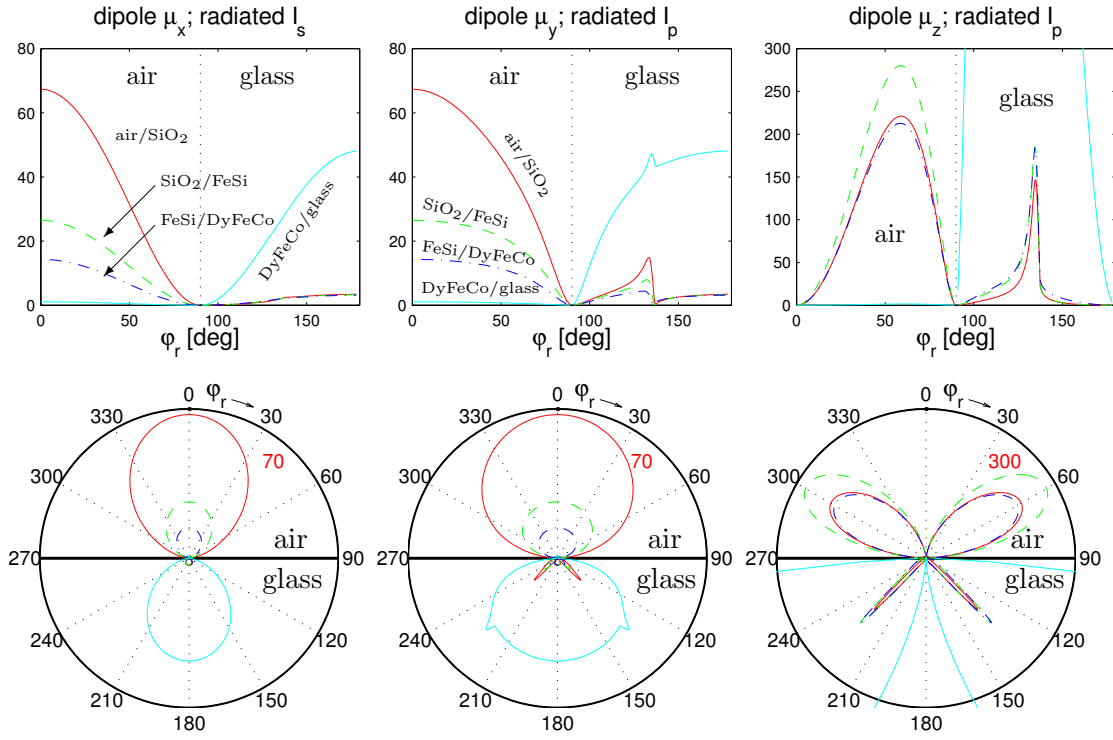
Figure 8.12: Angular dependence of the radiated intensity of $\mathbf{s}$ and $\mathbf{p}$ polarized light, $I_{\mathbf{s}}$, $I_{\mathbf{p}}$ emitted by unitary dipoles $\boldsymbol{\mu}^{(2\omega)}$ oriented in x, y and z directions and located at each interface of the air/SiO$_2$(10 nm)/ FeSi(5 nm)/DyFeCo(30 nm)/glass structure at $E = 3.1$ eV. Both figures in each column contain the same informations, visualized either in cartesian or polar referentials. The light intensity value of the circle terminating the polar graph is denoted by a red number situated inside the graph.
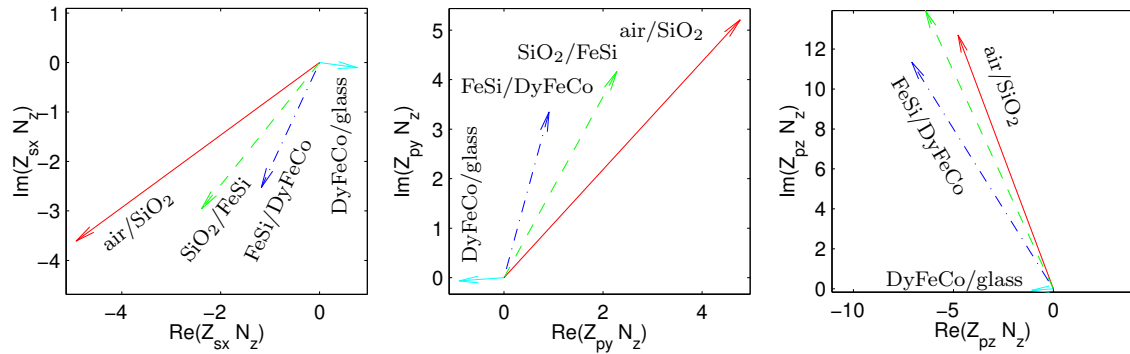
Figure 8.13: Values of the outcoming Fresnel elements $Z^{(2\omega)}_{\mathbf{s}x,\nu,-}$, $Z^{(2\omega)}_{\mathbf{p}y,\nu,-}$ and $Z^{(2\omega)}_{\mathbf{p}z,\nu,-}$ for the air/ SiO$_2$(10 nm)/FeSi(5 nm)/DyFeCo(30 nm)/glass structure, for an radiation angle $\varphi_r = 45°$, and photon energy $E = 3.1$ eV. The plotted quantity is $N^{(2\omega)}_{z,0} Z^{(2\omega)}_{ij,\nu,-}$, because the light intensity is proportional to it, i.e. $I^{(2\omega)}_0 \sim |N^{(2\omega)}_{z,0} Z^{(2\omega)}_{ij,\nu,-}|$.

in the following. On the other hand, the radiation of the dipole component $\mu_z^{(2\omega)}$ into the air is more efficient than that of $\mu_x^{(2\omega)}$ or $\mu_y^{(2\omega)}$ components (by about a factor three). Furthermore, the radiation of the $\mu_z^{(2\omega)}$ component does not depend significantly on the dipole depth.

The previous statements are also shown on Figure 8.13, where the outcoming generalized Fresnel elements $Z_{sx,\nu,-}^{(2\omega)}$, $Z_{py,\nu,-}^{(2\omega)}$ and $Z_{pz,\nu,-}^{(2\omega)}$, describe the emitted radiation into air, by the $\mu_x^{(2\omega)}$, $\mu_y^{(2\omega)}$, $\mu_z^{(2\omega)}$ dipole components, respectively. Figure 8.13 presents the Fresnel elements in the polar form for the FeSi/DyFeCo structure, for $\varphi_r = 45°$, and a 2ω-photon energy $E = 3.1\,eV$. Note that the relation between the radiated light intensity (in a.u.) and $Z_{ij,\nu,d}^{(2\omega)}$ coefficients writes $I_s = N_0^{(2\omega)}|N_{z,0}^{(2\omega)} Z_{sx,\nu,-}|^2$, $I_p = N_0^{(2\omega)}|N_{z,0}^{(2\omega)} Z_{py,\nu,-}|^2$ and $I_p = N_0^{(2\omega)}|N_{z,0}^{(\omega)} Z_{pz.\nu,-}|^2$, where $N_0^{(2\omega)}$ is the refractive index of the air at 2ω frequency, and $N_{z,0}^{(2\omega)}$ the z-component of the reduced wavevector in air. That is why, I prefer to represent on Figure 8.13 the quantity $N_{z,0}^{(2\omega)} Z_{ij,\nu,-}^{(2\omega)}$ instead of $Z_{ij,\nu,-}^{(2\omega)}$. Figure 8.13 relies to a deeper location of radiating dipoles. Both the modulus and phase of $Z_{sx,-}^{(2\omega)}$, $Z_{py,-}^{(2\omega)}$ elements are decreasing continuously with the depth. The situation is not so straightforward for the $Z_{pz,\nu,-}^{(\omega)}$ elements (i.e. the $\mu_{z,\nu}^{(2\omega)}$ radiation), where all contributions from the first three interfaces have approximately the same modulus and the phase. The $Z_{pz,\nu,-}^{(2\omega)}$ element decreases more slowly with depth than $Z_{sx,-}^{(2\omega)}$ and $Z_{py,-}^{(2\omega)}$ elements.

In conclusion, the most relevant quantity entering for the in-depth sensitivity of MOSHG in the FeSi/DyFeCo structure is the profile of the $E_z^{(\omega)}$ through the structure if χ-tensors at different interfaces are assumed to be the same. The radiation given by point dipoles located at different interfaces give similar intensities.

8.8.3   MOSHG data and discussion for the FeSi/DyFeCo structure

MOSHG data on the FeSi/DyFeCo sample are presented on Figures 8.14 and 8.15. Experiments were performed in reflection ($\varphi = 45°$), and the fundamental light beam is entering by the SiO$_2$ layer.

Let us first compare the transverse ($\boldsymbol{H} \parallel \hat{x}$) pp and sp-MOSHG hysteresis loops presented on Figure 8.14.

Figure 8.14: Transverse ($\boldsymbol{H} \parallel \hat{x}$) MOSHG hysteresis loops of the FeSi/DyFeCo structure measured (a) in pp configuration (b) in sp configuration. The incidence angle is $\varphi = 45°$.

The coercivity of both loops are quite different, being 5 Oe in the `pp` configuration and 13 Oe in the `sp` configuration. Note th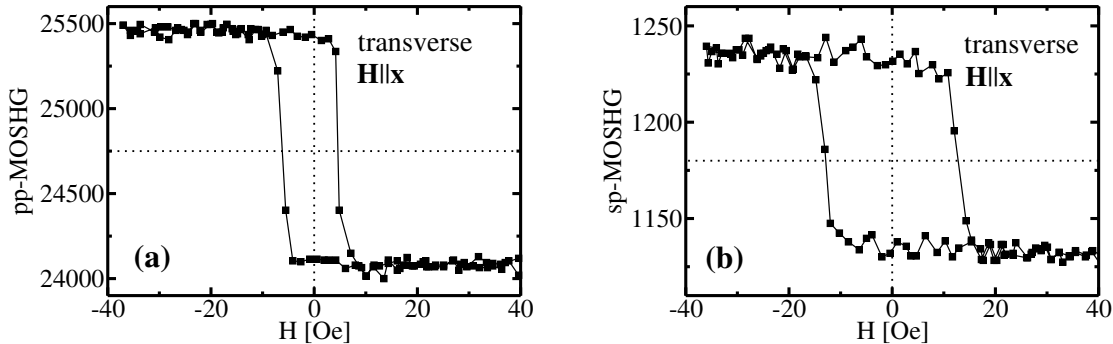at incident light intensity is comparable for both polarizations, i.e. one expects the same sample heating, if present. The difference in coercivity is explained as follow: the spins located at the top of the FeSi layer reverse quite easily for H applied in-plane, since they are not strongly coupled to the harder DyFeCo spins. Thus, when sweeping the field, the spins first rotate at the top of the FeSi layer. This gives rise to a "spiral-like" spin structure from the top to the inside of the FeSi layer. As the external magnetic field is increased, all spins are rotated inside a 5 nm thick planar Bloch wall. This magnetic behavior, together with observed properties of the MOSHG hysteresis loops (the `pp`-loop is more square and has smaller coercivity than the `sp`-loop), leads to following experimental evidences:

(i) the transverse `pp`-MOSHG probes more the magnetization of the top FM SiO_2/FeSi interface.

(ii) the transverse `sp`-MOSHG is sensitive to both the first and second FM interfaces, SiO_2/FeSi and FeSi/DyFeCo.

The point (i) is consistent with the selection rules (Table 8.2) and the estimation of the electric field at interfaces in `pp` configuration. The fundamental `p`-polarized field contains both $E_y^{(\omega)}$ and $E_z^{(\omega)}$ components. The selectivity of MOSHG to the top FM SiO_2/FeSi interface is explained from the profile of $E_z^{(\omega)}$ (Figure 8.10), which has a large value at the SiO_2/FeSi interface compared to other FM interfaces.

Let us consider now the relation between the dipoles components and of the electric field at ω, as deduced from MOSHG selection rules (see Table 8.2). The magnetic signal in transverse `pp` configuration is related to $\mu_y^{(2\omega)} = \chi_{yyy}(E_y^{(\omega)})^2 + \chi_{yzz}(E_z^{(\omega)})^2$ and $\mu_z^{(2\omega)} = \chi_{zzy}E_y^{(\omega)}E_z^{(\omega)}$. Since experimental data prove that we are mainly sensitive to the top FM SiO_2/FeSi interface, this means that χ_{yyy} is negligible as compared to χ_{yzz} and χ_{zzy}. Moreover, from comparison of `pp` and `ps` loops, it is shown later that the contribution of χ_{yzz} has to be small as compared to χ_{zzy}. Thus, it can be concluded that the observed magnetic signal in transverse `pp` configuration originates mainly form the $\mu_z^{(2\omega)} = \chi_{zzy}E_y^{(\omega)}E_z^{(\omega)}$ term. This conclusion is supported by the fact that the dipole radiation coming from the μ_z component (and thus from χ_{zzy}) is about three times more efficient than that originating from $\mu_y^{(2\omega)}$ (Figures 8.12 and 8.13). Furthermore, as pointed out by Petukhov and Liebsch [137] and if one extends the *ab-initio* results for Al(111), the radiation of a dipole component $\mu_z^{(2\omega)}$ originates from a much thinner interface region (~ 0.1 nm) than the $\mu_x^{(2\omega)}$ and $\mu_y^{(2\omega)}$ components (~ 1 nm). This supports the high selectivity of the transverse `pp` configuration to the upper SiO_2/FeSi FM interface. Similar results were indirectly found by Güdde *et al.* [138] for ultrathin Co and Ni films deposited on Cu(001).

The point (ii) is consistent with the characteristic properties of the transverse `sp` configuration. The fundamental light beam is characterized by an $E_x^{(\omega)}$ component keeping nearly the same value at both SiO_2/FeSi and FeSi/DyFeCo FM interfaces (Figure 8.10). Thus, the dipoles located at both FM interfaces are exited by similar fields. The magnetic signal is related to $\mu_y^{(2\omega)} = \chi_{yxx}(E_x^{(\omega)})^2$ (see Table 8.2). The radiated light intensity by the $\mu_y^{(2\omega)}$ dipole component is stronger for the upper SiO_2/FeSi FM interface by a factor 1.6 than that for the bottom FeSi/DyFeCo. Thus, in a first approximation, both contributions can be assumed to be the same (Figures. 8.12 or 8.13). Supposing that

χ_{yxx} for both SiO_2/FeSi and FeSi/DyFeCo interfaces are identical, the contribution of the upper SiO_2/FeSi interface to the total MOSHG signal becomes about two times larger than for the bottom FeSi/DyFeCo interface. This result is even more supported by the fact that $\mu_y^{(2\omega)}$ investigate a thicker zone than $\mu_z^{(2\omega)}$ [137].

Now, let us comment the hysteresis loops presented on Figure 8.15.
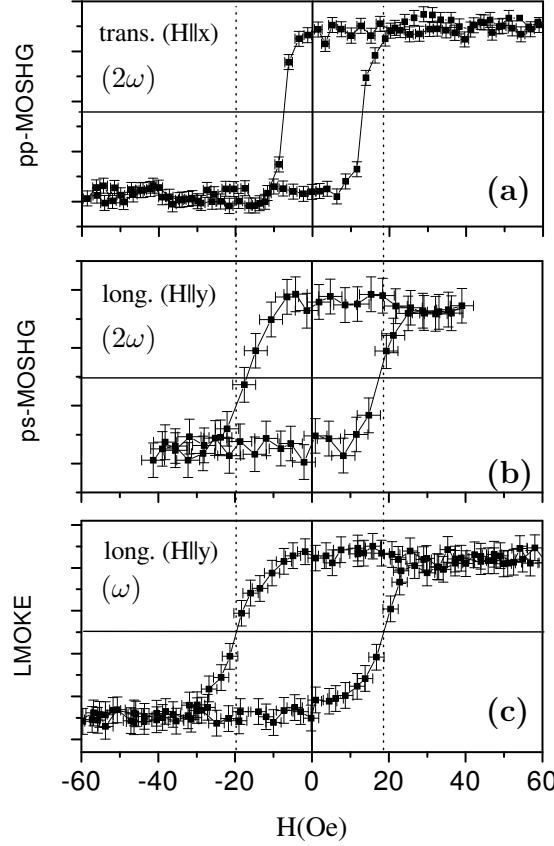
Figure 8.15: MOSHG and LMOKE loops of the FeSi/DyFeCo structure measured (a) in `pp` configuration, $H \parallel \hat{x}$; (b) in `ps` configuration, $H \parallel \hat{y}$. (c) LMOKE hysteresis loop measured in the same thermal condition (see Section 8.1 or Figure 8.1). The incidence angle is always $\varphi = 45°$.

LMOKE and MOSHG hysteresis loops are measured with the same light flux, i.e. in the same heating conditions. The MOSHG loop, measured in longitudinal `ps` configuration, is quite similar to that measured by MOSHG in transverse `sp` configuration. The term responsible of the magnetic signal in the transverse `ps` configuration is $\mu_x^{(2\omega)} = \chi_{xyy}(E_y^{(\omega)})^2 + \chi_{xzz}(E_z^{(\omega)})^2$. The large coercivity of the longitudinal `ps` MOSHG loop means that it depends on both FM interfaces. Thus, the contribution of $\chi_{xzz}(E_z^{(\omega)})^2$ must be smaller than that coming from the $\chi_{xyy}(E_y^{(\omega)})^2$ term. This statement, associated with the symmetry relation $\chi_{xzz} = -\chi_{yzz}$ (Table 8.1 or 8.3), was used in the previous discussion [related with the point (i)] to state that the $\mu_z = \chi_{zzy}E_y^{(\omega)}E_z^{(\omega)}$ term was dominant in the `pp` configuration. LMOKE checks more uniformly the magnetization in depth, so that its hysteresis loop (Fig. 8.15c) shows a smoother slope that reveals the distribution of coercivity at several depths.

8.8.4   Conclusion for FeSi/DyFeCo structure

On the SiO_2/FeSi/DyFeCo/glass system we have demonstrated that the transverse `pp` configuration is much more selective to the first FM interface (SiO_2/FeSi) than transverse `sp` and longitudinal `ps` configurations. The most efficient factor that explains this fact is the step-like profile of the z-component of the electric field $E_z^{(\omega)}$, together with the large values of the linear permittivity tensor elements $\varepsilon_{0,\nu}^{(\omega)}$ for metals. There is no pronounced differences between intensities radiated by dipoles located at different interfaces in the structure. Furthermore, we have determined the most efficient terms responsible of the magnetic signal for each MOSHG configuration, i.e. $\mu_z^{(2\omega)} = \chi_{zzy}E_y^{(\omega)}E_z^{(\omega)}$ for the `pp` configuration, $\mu_x^{(2\omega)} = \chi_{xyy}(E_y^{(\omega)})^2$ for the `ps` configuration, and $\mu_y^{(2\omega)} = \chi_{yxx}(E_x^{(\omega)})^2$ for the `sp` configuration. The most efficient contributions are underlined on Table 8.3. One deduces $|\chi_{zzy}| \gg |\chi_{yyy}|$, $|\chi_{zzy}| \gg |\chi_{yzz}|$ and $|\chi_{xyy}| \gg |\chi_{xzz}|$, for the SiO_2/FeSi interface, with $\chi_{yzz} = -\chi_{xzz}$. Finally, our results suggests that $\mu_z^{(2\omega)}$ originates from a thinner region at the interface than the transverse components $\mu_x^{(2\omega)}$, $\mu_y^{(2\omega)}$ [137].

8.9   MOSHG in the Co/NiO/NiFe trilayer

In this Section, we compare the MOSHG and MOKE data for the Co(FM)/NiO(AFM)/NiFe(FM) trilayer structure, and discuss about the depth sensitivity of MOSHG to interfaces.

8.9.1   Sample properties

In general, the unidirectional exchange coupling at the interface between a ferromagnetic layer (FM) and an antiferromagnetic layer (AFM), discussed in the literature since the 60's, manifests itself, besides many other effects, by a shift of the hysteresis loop and an enhancement of the coercivity of the FM layer [146].

FeNi/NiO/Co multilayers, more exactly CoO(2nm)/Co(2nm)/NiO($t^{(NiO)}$)/NiFe(10nm)/Cu(5nm)/SiO_2(80nm)/Si, have been fabricated and previously studied in the team of B. Dieny, SPINTEC, Grenoble [147, 148]. The multilayer was initially covered by a non-protected Co layer. Consistently with some results obtained in Grenoble, one assumes that Co is oxidized as CoO over a 2 nm thickness. The sample preparation and its structural and magnetic properties have been reported elsewhere [147, 148]. Here, we only mention some of these results which are important for the further interpretation of our data.

We report on MOSHG studies on Co/NiO/FeNi samples with two different NiO thicknesses, $t^{(NiO)} = 4$ nm and 8 nm. In this system the coupling between Co and permalloy (FeNi) is mediated by the AFM NiO spacer. The Co layer is shown to exhibit an uniaxial anisotropy resulting of an oblique deposition of the NiO spacer layer [147]. Both FM layers exhibit a negligible exchange bias, as expected in low-anisotropy NiO-exchanged coupled systems [104, 147]. The NiFe layer does not provide intrinsically any magnetization easy axis. The coupling between both FM layers is reduced when increasing the NiO spacer thickness. For $t^{(NiO)} = 8$ nm, the NiFe and Co layer magnetizations are found to be parallel, whereas for $t^{(NiO)} = 4$ nm, the coupling between the two FM layers is found to be at 90°. This 90° coupling is assumed to be due to the interface roughness combined with a small value of the effective NiO anisotropy [147, 148].

Let us discuss on MOSHG experiments. The light was always entering from the CoO side, with an incidence angle $\varphi = 45°$, and a photon energy $E = 1.54\,\text{eV}$ ($\lambda = 800\,\text{nm}$).

8.9.2   Incoming Fresnel elements for the Co/NiO/FeNi structure

The profile of the electric field $\boldsymbol{E}^{(\omega)}$ in the Co/NiO(4 nm)/FeNi structure is presented on Figure 8.16.
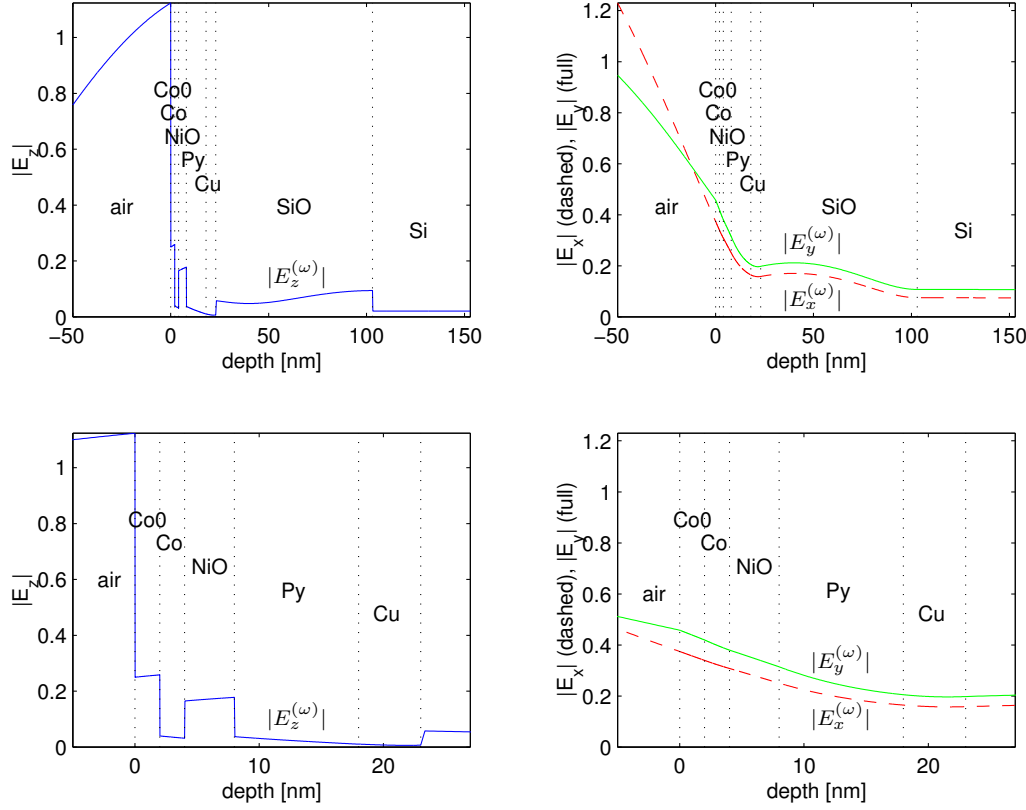
Figure 8.16: Profile of the electric field amplitude components in the Co/NiO(**4 nm**)/FeNi structure. The two bottom graphs show a zoom of the upper ones. Py (permalloy) denotes the FeNi layer.

Again, as in the previous cases, the profile of the transverse components $E_x^{(\omega)}$, $E_y^{(\omega)}$ is continuous through the interfaces and their amplitudes are smoothly decreasing when going deeper inside the structure. The ratio of the amplitudes $E_x^{(\omega)}$ (or $E_y^{(\omega)}$) exhibited at the first FM (CoO/Co) and the last FM (NiFe/Cu) interface is approximately equal to 2. The smooth decrease of the $E_x^{(\omega)}$, $E_y^{(\omega)}$ amplitudes is also revealed on Figure 8.17, presenting the elements of the incoming Fresnel matrix $\boldsymbol{\mathsf{X}}_\nu^{(\omega)}$, for the $X_{x\mathsf{s},\nu}^{(\omega)}$ and $X_{y\mathsf{p},\nu}^{(\omega)}$ elements. When the interface is deeper in the sample, both the amplitude and phase of the $\boldsymbol{\mathsf{X}}_\nu^{(\omega)}$-matrix elements are smoothly decreasing in a very similar way than $X_{x\mathsf{s},\nu}^{(\omega)}$ and $X_{y\mathsf{p},\nu}^{(\omega)}$.

On one hand, the profile of the normal component $E_z^{(\omega)}$ exhibits discontinuities at interfaces (Figure 8.16). Since the Co layer is sandwiched between two NiO and CoO oxide layers, there is a relative large jump of $E_z^{(\omega)}$ on both sides of the Co layer. On the other hand, the FeNi layer is located between an oxide layer (NiO) and a metal (Cu).
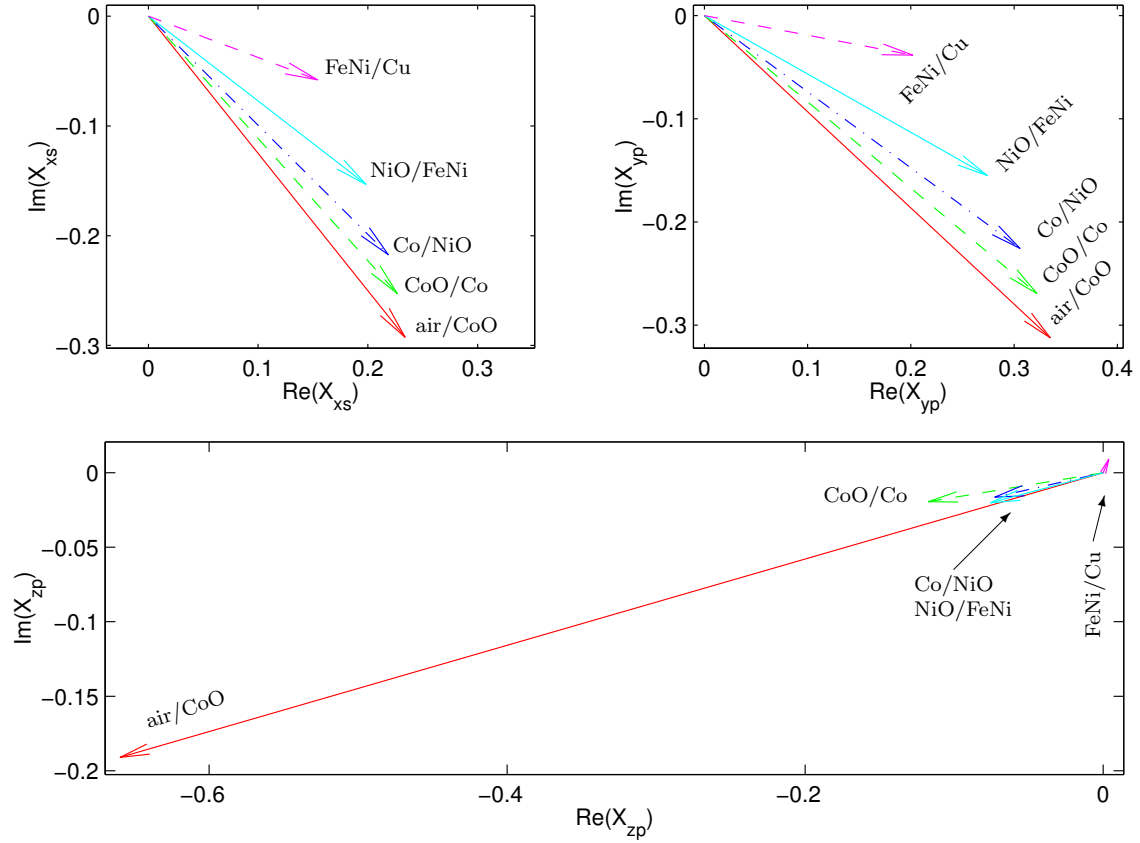
Figure 8.17: Incoming Fresnel elements $X_{xs,\nu}^{(\omega)}$, $X_{yp,\nu}^{(\omega)}$ and $X_{zp,\nu}^{(\omega)}$ for the Co/NiO(**4 nm**)/FeNi structure. The $X_{zp,\nu}^{(\omega)}$ element is calculated from the average of $E_z^{(\omega)}$ values calculated just above and under the interface.

Thus, a jump of $E_z^{(\omega)}$ is only present at the NiO/FeNi interface, but not at the FeNi/Cu interface. These features are also visible on $X_{zp,\nu}^{(\omega)}$ (Figure 8.17). The largest value of $X_{zp,\nu}^{(\omega)}$ comes from the air/CoO interface. All FM/oxide (CoO/Co, Co/NiO, NiO/FeNi) interfaces provide approximately the same amplitude and phase. In counterpart, the value of $X_{zp,\nu}^{(\omega)}$ for the last FM interface is rather small.

8.9.3   Outcoming Fresnel elements for the Co/NiO/FeNi structure

Figure 8.18 shows the light intensity radiated by an unitary dipole oriented in the x, y or z directions and located at the first five successive interfaces (up to the NiO/Cu interface). The radiation from the $\mu_x^{(2\omega)}$, $\mu_y^{(2\omega)}$ components is weaker for the dipoles located deeper in the multilayer structure. The emitted light intensity at 2ω of dipoles located at the NiO/FeNi interface is about 30% smaller than that of dipoles located at the CoO/Co interface. The same result is presented on Figure 8.19 for the $Z_{sx,\nu}^{(2\omega)}$ and $Z_{py,\nu}^{(2\omega)}$ components. For more and more buried interfaces, both their amplitude and phase decrease.

The radiation of the $\mu_z^{(2\omega)}$ component is different. The light emitted by unitary dipoles located at different interfaces has approximately the same intensity. These results are
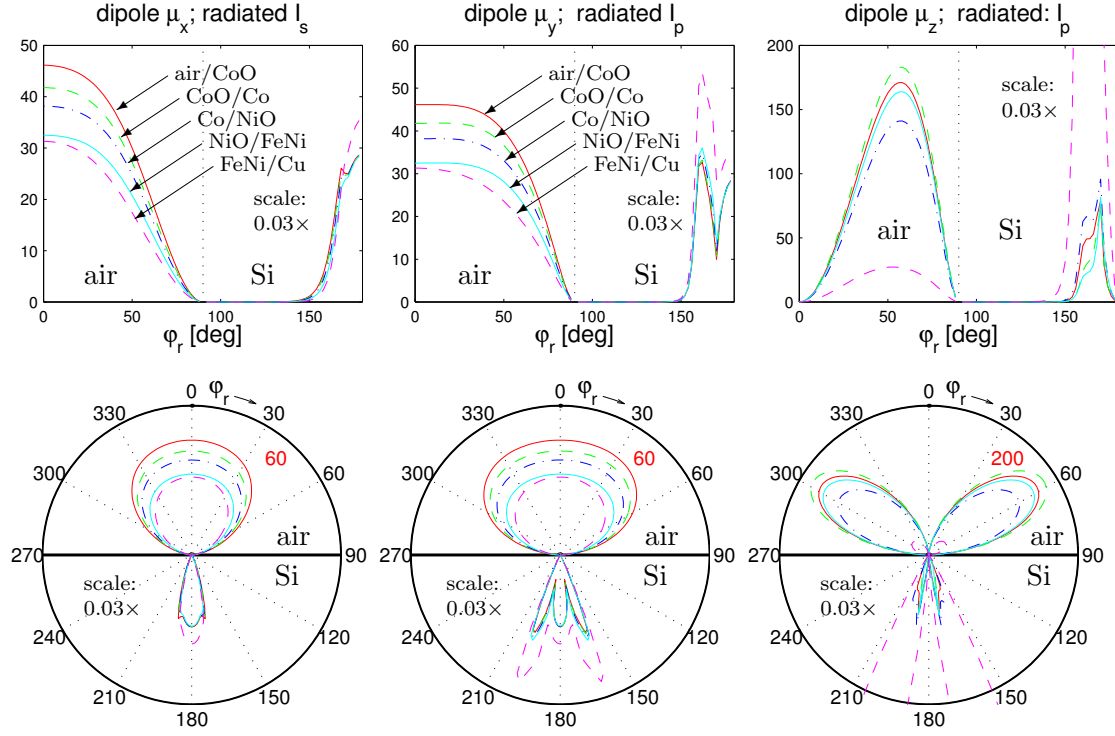
Figure 8.18: Angular dependence of the radiated intensity of **s** and **p** polarized light I_s and I_p emitted by a unitary dipole $\boldsymbol{\mu}^{(2\omega)}$ oriented in x, y, z directions in the Co/NiO(**4 nm**)/FeNi structure, and located at each interface ($E = 3.1\,\mathrm{eV}$). Both figures in each column contain the same informations, visualized either in cartesian or polar referentials. The light intensity value of the circle terminating the polar graph is denoted by a red number located inside the graph.
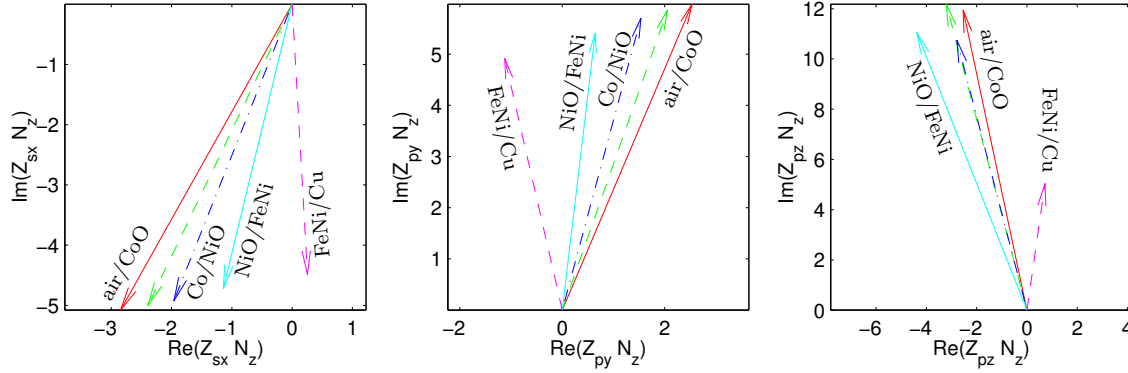
Figure 8.19: Outcoming Fresnel elements $Z^{(2\omega)}_{\mathrm{s}x,\nu,-}$, $Z^{(2\omega)}_{\mathrm{p}y,\nu,-}$ and $Z^{(2\omega)}_{\mathrm{p}z,\nu,-}$ for the Co/NiO(**4 nm**)/FeNi structure, for an radiation angle $\varphi_r = 45°$ at a photon energy $E = 3.1\,\mathrm{eV}$. The presented quantity is $N^{(2\omega)}_{z,0} Z^{(2\omega)}_{ij,\nu,-}$, because the light intensity is proportional to it, i.e. $I^{(2\omega)}_0 \sim |N^{(2\omega)}_{z,0} Z^{(2\omega)}_{ij,\nu,-}|$.

represented also on Figure 8.19, where it is shown that all interfaces provide approximately similar values of $Z_{\mathrm{p}z,\nu}^{(2\omega)}$.

8.9.4 MOSHG results on the Co/NiO(8 nm)/NiFe system

The MOSHG experimental data for the Co/NiO(8 nm)/NiFe sample are presented on Figure 8.20 for transverse pp, sp and longitudinal ps-MOSHG configurations.

In all cases, the magnetic field was applied along the easy Co axis, denoted by a (b is the hard-axis of Co, i.e. $a \perp b$). The external magnetic field was applied in the transverse direction ($\boldsymbol{H} \parallel \hat{x}$) in the case of pp and sp configurations and in longitudinal one ($\boldsymbol{H} \parallel \hat{y}$)
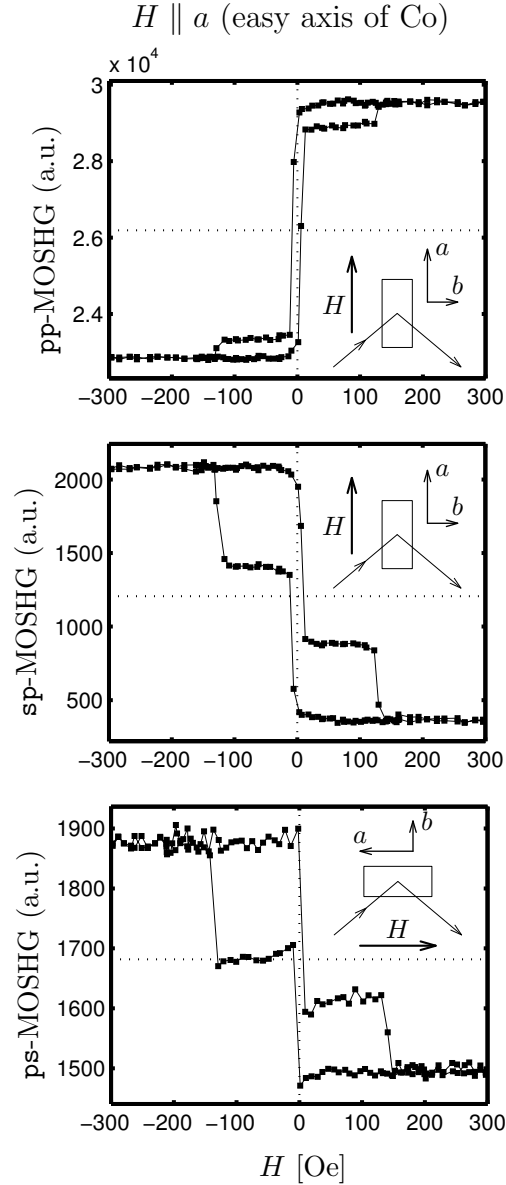
Figure 8.20: MOSHG hysteresis loops of the CoO(2 nm)/Co(2 nm)/NiO(**8 nm**)/FeNi(10 nm)/Cu(5 nm)/ SiO$_2$(80 nm)/Si sample. The magnetic field was applied along the Co easy anisotropy axis. In zero field the Co and FeNi magnetizations lie along the a axis.

for the `ps` configuration. Thus (Table 8.2), the detected components of the magnetization are always in the direction of the applied H, i.e. in the direction of the Co easy axis.

Figure 8.20 shows that both Co and NiFe interfaces provide square hysteresis loops with coercive field of 130 Oe and 12 Oe, respectively. Similar results were obtained in LMOKE. This means, that in zero field, the magnetization of both Co and FeNi layers lies along a, and similar spin configurations are tested at their interfaces. We can see that the `pp` configuration is here much more sensitive to one of the interface of the deeper FeNi interfaces (oppositely to the previous FeSi/DyFeCo case where the MOSHG was more selective to the top FM interface), while the `sp` and `ps` MOSHG configurations are sensitive to all FM interfaces (CoO/Co, Co/NiO, NiO/FeNi, FeNi/Cu). Let us interpret now these results.

transverse `sp` configuration: From a theoretical point of view, the `sp` configuration is only sensitive to the transverse m_x magnetization, since $\mu_x^{(2\omega)} = \chi_{zxx}^{(m)}(E_x^{(\omega)})^2$ (Table 8.2). Because $E_x^{(\omega)}$ is approximately identical for all FM interfaces, the `sp` configuration is sensitive to all FM interfaces, in agreement with the observed data.

longitudinal `ps` configuration: The `ps` configuration is sensitive to both polar, m_z, and longitudinal, m_y, magnetizations. Since, the sample magnetization is always in-plane (tested by PMOKE), we are only sensitive to m_y.

The magnetic signal related to m_y magnetization is given by $\mu_x^{(2\omega)} = \chi_{xyy}(E_y^{(\omega)})^2 + \chi_{xzz}(E_z^{(\omega)})^2$ [Table 8.2]. Since there is an experimental evidence that the magnetic signal comes from all FM interfaces (CoO/Co, Co/NiO, NiO/FeNi, FeNi/Cu), as in `sp` configuration, the $\mu_x^{(2\omega)}$ dipole must be mainly related to the $\chi_{xyy}(E_y^{(\omega)})^2$ term, leading to $|\chi_{xyy}| \gg |\chi_{xzz}|$.

The similarity between `sp` and `ps`-MOSHG loops is strongly supported by the symmetry arguments predicting $\chi_a = \chi_{yxx} = -\chi_{xyy}$ (Table 8.1 and 8.3). Thus, (neglecting the $\mu_x^{(2\omega)} = \chi_{xzz}(E_z^{(\omega)})^2$ term in `ps` configuration), the `ps` and `sp` configurations are analogously given by $\mu_x^{(2\omega)} = \chi_a(E_y^{(\omega)})^2$ and $\mu_y^{(2\omega)} = \chi_a(E_x^{(\omega)})^2$, respectively. Since the in-depth profile of $E_x^{(\omega)}$ and $E_y^{(\omega)}$ are practically identical (see Figure 8.16), both configurations provide nearly the same dipole moments, which radiate in a similar manner (Figures 8.18 and 8.19).

However, experimental hysteresis loops measured in `sp` and `ps` configurations are not exactly identical (Figure 8.20). The `ps` loop is more square and involves a contribution which is quadratic in magnetization (the Co jumps have different size for $H > 0$ or $H < 0$).

The origin of the quadratic contribution can be explained as follows: as discussed in Section 8.4.2, a pure `ps` configuration does not contain any non-magnetic SHG signal, as needed to restore a magnetic signal [Table 8.2, Eq.(8.18)]. Thus, the analyzer has been slightly misoriented from the `s` orientation to transmit partly `p` polarized light, which contains light emitted by non-magnetic sources. Then, the resulting magnetic signal, can depend on m_x. The higher squareness for the `ps` loop can be expected from the superposition of the m_x loop [143]. Furthermore, for a small misorientation of the analyzer by an angle ζ_a, the contribution of the $|\mathcal{E}_{0,\mathbf{s},-}^{(2\omega,m)}|^2 m_y^2 \cos^2 \zeta_a$ term, quadratic with m_y [see Eq. (8.18)], can be detectable.

This can explain well the observed quadratic contribution in the `ps` hysteresis loop (Figure 8.20).

pp configuration: The `pp` hysteresis loop, presented on Figure 8.20, clearly shows that MOSHG is mainly determined by the magnetic behavior of the NiFe interfaces, which are located deeper than the Co interfaces in the structure.

The `pp` configuration is only sensitive to the transverse m_x magnetization, through the $\mu_y^{(2\omega)} = \chi_{yyy}(E_y^{(\omega)})^2 + \chi_{yzz}(E_z^{(\omega)})^2$ and $\mu_z^{(2\omega)} = \chi_{zzy}E_y^{(\omega)}E_z^{(\omega)}$ expressions (Table 8.2). As in the previous Section 8.8.3, the dominant term is $\mu_z^{(2\omega)} = \chi_{zzy}E_y^{(\omega)}E_z^{(\omega)}$, since the `pp`-loop depends mainly on the magnetization state of FeNi interfaces. Thus, the dominant term depends on $E_z^{(\omega)}$ leading to a small $\chi_{yyy}(E_y^{(\omega)})^2$ term. Furthermore, $\chi_{yzz}(E_z^{(\omega)})^2$ is certainly small, since it appears also in the `ps` configuration as $\chi_{xzz}(E_z^{(\omega)})^2$, without giving any MOSHG.

Let us explain, why now the `pp` configuration is more sensitive to the interfaces of the deeper FM layer (NiO/FeNi or FeNi/Cu interface), contrarily to the situation found for the FeSi/DyFeCo structure (Section 8.8). The explaination is connected to the in-depth profile of $E_z^{(\omega)}$ (Figure 8.16): the Co layer is sandwiched between two oxide layers, whose optical properties are nearly similar. Thus, the jumps of $E_z^{(\omega)}$ at each CoO/Co and Co/NiO interface are approximately the same. Furthermore, since both interfaces concern oxides, we can assume that their χ values are similar. These comparable MOSHG contributions have however opposite sign, so that one expects cancelation of the total MOSHG signal for the two interfaces. On the other hand, the FeNi layer is sandwiched between a metal (Cu) and an oxide (NiO). This leads to a large value for $E_z^{(\omega)}$, but only at the NiO/FeNi interface. Thus, it can be concluded that the `pp`-MOSHG originates mainly from this NiO/FeNi interface alone.

8.9.5 MOSHG results on the Co/NiO(4 nm)/NiFe system

Now, let us explain the observed MOSHG data on the Co/NiO(**4 nm**)/NiFe multilayer structure. The explaination might be very similar to that proposed for Co/NiO(**8 nm**)/NiFe structure.

The LMOKE and MOSHG results on the Co/NiO(**4 nm**)/NiFe structure are depicted on Figure 8.21. The magnetic field is applied along (left column) or perpendicular (right column) to the easy Co axis, denoted by a. In this sample, contrarily to the $t^{(\text{NiO})} = 8$ nm one, in zero field the magnetization of FeNi is rotated by 90° with respect to the Co easy axis.

Let us discuss the case where $H \parallel a$ (left column). Consistently with this 90° coupling, the Co layer gives a square LMOKE hysteresis loop, while the FeNi layer gives an S-shape loop. As in the case of the previous $t^{(\text{NiO})} = 8$ nm structure, the transverse MOSHG `pp` configuration checks more the magnetization of FeNi interfaces (later, it is shown that it is dominantly sensitive to NiO/FeNi interface). In counterpart, transverse `sp` and longitudinal `ps` configurations are sensitive to the magnetization of all FM interfaces. As discussed above, `sp` and `ps` configurations provide very similar loops, consistently with the fact that they are due to analogous dominant SHG sources. However, here the longitudinal `ps` configuration gives an additional loop contribution of opposite sign, with
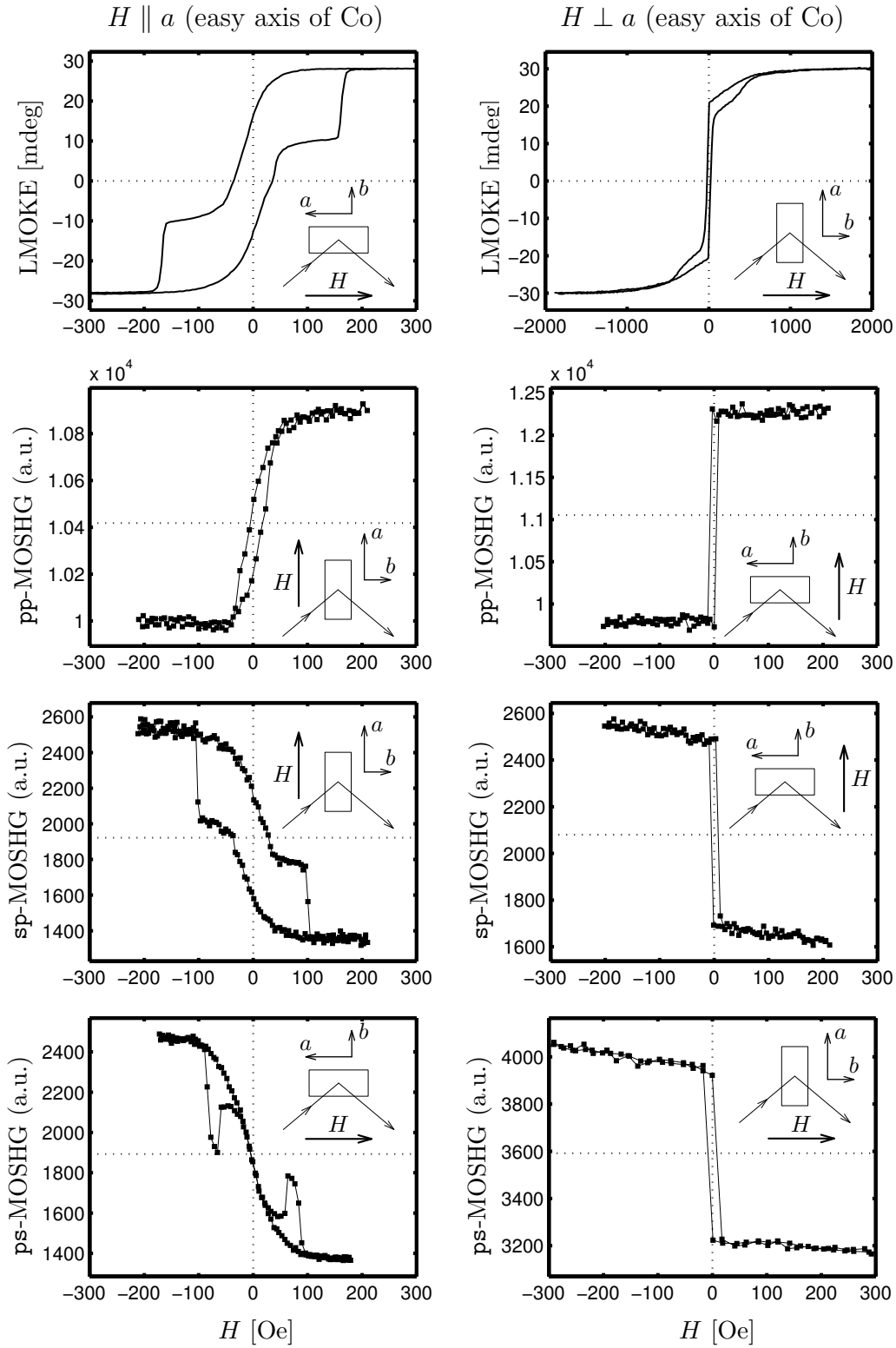
Figure 8.21: Hysteresis loops of LMOKE (1-st row) and MOSHG of the CoO(2 nm)/Co(2 nm)/ NiO(**4 nm**)/FeNi(10 nm)/Cu(5 nm)/SiO$_2$(80 nm)Si sample. The first (second) column shows loops, obtained in a magnetic field H applied parallel (perpendicular) to the easy anisotropy axis of Co.

a coercive field of about 60 Oe. It certainly originates from the slight misorientation of the analyzer from the `s` direction (Section 8.4.2) which gives rise to `p` emitted light sensitive to m_x [Eq. (8.18)]. Since for applied fields smaller than 80 Oe, the Co magnetization remains saturated along "a", the magnetization jump concerns only FeNi interfaces. This magnetization jump is only visible along the "b" axis and not along the "a" axis. This jump of the m_b magnetization component of the FeNi interfaces can be explained either by the presence of two symmetric equivalent easy-axis with respect to the "a" axis, or from the possible coexistence of two type of in-plane magnetic domains. In that case, the jump could correspond to transition to a single domain state.

When H is applied along the FeNi easy axis ($H \perp a$) (right column in Figure 8.21), the LMOKE Co loop contribution show an S-shape. However, when measuring the MOSHG loop under $\boldsymbol{H} \parallel b$, the applied field is too small to modify much the magnetization direction of the Co interfaces. On the right column of Figure 8.21, we can see that the selectivity of MOSHG to the different FM interfaces is similar to that found for the previous $t^{(\mathrm{NiO})} = 8$ nm structure: the `pp` configuration is more sensitive to the FeNi interface, and thus the hysteresis loop looks perfectly square with a small coercivity. On the other hand, the `ps` and `sp` configurations are sensitive to the magnetization of both FeNi and Co interfaces, where the Co interfaces give only a linear variation with field superimposed to the `sp` and `ps` MOSHG FeNi loops. The non-symmetric slope in positive and negative field in the `ps` configuration is again a consequence of a superimposed quadratic term in m_x^2 [Eq. (8.18)].

8.10   Conclusion of Chapter 8

In conclusion, we have demonstrated experimentally on two different structures, a FeSi/DyFeCo FM bilayer and a Co/NiO/FeNi trilayer, that different MOSHG configurations show different depth sensitivity to magnetic interfaces in these multilayer structures.

In particular, the transverse `pp`-MOSHG configuration is more sensitive to interfaces between the FM metal and a material providing a small value of the linear diagonal permittivity $\epsilon_{0,\nu}^{(\omega)}$. This condition is usually fulfilled for air/FM, oxide/FM type of interfaces. Then, the value of $E_z^{(\omega)}$ on these interfaces is much larger than that expected at metal/metal interfaces. The dominant contribution to the magnetic signal in the `pp` configuration is found to be $\mu_z^{(2\omega)} = \chi_{zzy}E_y^{(\omega)}E_z^{(\omega)}$. Thus, the MOSHG intensity, which proportional to the second power of $E_z^{(\omega)}$, is strongly enhanced at FM/dielectric interfaces.

On the other hand, in transverse `sp` and longitudinal `ps` configurations, the MOSHG magnetic signal depends more on all interfaces through the multilayer structure. This is caused by the fact that the profile of the tangential components $E_x^{(\omega)}$, $E_y^{(\omega)}$ does not vary much through the ultrathin multilayer structure. In the `ps` configuration, we have furthermore found that $|\chi_{xyy}| \gg |\chi_{xzz}|$, which is experimentally confirmed for the two investigated samples. The `ss` configuration will not provide different MOSHG light intensity from different interfaces, since the $\mu_x^{(2\omega)} = \chi_{xxx}(E_x^{(\omega)})^2$ term is responsible of the magnetic signal. As experimentally evidenced, the magnetic signal in the `ss` configuration is predicted to be small since $\chi_{xxx} = -\chi_{yyy}$ (Table 8.3).

The intensity of emitted light is dependent on the dipole in-depth location. This dependence is more pronounced for the radiation given by $\mu_x^{(2\omega)}$ and $\mu_y^{(2\omega)}$ moments than for $\mu_z^{(2\omega)}$. When dipoles are embedded into a quite transparent material, the radiated light intensity into the air does not depend significantly on the dipole in-depth location.

Contrarily, for metals, the dipoles provide a MOSHG signal which varies with the in-depth position of the dipole close to the first air/metal interface. However, the difference of light intensity radiated by two dipoles located at different depths separated by $\sim 10\,\mathrm{nm}$ is about a factor two, and is weaker for a deeper dipole. Thus, the variation of the emitted light intensity with the dipole depth position can be, in a first approximation, neglected. Analytical formula of the dipole radiation from a multilayer structure would provide a better insight into this problematic.

For the first time, I have expressed rules which give some insight about the in-depth selectivity of the MOSHG to buried interfaces in different MOSHG configurations.

8.11   Appendix I of Chapter 8

In this Appendix, I give the optical constants used for calculations of generalized incoming and outcoming Fresnel elements (Table 8.5). The optical constant were mostly extracted from Ref. [149]. Optical constants for $Dy_{0.30}Fe_{0.58}Co_{0.12}$ are available only for $E = 1.47\,\mathrm{eV}$ [144], thus I used artificially this value for both $E = 1.55\,\mathrm{eV}$ and $E = 3.1\,\mathrm{eV}$ photon energies[⋆].

material	$N^{(\omega)}$ $E = 1.55\,\mathrm{eV}$	$\varepsilon_0^{(\omega)}$ $E = 1.55\,\mathrm{eV}$	$N^{(2\omega)}$ $E = 3.1\,\mathrm{eV}$	$\varepsilon_0^{(2\omega)}$ $E = 3.1\,\mathrm{eV}$
air	1	1	1	1
CoO	2.12	4.49	2.26 + 0.027i	5.12 + 0.12i
Co	2.48 + 4.79i	-16.77 +23.75i	1.58 + 2.96i	-6.24 + 9.33i
NiO	2.37 + 0.0012i	5.59 + 0.0055i	2.55 + 0.0003i	6.48 + 0.0013i
NiFe (Py)	2.18 + 4.68i	-17.13 +20.35i	1.69 + 3.34i	-8.32 +11.30i
Cu	0.25 + 5.08i	-25.69 + 2.55i	1.18 + 2.21i	-3.50 + 5.22i
SiO_2	1.74	3.03	1.76	3.11
Si	3.68 + 0.0063i	13.55 + 0.046i	5.56 + 0.29i	30.88 + 3.22i
Fe (also for $Fe_{0.96}Si_{0.04}$)	2.90 + 3.36i	-2.85 +19.50i	2.26 + 2.60i	-1.61 +11.74i
$Dy_{0.30}Fe_{0.58}Co_{0.12}$[⋆]	3.67 + 3.85i	-1.35 +28.26i	3.67 + 3.85i	-1.35 +28.26i
glass	1.45	2.11	1.47	2.16

Table 8.5: Optical constants of materials used in Chapter 8.

Chapter 9

Conclusion

In this work, I have treated some open problems concerning the investigation and interpretation of magnetic properties of thin film multilayers by means of Magneto-Optics (MO). More precisely, the Magneto-Optical Kerr Effect (MOKE) and Magneto-Optical Second Harmonic Generation (MOSHG) of light. This contribution is of importance for the investigation of the complex magnetization behaviour in magnetic multilayers and at interfaces. Thus, my studies can help to understand some important problems related to magnetic recording or to spin-electronic media.

It is well known that the interface between a ferromagnetic (FM) and a non-ferromagnetic (non-FM) layer plays a major role in determining the magnetic properties of multilayer structures. I have introduced here a new technique allowing to separate the MOKE contribution, coming from such interfaces, and from the contribution of the rest of the FM layer. This technique deals with the experimental dependence of the MOKE, $\Phi = A + Bt^{(\text{fm})}$ with the thickness of the FM layer $t^{(\text{fm})}$. I have shown that, if both real and imaginary parts of A, B are known, the ratio A/B is directly linked to the MO properties of the interface alone, independently of the other properties of the multilayer and of the light characteristics. I applied with success this method to study the Au/Co/Au(111) interfaces. My theoretical treatment demonstrates that A/B is a pertinent quantity selective only to interfaces. The comparison of the photon energy dispersion of the experimental A/B ratio with calculations of all possible MO contributions, allowed us to conclude that the main MO effect is coming from the modification of the electronic structure at interfaces.

A difficult practical problem is also to separate the magnetic contributions of individual FM layers in a multilayer structure. For that purpose, I show how we can measure selectively the MOKE contributions coming only from one FM layer, canceling the contributions from the others. For this purpose, I have introduced a new presentation of the MOKE as a vector in the complex $\theta\epsilon$-plane, and showed that the measurement of the MOKE signal can be understood as the projection of the Kerr vector onto a well defined projection axis. In the frame of this formalism, I have unified some previously proposed solutions for separating MOKE from single FM layer in a FM bilayer structure. Furthermore, I have introduced two new techniques, the "Parallel Kerr vectors" and the "Cascade Numerical Projection", for separating FM signals issued from all individual FM layers, in a system composed of several FM layers. I also proposed a simple procedure to determine the depth of a FM layer associated with a given MOKE signal component, if all FM layers in the structure provide a square hysteresis loop with different coercive fields. All these

159

techniques were successfully tested on a GaMnAs double junction, on $(Au/Co)_3$ and on the $TbFe/Si_3N_4$ structure, i.e. in three potential media for applications to spin-electronics or magneto-optical recording.

Performing MOKE measurements in ultrathin Co layers deposited on a Au vicinal surface, we discovered an unpredicted MOKE effect. We evidenced it for light propagating along the film normal and linear with in-plane magnetization, when applying a magnetic field in the sample plane. We called it Vicinal-Induced Surface MOKE (VISMOKE) and studied it for the first time. This effect is exhibited by FM layers deposited on a low symmetry surface (e.g. a vicinal surface), with one mirror symmetry plane. VISMOKE is found to be a second-order MO effect originating from both magnetic and structural perturbations of the FM layer permittivity tensor. VISMOKE has been found to vanish when magnetization is perpendicular to the mirror plane of symmetry, i.e. when magnetization is parallel to vicinal steps. VISMOKE was evidenced in a Co layer deposited on a Au(322) vicinal surface. Furthermore, the existence of a non-magnetic perturbation, responsible of VISMOKE, has been proved directly through "structural" reflectivity measurements.

There is only few ways allowing to investigate the magnetism of buried interfaces in multilayer structures. Magneto-Optics on the Second Harmonic Generation (MOSHG) of ligth seemed to be an elegant method to solve sometimes this problem. However, an exact theory which was able to predict MOSHG in non-homogeneously magnetized films was lacking. I propose here an original treatment, based on the radiation of an ensemble of point dipoles. To treat this problem in a rigourous mathematic fashion, I introduced the so-called q-space (Sect. 3.1). The presence of a radiating point dipole on an interface leads to the modification of the boundary conditions. These boundary conditions are incorporated inside the classical 4×4 matrix formalism, allowing to introduce the depth and the spatial distribution of radiating dipoles inside a non-isotropic structure. As a consequence of the rigorous definition of the q-space, the radiated light intensity is found to be $I \sim |k_z \mathcal{E}|^2$, an important point never pointed out for SHG radiation so far.

Up to now, there was no theory predicting which interface gives the larger MOSHG contribution in a multilayer structure. Such informations are awaited and I have brought my own contribution into this complex problem. I used the numeric implementation of my SHG formalism to study the MOSHG depth sensitivity for interfaces, considering generalized Fresnel coefficients. It consists of (i) the determination of the electric field profile of the incident electromagnetic radiation at fundamental frequency through the structure and (ii) the radiation of point dipoles located at each interface. We compared these generalized Fresnel coefficients to experimental data obtained on FeSi/DyFeCo and Co/NiO/NiFe film structures. The magnetic contrast in the pp-MOSHG configuration is always more sensitive to air/metal or dielectric/metal interfaces than to metal/metal interfaces. This is due to the fact that, in this configuration, the light radiation is mainly generated by the $E_z^{(\omega)}$ component of the fundamental electric field, which is very small at metal/metal interfaces, as due to large values of the metal permittivities. On the other hand, ps and sp-MOSHG configurations are found to be mainly induced by the $E_x^{(\omega)}$, $E_y^{(\omega)}$ fields. Since these last profiles are nearly constant over the multilayer structure, the magnetic contrast becomes quite similar for all interfaces in the multilayer structure. The radiation emitted by point dipoles into the air is found to be nearly not dependent on their in-depth position in the ultrathin structures.

Some parts of the present work has been already submited or even published [57, 97, 125, 131].

Appendix A

Definitions and conventions

The aim of this Appendix is to summarize the main definitions and conventions which are widely used all over this document.

Time convention: I use a complex representation for all time-alternating variables, to describe their time and spatial evolutions (for detail see Section 2.1). For example, if $\boldsymbol{E}^{(\omega)}$ is the electric field vector in the *complex representation*, then $\Re(\boldsymbol{E}^{(\omega)}\exp[-i\omega t])$ is real and measurable at a given time t. The sign in the exponent is just a matter of convention and here the time convention $\exp[-i\omega t]$ is used.

If this sign is changed, all complex variables become complex conjugate.

Using time convention, the refractive index writes $N^{(\omega)} = n^{(\omega)} + ik^{(\omega)}$ with $n^{(\omega)} > 0$, $k^{(\omega)} > 0$. The diagonal permittivity in an isotropic media $\varepsilon_0^{(\omega)}$ obeys to $\Im[\varepsilon_0^{(\omega)}] = \Im[(N^{(\omega)})^2] = 2n^{(\omega)}k^{(\omega)} \geq 0$.

Axis referentials: Throughout this manuscript I use the following Cartesian referentials, presented on Figure A.1:

- *Cartesian referential for the sample* $(\hat{x}, \hat{y}, \hat{z})$: The z-direction is the normal to the film surface; it is oriented towards the film structure. The plane of incident/reflected/radiated light is reported as the yz-plane. In another words, the x-component of the wavevector $\boldsymbol{k}^{(\omega)}$ (or of its reduced counterpart $\boldsymbol{N}^{(\omega)}$) is always zero, $k_x^{(\omega)} = 0$.

- *Cartesian referential for the incident light* $(\hat{s}_+, \hat{p}_+, \hat{k}_+)$: The incident light can be linearly polarized in the plane of incidence (p) or perpendicular to it (s). Thus $\hat{s}_+$-direction is oriented along $\hat{x}$. $\hat{k}_+$ is the wavevector direction, i.e. the direction of light propagation. The $\hat{p}_+$-direction is defined so that the Cartesian referential $\hat{s}_+\hat{p}_+\hat{k}_+$ is right-handed.

  Note that superscript "+" tells that the light is propagating in the z-direction, i.e. $\Re(k_z^{(\omega)}) > 0$.

- *Cartesian referential for reflected or radiated light* $(\hat{s}_-, \hat{p}_-, \hat{k}_-)$: The definition is the same as for the incident light.

Sign of MOKE: The Kerr rotation θ is positive if θ rotates clockwise, when looking at the reflected light beam. The Kerr ellipticity ϵ is positive if $\boldsymbol{E}$ rotates clock-wise
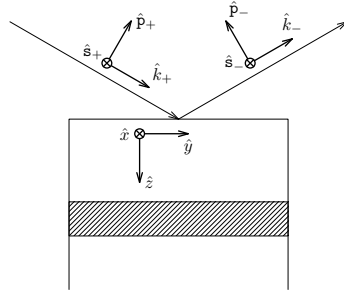
Figure A.1: Definition of the Cartesian referentials for the sample $(\hat{x}, \hat{y}, \hat{z})$ and the incidence $(\hat{s}_+, \hat{p}_+, \hat{k}_+)$ and the reflected (or radiated) $(\hat{s}_-, \hat{p}_-, \hat{k}_-)$ light referentials.
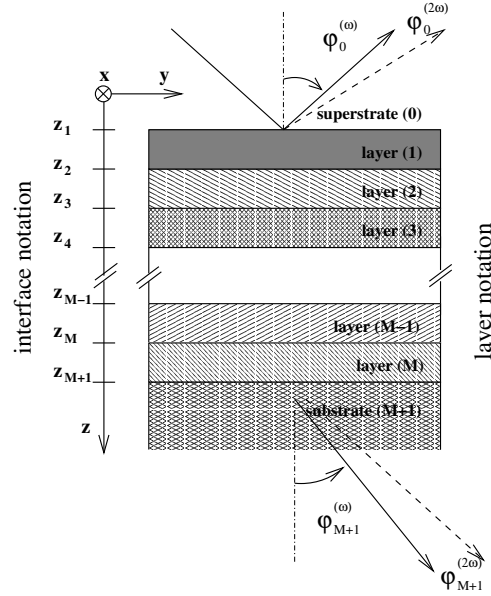
Figure A.2: Designation of layers and interfaces. The superstrate is denoted by 0 and the first interface by 1.

when looking at the reflected light beam [Section 2.2(i)]. Taking into account time and axis sign conventions, this leads to [Section 2.2(ii), Eq. (2.13)]

$$\Phi_{\mathbf{s}} = \theta_{\mathbf{s}} + i\epsilon_{\mathbf{s}} = -\frac{r_{\mathbf{ps}}}{r_{\mathbf{ss}}} \qquad \Phi_{\mathbf{p}} = \theta_{\mathbf{p}} + i\epsilon_{\mathbf{p}} = \frac{r_{\mathbf{sp}}}{r_{\mathbf{pp}}}, \qquad (A.1)$$

where $r_{\mathbf{ss}}$, $r_{\mathbf{ps}}$, $r_{\mathbf{sp}}$ and $r_{\mathbf{pp}}$ reflection coefficients refer to **s** and **p** incident and reflected light polarizations [Eq. (2.10)]. $\Phi_{\mathbf{s}}$, $(\Phi_{\mathbf{p}})$ is called **s**, (**p**)-MOKE.

Layers and interfaces in the multilayer structure: The labelling of the layers and interfaces in the multilayer structure is reported in Figure A.2. The superstrate is denoted by 0, the first interface by 1. In this work, superstrate denotes the medium, from which the incident light is coming. Thus, when an incident light falls on the sample from a glass side, the superstrate is the glass.

Convention for Fourier transformation: The Fourier transformation writes:

$$F(k_x^{(\omega)}) = k_0^u \int \mathrm{d}x \, \exp[-ik_x^{(\omega)}x]f(x) \tag{A.2}$$

and for its inversion

$$f(x) = \frac{1}{2\pi k_0^u} \int \mathrm{d}k_x^{(\omega)} \, \exp[ik_x^{(\omega)}x]F(k_x^{(\omega)}), \tag{A.3}$$

where k_0^u is a unity factor (in units m^{-1}) equalizing the units of $f(x)$ and $F(k_x^{(\omega)})$. For numerical calculations, we use $k_0^u = \omega/c$, ω being the light frequency and c the light velocity in vacuum.

Thus, the Dirac δ-function $\delta(x - x_0)$ function can be expressed as

$$\frac{1}{k_0^u}\delta(x - x_0) = \frac{1}{2\pi k_0^u} \int \mathrm{d}k_x^{(\omega)} \, \exp[ik_x^{(\omega)}(x - x_0)]. \tag{A.4}$$

and $\delta(k_x^{(\omega)} - k_{x0}^{(\omega)})$ as

$$k_0^u\delta(k_x^{(\omega)} - k_{x0}^{(\omega)}) = \frac{k_0^u}{2\pi} \int \mathrm{d}x \, \exp[-i(k_x^{(\omega)} - k_{x0}^{(\omega)})x]. \tag{A.5}$$

Appendix B

Jones formalism

The Jones formalism [18, 19] describes the variation of the light polarization after transmission or reflection on various optical components, e.g. a polarizer, a compensator, phase plate etc. In this work I limit myself to the Jones formalism, written in the linear (s and p) basis [Eq. (2.9)]

$$\boldsymbol{J}^{(\omega)} = \begin{bmatrix} \mathcal{E}_\mathsf{s}^{(\omega)} \\ \mathcal{E}_\mathsf{p}^{(\omega)} \end{bmatrix}, \tag{B.1}$$

where $\boldsymbol{J}^{(\omega)}$ is the Jones vector and $\mathcal{E}_\mathsf{s}^{(\omega)}$, $\mathcal{E}_\mathsf{p}^{(\omega)}$ are the modal amplitudes of the s and p polarized light. In this linear (s, p) basis, the response of some optical elements used is this work are summarized in Table B.1.

optical element		principal axis $\parallel \hat{s}$	response at general orientation α
light from s-polarizer	$\boldsymbol{J}_{in}$	$\begin{bmatrix} 1 \\ 0 \end{bmatrix}$	$\begin{bmatrix} \cos\alpha \\ \sin\alpha \end{bmatrix}$
sample	**R**	$\begin{bmatrix} r_\mathsf{ss} & r_\mathsf{sp} \\ r_\mathsf{ps} & r_\mathsf{pp} \end{bmatrix}$	—
Babinet-Soleil compensator	**C**	$\begin{bmatrix} e^{i\delta/2} & 0 \\ 0 & e^{-i\delta/2} \end{bmatrix}$	$\begin{bmatrix} \cos\delta + i\sin\delta\cos2\alpha & i\sin\delta\sin2\alpha \\ i\sin\delta\sin2\alpha & \cos\delta + i\sin\delta\cos2\alpha \end{bmatrix}$
photoelastic modulator	**M**	$\begin{bmatrix} e^{i\zeta/2} & 0 \\ 0 & e^{-i\zeta/2} \end{bmatrix}$ where $\zeta = \zeta_0 \sin 2\pi f t$	$\begin{bmatrix} \cos\zeta + i\sin\zeta\cos2\alpha & i\sin\zeta\sin2\alpha \\ i\sin\zeta\sin2\alpha & \cos\zeta + i\sin\zeta\cos2\alpha \end{bmatrix}$, where $\zeta = \zeta_0 \sin 2\pi f t$
analyzer in s direction	**A**$(0°)$	$\begin{bmatrix} 1 & 0 \\ 0 & 0 \end{bmatrix}$	$\begin{bmatrix} \cos^2\alpha & \cos\alpha\sin\alpha \\ \cos\alpha\sin\alpha & \sin^2\alpha \end{bmatrix}$
analyzer at 45°	**A**$(45°)$	$\frac{1}{2}\begin{bmatrix} 1 & 1 \\ 1 & 1 \end{bmatrix}$	$\frac{1}{2}\begin{bmatrix} 1 - \sin2\alpha & \cos2\alpha \\ \cos2\alpha & 1 + \sin2\alpha \end{bmatrix}$

Table B.1: Responses of some optical elements expressed in the Jones formalism. The principal axes of the elements are either parallel to the s-axis, or in a general orientation α from the s axis. The quantities ζ, f stand for the amplitude and modulation frequency of the photoelastic modulator, respectively.

Appendix C

Mathematical properties of the q-space

This Appendix shortly presents some useful mathematical properties of the q-space (defined in Section 3.1), in which the electric field inside multilayers is described. The main results of this Appendix are:

(i) the discontinuity of the electric field in the q-space along the z-direction appears *only* when there is a discontinuity of the electric field in the r-space along the same z-direction.

(ii) The discontinuity in the q-space along the z-direction is not achieved in the presence of

 – r-space discontinuities in the x or y direction
 – singularities of the Dirac δ-function or of its derivatives in any direction.

These statements are fundamental to derive the modification of boundary conditions in the presence of a radiating point dipole (Appendix D.3).

The q-space is defined by Equation (3.4)

$$\boldsymbol{E}(\boldsymbol{r}) = \frac{1}{(2\pi)^2}\frac{1}{(k_0^u)^2}\iint \mathrm{d}^2\boldsymbol{q}\,\boldsymbol{\mathcal{E}}_{\boldsymbol{q},\nu,\Sigma,\Sigma}\,\exp[i\,\boldsymbol{q}\cdot\boldsymbol{\rho}], \tag{C.1}$$

where $\boldsymbol{E}(\boldsymbol{r})$ stands for the electric field in r-space and $\boldsymbol{\mathcal{E}}_{\nu,\Sigma,\Sigma}$ is the electric field in the q-space. The later one can be decomposed into four modal amplitudes, i.e. $\boldsymbol{\mathcal{E}}_{\nu,\Sigma,\Sigma} = \sum_{\Pi=1,2}\sum_{d=\pm}\boldsymbol{\mathcal{E}}_{\nu,p,d}$, where ν, Π, d denote layer number, the polarization state and the propagation direction, respectively.

Three examples of conversions between r- and q-space are presented below. We mainly treat discontinuities, singularities and their derivatives. This corresponds to the analysis of a point dipole radiation, for which the sources can be described by Dirac δ-functions (see Section D.2).

Monochromatic plane wave: The electric field of a monochromatic wave plane with the wavevector $\boldsymbol{k}_0 = [k_{x0}, k_{y0}, k_{z0}]$, in the direct space, expresses as $\boldsymbol{E}(\boldsymbol{r}) = \boldsymbol{E}_0\,\exp[ik_{x0}x + ik_{y0}y + ik_{z0}z]$. Inserting this expression into Eq. (C.1), we deduce:

(i) If $k_{z0} > 0$, i.e., $k_{z,\nu,p,+} \equiv k_{z0}$, the modal vector amplitudes in the q-space are equal to $\boldsymbol{\mathcal{E}}_{\nu,\Sigma,+} = \boldsymbol{E}_0\delta(\boldsymbol{q}-\boldsymbol{q}_0)(2\pi k_0^u)^2\exp[ik_{z0}z_\nu]$ and $\boldsymbol{\mathcal{E}}_{\nu,\Sigma,-} = 0$.

(ii) If $k_{z0} < 0$, i.e., $k_{z,\nu,p,-} \equiv k_{z0}$, the modal vector amplitudes are equal to $\boldsymbol{\mathcal{E}}_{\nu,\Sigma,-} = \boldsymbol{E}_0 \delta(\boldsymbol{q} - \boldsymbol{q}_0)(2\pi k_0^u)^2 \exp[ik_{z0}z_\nu]$ and $\boldsymbol{\mathcal{E}}_{\nu,\Sigma,+} = 0$. In both expressions, $\boldsymbol{q}_0 = [k_{x0}, k_{y0}]$.

Electric field in the presence of discontinuities or singularities along the x-direction: The field distribution which contains a discontinuity or singularities of the Dirac δ-function type, and its derivatives with respect to x-direction, can be written as

$$\boldsymbol{E}(x,y,z_\nu) = \Delta \boldsymbol{E} \vartheta(x - x_0) + \boldsymbol{E}_\delta \frac{1}{k_0^u} \delta(x - x_0) + \boldsymbol{E}_{\partial\delta} \frac{1}{(k_0^u)^2} \frac{\partial}{\partial x} \delta(x - x_0) + \cdots, \qquad \text{(C.2)}$$

where $\vartheta(x - x_0)$ is the Heaviside step-function with an unit step located at $x = x_0$. Consequently, the modal vector amplitudes in the $\boldsymbol{q}$-space are

$$\boldsymbol{\mathcal{E}}_{\nu,\Sigma,\Sigma} = 2\pi k_0^u \, \delta(k_y) \, \exp[-ik_x x_0] \left(\frac{k_0^u}{ik_x} \Delta \boldsymbol{E} + \boldsymbol{E}_\delta + \frac{ik_x}{k_0^u} \boldsymbol{E}_{\partial\delta} + \cdots \right), \qquad \text{(C.3)}$$

as follows from Eq. (C.1) and the properties of the Fourier transform (Appendix A). This case can be straightforwardly generalized to the case where discontinuities and singularities are present everywhere, or in the y direction.

Some remark can be done on Equation (C.3):

(i) For every value of z, the field distributions which contain discontinuities or singularities in the x and y dimensions, such as these given by Eq.(C.2), are expressed by a continuous function in the corresponding $\boldsymbol{q}$-space.

(ii) The dependence of the electric field in both $\boldsymbol{k}$ and $\boldsymbol{q}$-spaces, $\boldsymbol{E}(\boldsymbol{r})$ and $\boldsymbol{\mathcal{E}}_{\nu,\Sigma,\Sigma}$, on z is given by the dependence of $\Delta \boldsymbol{E}$, $\boldsymbol{E}_\delta$, $\boldsymbol{E}_{\partial\delta}$, etc., on z.

Thus, the discontinuities or singularities in the z-dimension are conserved during the transformation between the $\boldsymbol{r}$-space and $\boldsymbol{q}$-space, and thus need to be treated separately, as discussed below.

Electric field with a discontinuity or singularity along the z-direction: The field distribution containing a discontinuity or a singularity located at the position of the ν-th interface, i.e., at $z = z_\nu$, can be written as

$$\boldsymbol{E}(\boldsymbol{\rho}, z) = \{\boldsymbol{E}(\boldsymbol{\rho}, z)\} + \Delta \boldsymbol{E} \, \vartheta(z - z_\nu) + \boldsymbol{E}_\delta \frac{1}{k_0^u} \delta(z - z_\nu), \qquad \text{(C.4)}$$

where $\{\boldsymbol{E}(\boldsymbol{\rho}, z)\}$ denotes the regular smooth part of the function and $\boldsymbol{\rho} \equiv [x, y]$. $\Delta \boldsymbol{E}$ and $\boldsymbol{E}_\delta$ represent the magnitudes of the discontinuity and singularity, respectively.

If the discontinuity and singularity are constant with respect to x and y co-ordinates, Eq. (C.4) can be transformed into the $\boldsymbol{q}$-space as

$$\boldsymbol{\mathcal{E}}_{\nu,\Sigma,\Sigma} = \{\boldsymbol{\mathcal{E}}_{\nu,\Sigma,\Sigma}\} + \Delta \boldsymbol{E} \, (2\pi k_0^u)^2 \, \vartheta(z - z_\nu) \, \delta(\boldsymbol{q}) + \boldsymbol{E}_\delta \, (2\pi)^2 k_0^u \delta(z - z_\nu) \, \delta(\boldsymbol{q}). \qquad \text{(C.5)}$$

If the discontinuity/singularity is not constant with respect to x and y, the result is formally the same as in Eq. (C.5), but $\delta(\boldsymbol{q})$ is modified accordingly to the variation of the field in the x and y directions. Thus, the discontinuity, or singularity, is conserved when transforming the electric field from the $\boldsymbol{r}$ to the $\boldsymbol{q}$-space.

Comparing equations (C.4) and (C.5), one finds a discontinuity of the field in the vicinity of the $z = z_\nu$ plane

$$\boldsymbol{E}(\boldsymbol{\rho}, z_\nu + \epsilon) - \boldsymbol{E}(\boldsymbol{\rho}, z_\nu - \epsilon) = \Delta \boldsymbol{E}. \qquad \text{(C.6)}$$

where $\epsilon \to 0$. The Eq. (C.6) is transformed into the $\boldsymbol{q}$-space as

$$\boldsymbol{\mathcal{E}}_{\nu+\epsilon,\Sigma,\Sigma} - \boldsymbol{\mathcal{E}}_{\nu-\epsilon,\Sigma,\Sigma} = (2\pi k_0^u)^2 \Delta \boldsymbol{E}\, \delta(\boldsymbol{q}), \tag{C.7}$$

where $\boldsymbol{\mathcal{E}}_{\nu\pm\epsilon,\Sigma,\Sigma}$ denotes the modal vector amplitude expressed in the $\boldsymbol{q}$-space, located at $z = z_\nu \pm \epsilon$. This equation implies that the discontinuity of the field distribution across $z = z_\nu$ is maintained also in the $\boldsymbol{q}$-space, and such a discontinuity is *not* affected by the presence of a singularity in the z dimension located at $z = z_\nu$ in the direct space.

Conclusion of Appendix C:

   (i) discontinuities or singularities of the field distribution in the x and y direction in the $\boldsymbol{r}$-space do not modify the boundary conditions expressed in the $\boldsymbol{q}$-space.

  (ii) the boundary conditions in the $\boldsymbol{q}$-space are not affected by the presence of a singularity of Dirac δ-function type or its derivatives in the z direction, but only by the presence of a field discontinuity in the z-direction of the $\boldsymbol{r}$-space.

These properties will be useful in the next Appendix D, where the boundary conditions in the presence of a radiating point dipole are derived.

Appendix D

Modification of the boundary conditions in the presence of a radiating point dipole

This Appendix presents the modification of boundary conditions in the presence of a radiating point dipole located at the ν-th interface, inside an ultrathin sheet. It is first expressed in the r-space and subsequently in the q-space (defined in the Section 3.1).

The correct treatment of boundary conditions for the SHG field was recently proposed by Atkinson and Kubarev [129], but expressed only in the r-space. In their work, the radiation source is a thin sheet with polarization $\boldsymbol{P}^{(2\omega)}$, and they exclude sources, i.e. $\boldsymbol{j}^{(2\omega)} = 0$, $\rho^{(2\omega)} = 0$. Here I solve this problem from a different point of view. I consider material equations in the $\boldsymbol{D}^{(2\omega)} = \varepsilon_0 \varepsilon^{(2\omega)} \boldsymbol{E}^{(2\omega)}$ form (even at the position of the dipole), but non-zero sources $\boldsymbol{j}^{(2\omega)}$ and $\rho^{(2\omega)}$. Because both approches describe the same situation, the final results in both approaches in the r-space must be identical. However, my SHG description by a radiating point dipole allows to calculate the radiated SHG field from a system with lateral non-uniform distributions of radiating dipoles [131]. Furthermore, it allows to understand better the transfer between the fundamental (ω) and the radiated SHG field (2ω), since a point dipole scheme is more easy-to-imagine.

D.1 Maxwell equations

Maxwell equations in the direct r-space, with fields $\boldsymbol{E}^{(2\omega)}$, $\boldsymbol{D}^{(2\omega)}$, $\boldsymbol{H}^{(2\omega)}$, $\boldsymbol{B}^{(2\omega)}$ and sources $\boldsymbol{j}^{(2\omega)}$ and $\rho^{(2\omega)}$ oscilating at frequency 2ω, write

$$\nabla \cdot \boldsymbol{D}^{(2\omega)} = \rho^{(2\omega)} \quad \text{(a)} \qquad \nabla \times \boldsymbol{E}^{(2\omega)} = i2\omega \boldsymbol{B}^{(2\omega)} \quad \text{(b)}$$
$$\nabla \cdot \boldsymbol{B}^{(2\omega)} = 0 \quad \text{(c)} \qquad \nabla \times \boldsymbol{H}^{(2\omega)} = \boldsymbol{j}^{(2\omega)} - i2\omega \boldsymbol{D}^{(2\omega)} \quad \text{(d)}.$$
(D.1)

The material equations are

$$\boldsymbol{D}^{(2\omega)} = \varepsilon_0 \varepsilon^{(2\omega)} \boldsymbol{E}^{(2\omega)}$$
$$\boldsymbol{B}^{(2\omega)} = \mu_0 \boldsymbol{H}^{(2\omega)},$$
(D.2)

where ε_0 and μ_0 are the vacuum permeability and permittivity, respectively, and $\varepsilon^{(2\omega)}$ is a complex permittivity tensor. The medium is assumed to be magnetically non-active (Section 2.3.2), and thus $\boldsymbol{B}^{(2\omega)} = \mu_0 \boldsymbol{H}^{(2\omega)}$.

D.2   Definition of the source of SHG field

As already discussed, the SHG field is assumed to be generated by a point electric dipole of complex moment $\boldsymbol{\mu}_\nu^{(2\omega)}$ oscillating at frequency 2ω located at a position $\boldsymbol{r}_\nu = [x_\nu, y_\nu, z_\nu]$, on the ν-th interface. Thus the electric dipoles density $\boldsymbol{\mu}(\boldsymbol{r}, t)$ writes

$$\boldsymbol{\mu}(\boldsymbol{r}, t) = \boldsymbol{\mu}_\nu^{(2\omega)} \delta(\boldsymbol{r} - \boldsymbol{r}_\nu) \exp[-i2\omega t]. \tag{D.3}$$

In this equation, the complex moment $\boldsymbol{\mu}_\nu^{(2\omega)}$ of the dipole is given by the equation $\boldsymbol{\mu}_\nu^{(2\omega)} = \chi \otimes \boldsymbol{E}_\nu^{(\omega)} \boldsymbol{E}_\nu^{(\omega)}$ [Eq. (7.2)], where the field at ω for the ν-th interface $\boldsymbol{E}_\nu^{(\omega)}$ is calculated from Eq. (3.32).

In Maxwell's equations (D.1), the surface current density $\boldsymbol{j}^{(2\omega)}$ and the charge density $\rho^{(2\omega)}$ act as sources of electromagnetic field. The current density is obtained by the time-derivative of the electric dipole density, so that [19, 17]

$$\boldsymbol{j}(\boldsymbol{r}, t) = \frac{\partial \boldsymbol{\mu}(\boldsymbol{r}, t)}{\partial t} = \boldsymbol{j}^{(2\omega)} \exp[-i2\omega t] \tag{D.4}$$

where

$$\boldsymbol{j}^{(2\omega)} = -i2\omega \boldsymbol{\mu}_\nu^{(2\omega)} \delta(\boldsymbol{r} - \boldsymbol{r}_\nu). \tag{D.5}$$

With regard to the charge density $\rho^{(2\omega)}$, we consired first a non-oscillating point dipole parallel to the z-axis. Such a dipole consists of a positive Q and a negative $-Q$ point charge, located at $z = z_\nu - \epsilon$ and $z = z_\nu + \epsilon$, $\epsilon \to 0$, respectively. The charge density corresponding to such a charge distribution can be formally expressed as

$$\rho = Q\,\delta(x - x_\nu)\,\delta(y - y_\nu) \lim_{\epsilon \to 0} \left[\delta(z - (z_\nu - \epsilon)) - \delta(z - (z_\nu + \epsilon)) \right]. \tag{D.6}$$

Since the dipole moment is $\mu_z = 2Q\epsilon$, a simple modification of Eq. (D.6) leads to the expression

$$\rho = -\mu_z\,\delta(x - x_\nu)\,\delta(y - y_\nu)\,\frac{\partial}{\partial z}\delta(z - z_\nu). \tag{D.7}$$

Considering now an oscillating point dipole with any orientation. Then, the above charge density expression can be generalised as

$$\rho(\boldsymbol{r}, t) = \rho^{(2\omega)} \exp[-i2\omega t], \tag{D.8}$$

where

$$\rho^{(2\omega)} = -\boldsymbol{\mu}_\nu^{(2\omega)} \cdot \nabla\delta(\boldsymbol{r} - \boldsymbol{r}_\nu). \tag{D.9}$$

In this equation, $\nabla\delta$ denotes the gradient of the δ-function.

D.3   Boundary conditions in the presense of a point dipole

In this Section, we analyse the influence of an oscillating dipole on the normal and transversal components of the field vectors. A previous treatment reported in ref. [129] cannot be used directly here since the authors consider an homogeneous and infinitesimally thin polarisation *sheet* rather than a point dipole. Nevertheless, their formalism can be advantageously applied in our analysis. Then the $\boldsymbol{r}$-space expressions will be transformed into

the $\boldsymbol{q}$-space in a manner that they can be afterward directly incorporated into the matrix formalism describing the propagation of light in the multilayer structure.

Recall (Section 7.3) that the electric point dipole of moment $\boldsymbol{\mu}_\nu^{(2\omega)}$ is assumed to be placed inside ultrathin sheet, which is located at the ν-th interface (Figure 7.2). Although this sheet is later assumed to be vacuum one, in this Appendix, I consider that the sheet has a general permittivity $\overline{\varepsilon}_\nu^{(2\omega)}$.

In the following, I add an *overbar above all variables, which are related to the electromagnetic waves inside the ultrathin sheet,* e.g. $\overline{\varepsilon}_\nu^{(2\omega)}$, $\overline{\boldsymbol{N}}_\nu^{(2\omega)}$, $\hat{\overline{e}}_{\nu,\mathbf{s/p},\pm}^{(2\omega)}$, $\overline{\boldsymbol{E}}$, $\overline{\boldsymbol{\mathcal{E}}}$, etc. to distinguish between the variables inside the ultrathin sheet located at the ν-th interface and those inside ν-th layer.

Let us consider a function f which contains discontinuities and singularities of the Dirac δ-function type or its derivatives at places denoted by $x_{i,\nu}$,

$$f = \{f\} + \Delta f \vartheta(x_i - x_{i,\nu}) + f_\delta \frac{1}{k_0^u}\delta(x_i - x_{i,\nu}) + f_{\partial\delta}\frac{1}{(k_0^u)^2}\frac{\partial}{\partial x_i}\delta(x_i - x_{i,\nu}) + \dots \quad \text{(D.10)}$$

Then, the first derivative of such a function can be written as [35, 129]

$$\frac{\partial f}{\partial x_i} = \left\{\frac{\partial f}{\partial x_i}\right\} + [f(x_{i,\nu+\epsilon}) - f(x_{i,\nu-\epsilon})]\,\delta(x_i - x_{i,\nu}) + f_\delta\frac{\partial}{\partial x_i}\delta(x_i - x_{i,\nu}) + f_{\partial\delta}\frac{\partial^2}{\partial x_i^2}\delta(x_i - x_{i,\nu}) + \cdots,$$

$$\text{(D.11)}$$

where $\{\partial f/\partial x_i\}$ denotes the derivative of the function almost everywhere and $f(x_{i,\nu\pm\epsilon})$ denotes the value of f at $x_i = x_{i,\nu} \pm \epsilon$, $\epsilon \to 0$. In the context of the following analysis, the function f can be any of the components of the field vectors. Equation (D.11) has an important implication: Since the sources of the SHG field in the Maxwell equations (D.1) contain singularities of the Dirac δ-function type and its derivatives [Eqs. (D.5) and (D.9)], the field vectors must contain discontinuities as well as singularities of the same type.

Boundary conditions for $\overline{\boldsymbol{D}}$.   Considering the expression (D.9) for the charge density, the Maxwell equation (D.1a) can be rewritten as

$$\begin{aligned} \nabla \cdot \overline{\boldsymbol{D}} &= \{\nabla \cdot \overline{\boldsymbol{D}}\} + (\overline{D}_{z,\nu+\epsilon} - \overline{D}_{z,\nu-\epsilon})\,\delta(z - z_\nu) + \overline{D}_{z,\delta}\frac{1}{(k_0^u)}\frac{\partial}{\partial z}\delta(z - z_\nu) + \cdots \\ &= -\boldsymbol{\mu}_\nu^{(2\omega)} \cdot \nabla\delta(\boldsymbol{r} - \boldsymbol{r}_\nu). \end{aligned} \quad \text{(D.12)}$$

where non-expressed terms contain:
   (i) discontuities and singularities of the Dirac δ-function type, and its x and y derivates, at the point dipole position
   (ii) higher derivative order, $\partial^n/\partial^z\delta(z - z_\nu)$.

In Eq. (D.12), the terms containing discontinuities and singularities of the Dirac δ-function type in the x and y direction were omitted since they do not contribute to the boundary conditions, as already discussed in Section C. Comparing the terms at the same derivative order in $\delta(z - z_\nu)$, the boundary conditions for the $\overline{\boldsymbol{D}}$ vector in the $\boldsymbol{r}$-space can be written as

$$\{\nabla \cdot \overline{\boldsymbol{D}}\} = 0,$$

$$\overline{D}_{z,\nu+\epsilon} - \overline{D}_{z,\nu-\epsilon} = -\mu_{x,\nu}^{(2\omega)}\delta(y - y_\nu)\frac{\partial\delta(x - x_\nu)}{\partial x} - \mu_{y,\nu}^{(2\omega)}\delta(x - x_\nu)\frac{\partial\delta(y - y_\nu)}{\partial y}, \quad \text{(D.13)}$$

$$\overline{D}_{z,\delta} = -\mu_{z,\nu}^{(2\omega)}k_0^u\,\delta(x - x_\nu)\delta(y - y_\nu).$$

The first equation implies the continuity of the normal component of the $\overline{\boldsymbol{D}}$ vector everywhere except at the location of the point dipole [19, 17]. This is equivalent to the well-known boundary condition for a medium containing no free charges. The influence of the point dipole is described by the second and third equations. In particular, the discontinuity of the z-component of the $\overline{\boldsymbol{D}}$ field at the point dipole location is determined by the right-hand side of the second equation. Furthermore, the z-component of the $\overline{\boldsymbol{D}}$ vector contains a singularity which is expressed by the right-hand side of the third equation.

The form of the boundary conditions (D.13) in the $\boldsymbol{r}$-space is not very convenient for further mathematical treatment, due to the presence of the δ-function and its derivative. On the other hand, the boundary conditions can be elegantly expressed in the $\boldsymbol{q}$-space. In particular, using the properties of the $\boldsymbol{q}$-space discussed in Section C [see Eqs. (C.2) (C.3)], the second equation in Eq. (D.13) can be written as

$$\Delta\overline{\mathcal{D}}_{z,\nu,\Sigma,\Sigma} \equiv \overline{\mathcal{D}}_{z,\nu+\epsilon,\Sigma,\Sigma} - \overline{\mathcal{D}}_{z,\nu-\epsilon,\Sigma,\Sigma} = (-i\mu_{x,\nu}^{(2\omega)}k_x - i\mu_{y,\nu}^{(2\omega)}k_y)\,(k_0^u)^2\,\exp[-i\boldsymbol{q}\cdot\boldsymbol{\rho}_\nu], \quad \text{(D.14)}$$

where $\boldsymbol{\rho}_\nu = [x_\nu, y_\nu]$. This equation provides an explicit expression of the magnitude for the discontinuity of the z-component of the vector $\overline{\mathcal{D}}_{\nu,\Sigma,\Sigma}$.

The third equation in Eq. (D.13) implies that, in addition to the discontinuity at $z = z_\nu$, the z-component of the $\overline{\boldsymbol{D}}$ vector contains also a singularity that can be written as

$$\overline{\boldsymbol{D}}_\delta = -\mu_{z,\nu}^{(2\omega)}\delta(\boldsymbol{r} - \boldsymbol{r}_\nu)\,\hat{z}. \quad \text{(D.15)}$$

However, as mentioned in the discussion after Eq. (C.7), such a singularity does not affect the boundary condition (D.14). On the other hand, this singularity affects the boundary conditions for the $\overline{\mathcal{E}}$ and $\overline{\mathcal{H}}$ fields, as it is shown below.

Boundary conditions for $\overline{\boldsymbol{B}}$.   The boundary condition for the $\overline{\boldsymbol{B}}$ vector can be derived from the Maxwell equation (D.1c) using an equivalent procedure as for the $\overline{\boldsymbol{D}}$ vector. In the $\boldsymbol{r}$-space, the condition can be written as

$$\overline{B}_{z,\nu+\epsilon} - \overline{B}_{z,\nu-\epsilon} = 0. \quad \text{(D.16)}$$

In the $\boldsymbol{q}$-space, the boundary condition becomes

$$\Delta\overline{\mathcal{B}}_{z,\nu,\Sigma,\Sigma} \equiv \overline{\mathcal{B}}_{z,\nu+\epsilon,\Sigma,\Sigma} - \overline{\mathcal{B}}_{z,\nu-\epsilon,\Sigma,\Sigma} = 0. \quad \text{(D.17)}$$

This expression means that the z-component of the vector $\overline{\mathcal{B}}$ is continuous around the position of the point dipole.

Boundary conditions for $\overline{\boldsymbol{H}}$.   The boundary conditions for the field vector $\overline{\boldsymbol{H}}$ can be derived from the Maxwell equation (D.1d), where the curent density is given by Eq. (D.5). Assuming that the field distribution contains discontinuities and singularities of the Dirac δ-function type and its derivatives, the left-hand side of Eq. (D.1d) can be written as

$$\nabla \times \overline{\boldsymbol{H}} = \{\nabla \times \overline{\boldsymbol{H}}\} + \begin{bmatrix} \delta(x - x_\nu) \\ \delta(y - y_\nu) \\ \delta(z - z_\nu) \end{bmatrix} \times (\overline{\boldsymbol{H}}_{\nu+\epsilon} + \overline{\boldsymbol{H}}_{\nu-\epsilon}) + \cdots, \quad \text{(D.18)}$$

where the non-expressed terms are both derivatives of δ-function in the x and y directions and for higher order of derivatives of the $\delta(z - z_\nu)$ function in the z direction.

In this equation, the terms containing the discontinuities and singularities of the Dirac δ-function type in x and y dimensions were omitted since they do not contribute to the boundary conditions, as already discussed in Section C.

In the evaluation of the right-hand side of Eq. (D.1d), the singularity of the z-component of the vector $\overline{\boldsymbol{D}}$ [Eq. (D.15)] has to be considered. Comparing the terms at the same derivative order in $\delta(z - z_\nu)$, the boundary conditions for the vector $\overline{\boldsymbol{H}}$ in the $\boldsymbol{r}$-space can be written as

$$\{\nabla \times \overline{\boldsymbol{H}}\} = -i2\omega\{\overline{\boldsymbol{D}}\},$$

$$\overline{H}_{x,\nu+\epsilon} - \overline{H}_{x,\nu-\epsilon} = -is\omega\mu_{y,\nu}^{(2\omega)}\delta(x - x_\nu)\delta(y - y_\nu), \tag{D.19}$$

$$\overline{H}_{y,\nu+\epsilon} - \overline{H}_{y,\nu-\epsilon} = i2\omega\mu_{x,\nu}^{(2\omega)}\delta(x - x_\nu)\delta(y - y_\nu).$$

Again, the first equation implies the continuity of the tangential components of the vector $\overline{\boldsymbol{H}}$ everywhere except at the location of the point dipole. The influence of the point dipole is described by the second and third equations. In particular, the discontinuities of the x and y components of the field $\overline{\boldsymbol{H}}$ at the point dipole location are determined by the right-hand sides of the second and third equations, respectively. Since the right-hand side of Eq. (D.1d) does not contain any terms proportional to $\partial^n\delta(z - z_\nu)/\partial z^n$, where $n = 1, 2, \ldots$, the field vector $\overline{\boldsymbol{H}}$ has no singularities of the Dirac δ-function type or its derivatives at the position of the oscillating point dipole.

When the boundary conditions (D.19) are expressed in the $\boldsymbol{q}$-space, the following equations are found:

$$\Delta\overline{\mathcal{H}}_{x,\nu,\Sigma,\Sigma} \equiv \overline{\mathcal{H}}_{x,\nu+\epsilon,\Sigma,\Sigma} - \overline{\mathcal{H}}_{x,\nu-\epsilon,\Sigma,\Sigma} = -i2\omega\mu_{y,\nu}^{(2\omega)}(k_0^u)^2\exp[-i\boldsymbol{q}\cdot\boldsymbol{\rho}_\nu],$$

$$\Delta\overline{\mathcal{H}}_{y,\nu,\Sigma,\Sigma} \equiv \overline{\mathcal{H}}_{y,\nu+\epsilon,\Sigma,\Sigma} - \overline{\mathcal{H}}_{y,\nu-\epsilon,\Sigma,\Sigma} = i2\omega\mu_{x,\nu}^{(2\omega)}(k_0^u)^2\exp[-i\boldsymbol{q}\cdot\boldsymbol{\rho}_\nu]. \tag{D.20}$$

providing explicit expressions for the magnitudes of the discontinuities of the x and y components of the $\overline{\mathcal{H}}_{\nu,\Sigma,\Sigma}$ vector.

Boundary conditions for $\overline{\boldsymbol{E}}$. The boundary conditions for the vector $\overline{\boldsymbol{E}}$ can be derived from the Maxwell equation (D.1b). However, before the equations are explicitly written, the following comments need to be done. The medium surrounding the dipole is treated at a macroscopic level, i.e., described by the dielectric permittivity $\overline{\varepsilon}_\nu^{(\omega)}$ and the magnetic permeability μ_0. This means that the relations between the pairs of the electric and magnetic fields and inductions can be written as $\overline{\boldsymbol{D}} = \overline{\varepsilon}_0\varepsilon_\nu^{(2\omega)}\overline{\boldsymbol{E}}$ and $\overline{\boldsymbol{B}} = \mu_0\overline{\boldsymbol{H}}$, respectively. These equations are valid *everywhere*, i.e., even at the location of the point dipole. The former relation implies that the vector $\overline{\boldsymbol{E}}$ contains a singularity, which is related to the singularity $\overline{\boldsymbol{D}}_{\partial\delta}$ of the vector $\overline{\boldsymbol{D}}$ [see Eq. (D.15)] by $\overline{\boldsymbol{E}}_{\partial\delta} = \overline{\boldsymbol{D}}_{\partial\delta}/(\varepsilon_0\overline{\varepsilon}_\nu^{(2\omega)})$. The latter equation implies again, as for the vector $\overline{\boldsymbol{H}}$, that the vector $\overline{\boldsymbol{B}}$ contains no singularities at the dipole position.

When the above expressions are substituted into the Maxwell equation (D.1b), the comparison of the terms with the same derivative order in $\delta(z - z_\nu)$ leads to the following

set of equations:

$$\{\nabla \times \overline{\boldsymbol{E}}\} = i2\omega\{\overline{\boldsymbol{B}}\},$$

$$\overline{E}_{x,\nu+\epsilon} - \overline{E}_{x,\nu-\epsilon} = -\frac{1}{\varepsilon_0 \overline{\varepsilon}_\nu^{(2\omega)}} \mu_{z,\nu}^{(2\omega)} \delta(x-x_\nu)\frac{\partial}{\partial y}\delta(y-y_\nu),$$

$$\overline{E}_{y,\nu+\epsilon} - \overline{E}_{y,\nu-\epsilon} = -\frac{1}{\varepsilon_0 \overline{\varepsilon}_\nu^{(2\omega)}} \mu_{z,\nu}^{(2\omega)} \delta(y-y_\nu)\frac{\partial}{\partial x}\delta(x-x_\nu).$$

(D.21)

To obtain these expressions, the identity $\nabla \times \delta(\boldsymbol{r}-\boldsymbol{r}_\nu)\hat{z} = [\frac{\partial}{\partial y}\delta(\boldsymbol{r}-\boldsymbol{r}_\nu), -\frac{\partial}{\partial x}\delta(\boldsymbol{r}-\boldsymbol{r}_\nu),0]$ was used. Furthermore, again the terms containing the discontinuities and singularities of the Dirac δ-function type along the x and y directions were omitted since they do not contribute to the boundary conditions, as discussed in Section C.

The first equation in (D.21) implies the continuity of the tangential components of the vector $\overline{\boldsymbol{E}}$ everywhere except in the location of the point dipole, being equivalent to the well-known boundary condition. The discontinuities of the x and y components of the field $\overline{\boldsymbol{E}}$ at the location of the point dipole are determined by the right-hand sides of the second and third equations, respectively.

When the boundary conditions (D.21) are expressed in the $\boldsymbol{q}$-space, the following equations are found:

$$\Delta\overline{\mathcal{E}}_{x,\nu,\Sigma,\Sigma} \equiv \overline{\mathcal{E}}_{x,\nu+\epsilon,\Sigma,\Sigma} - \overline{\mathcal{E}}_{x,\nu-\epsilon,\Sigma,\Sigma} = -ik_x\frac{(k_0^u)^2}{\varepsilon_0\overline{\varepsilon}_\nu^{(2\omega)}}\mu_{z,\nu}^{(2\omega)}\exp[-i\boldsymbol{q}\cdot\boldsymbol{\rho}_\nu],$$

$$\Delta\overline{\mathcal{E}}_{y,\nu,\Sigma,\Sigma} \equiv \overline{\mathcal{E}}_{y,\nu+\epsilon,\Sigma,\Sigma} - \overline{\mathcal{E}}_{y,\nu-\epsilon,\Sigma,\Sigma} = -ik_y\frac{(k_0^u)^2}{\varepsilon_0\overline{\varepsilon}_\nu^{(2\omega)}}\mu_{z,\nu}^{(2\omega)}\exp[-i\boldsymbol{q}\cdot\boldsymbol{\rho}_\nu].$$

(D.22)

These equations provide explicit expressions for the magnitudes of the discontinuities of the x and y components of the $\overline{\mathcal{E}}_{\nu,\Sigma,\Sigma}$ vector.

D.4 Matrix representation of the boundary conditions in the $\boldsymbol{q}$-space

As mentioned earlier, the usual material equations $\overline{\boldsymbol{D}} = \varepsilon_0\overline{\varepsilon}_\nu^{(2\omega)}\overline{\boldsymbol{E}}$ and $\overline{\boldsymbol{B}} = \mu_0\overline{\boldsymbol{H}}$ are valid everywhere in the medium characterised by the macroscopic permittivity $\overline{\varepsilon}_\nu^{(2\omega)}$. Using Eq. (D.22) and the Maxwell equation (D.1b), one derives a relation between the modal vector amplitudes $\overline{\mathcal{E}}_{\nu,\Sigma,d}$ and $\overline{\mathcal{H}}_{\nu,\Sigma,d}$ in the form $\overline{\boldsymbol{N}}_{\nu,p,d}\times\overline{\mathcal{E}}_{\nu,\Sigma,d} = \eta_0\overline{\mathcal{H}}_{\nu,\Sigma,d}$, assuming independence of $\overline{\boldsymbol{N}}_{\nu,p,d}$ on polarization, i.e. $\overline{\boldsymbol{N}}_{\nu,p,d} = \overline{\boldsymbol{N}}_{\nu,1,d} = \overline{\boldsymbol{N}}_{\nu,2,d}$. Using these equations, the boundary conditions for the field vectors $\overline{\mathcal{E}}$ and $\overline{\mathcal{H}}$ expressed in the $\boldsymbol{q}$-space can be written in a compact matrix form [Eqs. (D.14)(D.17)(D.20)(D.22)]

$$
\begin{bmatrix}
\Delta\overline{\mathcal{E}}_{x,\nu,\Sigma,\Sigma} \\
\eta_0\Delta\overline{\mathcal{H}}_{y,\nu,\Sigma,\Sigma} \\
\eta_0\Delta\overline{\mathcal{H}}_{z,\nu,\Sigma,\Sigma} \\
\eta_0\Delta\overline{\mathcal{H}}_{x,\nu,\Sigma,\Sigma} \\
\Delta\overline{\mathcal{E}}_{y,\nu,\Sigma,\Sigma} \\
\Delta\overline{\mathcal{E}}_{z,\nu,\Sigma,\Sigma}
\end{bmatrix}
=
\begin{bmatrix}
1 & 1 & 0 & 0 & 0 & 0 \\
\overline{N}_{z,\nu,+}^{(2\omega)} & \overline{N}_{z,\nu,-}^{(2\omega)} & 0 & 0 & -N_x^{(2\omega)} & -N_x^{(2\omega)} \\
-N_y^{(2\omega)} & -N_y^{(2\omega)} & N_x^{(2\omega)} & N_x^{(2\omega)} & 0 & 0 \\
0 & 0 & -\overline{N}_{z,\nu,+}^{(2\omega)} & -\overline{N}_{z,\nu,-}^{(2\omega)} & N_y^{(2\omega)} & N_y^{(2\omega)} \\
0 & 0 & 1 & 1 & 0 & 0 \\
0 & 0 & 0 & 0 & 1 & 1
\end{bmatrix}
\begin{bmatrix}
\Delta\overline{\mathcal{E}}_{x,\nu,\Sigma,+} \\
\Delta\overline{\mathcal{E}}_{x,\nu,\Sigma,-} \\
\Delta\overline{\mathcal{E}}_{y,\nu,\Sigma,+} \\
\Delta\overline{\mathcal{E}}_{y,\nu,\Sigma,-} \\
\Delta\overline{\mathcal{E}}_{z,\nu,\Sigma,+} \\
\Delta\overline{\mathcal{E}}_{z,\nu,\Sigma,-}
\end{bmatrix}
=
$$

$$
= \frac{-ik_0^{(2\omega)}(k_0^u)^2}{\overline{\varepsilon}_\nu^{(2\omega)}\varepsilon_0} \exp[-i\boldsymbol{q}\cdot\boldsymbol{\rho}_\nu]
\begin{bmatrix}
N_x^{(2\omega)}\mu_{z,\nu}^{(2\omega)} \\[4pt]
-\mu_{x,\nu}^{(2\omega)}\overline{\varepsilon}_\nu^{(2\omega)} \\[4pt]
0 \\[4pt]
\mu_{y,\nu}^{(2\omega)}\overline{\varepsilon}_\nu^{(2\omega)} \\[4pt]
N_y^{(2\omega)}\mu_{z,\nu}^{(2\omega)} \\[4pt]
N_x^{(2\omega)}\mu_{x,\nu}^{(2\omega)} + N_y^{(2\omega)}\mu_{y,\nu}^{(2\omega)}
\end{bmatrix},
\tag{D.23}
$$

where $\Delta\overline{\mathcal{E}}_{x,\nu,\Sigma,\pm} \equiv \overline{\mathcal{E}}_{x,\nu+\epsilon,\Sigma,\pm} - \overline{\mathcal{E}}_{x,\nu-\epsilon,\Sigma,\pm}$ and similarly for the y and z components. Eq. (D.23) provides an important result: it shows explicitly the relation between the discontinuities of the modal vector amplitudes at the location of the point dipole, i.e., at $z = z_\nu$, and the strength of the point dipole $\boldsymbol{\mu}_\nu^{(2\omega)}$.

The 6×6 matrix in (D.23) is singular and thus the equation cannot be solved in the present form. This agrees with the fact that the x, y and z components of the vectors $\overline{\boldsymbol{\mathcal{E}}}_{\nu,\Sigma,\pm}$, and thus of $\Delta\overline{\boldsymbol{\mathcal{E}}}_{\nu,\Sigma,\pm}$, are not independent of each other. In particular, if we consider the s and p polarised modes with the corresponding magnitudes $\overline{\mathcal{E}}_{\nu,\mathbf{s},\pm}^{(2\omega)}$ and $\overline{\mathcal{E}}_{\nu,\mathbf{p},\pm}^{(2\omega)}$, and assume that the x component of the normalised wave vector $\overline{\boldsymbol{N}}_{\nu,\pm}^{(2\omega)}$ is equal to zero, then the y and z components of the modal vector amplitudes $\overline{\boldsymbol{\mathcal{E}}}_{\nu,\mathbf{p},\pm}$ are not independent. They are related by $\overline{\mathcal{E}}_{y,\nu,\mathbf{p},\pm}^{(2\omega)} = (\overline{N}_{z,\nu,\pm}^{(2\omega)}/\overline{N}_\nu^{(2\omega)})\overline{\mathcal{E}}_{\nu,\mathbf{p},\pm}^{(2\omega)}$ and $\overline{\mathcal{E}}_{z,\nu,\mathbf{p},\pm}^{(2\omega)} = -(N_{y,\nu}^{(2\omega)}/\overline{N}_\nu^{(2\omega)})\overline{\mathcal{E}}_{\nu,\mathbf{p},\pm}^{(2\omega)}$, as follows from Eqs. (3.8)(3.19). Considering these last relations, and removing all the linearly dependent columns and rows of the 6×6 matrix, Eq. (D.23) become

$$
\begin{bmatrix}
\Delta\overline{\mathcal{E}}_{x,\nu,\Sigma,\Sigma} \\[4pt]
\eta_0\Delta\overline{\mathcal{H}}_{y,\nu,\Sigma,\Sigma} \\[4pt]
\Delta\overline{\mathcal{E}}_{y,\nu,\Sigma,\Sigma} \\[4pt]
\eta_0\Delta\overline{\mathcal{H}}_{x,\nu,\Sigma,\Sigma}
\end{bmatrix}
=
\begin{bmatrix}
1 & 1 & 0 & 0 \\[4pt]
\overline{N}_{z,\nu,+}^{(2\omega)} & \overline{N}_{z,\nu,-}^{(2\omega)} & 0 & 0 \\[4pt]
0 & 0 & \overline{N}_{z,\nu,+}^{(2\omega)}/\overline{N}_\nu^{(2\omega)} & \overline{N}_{z,\nu,-}^{(2\omega)}/\overline{N}_\nu^{(2\omega)} \\[4pt]
0 & 0 & -\overline{N}_\nu^{(2\omega)} & -\overline{N}_\nu^{(2\omega)}
\end{bmatrix}
\begin{bmatrix}
\Delta\overline{\mathcal{E}}_{\nu,\mathbf{s},+} \\[4pt]
\Delta\overline{\mathcal{E}}_{\nu,\mathbf{s},-} \\[4pt]
\Delta\overline{\mathcal{E}}_{\nu,\mathbf{p},+} \\[4pt]
\Delta\overline{\mathcal{E}}_{\nu,\mathbf{p},-}
\end{bmatrix}
$$

$$
= \frac{-ik_0^{(2\omega)}(k_0^u)^2}{\overline{\varepsilon}_\nu^{(2\omega)}\varepsilon_0} \exp[-i\boldsymbol{q}\cdot\boldsymbol{\rho}_\nu]
\begin{bmatrix}
0 \\[4pt]
-\overline{\varepsilon}_\nu^{(2\omega)}\mu_{x,\nu}^{(2\omega)} \\[4pt]
\overline{\varepsilon}_\nu^{(2\omega)}\mu_{y,\nu}^{(2\omega)} \\[4pt]
N_y^{(2\omega)}\mu_{z,\nu}^{(2\omega)}
\end{bmatrix}.
\tag{D.24}
$$

Notice that the matrix binding the incoming and outcoming vectors is well-know as the dynamic $\mathbf{D}_\nu^{(2\omega)}$ matrix [defined by Eq. (3.14], because it connects the proper modes amplitudes and tangential components of electric and magnetic fields.

Since the 4×4 matrix is regular, the equation (D.24) can be solved

$$\Delta \overline{\boldsymbol{A}}_\nu^{(2\omega)} \equiv \begin{bmatrix} \Delta \overline{\mathcal{E}}_{\nu,\mathbf{s},+}^\mu \\ \Delta \overline{\mathcal{E}}_{\nu,\mathbf{s},-}^\mu \\ \Delta \overline{\mathcal{E}}_{\nu,\mathbf{p},+}^\mu \\ \Delta \overline{\mathcal{E}}_{\nu,\mathbf{p},-}^\mu \end{bmatrix} = \frac{-ik_0^{(2\omega)}(k_0^u)^2}{2\overline{\varepsilon}_\nu^{(2\omega)}\varepsilon_0} \exp[-i\boldsymbol{q}\cdot\boldsymbol{\rho}_\nu] \begin{bmatrix} -\frac{\overline{\varepsilon}_\nu^{(2\omega)}}{\overline{N}_{z,\nu}^{(2\omega)}}\mu_{x,\nu}^{(2\omega)} \\ \frac{\overline{\varepsilon}_\nu^{(2\omega)}}{\overline{N}_{z,\nu}^{(2\omega)}}\mu_{x,\nu}^{(2\omega)} \\ -\overline{N}_\nu^{(2\omega)}\mu_{y,\nu}^{(2\omega)} + \overline{N}_\nu^{(2\omega)}\frac{N_y^{(2\omega)}}{\overline{N}_{z,\nu}^{(2\omega)}}\mu_{z,\nu}^{(2\omega)} \\ -\overline{N}_\nu^{(2\omega)}\mu_{y,\nu}^{(2\omega)} - \overline{N}_\nu^{(2\omega)}\frac{N_y^{(2\omega)}}{\overline{N}_{z,\nu}^{(2\omega)}}\mu_{z,\nu}^{(2\omega)} \end{bmatrix}.$$

$$(D.25)$$

Considering again Eq. (3.19)(3.20), the expression (D.25) can be rewritten in a more compact and general form:

$$\Delta \overline{\boldsymbol{A}}_\nu^{(2\omega)} = [\Delta \overline{\mathcal{E}}_{\nu,\mathbf{s},+}^\mu, \Delta \overline{\mathcal{E}}_{\nu,\mathbf{s},-}^\mu, \Delta \overline{\mathcal{E}}_{\nu,\mathbf{p},+}^\mu, \Delta \overline{\mathcal{E}}_{\nu,\mathbf{p},-}^\mu], \tag{D.26}$$

where

$$\Delta \overline{\mathcal{E}}_{\nu,\mathbf{s},\pm}^\mu = \frac{i(k_0^u)^2}{2\varepsilon_0} \frac{k_0^{(2\omega)}}{\pm\overline{N}_{z,\nu}^{(2\omega)}} (\boldsymbol{\mu}_\nu^{(2\omega)} \cdot \hat{\overline{\boldsymbol{e}}}_{\nu,\mathbf{s},\pm}^{(2\omega)}) \exp[-i\boldsymbol{q}\cdot\boldsymbol{\rho}_\nu],$$

$$\Delta \overline{\mathcal{E}}_{\nu,\mathbf{p},\pm}^\mu = \frac{i(k_0^u)^2}{2\varepsilon_0} \frac{k_0^{(2\omega)}}{\pm\overline{N}_{z,\nu}^{(2\omega)}} (\boldsymbol{\mu}_\nu^{(2\omega)} \cdot \hat{\overline{\boldsymbol{e}}}_{\nu,\mathbf{p},\pm}^{(2\omega)}) \exp[-i\boldsymbol{q}\cdot\boldsymbol{\rho}_\nu],$$

$$(D.27)$$

where superscript $^\mu$ recalls that the discontinuity is caused by a point dipole.

This is the final result of this Appendix. It provides explicit formulae for the magnitude of the discontinuities of the $\mathbf{s}$ and $\mathbf{p}$ polarised modes at the position of the point dipole, i.e., on the plane $z = z_\nu$, expressed in the $\boldsymbol{q}$-space. This result is used in Section 7.3 to introduce dipole radiation into a 4×4 matrix formalism describing the propagation of the radiated light across the multilayer system.

Note, that right side of Eq. (D.24) contains the expressions of the discontinuities of tangential components of electric and magnetic fields. Thus, this result can be used if one wishes to incorporate steps in tangential components of electric and magnetic field into the matrix formalism.

Appendix E

Point dipole radiation in the $\boldsymbol{k}$-space

In this Appendix, I derive the radiation of a point dipole by an alternative approach than in the previous Appendix D. Here, I will found a solution for a point dipole radiation in the $\boldsymbol{k}$-space in order to show, that this space is not adapted for it.

E.1   Radiation sources

As in Appendix D [Eq. (D.5)], the radiation source is assumed to be an oscillating point dipole of complex moment $\boldsymbol{\mu}_\nu^{(2\omega)}$, located at position $\boldsymbol{r}_\nu$. Then the electric dipole density is $\boldsymbol{\mu}(\boldsymbol{r}, t) = \boldsymbol{\mu}_\nu^{(2\omega)} \exp[-i2\omega t]\delta(\boldsymbol{r} - \boldsymbol{r}_\nu)$. Thus, the current density $\boldsymbol{j}(\boldsymbol{r}, t)$ writes [Eqs. (D.4)(D.5)]

$$\boldsymbol{j}(\boldsymbol{r}, t) = -i2\omega\boldsymbol{\mu}_\nu^{(2\omega)}\, \delta(\boldsymbol{r} - \boldsymbol{r}_\nu) \exp[-i2\omega t]. \tag{E.1}$$

Transferring this current density into the $\boldsymbol{k}$-space, we arrive [Eqs. (3.2)(A.2)]

$$\boldsymbol{\mathcal{J}}_{\boldsymbol{k}} = -i2\omega(k_0^u)^3\boldsymbol{\mu}_\nu^{(2\omega)} \exp[-i\boldsymbol{k} \cdot \boldsymbol{r}_\nu] \exp[-i2\omega t]. \tag{E.2}$$

E.2   Point dipole radiation in $\boldsymbol{k}$-space

Transferring Maxwell equations [Eq. (D.1)] to the $\boldsymbol{k}$-space, we get the well-know relations [17]

$$i\boldsymbol{k} \cdot \boldsymbol{\mathcal{D}}_{\boldsymbol{k}} = \rho_{\boldsymbol{k}} \quad \text{(a)} \quad i\boldsymbol{k} \times \boldsymbol{\mathcal{E}}_{\boldsymbol{k}} = i2\omega\boldsymbol{\mathcal{B}}_{\boldsymbol{k}} \qquad \text{(b)}$$

$$i\boldsymbol{k} \cdot \boldsymbol{\mathcal{B}}_{\boldsymbol{k}} = 0 \qquad \text{(c)} \quad i\boldsymbol{k} \times \boldsymbol{\mathcal{H}}_{\boldsymbol{k}} = \boldsymbol{\mathcal{J}}_{\boldsymbol{k}} - i2\omega\boldsymbol{\mathcal{D}}_{\boldsymbol{k}}, \quad \text{(d)}$$

$$\tag{E.3}$$

where $\rho_{\boldsymbol{k}}$ denotes the charge density expressed in the $\boldsymbol{k}$-space.

Substituting Eq. (E.2) into the Maxwell equation (E.3d), and taking into account that $2\omega\mu_0\boldsymbol{\mathcal{H}}_{\boldsymbol{k}} = \boldsymbol{k} \times \boldsymbol{\mathcal{E}}_{\boldsymbol{k}}$ [Maxwell equation. (E.3b)] and $\boldsymbol{\mathcal{D}}_{\boldsymbol{k}} = \varepsilon^{(2\omega)}\varepsilon_0\boldsymbol{\mathcal{E}}_{\boldsymbol{k}}$, we arrive to

$$\frac{i}{2\omega\mu_0}\boldsymbol{k} \times (\boldsymbol{k} \times \boldsymbol{\mathcal{E}}_{\boldsymbol{k}}) = -i2\omega\varepsilon^{(2\omega)}\varepsilon_0\boldsymbol{\mathcal{E}}_{\boldsymbol{k}} - i2\omega\boldsymbol{\mu}_\nu(k_0^u)^3\boldsymbol{\mu}_\nu^{(2\omega)} \exp[-i\boldsymbol{k} \cdot \boldsymbol{r}_\nu]. \tag{E.4}$$

The form of this equation suggests that the electric field $\boldsymbol{\mathcal{E}}_{\boldsymbol{k}}$ is located in the plane which contains $\boldsymbol{\mu}_\nu^{(2\omega)}$ and is perpendicular to $\boldsymbol{k}$, because $\boldsymbol{k} \times (\boldsymbol{k} \times \boldsymbol{\mathcal{E}}_{\boldsymbol{k}})$ is always perpendicular

to $\boldsymbol{k}$. Thus, electric field can be written as

$$\boldsymbol{\mathcal{E}}_{\boldsymbol{k}} = \tau \left[\boldsymbol{\mu}_{\nu} + \varsigma \, \boldsymbol{k} \times (\boldsymbol{k} \times \boldsymbol{\mu}) \right], \tag{E.5}$$

where τ and ς are, for moment, some unknown constants. Substituting Eq. (E.5) to Eq. (E.4), these constants are found to be

$$\varsigma = \frac{1}{\boldsymbol{k} \cdot \boldsymbol{k} - (k^{(2\omega)})^2}$$

$$\tau = -\frac{(k_0^u)^3}{\varepsilon^{(2\omega)} \varepsilon_0} \exp[-i\boldsymbol{k} \cdot \boldsymbol{r}_{\nu}] \tag{E.6}$$

and we arrive to the $\boldsymbol{k}$-space expression of the electric field $\boldsymbol{\mathcal{E}}_{\boldsymbol{k}}$ created by an oscillating point dipole

$$\boldsymbol{\mathcal{E}}_{\boldsymbol{k}} = -\frac{(k_0^u)^3}{\varepsilon^{(2\omega)} \varepsilon_0} \left[\boldsymbol{\mu}_{\nu} + \frac{\boldsymbol{k} \times (\boldsymbol{k} \times \boldsymbol{\mu}_{\nu}^{(2\omega)})}{\boldsymbol{k} \cdot \boldsymbol{k} - (k^{(2\omega)})^2} \right] \exp[-i\boldsymbol{k} \cdot \boldsymbol{r}_{\nu}], \tag{E.7}$$

where $k^{(2\omega)} = 2\omega \sqrt{\varepsilon^{(2\omega)} \varepsilon_0 \mu_0}$, which is the length of the wavevector in the material, where the electric point dipole oscillates at the 2ω frequency. Recall that the $\boldsymbol{k}$-space is not a monochromatic space and thus $\boldsymbol{k}$ denotes all possible wavevectors. Thus, the Eq. (E.7) is diverging for $\sqrt{\boldsymbol{k} \cdot \boldsymbol{k}} = k^{(2\omega)}$. It means that modes having $\boldsymbol{k}$-vector corresponding to that of the radiated light have infinite value of $\boldsymbol{\mathcal{E}}_{\boldsymbol{k}}$. This corresponds to the well-known fact, that a dipole radiates light at its oscillatory frequency. This divergence explains why the $\boldsymbol{k}$-space is not a convenient space to describe the point dipole radiation and why I have introduced the $\boldsymbol{q}$-space to overcome this problem. Physically, this divergence has similar meaning as the Dirac δ-function specifying which light modes radiate.

List of variables

In general	
in bold (e.g. $\boldsymbol{E}$)	vector
in caligraphic letters (e.g. $\mathcal{E}$, $\mathcal{H}$)	variable in $\boldsymbol{q}$-space
sans serif bold (e.g. L)	tensor or matrix
with hat (e.g. $\hat{x}$, $\hat{e}$)	(i) unitary vector or (ii) (only in Sec. 2.3) quantum operator
with an overbar (e.g. $\overline{\boldsymbol{N}}$, $\hat{\bar{e}}$) or with subscript "vac"	related to the variables inside the ultrathin vacuum sheet located at the interface (Sec. 3.2.5, Sec. 7.3, App. D)
subscripted by ν	inside the ν-th layer in the vicinity of the ν-th interface (Fig. 3.2)
subscripted by $\nu \pm \epsilon$	at the position $z_\nu \pm \epsilon$, $\epsilon \to 0$, i.e. just above/under the ν-th interface (Sec. 7.3)
subscripted by s, p	corresponding to s, p-polarization (App. A)
subscripted by pol, lon, tra	referring to polar, longitudinal, transverse MOKE (Table 2.1)
subscripted by Π	light polarization. Either $\Pi = \{1, 2\}$ for a general polarization or $\Pi = \{\mathsf{s}, \mathsf{p}\}$ for s or p polarization (Sec. 3.1.1).
subscripted by $d = \pm$	direction of light propagation (Sec. 3.1.1)
subscripted by Σ	summation over a given index [Eq. (3.5)]
subscripted by $\boldsymbol{q}$, $\boldsymbol{k}$	belonging to the $\boldsymbol{q}$, $\boldsymbol{k}$-space
subscripted by "spd", "iface", "ml"	SHG radiation originating from a "single point dipole", the "entire interface" and the "entire multilayer structure" (Secs. 7.3 and 7.4)

superscripted by (ω), (2ω)	at fundamental (ω) or SHG (2ω) light frequency
superscripted by (i)	corresponding to the (i)th FM layer (Fig. 3.3)
superscripted by (tot)	summation over all FM layers or interfaces
superscripted by (fm), (nf)	related with FM, non-FM layers
superscripted by $\langle i, j \rangle$	between the i-th and j-th FM layer (see footnote in Sec. 5.4)
superscripted by (pln), (vic), (vp)	belonging to planar, vicinal, or "vicinal expressed as planar" interface (Sec. 6.4)
superscripted by (m), (nm)	magnetic, non-magnetic part (Sec. 8.1.2)
superscripted by apostrophe (')	effective value
superscript by dagger symbol †	complex conjugate
superscripted by T	vector transposition

symbol	meaning	definition or location
a	Co easy axis in the Co/NiO/NiFe system	only in Sec. 8.9
A	constant term in $\Phi = A + Bt^{(\mathrm{fm})} + C(t^{(\mathrm{fm})})^2$	Eqs. (4.1)(4.8)
A	$\mathsf{A} = \mathrm{i} N_z^{(\mathrm{nf})}/N^{(\mathrm{nf})}$	Eq. (6.7), Table 6.2
$\boldsymbol{A}_\nu^{(\omega)}$, $\boldsymbol{A}_\nu^{(2\omega)}$	vector of modal amplitudes	Eq. (3.13)
$\mathbf{A}$	analyzer described in the Jones formalism	Eqs. (2.21)
b	Co hard axis in the Co/NiO/NiFe system, $a \perp b$	only in Sec. 8.9
B	linear coefficient in $\Phi = A + Bt^{(\mathrm{fm})} + C(t^{(\mathrm{fm})})^2$	Eqs. (4.1)(4.8)
B	$\mathsf{B} = \mathrm{i} N_y N^{(\mathrm{nf})}/\varepsilon_0^{(\mathrm{fm})}$	Eq. (6.7), Table 6.2
$\boldsymbol{B}$	magnetic field vector in the $\boldsymbol{r}$-space	analogously to Eq. (3.4)
$\boldsymbol{\mathcal{B}}$	magnetic field vector in the $\boldsymbol{q}$-space	analogously to Eq. (3.4)
c	light velocity in vacuum	—
C	quadratic coefficient in $\Phi = A + Bt^{(\mathrm{fm})} + C(t^{(\mathrm{fm})})^2$	Eqs. (4.1)

C	response of the Babinet-Soleil compensator in the Jones formalism	App. B
d	direction of the light propagation, it can be either $d = +$ or $d = -$	Sec. 3.1.1
$d^{(\mathrm{nf})}$	overlayer thickness	Fig. 3.3
$d^{(\mathrm{nf},i)} \equiv d^{(i)}$	distance from the top of the multilayer (i.e. from the first interface) to the center of the i-th FM layer	Fig. 3.3
$\Delta d^{\langle i,j \rangle}$	$\Delta d^{\langle i,j \rangle} = d^{(i)} - d^{(j)}$, distance between the centers of the i-th and j-th FM layers	Sec. 5.4.1
$\boldsymbol{D} = [D_x, D_y, D_z]$	electric induction vector in the $\boldsymbol{r}$-space	analogously to Eqs. (3.2)(3.4)
$\boldsymbol{\mathcal{D}} = [\mathcal{D}_x, \mathcal{D}_y, \mathcal{D}_z]$	electric induction vector in the $\boldsymbol{q}$-space	analogously to Eq. (3.4)
$\mathsf{D}_\nu^{(\omega)}$, $\mathsf{D}_\nu^{(2\omega)}$	dynamic matrix	Eqs. (3.12)(3.14)
e	electron charge	only in Eq. (2.19)
$\hat{e}_{\nu,\mathsf{s},\pm}$, $\hat{e}_{\mathsf{p},\pm}$	modal vector polarizations	Eq. (2.4), Eq. (3.8)
E	photon energy	—
E_i, E_f	initial and final energies	Eq. (2.19)
$\boldsymbol{E} = [E_x, E_y, E_z]$	electric field vector in the $\boldsymbol{r}$-space	Eq. (3.4)
$\Delta\mathcal{E}_{\mathsf{s},\pm}^\mu$, $\Delta\mathcal{E}_{\mathsf{p},\pm}^\mu$	jump of the modal intensities in the presence of a radiating point dipole	Eq. (7.3)
$\mathcal{E}$	integral off-diagonal permittivity (only in Chapter 4)	Eq. (4.2), Sec. 4.3
$\mathcal{E}_A$	integral off-diagonal permittivity excess (only in Chapter 4)	Sec. 4.3, Eq. (4.5)
$\boldsymbol{\mathcal{E}} = [\mathcal{E}_x, \mathcal{E}_y, \mathcal{E}_z]$	modal vector amplitudes; it is identical to the electric field vector in the $\boldsymbol{q}$-space	Eq. (3.4)
f	modulation frequency of the photoelastic modulator or of the Faraday rotator	Sec. 2.4.1, Sec. 2.4.3
f	arbitrary 1D function	App. A, Sec. D.3

$f(E_i)$	Fermi-Dirac function at energy E_i	Eq. (2.19)
$\lvert f \rangle$	final state	Eq. (2.19)
F	Fourier transform of the function f	App. A
g	factor ± 1 in the relation between the measured Kerr signal and the Kerr rotation	Eq. (2.33)
$g(w)$	auxiliary 1D function	only in Sec. 7.5, part (i)–(iii)
$g^{(i)}$	distribution of Co layer thickness	only in Sec. 4.6.1
$\boldsymbol{H} = [H_x, H_y, H_z]$	magnetic induction vector in the $\boldsymbol{r}$-space	analogously to Eqs. (3.2)(3.4)
$\boldsymbol{\mathcal{H}} = [\mathcal{H}_x, \mathcal{H}_y, \mathcal{H}_z]$	magnetic induction vector in the $\boldsymbol{q}$-space	analogously to Eqs. (3.2)(3.4)
H_c	coercive field	—
$\mathcal{H}_{SO}, \mathcal{H}_{\text{ex}}$	spin-orbit and exchange Hamiltonians	Sec. 2.3.1
i	imaginary unit	—
$\langle i \rvert$	initial state	Eq. (2.19)
$I^{(\omega)}, I^{(2\omega)}$	light intensity	Sec. 7.5
$\Im$	imaginary part of the following expression	—
$\boldsymbol{j}^{(\omega)}, \boldsymbol{j}^{(2\omega)}$	density of the electrical current	Secs. D.1, D.2
J_0, J_1, J_2	Bessel functions of order 0, 1, 2	Eq.(2.23), Fig. 2.8
$\boldsymbol{J} = [\mathcal{E}_\mathsf{s}, \mathcal{E}_\mathsf{p}]^{\mathrm{T}}$	Jones vector	Eq. (2.9)
$\boldsymbol{J_k}$	electric current density in the $\boldsymbol{k}$-space	only in App. E
k_0^u	$k_0^u = \omega/c$, coefficient equalizing units	Eqs. (3.2)(3.4)(A.2)
k	$k = \sqrt{\boldsymbol{k} \cdot \boldsymbol{k}}$, Pythagorean length of the wavevector	—
k	imaginary part of the refractivity index N	only in App. A
$\boldsymbol{k} = [k_x, k_y, k_z]$	wavevector of light	Sec. 3.1
K_μ	2×2 rotation matrix by an angle μ	only in Eq. (6.8)
$\mathsf{K}_{M+1}^{(2\omega)}$	matrix relating the outcoming SHG field from the 1-st interface to the $A_{\nu,\text{spd}}^{(2\omega)}$	Eq. (7.11)

$l, \Delta l$	orbital number, and its difference	only in Sec. 2.3
L	number of the different experimental conditions (i.e. length of the vector $\boldsymbol{s}$)	only in Sec. 5.5
$\hat{\boldsymbol{L}}$	orbital momentum operator	only in Sec. 2.3.1
$\mathsf{L}_\nu^{(\omega)}$ ($\mathsf{L}_\nu^{(2\omega)}$)	matrix relating $\boldsymbol{A}_0^{(\omega)}$ ($\boldsymbol{A}_0^{(2\omega)}$) to $\boldsymbol{A}_\nu$ ($\boldsymbol{A}_\nu^{(2\omega)}$)	Eqs. (3.16)(3.17)
$m, \Delta m$	quantum magnetic number, and its difference	Sec. 2.3, Fig. 2.6
m_e	electron mass	only in Eq. (2.19)
$\boldsymbol{m} \equiv [m_x, m_y, m_z]$	vector of normalized magnetization	Sec. 2.2.1
$\boldsymbol{M}$	sample magnetization	—
M	modulator response in the Jones formalism	Eq. (2.20), App. B
n	real part of the refractive index N	only in App. A
N	number of the FM layers (i.e. length of the vector $\boldsymbol{\Upsilon}$)	only in Sec. 5.5
N	complex refractive index; it corresponds to the Pythagorean length of the reduced wavevector $\boldsymbol{N}$	Sec. 3.2.1
$N^{(0)}$	refractive index of the superstrate, i.e. of the medium, from which the light is coming from	Fig. 3.3
$\Delta N = (N_+ - N_-)/2$	circular briefringence	only in Eq. (3.1)
$\boldsymbol{N} = [N_x, N_y, N_z]$	reduced wavevector	Sec. 3.2.1
$\hat{p}_+, \hat{p}_-$	linear momentum operators	Sec. 2.3.2
p	$p = Q/Q(\varphi{=}0)$, quantity describing variation of Q with φ (only in Chapter 5)	Eq. (5.9)
$\boldsymbol{P}$	polarization	Sec. 7.2
$\mathsf{P}_\nu^{(\omega)}$	propagation matrix	Eqs. (3.12)(3.15)
q	depth sensitivity function	Sec. 5.4
$q^{\langle i,j \rangle}$	depth sensitivity function between the i-th and the j-th FM layer, i.e. ratio of Kerr effects originating from the i-th and the j-th FM layer	Sec. 5.4, Eq. (5.2)

$\boldsymbol{q} = [k_x, k_y]$	position of the light mode in the $k_x k_y$-plane	Sec. 3.1
Q	term describing the influence of the overlayer or the spacer on the Kerr effect Φ	Eq. (3.41)
Q	charge	only in Sec. D.2
r	far-field distance between $\boldsymbol{\mu}_\nu^{(2\omega)}$ and the detector	Sec. 7.5
$r_{\mathsf{ss}}, r_{\mathsf{pp}}$	diagonal reflection coefficients	Eq. (2.10), Table 2.1, App. B
$r_{\mathsf{sp}}, r_{\mathsf{ps}}$	off-diagonal reflection coefficients	Eq. (2.10), Table 2.1, App. B
$\boldsymbol{r}$	position vector	—
$\boldsymbol{r}_\nu$	position in the ν-th interface. i.e. $z = z_\nu$	—
$\mathbf{R}$	reflection matrix of the sample in the Jones formalism	Eq. (2.10), Table 2.1, Eq. (2.10)
$\mathbf{R}_\alpha$	3×3 rotation matrix by an angle α	only in Sec. 6.1.2
$\Re$	real part of the following expression	—
s	Kerr signal (i.e. what measures the MOKE setup)	Eq. (2.18)
$s^{(i)}$	Kerr signal originating from the i-th FM layer	Chapter 5
$\boldsymbol{s}$	vector of Kerr signals measured at different experimental conditions	only in Sec. 5.8.1
$S, \Delta S$	measured signal in optical reflectivity measurements	only in Sec. 6.3
$\hat{\boldsymbol{S}}$	spin momentum operator	only in Sec. 2.3
$\boldsymbol{S}$	Poynting vector	only in Eq. (7.30)
t	time	—
$t_{\mathsf{ss}}, t_{\mathsf{sp}}, t_{\mathsf{ps}}, t_{\mathsf{pp}}$	elements of the transmission matrix	Sec. 3.2.4
t_ν	thickness of the ν-th layer	Sec. 3.2,
$t^{(\mathrm{fm})}$	thickness of the FM layer	Sec. 3.3
$t^{(i)}$	thickness of the i-th FM layer	Sec. 3.3, Fig. 3.3
$t^{(\mathrm{in})}$	interlayer thickness	Sec. 4.3(vi), Fig. 4.2

t_s	memory depth of the vicinal interface	Sec. 6.1.2
T	transmission matrix	Sec. 3.2.4
$\mathbf{U}_\nu^{(\omega)}$	matrix relating $\boldsymbol{E}_\nu^{(\omega)}$ to $\boldsymbol{A}_\nu^{(\omega)}$	Eq. (3.35)
V_{s}, V_{p}	term describing variation of the Kerr effect Φ on the incidence angle φ	Eq. (3.44)
$\mathbf{V}^{(2\omega)}$	matrix expressing all terms of the product $\boldsymbol{\mu}^{(2\omega)} \cdot \hat{e}_{\mathrm{vac},\mathsf{s}/\mathsf{p},\pm}^{(2\omega)}$	Eq. (7.14)
w	superscript denoting different experimental conditions	only in Sec. 5.5
w, w_0	auxiliary variable	only in Sec. 7.5, part (i)–(iii)
W	matrix relating the Kerr signals vector $\boldsymbol{s}$ to the magnetization vector $\boldsymbol{\Upsilon}$	Eq. (5.20)
x	volume ratio of Co	only in Sec. 4.6.1
$\hat{x}$, $\hat{y}$, $\hat{z}$	unitary vectors in the x, y, z directions	App. A
$(\hat{x}, \hat{y}, \hat{z})$	Cartesian referential related to the light	Sec. 6.1.1, Fig. 6.1, App. A
$(\hat{X}, \hat{Y}, \hat{Z})$	sample Cartesian referential related to the sample	Sec. 6.1.1, Fig. 6.1
$X_{x\mathsf{s},\nu}^{(\omega)}$, $X_{y\mathsf{p},\nu}^{(\omega)}$, $X_{z\mathsf{p},\nu}^{(\omega)}$	generalized incoming Fresnel coefficients, i.e. components of the $\mathbf{X}_\nu^{(\omega)}$ matrix	Eq. (8.6)
$\mathbf{X}_\nu^{(\omega)}$	3×2 generalized incoming Fresnel matrix relating $\boldsymbol{E}_\nu^{(\omega)}$ to $\boldsymbol{J}_{0,+}^{(\omega)}$	Eq. (3.33)
$\mathbf{Y}_\nu^{(2\omega)}$	4×3 generalized outcoming Fresnel matrix relating $\boldsymbol{\mu}_\nu^{(2\omega)}$ and $\boldsymbol{A}_{\nu,\mathrm{spd}}^{(2\omega)}$	Eq. (7.12)
$Z_{\mathsf{s}x,\nu,d}$, $Z_{\mathsf{p}y,\nu,d}$, $Z_{\mathsf{p}z,\nu,d}$	generalized Fresnel outcoming elements, i.e. elements of $\mathbf{Z}_{\nu.d}^{(2\omega)}$	Eq. (8.8)
$\mathbf{Z}_{\nu,d}^{(2\omega)}$	2×3 generalized Fresnel outcoming matrix relating $\boldsymbol{\mu}_\nu^{(2\omega)}$ and $\boldsymbol{J}_d^{(2\omega)}$	Eq. (8.8)
α	rotation angle of the sample around z	Sec. 6.1.1, Fig. 6.1
α	orientation of the optical elements	only in App. B

β	first angle determining the magnetization direction	Sec. 6.1.1, Fig. 6.1
γ	second angle determining the magnetization direction	Sec. 6.1.1, Fig. 6.1
γ_0	magnetization tilt from the in-plane magnetization	Sec. 6.2.2
δ	phase retardation given by the Babinet-Soleil compensator	App. B, Sec. 2.4.2
$\delta()$, δ_{ij}	Dirac δ-function, Kronecker-δ	—
ϵ, $\epsilon_{\mathbf{s}}$ or $\epsilon_{\mathbf{p}}$	Kerr ellipticity or $\mathbf{s}$, $\mathbf{p}$ Kerr ellipticity	definition by Eq. (2.13)
$\epsilon^{(i)}$	Kerr ellipticity originating from the i-th FM layer	Chapter 5
ϵ_a	ellipticity of the light beam	Sec. 2.1.4
ϵ	infinitesimally small number, $\epsilon \to 0$	Secs. 3.2.5 and 7.3
ε_{ij}	permittivity tensor elements	—
ε_{xy}, ε_{xz}, ε_{yx}, ε_{yz}, ε_{zx}, ε_{zy}	off-diagonal permittivity elements of the FM layer	Eq. (3.38)
ε_{xx}, ε_{yy}, ε_{zz}	diagonal permittivity elements of the FM layer	Eq. (6.1), Table 6.1
ε_s	off-diagonal structural permittivity tensor element	Eq. (6.1), Table 6.1
ε_m	off-diagonal magnetic permittivity tensor element, $\varepsilon_m = -i\varepsilon_1^{(\mathrm{fm})}$	Eq. (6.1), Table 6.1
ε_0	absolute vacuum impedance	—
$\varepsilon_0^{(\omega)}$, $\varepsilon_0^{(2\omega)}$	diagonal part of the permittivity tensor	Eqs. (3.38)(3.45)
$\varepsilon_1^{(\mathrm{fm})}$	magnetic off-diagonal permittivity tensor element	Eq. (3.45)
ε_t	variation of the diagonal permittivity with the vicinality	Eq. (6.15)
$\boldsymbol{\varepsilon}$	permittivity tensor	—
$\boldsymbol{\varepsilon}_{\mathrm{str}}$, $\boldsymbol{\varepsilon}_{\mathrm{mag}}$	structural, magnetic part of the permittivity tensor	Sec. 6.1.2

ζ	(i) modulation angle of the photoelastic modulator	ad (i) Sec.(2.4.1)
	(ii) rotation angle for the light azimuth	ad (ii) Sec. (2.4.3)
ζ_0	maximum modulation angle of the photoelastic modulator	Sec. 2.4.1
ζ_1	maximum modulation angle of the first Faraday rotator	Sec. 2.4.3
ζ_2	compensation angle of the second Faraday rotator	Sec. 2.4.3
ζ_a	misorientation of the analyzer with respect to the **s** direction	Sec. 8.4.2
η_0	$\eta_0 = \mu_0/\varepsilon_0$ vacuum impedance	—
θ_a	azimuth of the light beam polarization	Sec. 2.1.4
θ or $\theta_\mathbf{s}$, $\theta_\mathbf{p}$	Kerr rotation or **s**, **p** Kerr rotation	definition in Eq. (2.13)
$\theta^{(i)}$	Kerr rotation originating from the i-th FM layer	Chapter 5
θ_r, θ_k	one of two angles giving orientation of the vector $\mathbf{r}$, $\mathbf{k}$, respectively	only in Sec. 7.5
θ_j	one of the angles giving orientation of the detector	only in Sec. 7.5
$\vartheta(z)$	Heaviside function, for $z < 0$, $\vartheta = 0$, for $z > 0$, $\vartheta = 1$	App. C
$\lambda^{(\omega)}$, $\lambda^{(2\omega)}$	light wavelength in vacuum	—
μ_0	absolute vacuum permeability	—
$\boldsymbol{\mu} = [\mu_x, \mu_y, \mu_z]$	point dipole moment	Sec. 7.2
μ	angle of rotation of the optical elements	only in Sec. 6.3
ν	layer or interface number	Fig. 3.2
ξ_a	phase shift between **s**, **p** electric waves	Sec. 2.1.4
ξ or $\xi_\mathbf{s}$, $\xi_\mathbf{p}$	Kerr phase	definition by Eq. (2.13)
$\xi^{(i)}$	Kerr phase originating from the i-th FM layer	Chapter 5
$\Delta\xi^{\langle i,j\rangle}$	$\Delta\xi^{\langle i,j\rangle} = \xi^{(i)} - \xi^{(j)}$, difference of Kerr phases between the i-th and the j-th FM layer	Eq. (5.2)

Π	light polarization being either $\{1, 2\}$ or $\{\mathtt{s}, \mathtt{p}\}$	Sec. 3.1.1
ρ	SHG magnetic contrast	Sec. 8.4.1
$\rho_{\mathtt{ss}}$, $\rho_{\mathtt{pp}}$	variation of the $r_{\mathtt{ss}}$, $r_{\mathtt{pp}}$ with $t^{(\mathrm{fm})}$. Their superscript $[(0), (0, t^{(\mathrm{fm})}), (1)$ and $(2)]$ denotes the order of dependence on the off-diagonal permittivity elements of the FM layer	Table 3.1
$\boldsymbol{\rho}_\nu$	$\boldsymbol{\rho}_\nu = [x_\nu, y_\nu]$, position vector in the ν-th interface	Eq. 3.4, Sec.7.4
σ_{ij}	conductivity tensor elements	Sec. 2.3.2
$\sigma^{(\mathrm{fm})}$	mean square deviation	Sec. 4.6.1
Σ	in superscript: denotes the summation over a given index	definition by Eq. (3.5)
ς	auxiliary variable	only in Eqs. (E.5)(E.6)
τ	auxiliary variable	only in Eqs. (E.5)(E.6)
τ	depth inside the structure	only in Sec. 4.3
$\boldsymbol{\Upsilon}$	vector of FM layer magnetizations, each vector element contains magnetization of one FM layer	Sec. 5.8.1
ϕ	$\phi = -\boldsymbol{k} \cdot \boldsymbol{r}$, phase factor	Eqs. (7.26)(7.29)
Φ, $\Phi_{\mathtt{s}}$ or $\Phi_{\mathtt{p}}$	(complex) MOKE or $\mathtt{s}$, $\mathtt{p}$-MOKE	definition: Eq. (2.13), analytical expressions: Eq. (3.42)
$\Phi_{\mathrm{pol}}^{(i)}$, $\Phi_{\mathrm{lon}}^{(i)}$	polar, longitudinal component of MOKE originating from the i-th FM layer	Eq. (3.46), Eq. (3.47)
$\Phi^{(i)}$	MOKE originating from the i-th FM layer	Sec. 3.3.3, Chapter 5
$\tilde{\Phi}_{\mathrm{tra}}$	transverse MOKE	Eq. (2.15), Sec. 5.4.4
$\Phi_{\mathrm{F},\mathtt{s}}$	complex Faraday effect	Sec. 3.2.4
φ	incidence angle of the light	—
φ_r	radiation angle of the light	Sec. 8.6.2, Fig. 8.4
φ_T	total reflection angle of the glass/air interface	Sec. 8.6.2, Fig. 8.4
φ_r, φ_k	one of the two angles giving the orientation of the vectors $\boldsymbol{r}$, $\boldsymbol{k}$, respectively	only in Sec. 7.5

φ_j	one of the angles giving the orientation of the detector	only in Sec. 7.5
χ	3-rd rank susceptibility tensor	Secs. 7.2, 8.1.2
χ	influence of the substrate to MOKE	Eq. (3.43)
$\tilde{\chi}_{\mathsf{s/p}}$	shortcut for $\chi_{\mathsf{s/p}} = -\chi V_{\mathsf{s/p}} Q N_z^{(\mathrm{nf})}/N^{(\mathrm{nf})}$	Eq. (4.2)
ψ	miscut angle	Fig. 6.11, only in Chapter 6
ψ	projection angle	Eq. (2.18)
$\omega, 2\omega$	light frequency	—
Ω_a	$\tan\Omega_a$ is the ratio of maximal values of the s, p electric intensities	Sec. 2.1.4
Ω or Ω_{s}, Ω_{p}	Kerr amplitude or s, p Kerr amplitude	definition by Eq. (2.13)
$\Omega^{(i)}$	Kerr amplitude originating from the i-th FM layer	Chapter 5
Ω_c	unit cell volume	only in Eq. (2.19)
$\otimes$	tensorial multiplication	Eq. (8.1)

Bibliography

[1] *Non-linear optics in metals*, edited by K. Bennemann (Clarendon Press, Oxford, 1998).

[2] A. Kirilyuk, *Nonlinear optics in application to magnetic surfaces and thin films (topical review)*, J. Phys. D: Appl. Phys. **35**, R189 (2002).

[3] A. Kirilyuk, T. Rasing, M. A. M. Haast, and J. C. Lodder, *Probing structure and magnetism of CoNi/Pt interfaces by nonlinear magneto-optics*, Appl. Phys. Lett. **72**, 2331 (1998).

[4] H. A. Wierenga, M. W. J. Prins, and T. Rasing, *Magnetization-induced optical second-harmonic generation from magnetic multilayers*, Physica B **204**, 281 (1995).

[5] M. Faraday, Philos. Trans. Roy. Soc. London **136**, 1 (1846).

[6] J. Kerr, Philos. Mag. **3**, 321 (1877).

[7] J. Ferré, in *Linear and non-linear magneto-optical effects: magnetism of thin film structures, in: Magnetism and Synchrotron Radiation*, edited by E. Beaurepaire, F. Scheurer, G. Krill, and J.-P. Kappler (Springer, Heidelberg, 2001), p. 316.

[8] J. Ferré, J. Jamet, and P. Meyer, *Magneto-optical studies of magnetic ultrathin film structures*, Phys. Stat. Sol. (a) **175**, 213 (1999).

[9] B. Koopmans, M. van Kampen, J. T. Kohlhepp, and W. J. M. de Jonge, *Ultrafast Magneto-Optics in Nickel: Magnetism or Optics?*, Phys. Rev. Lett. **85**, 844 (2000).

[10] A. Hubert and R. Schäfer, *Magnetic Domains: The Analysis of Magnetic Microstructures* (Springer-Verlag, Berlin, 1998).

[11] J. Pommier, P. Meyer, G. Pénissard, J. Ferré, P. Bruno, and D. Renard, *Magnetization reversal in ultrathin ferromagnetic films with perpendicular anisotropy: domain observation*, Phys. Rev. Lett. **65**, 2054 (1990).

[12] T. Ono, H. Miyajima, K. Shigeto, K. Mibu, N. Hosoito, and T. Shinjo, *Propagation of a Magnetic Domain Wall in a Submicrometer Magnetic Wire*, Science **284**, 468 (1999).

[13] T. Devolder, C. Chappert, Y. Chen, E. Cambuil, H. Bernas, J.-P. Jamet, and J. Ferre, *Sub 50 nm magnetic nanostructures fabricated by ion irradiation*, Appl. Phys. Lett. **74**, 3383 (1999).

[14] T. Aign, P. Meyer, S. Lemerle, J.-P. Jamet, V. Mathat, C. Chappert, J. Gierak, C. Vieu, F. Rousseaux, H. Launois, and H. Bernas, *Magnetization reversal in arrays of perpendicularly magnetized ultrathin dots coupled by dipolar interaction*, Phys. Rev. Lett. **81**, 5656 (1998).

[15] G. Baudot, V. Repain, H. Ellmer, S. Rousset, J. Ferré, J.-P. Jamet, and C. Chappert, *Self organization of magnetic surface anisotropy in Co ultrathin films grown on a periodically Au(111) faceted surface*, submitted to Europhys. Lett. .

[16] Z. Qiu and S. Bader, *Surface magneto-optical Kerr effect (SMOKE)*, J. Magn. Magn. Mater. **200**, 664 (1999).

[17] L. Landau and E. Lifschitz, *Electrodynamics of Continuous Media* (Pergamon Press, Oxford, 1960).

[18] R. Azzam and N. Bashara, *Ellipsometry and polarized light* (North Holland, Amsterdam, 1992).

[19] M. Born and E. Wolf, *Principles of Optics* (Pergamon, Oxford, 1959).

[20] F. Kahn, P. Pershan, and J. Remeika, *Ultraviolet Magneto-optical properties of single-crystal orthoferrites, garnets and other ferric oxide compounds*, Phys. Rev. **186**, 891 (1969).

[21] R. Ditchburn, *Light* (Wiley-Interscience Inc., New York, 1958).

[22] R. Osgood III, S. Bader, B. Clemens, R. White, and H. Matsuyama, *Second-order magneto-optic effects in anisotropic thin films*, J. Magn. Magn. Mat. **182**, 297 (1998).

[23] K. Postava, *Light propagation in magneto-optical multilayers: magnetization behavior*, Ph.D. thesis, Palacky University, Olomouc, Czech Republic and Institut National des Sciences Appliquées, Toulouse, France, (1997).

[24] R. Schäfer and A. Hubert, *A new magnetooptic effect related to non-uniform magnetization on the surface of a ferromagnet*, Phys. Stat. Sol. (a) **118**, 271 (1990).

[25] B. D. C. Cohen-Tannoudji and F. Laloë, *Mécanique quantique* (Hermann éditeurs des sciences et des arts, Paris, 2000).

[26] T. Huhne and H. Ebert, *Fully relativistic description of the magneto-optical properties of arbitrary layered systems*, Phys. Rev B **60**, 12982 (1999).

[27] *Magnétisme I et II*, edited by E. T. at al. (Presses Universitaires de Grenoble, Grenoble, 1999).

[28] P. Bruno, Y. Suzuki, and C. Chappert, *Magneto-optical Kerr effect in a paramagnetic overlayer on a ferromagnetic substrate: A spin-polarized quantum size effect*, Phys. Rev. B **53**, 9214 (1996).

[29] W. A. Harrison, *Solid State Theory* (Dover Publications, Inc., New York, 1979), or any good book concerning optical properties of solids.

[30] R. Kubo, J. Phys. Soc. Japan **12**, 570 (1957).

[31] H. Hulme, Proc. R. Soc. London **A135**, 237 (1932).

[32] Š. Višňovský, M. Nývlt, V. Prosser, R. Lopušník, R. Urban, J. Ferré, G. Pénissard, D. Renard, and R. Krishnan, *Polar magneto-optics in simple ultrathin-magnetic-film structures*, Phys. Rev. B **52**, 1090 (1995).

[33] J. Ferré and G. Gehring, *Linear optical birefringence of magnetic crystals*, Rep. Prog. Phys. **47**, 513 (1984).

[34] J. Badoz, M. Silverman, and J. Canit, *Wave propagation through a medium with static and dynamic birefringence: theory of the photoelastic modulator*, J. Opt. Soc. Am. A **7**, 672 (1989).

[35] K. Rektorys, *The overview of used mathematics (6-th edition)* (Prometheus, Praha, 1995).

[36] M. Nývlt, *Optical interactions in ultrathin magnetic film structures*, PhD. dissertation, Charles University, Prague, 1996.

[37] G. Pénissard, *Effects magneto-optiques de structures en couches ultra-minces Au/Co*, Ph.D. thesis, Université de Paris XI, Orsay, France, (1993).

[38] R. R. Birss, *Symmetry and magnetism* (North-Holland Publishing Company, Amsterdam, 1964).

[39] D. Smith, *Magneto-optical scattering from multilayer magnetic and dielectric films*, Opt. Acta **12**, 193 (1964).

[40] P. Yeh, *Optics of anisotropic layered media: a new 4×4 matrix algebra*, Surf. Sci. **96**, 625 (1980).

[41] Š. Višňovský, *Magneto-optical ellipsometry*, Czech. J. Phys. B **36**, 625 (1986).

[42] Š. Višňovský, M. Nývlt, V. Prosser, J. Ferré, G. Pénissard, D. Renard, and G. Sczigel, *Magneto-optical effects in Au/Co/Au ultrathin film sandwiches*, J. Magn. Magn. Mater. **128**, 179 (1993).

[43] M. Mansuripur, *The physical principles of magneto-optical recording* (Cambridge University Press, Cambridge, 1998).

[44] Š. Višňovský, *Theory of Magneto-Optical Effects in Magnetic Multilayers (Invited)*, J. Magn. Soc. Jap **15**, Suppl. S1, 67 (1991).

[45] J. Zak, E. R. Moog, C. Liu, and S. D. Bader, *Additivity of the Kerr effect in thin-film magnetic systems*, J. Magn. Magn. Mater. **88**, L261 (1990).

[46] Š. Višňovský, *Magneto-optical effects in ultrathin structures at longitudinal magnetization*, Czech. Jour. of Phys. **B48**, 1083 (1998).

[47] C. Y. You and S. C. Shin, *Generalized analytic formulae for magneto-optical Kerr effect*, J. Appl. Phys. **84**, 541 (1998).

[48] G. Traeger, L. Wenzel, and A. Hubert, *Computer Experiments on the information depth and the figure of merit in magneto-optics*, Phys. Stat. Sol. (a) **131**, 201 (1992).

[49] A. Hubert and G. Traeger, *Magneto-optical sensitivity functions of thin-film systems*, J. Magn. Magn. Mater. **124**, 185 (1993).

[50] Š. Višňovský, R. Lopušník, M. Nývlt, V. Prosser, J. Ferré, C. Train, P. Beauvillain, D. Renard, R. Krishnan, and J. Bland, *Analytical expressions for polar magneto-optics in magnetic multilayers*, Czech J. Phys. **50**, 857 (2000).

[51] P. Bertrand, C. Hermann, G. Lampel, J. Peretti, and V. Safarov, *General analytical treatment of optics in layered structures: application to magneto-optics*, Phys. Rev. B **64**, 235421 (2001).

[52] Š. Višňovský, *Optics of magnetic multilayers*, Czech. Jour. of Phys. **41**, 663 (1991).

[53] L. Polerecky, J. Hamrle, and B. MacCraith, *Theory of radiation of dipoles placed within a multilayer system*, Applied Optics **39**, 3968 (2000).

[54] G. Tessier, *Étude d'interfaces magnétiques par doublage de fréquence optique*, Ph.D. thesis, Université Paris-Sud, Orsay, 1999.

[55] Z. Qiu, J. Pearson, and S. Bader, *Additivity of magneto-optical Kerr signal in ultrathin Fe(110)/Ag(111) superlattices*, Phys. Rev. B **45**, 7211 (1992).

[56] Š. Višňovský, J. Gřondilová, J. Hamrle, R. Lopušník, and N. Keller, *Polar and longitudinal MOKE in magnetic film/spacer/magnetic substrate system*, Czech. J. Phys. **51**, 1215 (2001).

[57] J. Hamrle, M. Nývlt, Š. Višňovský, R. Urban, P. Beauvillain, R. Mégy, J. Ferré, L. Polerecký, and D. Renard, *Magneto-optical properties of ferromagnetic/nonferromagnetic interfaces: application to Co/Au(111)*, Phys. Rev. B **64**, 155405 (2001).

[58] U. Gradmann, *Magnetic Surface Anisotropies*, J. Magn. Magn. Mater. **54**, 733 (1986).

[59] N. C. Koon, B. T. Jonker, F. A. Volkening, J. J. Krebs, and G. A. Prinz, *Direct evidence for perpendicular spin orientations and enhanced hyperfine fields in ultrathin Fe(100) films on Ag(100)*, Phys. Rev. Lett. **59**, 2463 (1987).

[60] C. Chappert and P. Bruno, *Magnetic anisotropy in metallic ultrathin films and related experiments on cobalt films*, J. Appl. Phys. **64**, 5736 (1988).

[61] C. Liu, E. R. Moog, and S. D. Bader, *Polar Kerr-effect observation of perpendicular surface anisotropy for ultrathin fcc Fe grown on Cu(100)*, Phys. Rev. Lett. **60**, 2422 (1988).

[62] J. C. S. Kools, *Exchange-biased spin-valves for magnetic storage*, IEEE Trans. Magn. **32**, 3165 (1996).

[63] S. Tehrani, J. M. Slaughter, E. Chen, M. Durlam, J. Shi, and M. DeHerrera, *Program and outlook for MRAM technology*, IEEE Trans. Magn. **35**, 2814 (1999).

[64] S. T. Purcell, M. T. Johnson, N. W. E. McGee, J. J. de Vries, W. B. Zeper, and W. Hoving, *Local structural and polar Kerr effect measurements on an ultrathin epitaxial Co wedge grown on Pd(111)*, J. Appl. Phys. **73**, 1360 (1993).

[65] N. W. E. McGee, M. T. Johnson, J. J. de Vries, and J. aan de Stegge, *Localized Kerr study of the magnetic properties of an ultrathin epitaxial Co wedge grown on Pt(111)*, J. Appl. Phys. **73**, 3418 (1993).

[66] C. Train, P. Beauvillain, V. Mathet, G. Pénissard, and P. Veillet, *Spectroscopic polar magneto-optical Kerr rotation on Co/Pt interface*, J. Appl. Phys. **86**, 3165 (1999).

[67] S. Uba, L. Uba, A. N. Yaresko, A. Y. Perlov, V. N. Antonov, and R. Gontarz, *Experimental and ab-initio theoretical study of optical and magneto-optical properties of Co/Cu multilayers*, J. Phys. Cond. Matter **9**, 447 (1997).

[68] S. Uba, A. N. Yaresko, L. Uba, A. Y. Perlov, V. N. Antonov, R. Gontarz, and H. Ebert, *.Influence of alloy composition and local environment on the magneto-optical properties of Co_xPd_{1-x} alloys*, Phys. Rev. B **57**, 1534 (1998).

[69] K. Sato, E. Takeda, M. Akita, M. Yamaguchi, K. Takanashi, S. Mitani, H. Fujimori, and Y. Suzuki, *Magneto-optical spectra of Fe/Au artificial superlattices modulated by integer and noninteger atomic layers*, J. Appl. Phys. **86**, 4985 (1999).

[70] S. D. Bader and J. Erskine, *in: Ultrathin Magnetic Structures II, B. Heinrich and J.A.C. Bland Eds.* (Springer-Verlag, Berlin, Heidelberg, 1994).

[71] V. Kamberský, L. Wenzel, and A. Hubert, *Magneto-optical interference and diffraction in isotropic and uniaxial multilayers*, J. Magn. Magn. Mater. **189**, 149 (1998).

[72] C. Marlière, D. Renard, and J.-P. Chauvineau, *Study of interface roughness and crystallographic structure of Au/Co/Au sandwiches*, Thin Solid Films **201**, 317 (1991).

[73] J. Corno, M. Galtier, D. Renard, J. P. Renard, and F. Trigui, *In situ resistivity and magnetoresistance studies of Co/Au(111) single layers and bilayers*, Eur. Phys. J. B **10**, 223 (1999).

[74] B. Voigtländer, G. Meyer, and N. M. Amer, *Epitaxial growth of thin magnetic cobalt films on Au(111) studied by scanning tunneling microscopy*, Phys. Rev. B **44**, 10354 (1991).

[75] C. Chappert, K. L. Dang, P. Beauvillain, H. Hurdequint, and D. Renard, *Ferromagnetic resonance studies of very thin cobalt films on a gold substrate*, Phys. Rev. B **34**, 3192 (1986).

[76] F. Hakkens, A. De Veirman, W. Coene, and F. den Broeder, *Transmission electron microscopy study of Co/Pd and Co/Au multilayers*, J. Mater. Res. **8**, 1019 (1993).

[77] N. Mliki, K. Abdelmoula, C. Leroux, and G. Nihoul, *Visibility of cobalt ultrathin films in standart bright field electron microscopy: possibilities of qualitative observations*, Phil. Mag. B **71**, 913 (1995).

[78] C. Train, M. Nývlt, B. Bartenlian, P. Beauvillain, V. Mathet, R. Mégy, and Š. Višňovský, *Spectroscopic PMOKE evidence of Au/Co segragation in $Au_{50}Co_{50}$ cover layer deposited on Co(0001)/Au(111) with perpendicular anisotropy*, J. Magn. Magn. Mater. **165**, 417 (1997).

[79] V. Grolier, D. Renard, B. Bartenlian, P. Beauvillain, C. Chappert, C. Dupas, J. Ferré, M. Galtier, E. Kolb, M. Mulloy, J.-P. Renard, and P. Veillet, *Unambiguous evidence of oscillatory magnetic coupling between Co layers in ultrathin vacuum grown Co/Au(111)/Co trilayers*, Phys. Rev. Lett. **71**, 3023 (1993).

[80] H. Ding, S. Pütter, H. Oepen, and J. Kirschner, *Spin-reorientation transition in thin films studied by the component-resolved Kerr effect*, Phys. Rev. B **63**, 134425 (2001).

[81] P. Bruno, G. Bayreuther, P. Beauvillain, C. Chappert, G. Lugert, D. Renard, J. Renard, and J. Seiden, *Hysteresis properties of ultrathin ferromagnetic films*, J. Appl. Phys. **68**, 5759 (1990).

[82] R. Urban, M. Nývlt, Š. Višňovský, J. Ferré, D. Renard, M. Galtier, and P. Beauvillain, *Effect of roughness on the interface contribution to polar Kerr effect in Au/Co ultrathin film structures*, J. Magn. Soc. Jpn. **22**, Suppl. S2, 197 (1998).

[83] V. Grolier, J. Ferré, A. Maziewski, E. Stefanowicz, and D. Renard, *Magneto-optical anisometry of ultrathin cobalt films*, J. Appl. Phys. **73**, 5939 (1993).

[84] P. B. Johnson and R. W. Christy, *Optical constants of transitions metals*, Phys. Rev. B **9**, 5056 (1974).

[85] H. Brändle, D. Weller, J. C. Scott, S. S. P. Parkin, and C.-J. Lin, *Optical and magneto-optical characterization of evaporated Co/Pt alloys and multilayers*, IEEE Trans. Magn. **28**, 2967 (1992).

[86] T. Katayama, Y. Suzuki, H. Awano, Y. Nishihara, and N. Koshizuka, *Enhancement of the magneto-optical Kerr rotation in Fe/Cu bilayered films*, Phys. Rev. Lett. **60**, 1426 (1988).

[87] W. Geerts, Y. Suzuki, T. Katayama, K. Tanaka, K. Ando, and S. Yoshida, *Thickness-dependent oscillation of the magneto-optical properties of Au-sandwiched (001) Fe films*, Phys. Rev. B **50**, 12581 (1994).

[88] R. Mégy, A. Bounouh, Y. Suzuki, P. Beauvillain, P. Bruno, C. Chappert, B. Lecuyer, and P. Veillet, *Magneto-optical-Kerr-effect study of spin-polarized quantum-well states in a Au overlayer on a Co(0001) ultrathin film*, Phys. Rev. B **51**, 5586 (1995).

[89] W. R. Bennett, W. Schwarzacher, and W. F. Egelhoff, Jr., *Concurrent enhancement of Kerr rotation and antiferromagnetic coupling in epitaxial Fe/Cu/Fe structures*, Phys. Rev. Lett. **65**, 3169 (1990).

[90] M. Nývlt, Š. Višňovský, J. Ferré, D. Renard, and M. Galtier, *Spectroscopic study of oscillatory polar Kerr effect in Co/Au(111)/Co magnetic bilayers*, 15th International Colloquium on Magnetic Films & Surfaces, Queensland, Australia (1997).

[91] D. E. Aspnes, in *Handbook of optical constants of solid*, edited by E. Palik (Academic Press Handbook Series, London, 1985).

[92] M. Abe and M. Gomi, *Magneto-optical effect and effective dielectric tensor in composite material containing magnetic fine particles or thin layers*, Jpn. J. Appl. Phys. **23**, 1580 (1984).

[93] R. Schäfer, *Magneto-optical domain studies in coupled magnetic multilayers*, J. Magn. Magn. Mater. **148**, 226 (1995).

[94] G. Pénissard, P. Meyer, J. Ferré, and D. Renard, *Magneto-optic depth sensitivity to local magnetization in a simple ultrathin film structure*, J. Magn. Magn. Mater. **146**, 55 (1995).

[95] J. Ferré, P. Meyer, M. Nývlt, Š. Višňovský, and D. Renard, *Magneto-optical depth sensitivity in a simple ultrathin film structure*, J. Magn. Magn. Mater. **165**, 92 (1997).

[96] M. Pufall, C. Platt, and A. Berger, *Layer-resolved magnetometry of a magnetic bilayer using the magneto-optical Kerr effect with varying angle of incidence*, J. Appl. Phys. **85**, 4818 (1999).

[97] J. Hamrle, J. Ferré, M. Nývlt, and Š. Višňovský, *In-depth resolution of magneto-optical Kerr effect in ferromagnetic multilayers*, Phys. Rev. B **66**, 224423 (2002).

[98] G. Prinz, *Magnetoelectronics*, Science **282**, 1660 (1998).

[99] J. Bland, C. Daboo, M. Patel, and T. Fujimoto, *Interface selective vector magnetometry of FeNi/Cu/Co trilayer spin-valve structures*, Phys. Rev. B **57**, 10272 (1998).

[100] Y. Kobayashi, S. Nasu, T. Emoto, and T. Shinjo, ^{197}Au *Mössbauer study of Au/M (M=Fe, Co, Ni) multilayers*, J. Magn. Magn. Mater. **156**, 45 (1996).

[101] T. Emoto, N. Hosoito, and T. Shinjo, *Magnetic polarization in Au layers of Au/M (M=Fe, Co, Ni) multilayers with* ^{119}Sn *probes studied by Mössbauer spectroscopy*, J. Magn. Magn. Mater. **189**, 136 (1998).

[102] F. Nolting, A. Scholl, J. Stöhr, J. Seo, J. Fompeyrine, H. Siegwart, J.-P. Locquet, S. Anders, J. Luning, E. Fullerton, M. Toney, M. Scheinfein, and H. Padmore, *Direct observation of the alignment of ferromagnetic spins by antiferromagnetic spins*, Nature **405**, 767 (2000).

[103] H. Ohldag, T. Regan, J. Stöhr, A. Scholl, F. N. nad J. Lüning, C. Stamm, S. Anders, and R. White, *Spectroscopic identification and direct imaging of interfacial magnetic spins*, Phys. Rev. Lett. **87**, 247201 (2001).

[104] J. Camarero, Y. Pennec, J. Vogel, M. Bonfim, S. Pizzini, M. Cartier, F. Ernult, F. Fettar, and B. Dieny, *Dynamic properties of magnetization reversal in exchange-coupled NiO/Co bilayers*, Phys. Rev. B **64**, 172402 (2001).

[105] M. Bonfim, G. Ghiringhelli, F. Montaigne, S. Pizzini, N. Brookes, F. Petroff, J. Vogel, J. Camarero, and A. Fontaine, *Element-Selective Nanosecond Magnetization Dynamics in Magnetic Heterostructures*, Phys. Rev. Lett. **86**, 3646 (2001).

[106] F. Ott, *Réflectivité de neutrons polarisés. Diffusion hors spéculaire sur des structures périodiques.*, Ph.D. thesis, Saclay, France, (1998).

[107] V. Grolier, *Propriétés magnétiques statiques et dynamiques des couches ultra-minces Co/Au: étude magnéto-optique.*, Ph.D. thesis, Université Paris XI, Orsay, (1994).

[108] K. Nakagawa and A. Itoh, *Multi-wavelengths read-out for multi-valued MO recording*, J. Magn. Soc. Jpn. **20**, 73 (1996).

[109] T. Dietl, H. Ohno, and F. Matsukura, *Hole-mediated ferromagnetism in tetrahedrally coordinated semiconductors*, Phys. Rev. B **63**, 195205 (2002).

[110] T. Hayashi, S. Katsumoto, Y. Hashimoto, A. Endo, M. Kawamura, M. Zalatutdinov, and Y. Iye, Physica B **284-288**, 1175 (2000).

[111] G. Moore, M. Moreno, J. Ferré, and L. Daweritz, *Magnetic anisotropy and switching process in the diluted GaMnAs magnetic semiconductor films*, to be published .

[112] M. Nývlt, J. Ferré, J. Jamet, P. Houdy, P. Boher, Š. Višňovský, R. Urban, and R. Lopušník, *Magneto-optical effects in a stack of magnetic multilayer-dielectric films*, J. Magn. Magn. Mater. **156**, 175 (1996).

[113] J. Pommier, J. Jamet, J. Ferré, P. Houdy, P. Boher, and F. Pierre, *Magnetic and magneto-optical properties of Tb/Fe multilayers*, J. Magn. Magn. Mater. **136**, 251 (1994).

[114] N. Saito, R. Sato, N. Kawamura, and M. Kajiura, *Multi-valued Magneto-Optical Recording in TbFe/SiO Compositionally Modulated Films*, Jap. J. Appl. Phys. **28**, 343 (1989).

[115] J. Tappert, S. Neumann, J. Jungermann, W. Kim, T. Ruckert, R. Brand, W. Keune, and W. Kleemann, *Fe spin structure in Tb/Fe multilayers*, Phil. Mag. B **80**, 257 (2000).

[116] K. Nakagawa, A. Itoh, K. Shimazaki, M. Yoshihiro, and N. Ohta, *High SNR readout method for double layered MO disk with single wavelength LASER beam*, J. Mag. Soc. Jpn. **23**, 221 (1999).

[117] W. Press, S. Teukolsky, W. Vetterling, and B. Flannery, *Numerical recipes in C: The art of scientific computing* (Cambridge University Press, Cambridge, 1992).

[118] V. Repain, *Auto-organisation sur les surfaces cristallines et applications à la croissance de nanostructures*, Ph.D. thesis, Université Paris VII, (2001).

[119] S. Rousset, F. Pourmir, J. Berroir, J. Klein, J. Lecoeur, P. Hecquet, and B. Salanon, *Self-organization on Au(111) vicinal surfaces and the role of surface stress*, Surf. Sci. **422**, 33 (1999).

[120] R. Phaneuf, N. Bartelt, E. Williams, W. Scwiech, and E. Bauer, *Low-Energy-Electron-Microscopy investigations of orientational phase separation on vicinal Si(111) surfaces*, Phys. Rev. Lett. **67**, 2986 (1991).

[121] R.K.Kawakami, E. Escorcia-Aparicio, and Z. Qiu, *Symmetry-induced magnetic anisotropy in Fe films grown on a stepped Ag(100)*, Phys. Rev. Lett. **77**, 2570 (1996).

[122] A. Frank, J. Jorzick, M. Rickart, M. Bauer, J. Fassbender, S. Demokritov, B. Hillebrands, M. Scheib, A. Keen, A. Petukhov, A. Kirilyuk, and T. Rasing, *Growth and magnetic properties of Fe films on vicinal TO(001) substrates*, J. Appl. Phys. **87**, 6092 (2000).

[123] P. Haibach, M. Huth, and H. Adrian, *Step-edge induced anisotropic domain-wall propagation*, Phys. Rev. Lett. **84**, 1312 (2000).

[124] A. Pethukov, A. Kirilyuk, and T. Rasing, *Surface-induced transverse magneto-optical Kerr effect*, Phys. Rev. B **59**, 4211 (1999).

[125] J. Hamrle, J. Ferré, J. Jamet, V. Repain, G. Baudot, and S. Rousset, *Vicinal interface sensitive magneto-optical Kerr effect: Application to Co/Au(322)*, Phys. Rev. B **67**, 155411 (2003).

[126] J. Kvasnica, *Statistická fyzika* (Academia, Praha, 1998 (2nd edition)), [in czech].

[127] E. Kondorsky, J. Phys (Moscow) **2**, 161 (1940).

[128] G. Spierings, V. Koutsos, H. Wierenga, M. Prins, D. Abraham, and T. Rasing, *Interface magnetism studied by optical second harmonic generation*, J. Magn. Magn. Mater **121**, 109 (1993).

[129] R. Atkinson and N. Kubrakov, *Boundary conditions in the simplest model of linear and second harmonic magneto-optical effects*, Phys. Rev. B **65**, 014432 (2002).

[130] A. Zvezdin and N. Kubrakov, *Nonlinear magneto-optical Kerr effects*, Zh. Éksp. Teor. Fiz. (J. of Exp. and Theor. Phys.) **89**, 77 (1999).

[131] J. Hamrle, L. Polerecký, and J. Ferré, *Theory of SHG from multilayer systems based on electric point-dipole radiation—application to magnetic multilayers*, submitted to PRB (2003).

[132] B. Saleh and M. Teich, *Fundamentals of Photonics* (John Wiley & Sons, inc., New York, 1991).

[133] V. V. Pavlov, G. Tessier, C. Malouin, P. Georges, A. Brun, D. Renard, P. Meyer, J. Ferré, and P. Beauvillain, *Observation of magneto-optical second-harmonic generation with surface plasmon excitation in ultrathin Au/Co/Au films*, Appl. Phys. Lett. **75**, 190 (1999).

[134] G. Tessier, C. Malouin, P. Georges, A. Brun, D. Renard, V. V. Pavlov, P. Meyer, J. Ferré, and P. Beauvillain, *Magnetization-induced second-harmonic generation enhanced by surface plasmons in ultrathin Au/Co/Au metallic films*, Appl. Phys. B **68**, 545 (1999).

[135] B. Sedlák and I. Štoll, *Elektřina a magnetismus* (Academia, Praha, 1993).

[136] J. Sipe, D. Moss, and H. van Driel, *Theory for the nonlinear magneto-optical Kerr effect at ferromagnetic transition-metal surfaces*, Phys. Rev. B **35**, 1129 (1987).

[137] A. Petukhov and A. Liebsch, *Surface anisotropy in optical second harmonic generation I. Al(111)*, Surface Science **334**, 195 (1995).

[138] J. Güdde, J. Hohlfeld, and E. Matthias, *About the depth sensitivity of second-harmonic radiation in ultra-thin metal films*, Appl. Phys. B **74**, 691 (2002).

[139] U. Conrad, J. Güdde, V. Jähnke, and E. Matthias, *Phase effects in magnetic second-harmonic generation on ultrathin Co and Ni films on Co(001)*, Phys. Rev. B **63**, 144 417 (2001).

[140] Y. Wu, R. Vollmer, H. Regensburger, X.-F. Jin, and J. Kirschner, *Magnetization induced Second Harmonic Generation from the Ni/Cu interface in multilayers on Cu(001)*, Phys. Rev. B **63**, 054401 (2001).

[141] U. Pustogowa, W. Hübner, and K. Bennemann, *Theory for the nonlinear magneto-optical Kerr effect at ferromagnetic transition-metal surfaces*, Phys. Rev. B **48**, 8607 (1993).

[142] R. Pan, H. Wei, and Y. Shen, *Optical second-harmonic generation from magnetized surfaces*, Phys. Rev. B **39**, 1229 (1989).

[143] V. Pavlov, J. Ferré, P. Meyer, G. Tessier, P. Georges, A. Brun, P. Beauvillain, and V. Mathet, *Linear and non-linear magneto-optical studies of Pt/Co/Pt thin films*, J. Phys.: Condens. Matter **13**, 9867 (2001).

[144] R. Sbiaa, *Multicouches magnétooptiques de terres rares et de métaux de transition couplées par échange*, Ph.D. thesis, Université Paris 7, (1996).

[145] R. Sbiaa, private communication (unpublished).

[146] W. H. Meiklejohn and C. P. Bean, *New magnetic anisotropy*, Phys. Rev. **102**, 1413 (1956).

[147] J. Camarero, Y. Pennec, J. Vogel, M. Bonfim, S. Pizzini, F. Ernult, F. Fettar, F. Garcia, F. Lancon, L. Billard, B. Dieny, A. Tagliaferri, and N. Brookes, *Perpendicular interlayer coupling in FeNi/NiO/Co trilayers*, not yet published (2003).

[148] F. Ernult, *Anisotrpie d'echange et frustration magnétique dans des bicouches ferro/antiferro et des tricouches ferro/antiferro/ferromagnétique*, Ph.D. thesis, Université Joseph Fourier, Grenoble, France, (2002).

[149] *Handbook of optical constants of solid*, edited by E. Palik (Academic Press Handbook Series, London, 1985).